Plasma Physics Reports, Vol. 27, No. 3, 2001, pp. 181–194. Translated from Fizika Plazmy, Vol. 27, No. 3, 2001, pp. 195–208.

TOKAMAKS

Study of Discharge Quenching in the T-10 Tokamak by Injecting High-*Z* Impurity Pellets

V. M. Timokhin, V. Yu. Sergeev, and B. V. Kuteev

St. Petersburg State Technical University, Politekhnicheskaya ul. 29, St. Petersburg, 195251 Russia

Received October 27, 1999; in final form, September 27, 2000

Abstract—The problem of the fast quenching of a discharge in tokamaks by injecting high-*Z* impurity pellets is considered. Results are presented from experiments in the T-10 tokamak, in which a substantial decrease (up to 70%) in the thermal plasma energy was observed. A one-dimensional transport code is developed to describe tokamak-discharge quenching. The code is used to simulate the experiments on quenching the T-10 discharge. It is shown that the injection of a high-*Z* pellet into the T-10 plasma changes the transport coefficients as compared to their steady-state values derived from the energy balance or scalings. *© 2001 MAIK "Nauka/Interperiodica".*

1. INTRODUCTION

Fast removal of thermal and magnetic energy from the plasma of a tokamak reactor is necessary under emergency conditions and may also be required under standard operating conditions. Among the emergency conditions, first of all, we mention the major disruption and instability related to the vertical displacement of the plasma column as well as any other undesirable processes requiring urgent termination (quenching) of a discharge.

Even in modern facilities, during an uncontrollable major disruption or vertical-displacement event, the stored plasma energy may be released locally at the divertor elements, which results in their destruction. In addition, the conducting elements of the installation are exposed to extreme mechanical loads due to currents induced in them. Both of these factors reduce the reliability and lifetime of the machine.

The problem of fast discharge quenching becomes even more important for the ITER tokamak reactor, in which the stored plasma energy is expected to attain 3 GJ [1]. This energy is high enough to evaporate several kilograms of the wall material, which is unacceptable. Switching to the regime of fast discharge termination in response to an instability precursor may become an efficient means for maintaining normal device operation. On the other hand, under standard operating scenarios, shortening the time required for quenching the discharge decreases pauses in the device operation, thereby increasing the mean power. That is why methods of fast discharge quenching have actively been sought in recent years.

The simplest way of quenching a discharge is to produce an intense source of radiation power loss in a plasma in order for the plasma energy to be converted into radiant energy and be dissipated uniformly on the surface of the first wall. In this case, the loads on the first wall of the device are expected not to exceed allowable values [2]. As methods for delivering a radiating material into a plasma, the injection of gas and liquid jets or pellets are considered [1]. It was pointed out that the main problems associated with plasma cooling and increasing the plasma density are a major disruption, the probability of which is high if the corresponding density limit is exceeded [3], and the generation of a beam of runaway electrons [4]. Favorable conditions for the generation of runaways are created due to a substantial growth in the toroidal electric field as a consequence of both the decrease in the plasma temperature and the increase in the effective ion charge number. According to the current concept, the generation of runaways is associated with the avalanche effect, which is related to the transition of thermal electrons to the runaway regime after one close collision with a relativistic runaway electron [4].

The influence of the nuclear charge number on the plasma behavior during discharge quenching by different materials is still unclear. Low-*Z* materials are unlikely to cause an avalanche of runaway electrons. However, to reach the required level of radiation power loss, the amount of such material introduced into the plasma should be hundreds of times larger than the density limit [3], in which case the probability that a disruption will occur before most of the energy is removed from the plasma is evidently high. For high-*Z* materials, such as krypton and xenon, the radiation power loss ensuring the energy decay on time scales on the order of tens of milliseconds may be achieved if the density is twice as high as the density limit [2]. Such an excess can hardly be dangerous. Thus, experiments in the ASDEX Upgrade tokamak showed that exceeding the density limit by a factor of 2 after the injection of a deuterium pellet did not produce a disruption [5]. At the same time, for high-*Z* impurities ($Z > 6$), a more efficient generation of runaways is predicted [6]. In sum-

1063-780X/01/2703-0181$21.00

mary, the use of high-Z impurities for quenching ITER discharges depends on the efficiency of runaway generation and also on the development of methods for suppressing it.

Experimental studies of discharge quenching by injecting pellets with different nuclear charge numbers were carried out in the ASDEX Upgrade, T-10, JET, DIII-D, and JT-60 tokamaks [5, 7–9]. The information obtained on the plasma behavior is quite encouraging for heavy materials. Thus, in the ASDEX Upgrade, the discharge was quenched within 10–20 ms after the injection of a neon pellet and no runaway generation was observed [5]. In addition, it was pointed out that both mechanical loads on the constructing elements and the heat flux onto divertor plates were reduced substantially in comparison with their level during a usual disruption.

The generation of runaways observed in JT-60 was efficiently suppressed by small, externally produced helical perturbations of the magnetic field [9]. The plasma energy completely decayed within 5–10 ms after the injection of a large Ne pellet.

The modeling of the processes accompanying fast discharge quenching is currently in its initial stage. The only one-dimensional model, which is described in [6], fails to account for some important factors; in particular, it uses a simplified initial density distribution of the injected impurity (it is assumed to be proportional to the initial plasma density). Furthermore, the crossed terms describing how the heat and particle fluxes affect each other are omitted in the model. In our opinion, such simplifications may substantially change the conclusions inferred from this model in [6]. The development of an adequate model of discharge quenching and its testing using the available experimental database are currently among the central problems to be solved.

This paper is devoted to experimental studies of discharge quenching in the T-10 tokamak. In addition, our aim is to develop a 1D-model allowing one to take into account the initial impurity distribution and related heat and particle transport in order to describe the process of tokamak discharge quenching using pellet injection. In Section 2, we describe the experimental setup, the diagnostics used, and measurement techniques. Experimental results are presented and discussed in Section 3. The numerical model, basic equations, and the initial and boundary conditions are described in Section 4. In Section 5, we present the main simulation results and compare them with the experiment. In the Conclusion, the main results are summarized and the directions of further studies are outlined.

2. EXPERIMENTAL SETUP AND MEASUREMENT TECHNIQUES

Experiments on discharge quenching were carried out in the T-10 tokamak in the ohmic heating regime with the following parameters: plasma current I_p = 80–250 kA, loop voltage U_l = 1.2 V, toroidal magnetic field B_t = 2.5 T, limiter radius a_L = 0.3 m, total radiation power P_r = 70 kW, central electron temperature $T_e(0) \sim$ 1 keV, and line-averaged plasma density $\bar{n}_e = (2.5–4.5) \times 10^{19}$ m^{-3}.

The scheme of the experiment on pellet injection in the T-10 is described in detail in [11]. Impurities were intruded into the plasma by injecting pellets from top to bottom toward the axis of the plasma column. KCl or Ti pellets 0.3–0.6 mm in size were used. The injection velocity was V_p = 30–150 m/s. The size, velocity, and material of a pellet determined the radial profile and the power of the created radiation loss source. As a rule, pellets reached the middle of the minor radius a_L and the maximum amount of impurity material was deposited into this region. It should be noted that, since KCl is a fragile material, pellets sometimes broke down into several small fragments in the course of their acceleration. As a result, their penetration depth was reduced and the time interval during which impurities were injected into the plasma increased from ~1 ms (which is typical for the ablation of a single-piece pellet) to 2–4 ms. The reason for this spread in times is that fragments were accelerated in the gas flow to different velocities depending on their size.

Together with an injector, a number of auxiliary diagnostics were used in the experiments. A photographic camera installed on the outer side of the torus at an angle of 11° to the equatorial plane allowed us to trace the pellet trajectory. The exposure time (~15 ms) substantially exceeded the ablation time (<4 ms). From photographs, we could determine the pellet penetration depth and the impurity distribution along the minor radius. Examples of such photographs are presented in Fig. 1. It is seen that, in shot no. 61812 (Fig. 1a), a small single-piece pellet penetrates to a radius of 12 cm, whereas in shot no. 61905 (Fig. 1b), several fragments penetrating to 11 cm are evaporated.

A wide-angle photodetector installed in the injection port could measure visible radiation emitted from an evaporating pellet. As an example, Fig. 2 shows radiation signals for single-piece (Fig. 2a) and broken (Fig. 2b) pellets. This figure illustrates the fact that, if a pellet breaks down, the time interval during which an impurity is introduced into the plasma increases.

To monitor the penetration depth and velocity of a pellet and to refer the signal $I(r)$ to spatial coordinates, we used an array of collimated photodetectors, which was placed on the outside of the torus.

Pellets used in the experiment were small in size (<0.7 mm) and in mass (<10^{-3} g) and irregular in shape. For this reason, it was impossible to directly measure the amount of impurity injected into the plasma and the size of the injected pellet was estimated as follows.

From the known spatial profile of radiation of the pellet cloud $I(r)$, which was deduced from the wide-angle photodetector signal $I(t)$ or from photographs, we

calculated the increase in the line-averaged density, assuming the linear relation between the pellet ablation rate and radiation intensity:

$$\dot{N}(r) = \gamma I(r). \quad (1)$$

Dependence (1) is confirmed experimentally for lithium [12] and carbon [13] and agrees well with the results of calculations using the code of [14].

The increase in the electron density after injection was calculated neglecting the Shafranov shift and the radial plasma diffusion and assuming that perturbations of the electron density gained poloidal and toroidal symmetry in times much shorter than the radial-diffusion time. We used the following formula [12]:

$$\Delta n_e(r) = \frac{\dot{N} Z_{imp}(r)}{4\pi^2 R V_p r}, \quad (2)$$

where R and V_p are the major radius and the pellet velocity, respectively. The profile of the impurity charge number $Z_{imp}(r)$ was calculated self-consistently using the "average-ion" model [15] and the measured electron temperature profile $T_e(r)$. The increase in the density calculated from Eq. (2) for various viewing chords was compared with the experimental values obtained using interferometer signals. The change in the density was measured 2 ms after injection, when the toroidal symmetry had already been established and the diffusion expansion was still small. In this way, we chose the proportionality factor γ, which allowed us to determine the impurity ablation rate. Its value was used to calculate the effective diameter d_p of a pellet assuming that it is spherical in shape. The effective diameter was calculated by the formula

$$d_p = \left(\frac{6 m_{imp} \int_0^{\tau_{abl}} \dot{N} dt}{\pi \rho_{imp}} \right)^{1/3}, \quad (3)$$

where ρ_{imp} and m_{imp} are the mass density and the molecular mass of the pellet material, respectively, and τ_{abl} is the ablation time. For KCl, the mass density is $\rho_{KCl} = 1.99 \times 10^3$ kg/m^3 and $m_{KCl} = 1.24 \times 10^{-25}$ kg.

A rapid drift of the evaporated material along the major radius, which was predicted for a hydrogen pellet in [16, 17] and recently observed in experiments [18, 19], should not strongly affect the results of our measurements of the ablation rate. This assertion is based on the geometric features of the experiment. The lines of sight of the camera and wide-angle photodetector lie at a small angle to the major radius, whereas the pellets move vertically from top to bottom toward the axis of the plasma column. In addition, no significant drift of the pellet cloud was observed in the experiments on the injection of carbon pellets in the W7-AS stellarator [13].

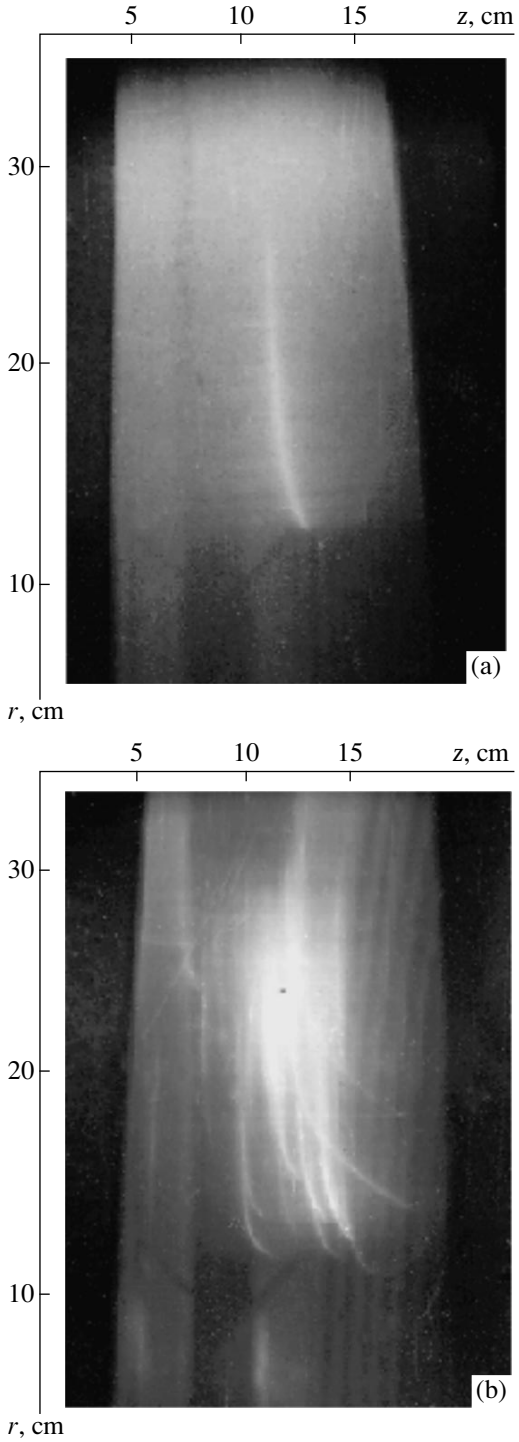

Fig. 1. Photographs of the trajectories of (a) a single-piece pellet (shot no. 61812) and (b) fragmented pellet (shot no. 61904).

For analysis and simulations, we used the data from the following main tokamak diagnostics: (i) A soft

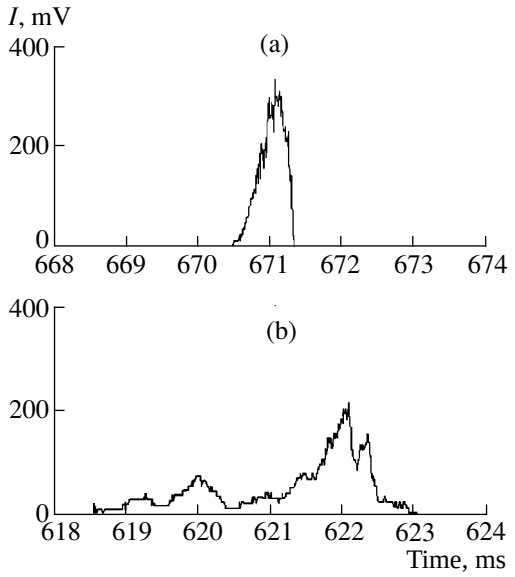

Fig. 2. Waveforms of the signals from the wide-angle photodetector $I(t)$ for shot nos. (a) 61812 and (b) 61904.

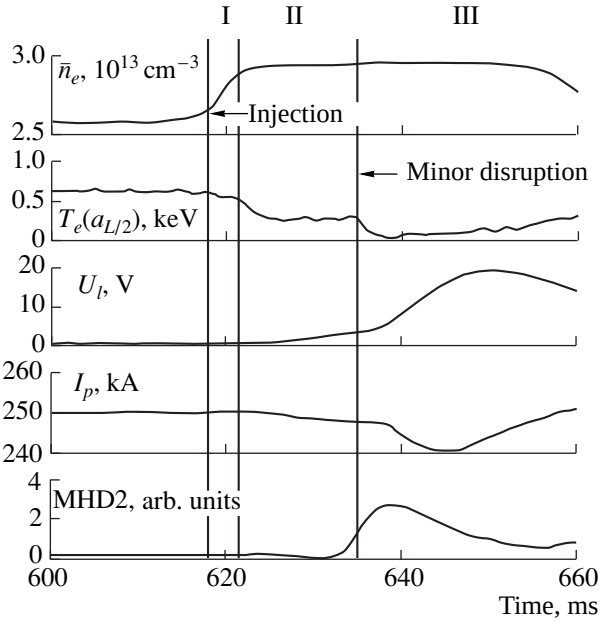

Fig. 3. Time evolution of the main plasma parameters after the injection of a KCl pellet (shot no. 61905). The main evolution stages are separated by vertical lines.

X-ray (SXR) amplitude analyzer [20] measured the electron temperature profile before pellet injection. In addition, a four-channel heterodyne receiver at the second harmonic of the electron cyclotron frequency could trace the time evolution of the electron temperature profile $T_e(r, t)$ [21]; the absolute values of the temperature were normalized to the temperature profile measured using the SXR diagnostics before pellet injection. (ii) An eight-chord microwave interferometer measured the time evolution of the electron density profile $n_e(r, t)$ [22]. (iii) The discharge current I_p and the loop voltage U_l were monitored using standard electromagnetic techniques. (iv) The MHD activity of the $m/n = 2/1$ mode in the discharge was monitored using MHD probes (MHD2 signals) [23].

3. EXPERIMENTAL RESULTS AND DISCUSSION

In experiments, pellets were injected in the steady-state (current plateau) and ramp-down phases of the discharge.

3.1. Injection of a KCl Pellet in the Steady-State Phase of the Discharge

Figure 3 shows the time evolution of the $\bar{n}_e$, $T_e(a_L/2)$, U_l, and MHD2 signals for a typical shot no. 61905; the pellet was injected in the steady-state phase of the discharge. The pellet entered the plasma at 619 ms; this time is marked in the plots by vertical lines. This discharge is characterized by the line-averaged density $\bar{n}_e \approx 2.6 \times 10^{19}$ m^{-3} and an effective pellet size d_p of about 390 μm (the penetration depth is $b \approx 10.5$ cm).

The evolution of the plasma parameters in the postinjection phase can be divided into several stages (Fig. 3). The first stage is determined by the processes of evaporation and ionization of the pellet material. It lasts for 1–4 ms, depending on the size, velocity, and integrity of the pellet. In the case of a single-piece pellet (Figs. 1a, 2a), this stage lasts no longer than 1.5 ms; otherwise (Figs. 1b, 2b), due to prolonged impurity injection, this stage can last up to 4 ms. A discharge with a long ablation and ionization stage is shown in Fig. 3.

In this stage, new cold electrons are produced in the plasma due to ionization of the impurity material, a radiation source is formed, and the plasma parameters gain poloidal and toroidal symmetry. The electron temperature decreases insignificantly (by 50–100 eV), whereas the electron density increases to values close to the maximum value.

In the second stage, the thermal plasma energy is converted into radiation emitted by the impurity injected into the plasma column. This is accompanied by radial diffusion of the impurity and an increase in the loop voltage (to 3–10 V) due to the generation of the induction field because of plasma cooling. In this stage, the electron temperature decreases markedly; the decrease in the thermal plasma energy can attain 70%. As a rule, this stage ends with a minor disruption, during which the electron temperature drops abruptly and the MHD activity increases. In the discharge illustrated in Fig. 3, a minor disruption occurs at 637 ms; this time

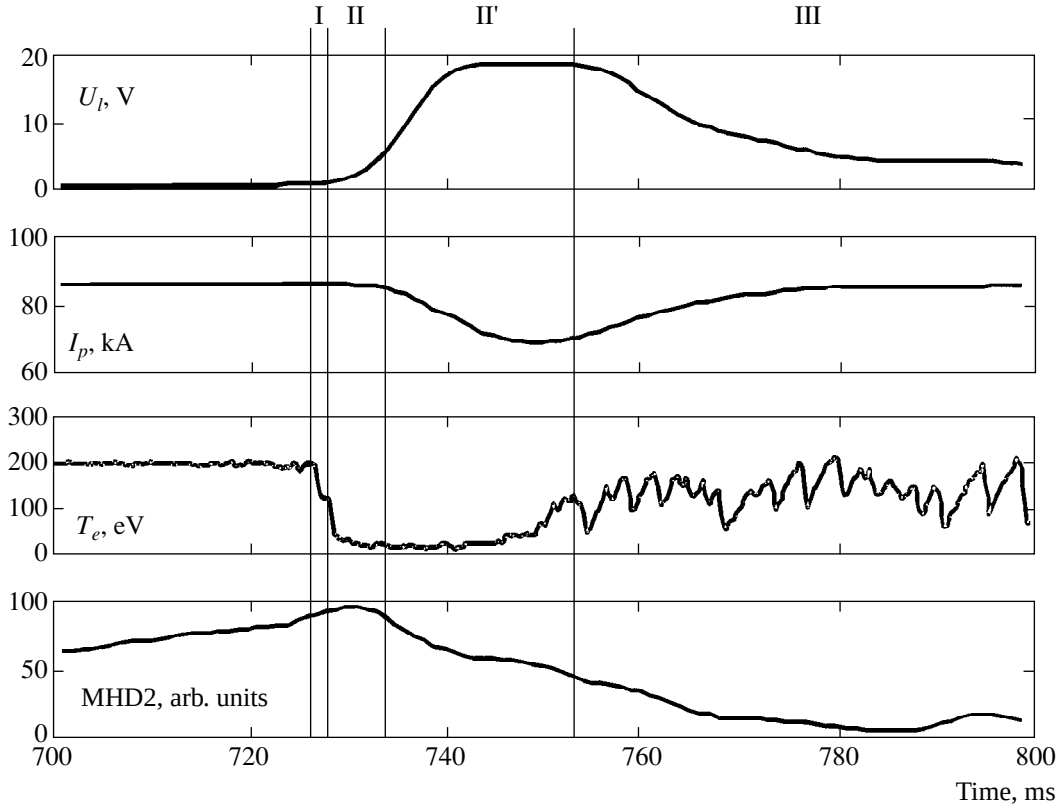

Fig. 4. Time evolution of the main plasma parameters after the injection of a Ti pellet (shot no. 65052).

is marked in the plots by vertical lines. The second stage lasts 5–30 ms and is usually much longer than the first stage. Sometimes, when small pellets are injected, a disruption does not occur at all and the distinct gradation between the second and third stages is absent.

The third stage lasts from the first minor disruption until the plasma parameters return to their steady-state values. This stage begins with an abrupt drop in the plasma temperature (2–5 ms after disruption, it decreases to its minimum value) and a substantial increase in the loop voltage to values above 30 V. It should be noted that interferometry frequently fails during this stage, which complicates the plasma density diagnostics for this stage. The first minor disruption may be followed by another minor disruption occurring after 20–30 ms or even several disruptions, which are also accompanied by an increase in the MHD activity and recovery of the temperature with a characteristic transport time. The duration of the third stage varies within a wide range depending on the pellet size and the number of minor disruptions. The main discharge parameters $\bar{n}_e$, T_e, and U_l relax to new steady-state values close to those in the preinjection phase 30–40 ms after the last minor disruption. This is because the impurity leaves the discharge during the characteristic diffusion time. When a KCl pellet is injected, the effective ion charge number Z_{eff} of the plasma increases by a factor of 2–3, which enhances the efficiency of ohmic plasma heating and affects the rate at which the temperature relaxes to its steady-state value.

The total plasma current during and after KCl pellet injection varies only slightly (<3%).

3.2. Injection of a Ti Pellet in the Steady-State Phase of the Discharge

Experiments with Ti pellet injection were carried out in regimes with a low current $I_p \approx 80$ kA and a line-averaged plasma density of $\bar{n}_e \approx 2 \times 10^{19}$ m^{-3}. In this case, the decrease in the total plasma current attained 20% of its plateau value. This corresponded to a decay of 50% of the magnetic energy of the plasma column. However, in this case as well, the current amplitude returned to its value before injection during 30–40 ms.

An example of a discharge in which the magnetic energy of the plasma column partially decays is illustrated in Fig. 4, which shows the evolution of the plasma parameters in shot no. 65052. In this case, a Ti pellet ~400 μm in size enters the plasma at 726 ms. Note that the stage of the thermal-energy decay shortens significantly (to 2–3 ms) in this discharge and there is a stage in which magnetic energy decays (Fig. 4, stage II"). Within the time interval from 735 to 760 ms, the feedback system cannot maintain the current constant and the current drops, whereas the loop voltage continues to grow. The saturation of the loop voltage

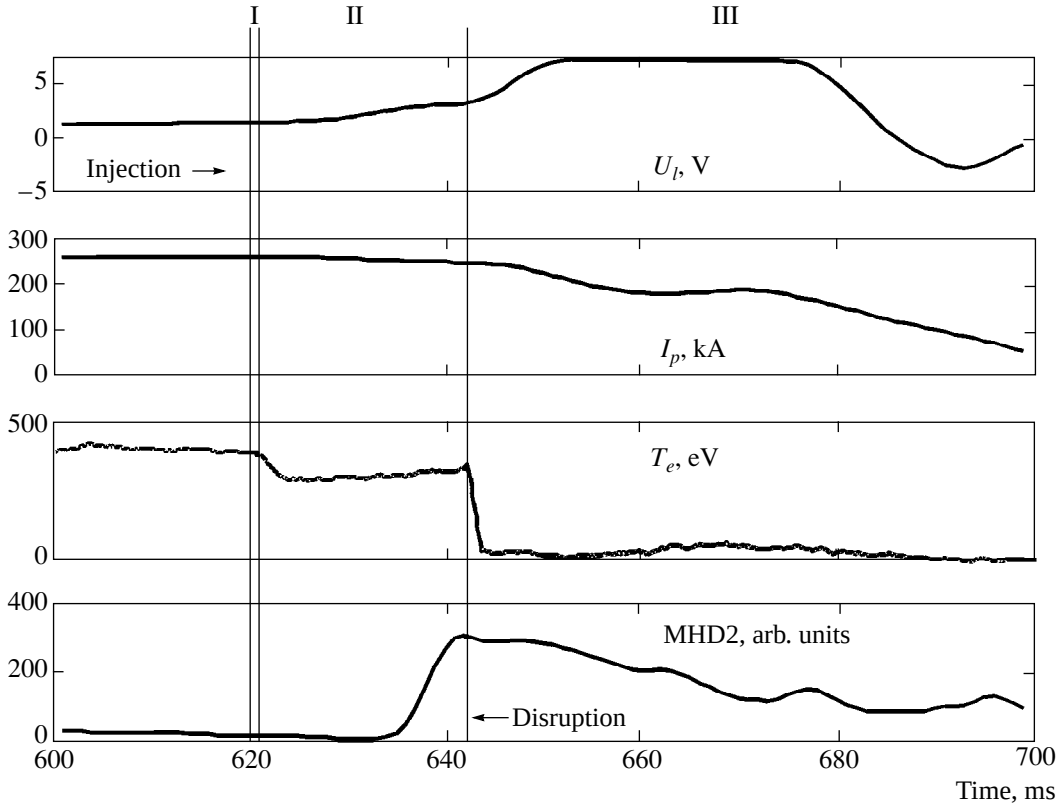

Fig. 5. Time evolution of the main plasma parameters after the injection of a KCl pellet in the current ramp-down phase (shot no. 62919).

signal at about 745 ms is a result of the overflow of an ADC register in the data acquisition system. We also note that the current decreases significantly when the plasma is cooled to a temperature on the order of 20–30 eV, which could not be achieved in the case of KCl pellet injection. The plasma temperature at which the magnetic plasma energy decays varies only slightly during the current quenching phase. In this case, the magnetic component of the plasma energy is converted into heat and, then, into radiation.

The MHD activity in this shot increases monotonically during the entire steady-state phase of the discharge, reaches its maximum 5 ms after injection, and then decreases sharply. The low MHD activity of the plasma after injection is probably the reason why no minor disruptions occur in this case. The discharge recovery occurs simultaneously with the build-up of sawtooth oscillations.

3.3. Injection of a KCl Pellet in the Current Ramp-down Phase

The evolution of the main plasma parameters in the case of pellet injection in the current ramp-down phase is similar to the case of injection in the current plateau phase. The main difference is that, in the current ramp-down phase, the plasma parameters after disruption are not restored (Fig. 5, shot no. 62919) and the thermal plasma energy decays almost completely in 30 ms.

With a given set of the parameters of the controlling program, the current in this discharge should fall to zero in a time of ~300 ms at a rate of 0.85 MA/s. Pellet injection shortens this time substantially; in this case, the current decays in a time of ~80 ms. From the loop voltage signal U_l in Fig. 5, it is seen that, in this case as well, the feedback system has no time to implement the program of maintaining the current-fall rate constant. As follows from the overflow of ADC registers in the data acquisition system, the loop voltage grows rapidly, while the current continues to fall.

3.4. Discussion of the Experimental Results

The table presents the main pellet parameters and the plasma parameters for the shots with KCl injection. These parameters will be used in further analysis. For each shot, the line-averaged plasma density before injection $\bar{n}_e$, the penetration radius b, the effective pellet size d_p, the maximum relative perturbation of the total number of plasma electrons $\Delta N_{e\max}/N_e$, the measured maximum relative decrease in the electron temperature at the center of the plasma column $-\Delta T_e(0)/T_e(0)$ and at the middle of the limiter radius

Parameters of the plasma and KCl pellets in the experiments on discharge quenching in the T-10 tokamak

Shot number	$\bar{n}_e$, 10^{19} m^{-3}	b, cm	d_p, μm	$N_{e\,\max}/N_e$, rel. units	$-\Delta T_e(0)/T_e(0)$, rel. units	$-\Delta T_e(a_L/2)/T_e(a_L/2)$, rel. units	Δt, ms
Steady-state phase of the discharge							
61811	2.55	11.5	–	–	0.2	0.25	–
61812	2.6	12	340	0.18(0.14)	0.25	0.45	35
61905	2.45	10.5	390	0.30(0.22)	0.45	0.55	13
61904	2.45	10	450	0.44(0.26)	0.55	0.7	6
61818	3.05	12	410	0.27	0.5	0.55	7
61819	3.05	11	–	–	0.5	0.6	6
61817	3.05	6	590	0.78	0.85	0.9	2
61898	4.1	8	–	–	0.2	0.3	15
61900	4.1	10.5	430	0.23	0.5	0.7	7
61897	4.1	8	430	0.23	0.5	0.7	4
61895	4.55	10.5	490	0.30	0.6	0.75	2
Current ramp-down phase							
62920	2.45	16	–	–	0.25	0.25	–
62919	2.45	8	–	–	0.3	0.45	22

$-\Delta T_e(a_L/2)/T_e(a_L/2)$, and the time intervals between the instant of injection and the first minor electron-temperature disruption (the total duration of stages I and II) Δt are presented.

The maximum perturbation of the total number of plasma electrons $\Delta N_{e\max}/N_e$ was calculated from the total impurity amount in the plasma, assuming that impurity is completely ionized. Actually, at temperatures of about 1 keV, the impurity is ionized only partially (Fig. 6). For some shots, the actual relative increase in the plasma density could not be determined because of the unstable operation of the microwave interferometer under conditions when the plasma density grew sharply. The measured values of the density increase (in the shots for which these measurements were successful) are given in the table in the same column (in brackets).

Note that Δt decreases as the plasma density in the preinjection phase or the impurity amount increases. In some shots with a small amount of the injected material, the disruption did not occur at all (see, e.g., shot no. 61811). This leads us to suggest that disruption occurs due to exceeding the density limit [3].

We also note that there is little difference between the value of the relative decrease in the electron temperature in the plasma center and that in the middle of the minor radius. In addition, this difference depends weakly on the pellet penetration depth (shot nos. 61900 and 61897). This evidences that impurities penetrate rapidly into the central plasma region.

It is seen from the table that, for a fixed relative value of the plasma density perturbation $\Delta N_{e\max}/N_e$, the discharge with a higher density is cooled more efficiently (compare, e.g., shot nos. 61905 and 61895). Evidently, this is due to a greater amount of impurity and higher radiation power per atom at a higher electron density.

The maximum pellet size was limited by the barrel diameter of the pellet gun and was equal to ~600 μm.

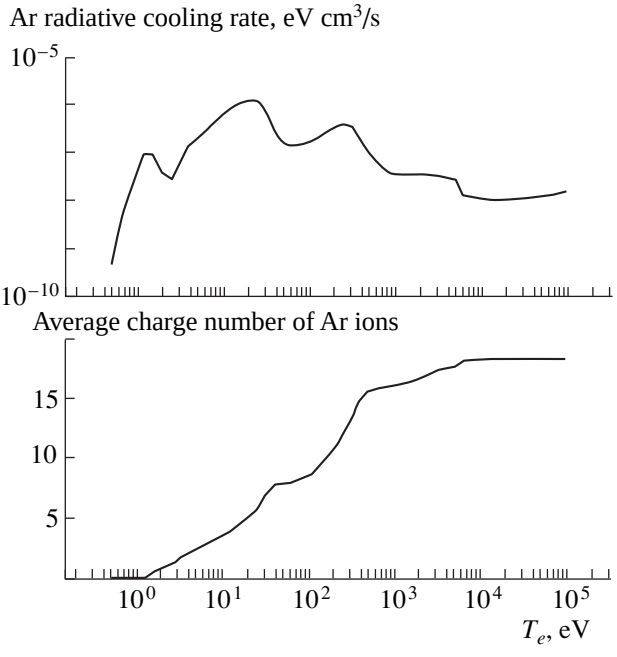

Fig. 6. Temperature dependences of the radiative cooling rate and the average charge number of argon ions calculated by the average-ion model [15] for the typical parameters of the T-10 plasma.

This size limited the number of injected impurity atoms by a level of 5×10^{18} (about 10% of the total number of plasma ions). The size limitation is the main reason why the plasma energy did not decay completely after injection. Injection only produced a substantial perturbation of the plasma parameters, which then usually returned to their steady-state values.

However, in experiments with KCl pellets, the thermal plasma energy decreased substantially. Thus, in shot no. 61817, the thermal energy decreased by 70%. In experiments with the injection of titanium, which has a higher emissivity, the magnetic energy could also decay in regimes with low densities and low currents. As was mentioned above, in shot no. 65052, the decrease in magnetic energy was about 50%. Hence, we can expect that the plasma energy in T-10 will decay completely if the amount of the injected impurity is increased by a factor of 2–3.

As to the reason why minor disruptions occur after the injection of a large amount of impurities, we may suggest that these disruptions are initiated by the growth of the $m/n = 2/1$ and $m/n = 3/2$ magnetic islands with their subsequent reconnection [7]. Probably, this growth is caused by the current redistribution provoked by pellet injection.

4. NUMERICAL MODEL

To simulate the process of plasma cooling after pellet injection, we developed a numerical code based on the following set of transport equations:

$$\frac{\partial n}{\partial t} + \frac{1}{r}\frac{\partial}{\partial r}(r\Gamma) = n_{imp}\frac{\partial Z_{imp}}{\partial t}, \tag{4}$$

$$\frac{\partial n_{imp}}{\partial t} + \frac{1}{r}\frac{\partial}{\partial r}(r\Gamma_{imp}) = 0, \tag{5}$$

$$\frac{3}{2}\frac{\partial nT}{\partial t} + \frac{1}{r}\frac{\partial}{\partial r}\left(r\left[q + \frac{5}{2}\Gamma T\right]\right) - \frac{\Gamma}{n}\frac{\partial nT}{\partial r} = n(Q_{oh} - Q_{imp} - Q_{br}), \tag{6}$$

$$\frac{\partial \sigma E}{\partial t} = \frac{c^2}{4\pi r}\frac{\partial}{\partial r}r\frac{\partial E}{\partial r}. \tag{7}$$

The set of equations written in cylindrical coordinates is solved with respect to the unknowns $n = n(r, t)$, $n_{imp} = n_{imp}(r, t)$, $T = T(r, t)$, and $E = E(r, t)$, which describe the profiles of the electron density, the density of injected-impurity ions, the electron temperature, and the toroidal electric field, respectively. Equations (4) and (5) describe the balance of electrons and impurity ions. It is assumed that the main source and sink on the right-hand side of Eq. (4) are the ionization and recombination of impurity ions. Here, Z_{imp} is the average impurity-ion charge number. When calculating the evolution of the plasma parameters, it is assumed that, at each time, the quasineutrality condition $n = n_D + Z_{imp}n_{imp}$ is satisfied, where n_D is the deuterium-ion density profile before pellet injection. Equation (6) describes the electron energy balance. Its right-hand side contains the main energy sinks Q_{br} and Q_{imp} (the bremsstrahlung power and the dominant-impurity radiation power) and the ohmic heating source Q_{oh}. Equation (7) is the Maxwell equation for the toroidal electric field. Here, the conductivity σ is assumed to be equal to the Spitzer conductivity and c stands for the speed of light in vacuum.

The electron and injected-impurity ion fluxes are written in the following form:

$$\Gamma = -D\frac{\partial n}{\partial r} + nV_p, \qquad \Gamma_{imp} = -D\frac{\partial n_{imp}}{\partial r} + n_{imp}V_p, \tag{8}$$

and the electron heat flux is

$$q = -\chi\frac{\partial T}{\partial r}. \tag{9}$$

The transport coefficients D and χ were assumed to be the same for electrons and impurity ions. They were chosen based on the Alcator scaling $D = \alpha/n$. The proportionality factor α and the ratio D/χ were the parameters of the problem.

The pinch velocity V_{ps} was determined from the measured electron density profile n_s in the preinjection phase and a given value of D_s using the formula

$$V_{ps} = \frac{D_s}{n_s}\frac{\partial n_s}{\partial r}. \tag{10}$$

When calculating further evolution, the ratio D_s/V_{ps} was assumed to be constant.

The main-impurity radiation power Q_{imp} and the average charge number of impurity ions Z_{imp} were calculated by the coronal equilibrium model in the average-ion approximation [15]. When calculating Q_{imp} and Z_{imp} for KCl, we used Ar data, which are known in more detail. The reason for this is that, in the temperature range of interest (100–1000 eV), the temperature dependences of Q_{imp} and Z_{imp} for average Ar ions are close to those for average KCl ions. Figure 6 shows the temperature dependences of the Ar radiation power and the average charge number of argon ions calculated by this model. The radiation power as a function of the temperature is nonmonotonic and is maximum near 20 eV.

The boundary conditions for Eqs. (4)–(7) were chosen as follows. At the plasma column axis, the condition $\left.\frac{\partial}{\partial r}\right|_{r=0} = 0$ was set for all of the functions. At the outer plasma boundary, the temperature and the electron density were fixed ($T(a, t) = \text{const}$ and $n(a, t) = \text{const}$) and the ion density of the injected impurity was

assumed to be zero: $n_{imp}(a, t) = 0$ (the absorbent wall). The electric field at the outer plasma boundary was a superposition of the field produced by the inductor according to the current-maintaining program and the plasma induction field. In this study, the boundary electric field was specified based on the experimentally measured loop voltage:

$$E(a, t) = U_l(t)/2\pi R. \quad (11)$$

The initial conditions for Eqs. (4)–(7) were calculated using the profiles of the parameters n, n_{imp}, T, and E in the preinjection phase. For the electron temperature and density, we used the data from interferometry and SXR diagnostics, respectively (Fig. 7). The n_{imp} and E profiles before injection were assumed to be constant over the minor radius ($n_{imp} = 0$). The value of E was calculated using Eq. (11) from the value of U_l in the preinjection phase for a given regime. From the profile $\dot{N}(r)$ derived from Eq. (1), the initial profile was determined:

$$n_{imp\,0}(r) = \frac{\dot{N}(r)}{4\pi^2 R V_p r}. \quad (12)$$

Assuming that the pressure was constant on a magnetic surface and the plasma parameters rapidly gained poloidal and toroidal symmetry, we determined the initial temperature and density profiles. To do this, we solved the following self-consistent set of equations:

$$\Delta p_0(r) = n(r)T(r) - n_0(r, T_0(r))T_0(r) = 0, \quad (13)$$

$$n_0(r, T_0(r)) = n(r) + n_{imp\,0}(r)Z_{imp}(r, T_0(r)). \quad (14)$$

The initial condition for the electric field E_0 was formulated in a similar way, assuming the current profile to be constant:

$$\Delta J_0(r) = \sigma(r, T(r))E(r) - \sigma_0(r, T_0(r))E_0(r) = 0. \quad (15)$$

In Eqs. (13)–(15), the zero index stands for the initial profiles and the profiles for the preinjection phase are written without indices. The initial conditions for shot no. 61812 and the steady-state profiles for this shot are shown in Fig. 7.

Calculation of the initial values by the method described above is correct if the total time required for a pellet to fly, evaporate, and ionize and for the plasma parameters to gain poloidal and toroidal symmetry is short compared to the time characteristic of further plasma evolution. In our case, these times are equal to 1–4 and 20–30 ms, respectively. Therefore, we can use the profiles obtained from Eqs. (12)–(15) as initial conditions for Eqs. (4)–(7). In general, when a fairly large amount of impurities is injected into the plasma, the process of discharge quenching lasts for several milliseconds; in this case, this approach is evidently inapplicable.

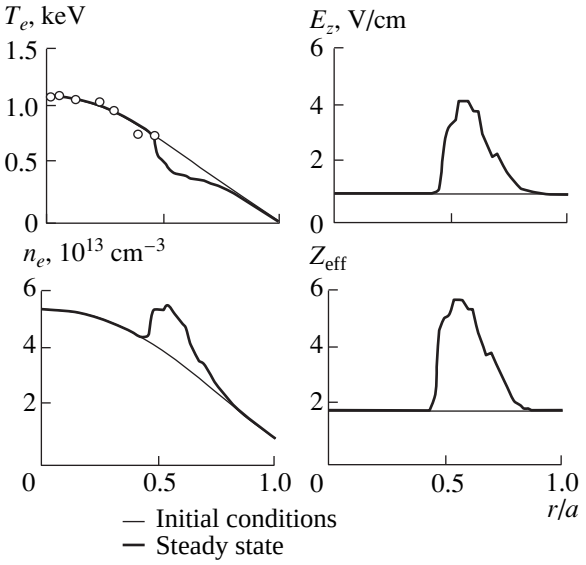

Fig. 7. The calculated profiles of the electron temperature T_e, toroidal electric field E_z, electron density n_e, and effective ion charge number Z_{eff} in the steady-state phase of the discharge (shot no. 61812) and the profiles of these quantities after pellet injection, which were used as the initial conditions for Eqs. (4)–(7). Circles show the experimental values of the electron temperature measured by SXR diagnostics before injection.

5. SIMULATION RESULTS

Shots for simulation were chosen taking into account the maximum available experimental data on both the evolution of the plasma parameters and the distribution of the injected impurity along the minor radius.

Figure 8 shows the results of simulations for shot no. 61812. In this shot, a KCl pellet containing about 6.5×10^{17} impurity atoms was injected into the plasma at 670 ms. The injection time is marked in the figure by a vertical line. In simulations, the transport coefficients were assumed to be equal to their steady-state values and it was assumed that $D/\chi = 1$. It is seen that, in this case, the increase in the line-averaged electron density as a function of time is described well by the model, whereas the measured decrease in the electron temperature in the central region of the plasma column is much more pronounced than the calculated one. Simulations even yield a weak increase in the electron temperature in the central region, which is explained by the relatively slow penetration of the emitting impurity into this region in comparison with the rearrangement of the current profile when the current is displaced from the cold plasma edge, where the injected impurity is mainly concentrated, toward the central region.

Figure 8 demonstrates the best simulation run; we failed to achieve a better agreement with the experiment by varying the plasma parameters. The simulation

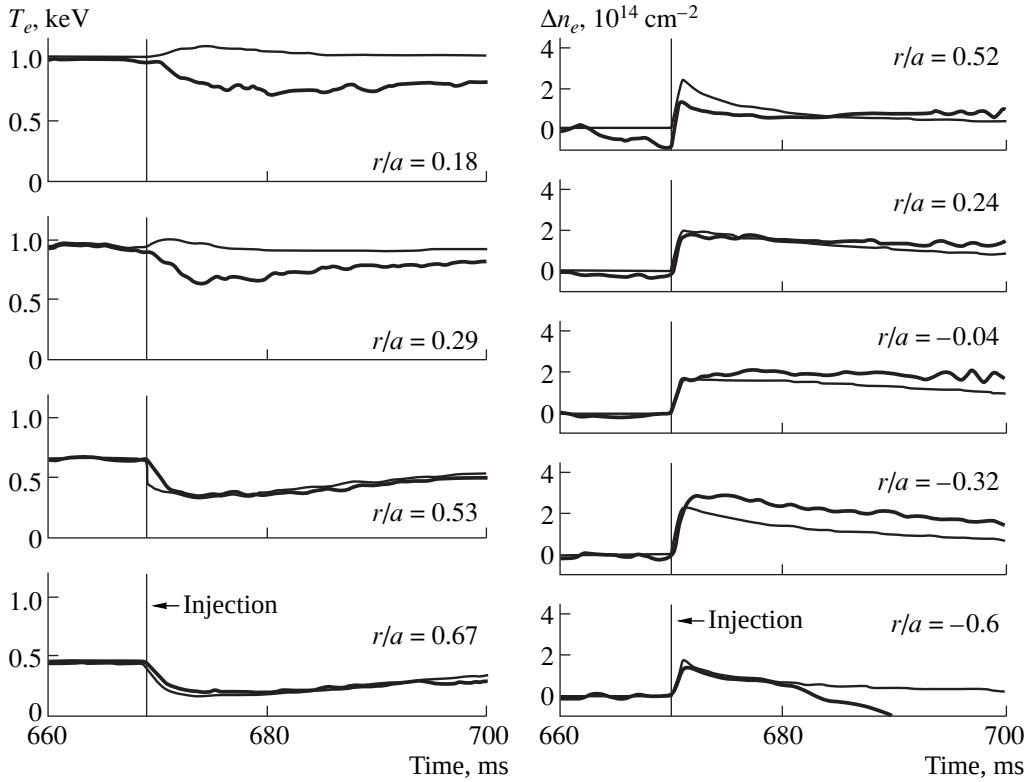

Fig. 8. Time evolution of the electron temperature (on the left) and line-averaged electron density (on the right) after pellet injection (shot no. 61812). Heavy lines show the experimentally measured evolution of the parameters, and light lines show the results of calculations without taking into account the enhanced-transport effects for $D/\chi = 1$. The viewing chords are indicated in the plots. The injection time is marked by light vertical lines.

parameters varied within the following ranges: $\alpha = (1–5) \times 10^{17}$ (cm s)$^{-1}$ and $D/\chi = 0.1–10$. We also took into account a possible error in determining the factor γ in Eq. (1), which gives the total number of impurity atoms brought with the pellet into the plasma (the effective pellet size). Accordingly, γ was varied within ±10% around its value calculated from the increase in the density due to injection [see Eq. (2)].

A criterion for the agreement between calculation and experiment was the minimum of the norm of the variance between the calculated and experimental time dependences of the plasma parameters:

$$\frac{1}{T}\sum_i \int \frac{(x^i_{calc}(t) - x^i_{exp}(t))^2}{\langle x^i_{exp}\rangle^2} dt. \qquad (16)$$

Here, $x^i_{exp}(t)$ is the experimental evolution of the ith parameter and $x^i_{calc}(t)$ is the calculated evolution. Integration and averaging were carried out over the entire time interval T in which calculations were compared with experiment, and summation was performed over all the parameters of interest.

Based on the analysis of simulation results, we can conclude that the behavior of the electron temperature measured in inner channels cannot be adequately described assuming that the transport coefficients D_s, χ_s, and V_{ps} remain unchanged (i.e., equal to their values in the preinjection phase) during plasma evolution. The character of the evolution shows that impurity injection substantially increases the transport coefficients. The increase in transport coefficients promotes the impurity penetration into the central region of the plasma column, which results in a stronger plasma cooling in this region and, as a consequence, a weaker distortion of the current profile. A similar effect, the so-called "enhanced transport" (ET), was revealed in certain existing devices and, at present, is under active study (see, e.g., [24, 25]).

To model the ET effect, the transport coefficients and the pinch velocity were multiplied by the factor

$$1 + F\exp(-t/\beta\tau_E). \qquad (17)$$

As a result, the transport coefficients increased by the factor $1 + F$, tending to their steady-state values in a time $\beta\tau_E$, where τ_E is the plasma energy confinement time. For T-10 discharge regimes used in these experiments, the time τ_E attained about 100 ms and varied only slightly from shot to shot. The parameters β and F determining the duration and amplitude of the transport-coefficient perturbations were chosen experimentally and were the parameters of the problem. The value

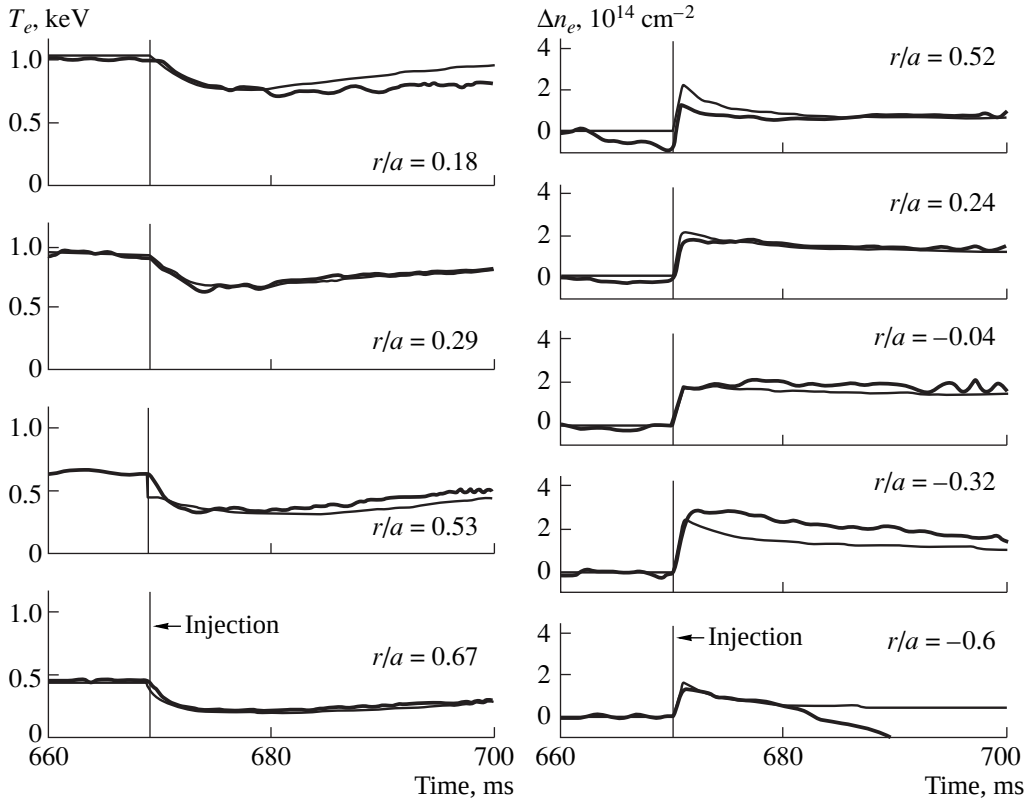

Fig. 9. Time evolution of the electron temperature (on the left) and line-averaged electron density (on the right) after pellet injection (shot no. 61812). Heavy lines show the experimentally measured evolution of the parameters, and light lines show the results of calculations taking into account the enhanced-transport effects for $D/\chi = 1/3$. The transport coefficients and the pinch velocity are multiplied by factor (17) with $F = 5$ and $\beta = 1/10$.

of β varied in the range 1/30–1/3, and the factor F varied within the range 1–10.

Figure 9 shows the results of simulations with allowance for the ET effect for the same shot no. 61812. The parameters characterizing transport-coefficient perturbations are $\beta = 1/10$ and $F = 5$; the ratio $D/\chi = 1/3$ corresponds to the threefold decrease in the diffusion coefficient D as compared to the simulations described above. This somewhat compensates for the increase in D due to the ET effect at a constant α. The other parameters are the same as in the simulations presented in Fig. 8. It is seen that, with the ET effect incorporated into it, the model satisfactorily describes the behavior of the electron temperature measured in inner channels and, as previously, describes well the behavior of the electron temperature measured in outer channels and the behavior of the plasma density measured by interferometry.

Figure 10 shows the results of calculations of the response of the electron temperature to KCl pellet injection in two other shots. In this case, the amount of injected impurity is somewhat greater than that for the shot considered above. In shot no. 61905, 1.0×10^{18} impurity atoms were injected, whereas in shot no. 61904, 1.5×10^{18} atoms were injected. The pellet flew into the plasma at 619 ms in both shots. In these shots, a minor disruption (marked by the second thin vertical line in the figure) occurred at 15 and 8 ms after injection, respectively. Since disruption mechanisms are not incorporated into the model, simulations can adequately describe the evolution of the plasma parameters only until a disruption.

From Fig. 10, it is seen that, as the amount of injected impurity increases, the discrepancy between the modeled and experimental behavior of the electron temperature measured in inner channels becomes more pronounced. Therefore, it may be suggested that the changes in the transport coefficients depend on the amount of the injected impurity. To verify this, we performed simulations in which the changes in the transport coefficients increased proportionally to the amount of atoms injected into the discharge ($F = 7.8$ for shot no. 61905 and $F = 11.5$ for shot no. 61904). The results of simulations are illustrated in Fig. 11. It is seen that the behavior of the electron temperature measured in inner channels is described better in this case. Most clearly, this is seen in shot no. 61904.

The physical picture of the ET effect is still poorly understood. One of the possible mechanisms for enhanced transport may be related to an increase in magnetic field fluctuations and, as a consequence, a

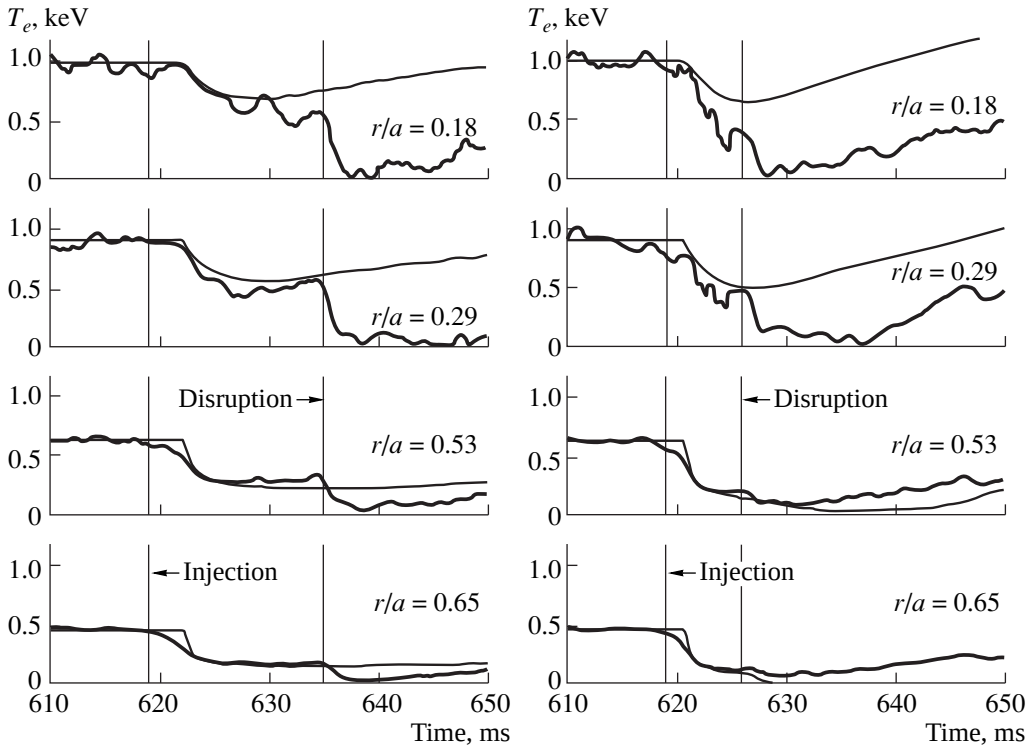

Fig. 10. Time evolution of the electron temperature in shot nos. 61905 (on the left) and 61904 (on the right) after pellet injection. The parameters and notation correspond to Fig. 9.

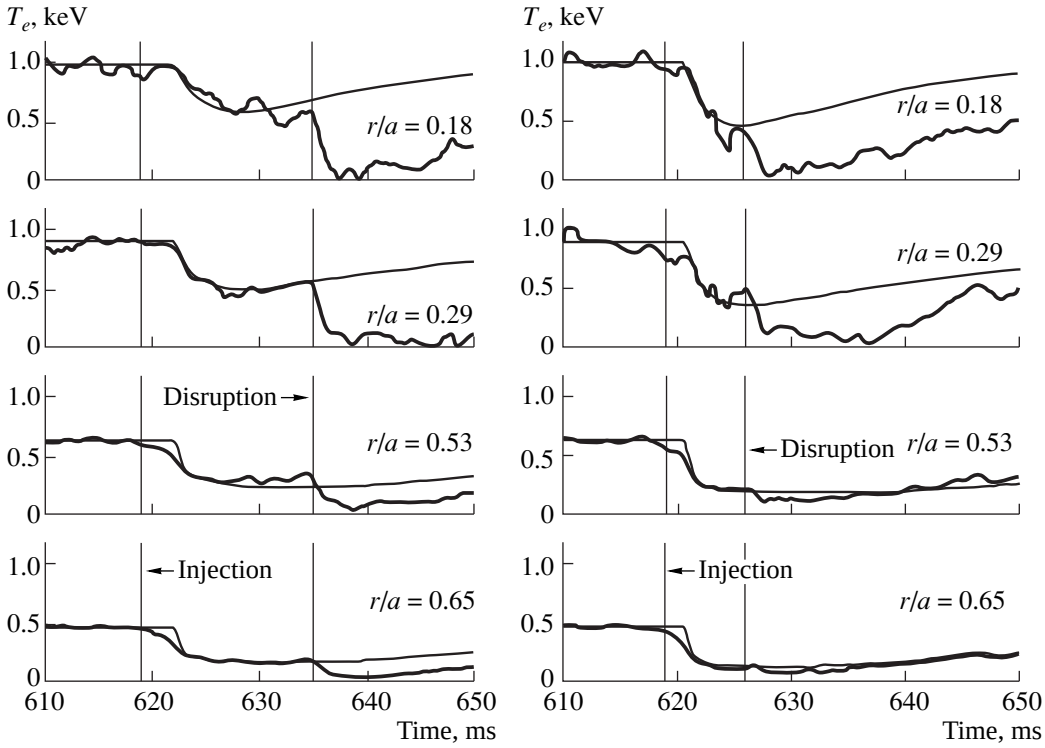

Fig. 11. Time evolution of the electron temperature in shot nos. 61905 (on the left) and 61904 (on the right) after pellet injection. The transport coefficients and the pinch velocity are multiplied by factor (17) with $\beta = 1/10$, $F = 7.8$ for shot no. 61905, and $F = 11.5$ for shot no. 61904.

partial destruction of magnetic surfaces. This explanation was proposed by Whyte *et al.* [26], who described the experiments on the injection of massive Ne pellets into the plasma of the D-IIID tokamak. Neon pellets penetrated to less than one-half of the minor radius ($r/a \sim 0.45$). Nevertheless, even 1 ms later, a substantial amount of the injected impurity penetrated into the central plasma region. Immediately after injection, significant fluctuations of the toroidal magnetic field ($\delta B/B \sim 0.02$) were observed. The estimates for the transport coefficients made in [26] using a model allowing for fluctuations of the magnetic filed [27] gave $D \sim 550\ m^2/s$, which agreed well with the observed times of impurity penetration into the central region of the plasma column (~1 ms).

6. CONCLUSION

Experiments on discharge quenching by injecting high-Z impurity pellets into the plasma have been carried out in the T-10 tokamak. The pellets were injected in both the current-plateau and ramp-down phases. The evolution of the plasma parameters can be divided into three main stages: the stage in which the pellet is evaporated and the distribution of the injected impurity gains poloidal and toroidal symmetry, the thermal-energy decay stage, and the stage of minor disruptions and relaxation of the plasma parameters to values close to those before injection. In some cases, after the injection of Ti pellets, the magnetic-energy decay stage was observed immediately after the thermal-energy decay stage.

The experiments have shown that, with technically attainable pellet sizes (less than 0.6 mm), the stored plasma energy did not decay completely and pellets only induced strong perturbations of the plasma parameters. Nevertheless, the relative decrease in the thermal plasma energy attained 70% and, in some cases, the energy of the poloidal magnetic field decreased by 50%. In this case, the injection of a high-Z impurity did not cause a major disruption. Pellet injection in the ramp-down phase made it possible to substantially accelerate the normal termination of the discharge (the quenching time decreased several times).

A one-dimensional transport code was developed in order to describe the response of the plasma parameters to the injection of a large amount of impurity. The code was used to simulate the shots with pellet injection. It is shown that the experiment (in particular, the behavior of the electron temperature in the central region of the plasma column) cannot be adequately described if the transport coefficients in the steady-state phase of the discharge are used to describe the evolution of the plasma parameters after injection. Presumably, this is due to the ET effect. The evolution of the plasma parameters can be described rather well assuming that, in a time on the order of 0.1 of the plasma energy confinement time, the transport coefficients increase 5–10 times throughout the plasma column. It is shown that the changes in transport coefficients increase as the amount of impurity injected into the discharge increases. One of the possible mechanisms for the observed ET effect could be the destruction of magnetic surfaces due to injection [26].

In the future, we plan to develop a model that more adequately (in comparison with the average-ion model) describes plasma radiation loss and the effective charge number of plasma ions. The effect of runaway electrons should also be included in the model. Moreover, in future experiments, it will be expedient to use an injector capable of injecting a greater amount of impurities.

ACKNOWLEDGMENTS

We thank the T-10 team for help in experiments and providing us with the experimental database. This work was supported in part by the Ministry of Science of the Russian Federation (under the program "Support of Post-Graduate Students," grant no. 375), INTAS (grant nos. 95-0575 and 97-11004), and the Russian Foundation for Basic Research (project no. 99-02-1764).

REFERENCES

1. *Physics and Plasma Operation Studies*, ITER Report No. S CA4 RE2.
2. B. V. Kuteev, V. Yu. Sergeev, and S. Sudo, Nucl. Fusion **10**, 1167 (1995).
3. K. Borrass, Nucl. Fusion **6**, 1035 (1991).
4. M. N. Rosenbluth and S. Putvinski, Nucl. Fusion **10**, 1355 (1997).
5. G. Pautasso, K. Buchl, J. C. Fuchs, *et al.*, Nucl. Fusion **36**, 1291 (1996).
6. S. Putvinski, N. Fujisawa, D. Post, *et al.*, J. Nucl. Mater. **241–243**, 316 (1997).
7. V. Yu. Sergeev, B. V. Kuteev, S. G. Kalmykov, *et al.*, in *Proceedings of the 22nd EPS Conference on Controlled Fusion and Plasma Physics, Bournemouth, 1995* [ECA, **19C** (1), 49 (1995)].
8. D. G. Whyte, T. E. Evans, A. G. Kellman, *et al.*, in *Proceedings of the 24th EPS Conference on Controlled Fusion and Plasma Physics, Berchtesgaden, 1997* [ECA, **21A** (3), 1137 (1997)].
9. R. Yoshino, T. Kondoh, Y. Neyatani, *et al.*, Plasma Phys. Controlled Fusion **39**, 313 (1997).
10. G. L. Schmidt, S. Ali-Arshad, D. Barlett, *et al.*, in *Proceedings of the 22nd EPS Conference on Controlled Fusion and Plasma Physics, Bournemouth, 1995* [ECA, **19C** (4), 21 (1995)].
11. S. M. Egorov, B. V. Kuteev, and I. V. Miroshnikov, Nucl. Fusion **32**, 2025 (1992).
12. V. Yu. Sergeev, E. S. Marmar, J. A. Snipes, *et al.*, Rev. Sci. Instrum. **63**, 4984 (1992).
13. L. Ledl, R. Burhenn, V. Sergeev, *et al.*, in *Proceedings of the 26th EPS Conference on Controlled Fusion and Plasma Physics, Maastricht, 1999* [ECA, **23J**, 1477 (1999)].
14. A. Ushakov, L. Ledl, G. Veres, *et al.*, in *Proceedings of the 26th EPS Conference on Controlled Fusion and*

Plasma Physics, Maastricht, 1999 [ECA, **23J**, 1481 (1999)].

15. R. Clark, J. Abdallah, and D. Post, J. Nucl. Mater. **220**, 1028 (1995).
16. V. Rozhansky, I. Veselova, and S. Voskoboynikov, Plasma Phys. Controlled Fusion **37**, 399 (1995).
17. P. B. Parks, W. D. Session, and L. R. Baylor, in *Proceedings of the 26th EPS Conference on Controlled Fusion and Plasma Physics, Maastricht, 1999* [ECA, **23J**, 1217 (1999)].
18. H. W. Muller, K. Buchl, H. Kaufmann, *et al.*, Phys. Rev. Lett. **83**, 2199 (1999).
19. J. de Kloe, E. Noordermeer, N. J. López Cardozo, and A. A. M. Oomens, Phys. Rev. Lett. **82**, 2685 (1999).
20. Yu. V. Esiptchuk and P. E. Kovrov, Preprint No. 3258/7 (IAE, Moscow, 1980).
21. V. V. Bagdasarov, in *Plasma Diagnostics*, Ed. by M. I. Pergament (Énergoatomizdat, Moscow, 1986), Vol. 4 (1), p. 113.
22. V. V. Bagdasarov, in *Plasma Diagnostics*, Ed. by M. I. Pergament (Énergoatomizdat, Moscow, 1986), Vol. 4 (1), p. 141.
23. Yu. V. Gvozdkov, Preprint No. 3618/7 (IAE, Moscow, 1982).
24. P. Mantica, G. Gorini, A. Cherubini, *et al.*, in *Proceedings of the 24th EPS Conference on Controlled Fusion and Plasma Physics, Berchtesgaden, 1997* [ECA, **21A** (1), 105 (1997)].
25. G. M. D. Hogeweij, C. C. Chu, D. F. da Cruz, *et al.*, in *Proceedings of the 22nd EPS Conference on Controlled Fusion and Plasma Physics, Bournemouth, 1995* [ECA, **19C** (2), 13 (1995)].
26. D. G. Whyte, T. E. Evans, A. W. Hyatt, *et al.*, Phys. Rev. Lett. **81**, 4392 (1998).
27. A. B. Rechester and M. N. Rosenbluth, Phys. Rev. Lett. **40**, 38 (1978).

Translated by N.F. Larionova

Plasma Physics Reports, Vol. 27, No. 3, 2001, pp. 195–204. Translated from Fizika Plazmy, Vol. 27, No. 3, 2001, pp. 209–218.

TOKAMAKS

Feedback Stabilization of Resistive Wall Modes in a Tokamak with a Double Resistive Wall

V. D. Pustovitov

Russian Research Centre Kurchatov Institute, pl. Kurchatova 1, Moscow, 123182 Russia

Received August 25, 2000

Abstract—A study is made of the problem of active stabilization of the resistive wall modes in a tokamak with two conducting walls between the plasma column and the stabilizing system. The problem is analyzed for a steady-state configuration (without rotation) in the standard cylindrical approximation under the assumption that the stabilizing system responds instantaneously to a magnetic field perturbation by generating an in-phase signal with the required amplitude. © *2001 MAIK "Nauka/Interperiodica".*

1. INTRODUCTION

It is well known that, in order to achieve high values of β (the ratio of the plasma pressure to the magnetic field pressure) in long-term tokamak discharges, it is necessary to solve the problem of the suppression of resistive wall modes (RWMs). Experiments aimed at studying the RWM instability in the DIII-D tokamak [1–6] show that this is indeed a serious problem. This is also a challenge for the development of the ITER tokamak reactor [7].

The most simple and realistic suppression method is active stabilization of the RWMs by external controlling magnetic fields capable of responding to a magnetic perturbation generated by the plasma (see [3–15] and the literature cited therein). The active stabilization system in DIII-D makes it possible to confine the plasma in a quiescent state for a substantially longer time and to achieve higher β values [3–6]. Both experiments and favorable theoretical predictions stimulate further efforts in this direction.

In the simplest analytic formulation of the RWM stabilization problem, there are three elements determining the behavior of RWMs: a plasma, a conducting wall (the only passive element), and stabilizing conductors [8, 10, 13]. However, real devices may have several passive conducting elements. For example, in ITER, it is proposed that there should be two resistive walls (separated by a finite distance) between the plasma and the stabilizing system (one may also speak of a double wall [7, p. 2593]). Our purpose here is to investigate RWM stabilization in a tokamak with a double resistive wall.

In Section 2, we formulate the problem and write out the basic equations. In Section 3, we briefly describe the standard cylindrical model employed in our analysis. In Section 4, we derive a dispersion relation for a tokamak with a double resistive wall and explain the physical meaning of the main parameter characterizing the plasma in our problem. In Section 5, we discuss the properties of the dispersion relation for a RWM in the presence of two resistive walls but in the absence of an external stabilizing magnetic field. In Section 6, we examine active RWM stabilization. In the Conclusion, we summarize the main results obtained.

This work is a natural continuation of papers [8, 13], which were aimed at studying the possibility of suppressing RWMs in a tokamak with a stabilizing system placed either just near a single conducting wall [8] or at a finite distance from it [13]. Of course, the problem at hand could be solved by precisely the same method as in [8, 13], in which case, however, both the derivations and the final results would be rather tangled. We apply another approach allowing a simple and illustrative description, even although we treated a problem that is more complicated than in [8, 13].

2. FORMULATION OF THE PROBLEM AND BASIC EQUATIONS

To solve the problem, we must calculate the perturbed magnetic field in three media: plasma, the vacuum region outside the plasma, and conducting metal walls that separate the vacuum region into several subregions.

The most complicated problem is that of calculating the field in the plasma, in which case it is necessary to solve reduced MHD equations. The complexity of the analytic problem forces one to treat only the simplest cases, when the problem can be reduced to solving one [8, 10, 13, 16–18] or several [19] one-dimensional equations.

It is well known that, in cylindrical geometry, such an equation is [17, 18, 20–22]

$$\frac{\gamma^2}{F}\nabla_\perp\left(\rho\nabla_\perp\frac{\tilde{\psi}}{F}\right) = -\nabla_\perp^2\tilde{\psi} + \mu_0\frac{mj'(r)}{rF}\tilde{\psi}, \qquad (1)$$

1063-780X/01/2703-0195$21.00

where $\nabla_\perp = \nabla - \hat{\mathbf{z}}(\hat{\mathbf{z}} \cdot \nabla)$, $\tilde{\psi} = \psi(r)\exp(im\theta - in\zeta + \gamma t)$, the perturbed magnetic field $\tilde{\mathbf{B}} = \nabla\tilde{\psi} \times \hat{\mathbf{z}}$ is expressed in terms of the function $\nabla\tilde{\psi} \times \hat{\mathbf{z}}$, $\hat{\mathbf{z}}$ is the unit vector along the z-axis of a cylindrical coordinate system $(r, \theta, z \equiv R\zeta)$ with $2\pi R$ the circumference of an equivalent torus, γ is the perturbation growth rate, t is the time, $F = (B_J/r)[m - nq(r)]$, $B_J(r)$ is the equilibrium magnetic field component, q is the safety factor, ρ is the plasma density, j is the z-component of the current density, and the prime denotes the radial derivative. Here and in other formulas, the magnetic constant (the vacuum magnetic permeability) $\mu_0 = 4 \times 10^{-7}$ H/m is present, because we are working in SI units.

Even Eq. (1), which is the simplest possible equation for the function $\tilde{\psi}$, turns out to be fairly complicated. For example, for a parabolic current profile, the solution to this equation is expressed in terms of hypergeometric functions [19, 23]. That is why, the stability of kink and tearing modes is often studied under the assumption of a uniform current density (see, e.g., [8, 16–18, 21, 22]).

For realistic current distributions, Eq. (1) must be solved numerically. On the other hand, the problem of RWM stabilization can be formulated in such a way that the desired dispersion relation would contain only one plasma parameter—the perturbation growth rate in the absence of active stabilization [8, 13]. In this formulation (which will be clarified below), the main task is to examine the behavior of the magnetic perturbation outside the plasma, i.e., in vacuum regions where all the characteristics are known, the geometry is fixed, and there is no need to calculate the force balance.

Outside the plasma, the magnetic perturbation is described by the Maxwell equations

$$\mathrm{rot}\,\mathbf{E} = -\frac{\partial \mathbf{B}}{\partial t}, \tag{2}$$

$$\mathrm{div}\,\mathbf{B} = 0, \tag{3}$$

$$\mathrm{rot}\,\mathbf{H} = \mathbf{j} \tag{4}$$

and Ohm's law for each of the conducting walls,

$$\mathbf{j} = \sigma_k \mathbf{E}. \tag{5}$$

Here, we use the standard notation: $\mathbf{E}$ and $\mathbf{H}$ are the electric and magnetic fields, $\mathbf{B} = \mu\mu_0\mathbf{H}$ is the magnetic induction, μ is the magnetic permeability of the medium, and σ_k is the electric conductivity of the kth wall.

In tokamaks, the thicknesses of the vacuum chamber and other conducting walls are small. Consequently, in our problem, all of the metal objects can be regarded as infinitely thin conducting shells. For a current-carrying shell in vacuum, we have (see, e.g., [24, 25])

$$\mu_0\mathbf{K} = \mathbf{n} \times (\mathbf{B}^{\mathrm{out}} - \mathbf{B}^{\mathrm{in}}), \tag{6}$$

where $\mathbf{K}$ is the surface current density, $\mathbf{n}$ is the unit normal to the surface, $\mathbf{B}^{\mathrm{out}}$ is the magnitude of $\mathbf{B}$ at the outer surface of the shell (on the side the unit normal $\mathbf{n}$ is directed), and $\mathbf{B}^{\mathrm{in}}$ is the magnitude of $\mathbf{B}$ at the inner surface. In our case, we have $\mathbf{K} = \mathbf{j}d_k$, where d_k is the wall thickness, which is assumed to be smaller than the characteristic wall dimension, e.g., the minor radius r_k in the cylindrical model. Taking into account Ohm's law, we obtain from Eq. (6)

$$\mathbf{E}(s_k) = \frac{\mathbf{n} \times (\mathbf{B}^{\mathrm{out}} - \mathbf{B}^{\mathrm{in}})}{\mu_0\sigma_s}, \tag{7}$$

where σ_s is the surface conductivity (for real conductors, $\sigma_s = \sigma_k d_k$) and the argument s_k refers to the corresponding surface. With allowance for Eq. (7), the projection of Eq. (2) onto the normal $\mathbf{n}$ has the form

$$\frac{\partial}{\partial t}B_n = -\nabla_\tau \cdot \frac{\mathbf{B}_\tau^{\mathrm{out}} - \mathbf{B}_\tau^{\mathrm{in}}}{\mu_0\sigma_s}, \tag{8}$$

where $B_n = \mathbf{n} \cdot \mathbf{B}$, $\mathbf{B}_\tau = \mathbf{B} - \mathbf{n}(\mathbf{n} \cdot \mathbf{B})$, $\nabla_\tau = \nabla - \mathbf{n}(\mathbf{n} \cdot \nabla)$, and the subscripts n and τ stand for the normal and tangential components, respectively.

Along with Eq. (8), we use the following consequence of Eq. (3):

$$\mathbf{n} \cdot \nabla(B_n^{\mathrm{out}} - B_n^{\mathrm{in}}) + \mathrm{div}(\mathbf{B}_\tau^{\mathrm{out}} - \mathbf{B}_\tau^{\mathrm{in}}) = 0, \tag{9}$$

which is valid at any surface. Note that, in general, the operators $[\nabla_\tau]$ in Eq. (8) and div in Eq. (9) are not the same.

By definition, the magnetic fields $\mathbf{B}_\tau^{\mathrm{out}}$ and $\mathbf{B}_\tau^{\mathrm{in}}$ in Eq. (8) are vacuum fields. Since the values of B_n are the same on both sides of any surface, the normal component B_n can also be regarded as a vacuum field component. Hence, under the assumption that the shells are infinitely thin, the problem of calculating the magnetic perturbation outside the plasma reduces to a problem for a vacuum region, i.e., to the equations $\mathrm{div}\,\mathbf{B} = 0$ and $\mathrm{curl}\mathbf{B}$ with the additional conditions (8) at every conducting shell. The perturbed magnetic fields obtained for the vacuum and plasma regions should be matched at the plasma–vacuum boundary. As a result, we arrive at the desired dispersion relation.

3. STANDARD CYLINDRICAL MODEL

In cylindrical geometry, the plasma column is regarded as a circular cylinder, the conducting walls are coaxial circular cylinders, and the perturbed magnetic field is a helically symmetric field, which is described in detail in the well-known paper by Morozov and Solov'ev [26].

In vacuum, the magnetic field can be described in terms of one scalar function (e.g., by the scalar potential). In the theory of MHD plasma stability, this is usu-

ally the radial component of the perturbed magnetic field,

$$\tilde{B}_r = B_r(r)\exp[i(m\theta - n\zeta) + \gamma t]. \quad (10)$$

Recall that r, θ, and $\zeta = z/R$ are cylindrical coordinates related to the symmetry axis, but we use the angular coordinate ζ (which corresponds to the toroidal angle) instead of the longitudinal coordinate z. In analyzing RWMs, magnetic perturbations with small toroidal and poloidal wavenumbers, m and n, are of particular importance. In this case, the exact expression for the radial component of the perturbed magnetic field [26] can be approximated by

$$B_r(r) = C(r^{m-1} + Dr^{-m-1}). \quad (11)$$

For each vacuum subregion, the constants C and D should be found by matching the solutions at the corresponding separating surfaces (see [13]).

The solutions should be matched with the help of Eq. (8), which should be satisfied at every conducting wall. At the surface of a circular cylinder, the equality $\nabla_\tau \cdot \mathbf{B}_\tau = \mathrm{div}\,\mathbf{B}_\tau$ holds, and we can use relationship (9) to eliminate $\mathbf{B}_\tau$ in Eq. (8), which thus becomes

$$\mu_0\sigma_s\frac{\partial}{\partial t}B_n = \mathbf{n}\cdot\nabla(B_n^{\mathrm{out}} - B_n^{\mathrm{in}}). \quad (12)$$

Substituting expression (10) into Eq. (12) yields

$$\hat{\gamma}_k = \left.\frac{rB_r'}{B_r}\right|_{\mathrm{in}}^{\mathrm{out}}, \quad (13)$$

where $\hat{\gamma}_k = \gamma\tau_k$, d_k and r_k are the thickness and minor radius of the kth wall, and $\tau_k = \mu_0\sigma_s r_k = \mu_0\sigma_k d_k r_k$ is the resistive wall diffusion time.

Then, our approach reduces to finding the coefficients C and D in expression (11) for each vacuum subregion. In principle, these coefficients can be calculated using a method analogous to that developed in [8, 13]. However, problems that are more complicated than those in [8, 13] involve more lengthy algebra and yield more complicated conditions for RWM stabilization. In order to overcome difficulties in this approach and to make the description simple and illustrative, we propose to operate with other constants accounting for the particular contributions of individual sources to the total magnetic field $B_r(r)$. A similar approach was applied in [10], in which, however, the role of the main parameters was played by the standard characteristics of the electric circuits (such as currents, resistances, and inductances). In contrast to [10], we will treat the problem using a smaller number of main parameters and a larger number of passive parameters. In speaking of the magnetic field, we imply the individual helical harmonic (10).

The magnetic field produced by an infinitely thin cylindrical shell of radius r_k can be specified as

$$B_r^{(k)}(r) = B_k\begin{cases} x^{m-1} & \text{for } x < x_k \ \text{(inside the shell)} \\ x_k^{2m}x^{-m-1} & \text{for } x > x_k \ \text{(outside the shell)}, \end{cases} \quad (14)$$

where

$$x \equiv r/r_1, \quad x_k \equiv r_k/r_1, \quad (15)$$

r_1 is the minor radius of the first conducting wall, and B_k is the value of $B_r^{(k)}$ at this wall ($x = 1$).

Representation (14) is especially convenient for our purposes because, according to Eq. (13), the jump in $B_r'(r)$ at the surface $r = r_k$ is determined exclusively by the magnetic self-field $B_r^{(k)}(r_k) = B_k x_k^{m-1}$ at this surface:

$$rB_r'\Big|_{\mathrm{in}}^{\mathrm{out}} = -2mB_k x_k^{m-1}. \quad (16)$$

With this notation, Eq. (13) becomes

$$\hat{\gamma}_k = -2m\frac{B_k x_k^{m-1}}{B_r(r_k)}, \quad (17)$$

where $B_r(r_k)$ is the total magnetic field at the surface $r = r_k$.

The complete set of equations consists of k equations (17) (k is the number of conducting walls), the continuity condition for $B_r(r)$, and Eq. (1) for the function $\tilde{\psi}$ in the plasma. In order to calculate the component $B_r(r)$ with allowance for jumps (17) at all separating surfaces, it is sufficient to know the value of $r\psi'(r)/\psi$ at the plasma boundary (rather than the overall behavior of the function $\tilde{\psi}$). In the plasma, the function $\psi(r)$ is determined by the equilibrium current profile [see Eq. (1)]. It is natural to assume that, when the feedback system is turned on, the current profile does not change; as a result, we can treat different external conditions keeping the function $r\psi'/\psi$ at the plasma boundary fixed. In this case, the quantity

$$\left.\frac{rB_r'}{B_r}\right|_{\mathrm{in}} \equiv -\Gamma_0 - (m+1) \quad (18)$$

at the inner surface of the first conducting wall also remains unchanged.

Here, the growth rate Γ_0 is introduced in the same manner as in [13]. Definition (18) means (see below) that Γ_0 is the dimensionless growth rate of an RWM in the presence of only one (the first) conducting wall and in the absence of external stabilizing fields. In our problem with two conducting walls, the introduced quantity Γ_0 seems to be somewhat artificial. However, below we will see that Γ_0 is a useful parameter, regardless of the

number of conducting walls. Keeping in mind that, in our model, the growth rate Γ_0 plays a key role because it is the only parameter characterizing the plasma, we will also describe the methods for determining Γ_0 from the experimentally measured quantities.

An important point here is that Γ_0 remains constant as the growth rate of the RWM changes under the action of the external stabilizing field. This conclusion can be supported not only by the above considerations but also by the results of simulations of RWMs in actual toroidal geometry [12, 14]: the plasma-produced perturbation was found to be almost insensitive to the controlling signal from the feedback system.

4. DISPERSION RELATION AND GROWTH RATE Γ_0

Here, we derive the dispersion relation that relates the growth rate of the RWM to the system parameters.

In the vacuum region just outside the first wall ($x_1 < x < x_2$), we have

$$B_r = (B_{pl} + B_1)x^{-m-1} + B_{\text{ext}}x^{m-1}, \tag{19}$$

where the constants correspond to the magnetic fields at the first wall ($x = 1$) at the initial instant $t = 0$: B_{pl} is the amplitude of the magnetic field generated by the plasma, B_1 is the magnetic field of the currents induced in the first wall, and B_{ext} is the amplitude of the magnetic field of the remaining external sources (the remaining conducting walls and stabilizing system). Expression (19) gives

$$\left.\frac{rB_r'}{B_r}\right|_{\text{out}} = -(m+1) + 2m\frac{B_{\text{ext}}}{B_\Sigma}, \tag{20}$$

where

$$B_\Sigma \equiv B_{pl} + B_1 + B_{\text{ext}} \tag{21}$$

is the perturbation amplitude at the first wall. For the first wall, Eq. (13), together with relationships (18) and (20), yields

$$\hat{\gamma}_1 = \left.\frac{rB_r'}{B_r}\right|_{\text{in}}^{\text{out}} = \Gamma_0 + 2m\frac{B_{\text{ext}}}{B_\Sigma}. \tag{22}$$

For the RWM to be exponentially damped at the rate $\hat{\gamma}_1 < 0$ [see representation (10)], it is necessary to satisfy the condition

$$\frac{B_{\text{ext}}}{B_\Sigma} \le -\frac{\Gamma_0}{2m}. \tag{23}$$

For RWMs, this stabilization condition is universal and remains valid (in the cylindrical model) regardless of the positions of the conducting walls and stabilizing system.

Since condition (23) plays a key role in the problem of RWM stabilization, we must redefine the parameter Γ_0 in an informal manner. The quantity Γ_0 can be regarded as the growth rate for a single wall, because, with no external magnetic field present ($B_{\text{ext}} = 0$), formula (22) gives $\hat{\gamma}_1 = \Gamma_0$. We suggest that, in the absence of active feedback, the RWM is unstable (all $\hat{\gamma}_k$ are positive). Accordingly, we have $\Gamma_0 > 0$.

We must express Γ_0 in terms of the actual physical quantities. To do this, it is necessary to use not only Eq. (22) for the first wall but also Eqs. (17) for all of the remaining passive elements.

In this way, we multiply the equation for the second conducting wall by τ_1/τ_2 to obtain

$$\hat{\gamma}_2\frac{\tau_1}{\tau_2} = \hat{\gamma}_1 = -2m\frac{B_2\tau_1/\tau_2^*}{B_\Sigma + B_{\text{ext}}(2m/\Delta\Gamma)}. \tag{24}$$

Here, we introduced the quantities

$$\tau_2^* \equiv \tau_2 x_2^{-2m}, \tag{25}$$

which can be referred to as the effective time of the second wall (see below), and

$$\Delta\Gamma \equiv \frac{2m}{x_2^{2m} - 1}. \tag{26}$$

Also, we take into account the fact that, for the second wall, the denominator in formula (17) can be expressed through the amplitudes of the partial fields (14):

$$\begin{aligned} B_r(r_2) &= (B_{pl} + B_1)x_2^{-m-1} + B_{\text{ext}}x_2^{m-1} \\ &= x_2^{-m-1}[B_\Sigma + B_{\text{ext}}(x_2^{2m} - 1)]. \end{aligned} \tag{27}$$

Using relationship (22), we eliminate B_Σ in Eq. (24) to arrive at

$$\hat{\gamma}_1(\hat{\gamma}_1 - \Gamma_\infty) + (\hat{\gamma}_1 - \Gamma_0)\frac{B_2}{B_{\text{ext}}}\Delta\Gamma\frac{\tau_1}{\tau_2^*} = 0, \tag{28}$$

where

$$\Gamma_\infty = \Gamma_0 - \Delta\Gamma. \tag{29}$$

Equation (28) can serve to determine $\hat{\gamma}_1$ only if we find a way to determine the ratio B_2/B_{ext}.

In [8, 13], neither Eq. (28) nor a similar equation appeared. In our problem, this equation arises from the presence of the second wall. This equation will be discussed in more detail in the next section. Here, we mention only one of its consequences.

Equation (28) makes it possible to express the formally introduced quantity Γ_0 in terms of the experimentally measured quantities:

$$\Gamma_0 = \hat{\gamma}_1 + \frac{\hat{\gamma}_1\Delta\Gamma}{\hat{\gamma}_1 + \Delta\Gamma(\tau_1/\tau_2^*)(B_2/B_{\text{ext}})}. \tag{30}$$

The growth rate $\hat{\gamma}_1$ is a measurable quantity, and the constants $\Delta\Gamma$ and τ_1/τ_2^* are determined exclusively by the parameters of the double wall and the poloidal mode number m. For a system with two conducting walls and without active stabilization, we have $B_2/B_{ext} = 1$, the growth rate Γ_0 (30) being completely determined by expression (30). Note also that, in this case,

$$1 \le \frac{\Gamma_0}{\hat{\gamma}_1} \le 1 + \frac{\tau_2^*}{\tau_1}. \quad (31)$$

The lower limit is achieved at $\tau_2^* = 0$, and the upper limit is reached when the second wall approaches the first wall.

Another method for determining Γ_0 experimentally can be described as follows. In cylindrical geometry, the equation $\mathrm{div}\mathbf{B} = 0$ for the helical perturbations yields

$$rB_r' + B_r = -m(1 + \delta^2)B_\theta. \quad (32)$$

The model implies that the quantity $\delta = nr/(mR)$ is small in comparison with unity. According to Eq. (10), the amplitude B_θ of the poloidal component of the magnetic perturbation is defined by the equality $\tilde{B}_\theta = B_\theta(r)\exp(\gamma t)\sin(m\theta - n\zeta)$. Hence, we obtain from Eq. (18)

$$\Gamma_0 = m\frac{B_\theta}{B_r}(1 + \delta^2) - m. \quad (33)$$

Here, all of the quantities should be taken at the inner surface of the first conducting wall. In the DIII-D tokamak, the magnetic detectors (sensors) are located precisely in this region [6]. For a different position of the sensors, the field components B_r and B_θ in the growth rate (33) are also easy to calculate from the measured quantities.

It is necessary to know Γ_0, first of all, in order to use condition (23) for RWM suppression. Below, we will show that knowledge of even approximate values of Γ_0 is quite sufficient for practical applications. The errors in determining the growth rate Γ_0 can be compensated for by increasing the amplification coefficient of the feedback system.

5. RWM IN A TOKAMAK WITH TWO WALLS

Equation (28) contains two unknown parameters: the growth rate $\hat{\gamma}_1$ and the ratio B_2/B_{ext}. By definition, B_{ext} is the amplitude of the magnetic field produced by the current-carrying conductors that are located outside of the first walls. In the case at hand, we have

$$B_{ext} = B_2 + B_f, \quad (34)$$

where B_f is the amplitude of the field generated by the feedback system at the first wall ($x = 1$) and B_2 is the amplitude of the field of the currents induced in the second wall.

For a tokamak with a double wall and without a feedback system, we have $B_{ext} = B_2$, in which case Eq. (28) reduces to the following quadratic equation for $\hat{\gamma}_1$:

$$\hat{\gamma}_1^2 - \hat{\gamma}_1(\Gamma_0 - \alpha\Delta\Gamma) - \Gamma_0\Delta\Gamma(\alpha - 1) = 0, \quad (35)$$

where

$$\alpha \equiv 1 + \tau_1/\tau_2^*. \quad (36)$$

Before proceeding to solutions to Eq. (36) with arbitrary values of $\Delta\Gamma$ and α, we consider three limiting cases.

In the absence of the second wall ($\tau_2^* = 0$, $\alpha = \infty$), Eq. (35) gives

$$\hat{\gamma}_1 = \Gamma_0, \quad (37)$$

which corresponds to Eq. (22) with $B_{ext} = 0$.

For a perfectly conducting (ideal) second wall ($\tau_2^* = \infty$ and $\alpha = 1$), Eq. (35) yields

$$\hat{\gamma}_1 = \Gamma_\infty, \quad (38)$$

where the symbol ∞ indicates that the second wall has infinite conductivity. In Eq. (38), the quantity Γ_∞ defined by relationship (29) can be negative provided that $\Delta\Gamma > \Gamma_0$. In this case, the RWM is completely stabilized by the ideal second wall, in the absence of which the mode should grow at rate (37). According to Eq. (26), the quantity $\Delta\Gamma$ depends only on the position of the second wall relative to the first wall: the farther the second wall is from the first wall, the smaller the quantity $\Delta\Gamma$. Above a certain critical distance (which is determined by the equality $\Delta\Gamma = \Gamma_0$) from the first wall, the second wall, even being perfectly conducting, ceases to stabilize the RWM completely.

The closer the second wall is to the first wall, the larger the quantity $\Delta\Gamma$, which becomes infinite at $x_2 = 1$ (when the second wall coincides with the first wall). In this limiting case, we obtain from Eq. (35)

$$\hat{\gamma}_1 \equiv \gamma\tau_1 = \Gamma_0\frac{\tau_1}{\tau_1 + \tau_2}. \quad (39)$$

This equality has a simple physical meaning: the two walls act as one wall whose characteristic time is equal to the sum $\tau_1 + \tau_2$.

The above distinctive features are clearly seen in Figs. 1 and 2, which illustrate not only these three limiting cases but also more interesting intermediate situations.

Figure 1 shows the dependence of $\hat{\gamma}_1/\Gamma_0$ on $\Delta\Gamma/\Gamma_0$ for several values of $\alpha = 1 + \tau_1/\tau_2^*$. We can see that the second wall has a pronounced effect on the growth rate

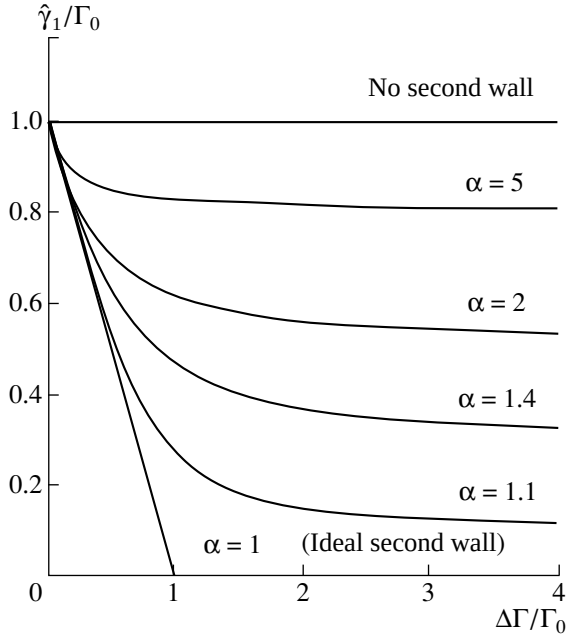

Fig. 1. Growth rate of an RWM vs. $\Delta\Gamma/\Gamma_0$ for different values of $\alpha = 1 + \tau_1/\tau_2^*$.

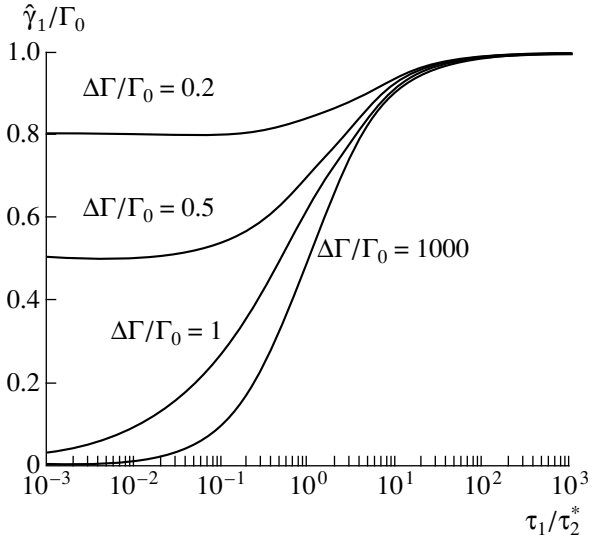

Fig. 2. Growth rate of an RWM vs. τ_1/τ_2^* for different values of $\Delta\Gamma/\Gamma_0$.

of the RWM when $\Delta\Gamma/\Gamma_0$ is above a certain critical value (of order unity) and α does not differ appreciably from unity.

As $\Delta\Gamma/\Gamma_0$ increases, the curves in Fig. 1 monotonically go down. For a given value of m, the quantity $\Delta\Gamma$ is determined only by the position of the second wall [see Eq. (26)]. Small values of $\Delta\Gamma/\Gamma_0$ correspond to large distances between the walls; as the second wall becomes closer to the first wall, $\Delta\Gamma/\Gamma_0$ increases. We can clearly see that, for any value of α, the growth rate decreases (from its initial value Γ_0) most sharply in the region $\Delta\Gamma/\Gamma_0 < 1$. Consequently, we can introduce the conditional boundary $\Delta\Gamma = \Gamma_0$ and speak of a near second wall (if $\Delta\Gamma > \Gamma_0$) and a distant second wall (if $\Delta\Gamma < \Gamma_0$). These conditions for the second wall to be near or distant relate the purely geometric parameter $\Delta\Gamma$ to the quantity Γ_0, which depends on the plasma-current and plasma-density profiles, and thereby should be regarded merely as relative conditions. The second wall may act as a near wall on the modes with small Γ_0 and as a distant wall on the modes with large Γ_0. Recall that the parameter $\Delta\Gamma$ is highly sensitive to the poloidal mode number m [see Eq. (26)]; as a result, in systems with a fixed geometry, different mode numbers m correspond to different values of $\Delta\Gamma$.

An ideal ($\alpha = 1$) second wall located close to the first wall can completely stabilize the RWM. However, since the conductivity of both of the walls is actually finite ($\alpha > 1$), the second wall placed near the first wall acts merely to reduce the growth rate. In the limit of large values of $\Delta\Gamma/\Gamma_0$, the growth rate is lower than that in a tokamak with no second wall by a factor of

$$\frac{\alpha}{\alpha - 1} = \frac{\tau_1 + \tau_2^*}{\tau_1}. \qquad (40)$$

The reciprocal of the quantity (40) corresponds to the horizontal asymptotes of the curves in Fig. 1. Note that, for $\Delta\Gamma/\Gamma_0$ on the order of unity, all of the curves are already fairly close to their asymptotes; as $\Delta\Gamma/\Gamma_0$ increases further (the second wall becomes closer to the first wall), the growth rate remains essentially unchanged.

The RWM is not only sensitive to the position of the second wall but is also influenced by its effective time τ_2^* [see relationship (40)]. Small values of τ_2^* correspond to large values of α at which the effect of the second wall is insignificant, so that we can speak of a "weak" wall. In contrast, the wall that reduces the growth rate by a factor of more than two, which corresponds to $\tau_2^* > \tau_1$, can be called a "strong" wall. Note that the effective time $\tau_2^* = \tau_2 x_2^{-2m}$ depends not only on the characteristic time τ_2 but also on the location of the second wall. The "strength" of the second wall decreases abruptly with distance from the first wall.

From Fig. 1, we can see that, in the region of small values of $\Delta\Gamma/\Gamma_0$ (distant second wall), the growth rate of the RWM decreases almost linearly as $\Delta\Gamma/\Gamma_0$ increases. In this range of $\Delta\Gamma/\Gamma_0$, the second resistive wall affects the RWM essentially as an ideal wall (a weak wall over a narrow interval of $\Delta\Gamma/\Gamma_0$ values or a strong wall over a broader interval). As $\Delta\Gamma/\Gamma_0$ increases, the resistivity of the second wall plays an increasingly important role: in Fig. 1, all of the curves with $\alpha > 1$

deviate from the straight line $1 - \Delta\Gamma/\Gamma_0$, which corresponds to an ideal wall. In the range $\Delta\Gamma/\Gamma_0 > 1$, the second wall should always be treated as resistive, even for very small values of τ_1/τ_2^*.

Of course, in the limit $\tau_1/\tau_2^* \ll 1$, the first wall has an insignificant impact on the RWM, in which case the growth rate is governed primarily by the parameters of the second wall. In Fig. 1, this situation is illustrated by the lowest curve (with $\alpha = 1.1$).

Figure 2 shows the growth rate of the RWM as a function of τ_1/τ_2^* for different values of $\Delta\Gamma/\Gamma_0$ (i.e., for different locations of the second wall). We clearly see that, for $\tau_1/\tau_2^* \geq 10$, the growth rate is affected by the second wall only slightly, no matter where the wall is placed. For τ_1/τ_2^* on the order of unity, the second wall can reduce the growth rate by a factor of two. Finally, for $\tau_1/\tau_2^* \ll 1$, the growth rate $\hat{\gamma}_1 \equiv \gamma\tau_1$ can be lowered substantially in comparison with Γ_0, especially when the second wall is close to the first wall ($\Delta\Gamma/\Gamma_0 \geq 1$). However, recall that, in this case, such low growth rates $\hat{\gamma}_1$ indicate that the quantity $1/\tau_1$ ceases to serve as an appropriate scale for estimating the growth rate.

6. ACTIVE STABILIZATION OF RWM

The external stabilizing field B_f enters the solution to Eq. (28) through the parameter

$$\frac{B_2}{B_{\text{ext}}} = 1 - \frac{B_f}{B_{\text{ext}}}, \tag{41}$$

where definition (34) for the field B_{ext} applies to a tokamak with a double wall. Using Eq. (22), we can express B_{ext} in terms of the measured field B_Σ, in which case formula (41) takes the form

$$\frac{B_2}{B_{\text{ext}}} = 1 - \frac{B_f}{B_\Sigma}\frac{2m}{\hat{\gamma}_1 - \Gamma_0}. \tag{42}$$

Substituting this expression into the dispersion relation (28) yields the following equation for $\hat{\gamma}_1$:

$$\hat{\gamma}_1^2 - \hat{\gamma}_1(\Gamma_0 - \alpha\Delta\Gamma) - \Gamma_0\Delta\Gamma(\alpha - 1)\left(1 + \frac{2m}{\Gamma_0}\frac{B_f}{B_\Sigma}\right) = 0, \tag{43}$$

which explicitly includes the stabilizing field B_f.

In the previous section, we have analyzed a freely growing RWM ($B_f = 0$). Now, our task is to determine the range of B_f in which the RWM can be suppressed.

For $B_f = 0$, Eq. (43) has two real roots with opposite signs. The positive root corresponds to an unstable RWM. The main properties of this solution to Eq. (43) are illustrated in Figs. 1 and 2.

For the RWM to be stabilized, Eq. (43) should have two negative roots. This is possible only when

$$K/K_0 > 1, \tag{44}$$

where

$$K \equiv -\frac{B_f}{B_\Sigma}, \quad K_0 \equiv \frac{\Gamma_0}{2m}. \tag{45}$$

The quantity K can be referred to as the gain factor of the stabilizing system. The minus sign is introduced in the definition of K in order to operate with positive values of K and K_0.

Condition (44) determines whether the roots X_1 and X_2 of Eq. (43) are both positive or negative. By virtue of the relationship

$$X_1 + X_2 = \Gamma_0 - \alpha\Delta\Gamma, \tag{46}$$

the sign of the roots is governed by the multiplier of $\hat{\gamma}_1$ in (43). The roots have the desired sign when

$$\Gamma_0 - \alpha\Delta\Gamma < 0. \tag{47}$$

If conditions (44) and (47) are both satisfied, the roots of Eq. (43) are negative and $\hat{\gamma}_1 < 0$, thereby indicating the suppression of the RWM. In this case, the quantity K_0 can be regarded as the minimum gain factor: for $K < K_0$, we have $\hat{\gamma}_1 > 0$; as K increases, $\hat{\gamma}_1$ decreases; and, at $K = K_0$, the growth rate of the RWM vanishes (Fig. 3). For larger values of K, the growth rate is negative.

For the given parameters of the double wall, condition (47) imposes a lower limit on Γ_0. In the case with no second wall ($\alpha \longrightarrow \infty$ or $\Delta\Gamma \longrightarrow \infty$), this condition always holds and the dispersion relation (43) reduces to the relation

$$\hat{\gamma}_1 = \Gamma_0 + 2m\frac{B_f}{B_\Sigma}, \tag{48}$$

which is shown by the upper line in Fig. 3 and corresponds to Eq. (12) from [13]. As before, the RWM stabilization condition is represented by inequality (44). The stabilization conditions derived in [13] for a tokamak with a single resistive wall and written in terms of other quantities are more complicated than condition (44), which, nevertheless, covers the main result obtained in [13].

For a tokamak with a double wall, condition (47) can be satisfied only when the values of $\Delta\Gamma/\Gamma_0$ are sufficiently large. Since the quantity $\Delta\Gamma$ is determined exclusively by the location of the second wall [see Eq. (26)], condition (47) reduces to the geometric limitation

$$r_2/r_1 < x_{\text{cr}}, \tag{49}$$

where the critical value x_{cr} is equal to

$$x_{\text{cr}}^{2m} = 1 + 2m\alpha/\Gamma_0 = 1 + \alpha/K_0. \tag{50}$$

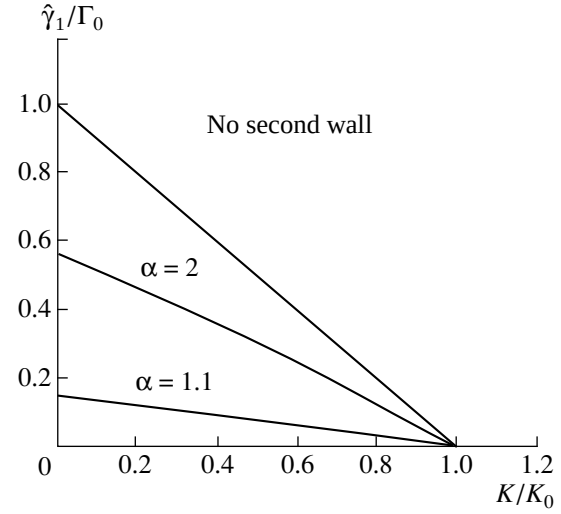

Fig. 3. Growth rate of an RWM vs. the amplification factor of the stabilizing system for $\Gamma_0 - \alpha\Delta\Gamma < 0$. The upper line corresponds to $\alpha = \infty$ (the case with no second wall). The middle and lower lines correspond to $\alpha = 2$ and 1.1, respectively; $\Delta\Gamma/\Gamma_0 = 2$.

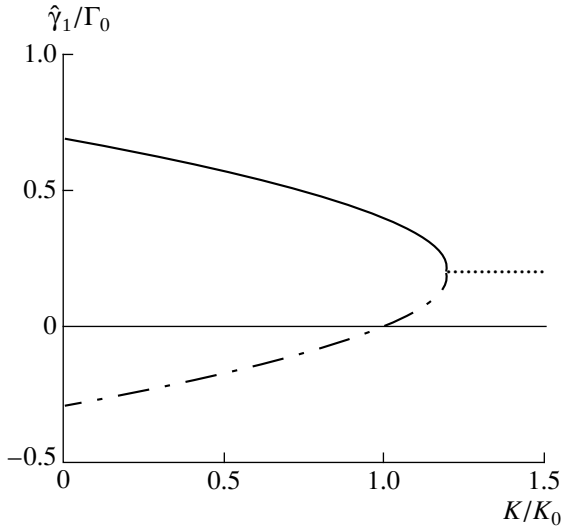

Fig. 4. Growth rate of an RWM vs. the amplification factor of the stabilizing system for $\Gamma_0 - \alpha\Delta\Gamma > 0$. The solid and dashed curves are two branches of the solution to Eq. (43) with $\Delta\Gamma/\Gamma_0 = 0.4$ and $\alpha = 1.5$. The dotted line is the real part of $\hat{\gamma}_1/\Gamma_0$ for $K/K_0 > 1.2$.

The smaller the value of α, the stronger the RWM is suppressed by the second wall located close to the first wall. In other respects, the dependence of $\hat{\gamma}_1$ on K is qualitatively the same over the entire range of the parameter α in Fig. 3.

If the distance from the second to the first wall is larger than the critical distance in condition (49), then we arrive at an inequality opposite to that in formula (47):

$$\Gamma_0 - \alpha\Delta\Gamma > 0, \tag{51}$$

in which case Eq. (43) has at least one positive root, regardless of the value of K. Consequently, in this case (and under the above assumptions that the field B_f and the perturbation generated by the plasma are inphase and depend on time in essentially the same manner), the external field B_f always ceases to stabilize the RWM.

This is a new result as compared to the case with one wall, where the RWM can always be stabilized by the external field [see dispersion relation (48)]. Figure 4 shows how $\hat{\gamma}_1$ changes with an increase in K under condition (51). For $K < K_0$, the growth rate decreases (but never vanishes) as K increases. In the case $K = K_0$, in which all of the curves in Fig. 3 converge to the same point $\hat{\gamma}_1 = 0$, the growth rate of the RWM remains finite under condition (51):

$$\hat{\gamma}_0 \equiv \hat{\gamma}_1(K_0) = \Gamma_0 - \alpha\Delta\Gamma. \tag{52}$$

For $K > K_0$, the growth rate continues to decrease as K increases; simultaneously, a new branch appears (see the lower dashed curve in Fig. 4) with a lower growth rate increasing from zero to the value $\hat{\gamma}_1 = \hat{\gamma}_0/2$ at which the branches merge into one. The value of K at the point at which the branches merge together can be readily found from Eq. (43). A further increase in K gives rise to the imaginary part of $\hat{\gamma}_1$, in which case, however, $\mathrm{Re}\hat{\gamma}_1 = \hat{\gamma}_0/2$ remains unchanged. In Fig. 4, this region is marked by the dotted line.

The existence of two solutions in the range $K > K_0$ allows us to speak of slow and fast RWMs. For $\Gamma_0 > \alpha\Delta\Gamma$, the fast and slow modes cannot be stabilized by simply increasing B_f so as to counterbalance the perturbation field. The fast mode exists in the entire range of Γ_0 values, whereas the slow mode can exist only in the range $\Gamma_0 > \alpha\Delta\Gamma$ and under the condition $K > K_0$. The slow mode differs qualitatively from the fast mode in that its growth rate increases with K.

For $K > K_0$, the stabilizing system should respond to the growing RWM so as to increase K. Raising the gain factor above K_0 is not dangerous; in contrast, it is even favorable for the complete stabilization of the fast mode (Fig. 3) or its partial suppression (Fig. 4). However, for $K > K_0$, the process of stabilization of the fast mode may be accompanied by destabilization of the slow mode.

One can imagine the following situation. Let the condition $\Gamma_0 < \alpha\Delta\Gamma$ be initially satisfied, in which case the mode is feedback-stabilized as is shown in Fig. 3. If, during the evolution of the equilibrium plasma parameters, Γ_0 increases to values sufficient to satisfy the opposite condition $\Gamma_0 > \alpha\Delta\Gamma$, then the slow mode is excited and immediately begins to be amplified by the stabilizing system, provided that it continues to operate in the normal regime (see the lower curve over the range $K/K_0 > 1$ in Fig. 4). A similar situation was

observed in the DIII-D experiments [6] in which the phase of the stable suppression of RWMs resulted in a rapid growth of the slow mode, which led to a minor disruption. According to [6], the DIII-D feedback systems functioned as was necessary to stabilize the fast mode, and the current in the stabilizing conductors rapidly increased to follow the fast growing magnetic perturbation, in which case, however, no stabilizing effect on the RWMs was observed. Presumably, in those experiments with active feedback stabilization, the RWMs in DIII-D were also destabilized by some other (as yet unknown) mechanisms. Nevertheless, the fact that analogous (and very undesirable) effects were observed experimentally and revealed theoretically indicates new difficulties in the problem of RWM stabilization and necessitates further investigations in this direction based on more sophisticated models.

Finally, we estimate the field B_f required for the stabilization of RWMs in the model proposed here.

Expressions (17) and (22) for $\hat{\gamma}_1$ yield

$$\Gamma_0 = -2m\frac{B_1 + B_{\text{ext}}}{B_\Sigma}, \tag{53}$$

so that we have

$$B_f = -B_\Sigma\left\{\frac{\Gamma_0}{2m} + \frac{B_1}{B_\Sigma} + \frac{B_2}{B_\Sigma}\right\}. \tag{54}$$

Here, B_Σ is the measured field; Γ_0 can be determined from the experimentally measured growth rate [see Figs. 1, 2, and relationship (30)], or from the measured amplitudes of the magnetic field perturbation [see expression (33)], or can be calculated if the current density profile is known; and the poloidal mode number m is found by Fourier analysis of the measured field. According to Eq. (17), the stability threshold for RWMs corresponds to $B_1 = B_2 = 0$, in which case formula (54) makes it possible to determine the desired field B_f. Under the conditions prevailing in present-day experiments [3–6], this field is about several gausses. Recall that B_f is the amplitude of the first harmonic of the controlling magnetic field at the first wall ($r = r_1$). For a given amplitude B_f, the desired magnitude of the current in the stabilizing windings increases proportionally to x^{m-1} as the feedback system is displaced farther from the first wall.

7. CONCLUSION

We have analyzed the situation with an unstable RWM in the absence of an active stabilizing system. Our primary goal was to derive the criterion for feedback suppression of this mode. The main difference between our formulation of the problem and that used in [8, 13] is that we considered a tokamak with a double wall, as is the case in the ITER tokamak [7].

We treated the problem using the standard cylindrical model, without making any assumptions about the current density profile in the plasma. We assumed that the conducting walls are infinitely thin and that the stabilizing system responds instantaneously to the changes in the magnetic field perturbation to be suppressed.

The criterion for feedback suppression of an RWM is inequality (44); however, for a tokamak with a double wall, its applicability range is limited. For a tokamak with one wall, the growth rate of an RWM is linearly related to the external stabilizing magnetic field (48), so that, theoretically, any mode can be feedback-stabilized. The situation with a tokamak with a double wall is different: if the distance from the second to the first wall is larger than a certain critical distance, then the dispersion relation (43) is nonlinear and the modes that start to grow at a rate faster than a certain threshold rate can never be stabilized. Also, a new branch of slow modes appears that immediately begins to be amplified by the feedback system operating in the normal regime, in which the gain is larger than K_0 (Fig. 4).

An incomplete feedback stabilization of RWMs in a tokamak with a double wall is a rather new problem that has not been predicted theoretically. A similar phenomenon, whose nature remains as yet unclear, has been recently encountered in the DIII-D experiments [6]. Hence, the problem of stabilizing RWMs turns out to be more difficult than expected.

ACKNOWLEDGMENTS

I am grateful to Yu.V. Gribov and V.S. Mukhovatov for bringing this problem to my attention and inspiring this work, and to A.B. Mikhaĭlovskiĭ and S.V. Konovalov for continuous encouragement. This work was supported in part by the Russian Foundation for Basic Research, project no. 00-15-96526 (under the program “Leading Scientific Schools”).

REFERENCES

1. E. J. Strait, T. S. Taylor, A. D. Turnbull, *et al.*, Phys. Rev. Lett. **74**, 2483 (1995).
2. T. S. Taylor, E. J. Strait, L. L. Lao, *et al.*, Phys. Plasmas **2**, 2390 (1995).
3. A. M. Garofalo, A. D. Turnbull, M. E. Austin, *et al.*, Phys. Rev. Lett. **82**, 3811 (1999).
4. A. M. Garofalo, A. D. Turnbull, E. J. Strait, *et al.*, Phys. Plasmas **6**, 1893 (1999).
5. E. J. Strait, A. M. Garofalo, M. E. Austin, *et al.*, Nucl. Fusion **39**, 1977 (1999).
6. A. M. Garofalo, E. J. Strait, J. M. Bialek, *et al.*, Nucl. Fusion **40**, 1491 (2000).
7. ITER Physics Basis Editors *et al.*, Nucl. Fusion **39**, 2137 (1999).
8. A. B. Mikhaĭlovskiĭ and B. N. Kuvshinov, Fiz. Plazmy **22**, 188 (1996) [Plasma Phys. Rep. **22**, 172 (1996)].

9. T. H. Jensen and R. Fitzpatrick, Phys. Plasmas **4**, 2997 (1997).
10. M. Okabayashi, N. Pomphrey, and R. E. Hatcher, Nucl. Fusion **38**, 1607 (1998).
11. A. H. Boozer, Phys. Plasmas **6**, 3180 (1999).
12. Y. Q. Liu and A. Bondeson, Phys. Rev. Lett. **84**, 907 (2000).
13. A. B. Mikhaĭlovskiĭ and V. D. Pustovitov, Fiz. Plazmy **26**, 511 (2000) [Plasma Phys. Rep. **26**, 477 (2000)].
14. Y. Q. Liu, A. Bondeson, C. M. Fransson, *et al.*, Phys. Plasmas **7**, 3681 (2000).
15. C. M. Fransson, B. Lennartson, C. Breitholtz, *et al.*, Phys. Plasmas **7**, 4143 (2000).
16. L. E. Zakharov and S. V. Putvinskiĭ, Fiz. Plazmy **13**, 118 (1987) [Sov. J. Plasma Phys. **13**, 68 (1987)].
17. J. M. Finn, Phys. Plasmas **2**, 198 (1995).
18. D.-Y. Lee, Phys. Plasmas **5**, 4098 (1998).
19. B. N. Kuvshinov and A. B. Mikhaĭlovskiĭ, Fiz. Plazmy **22**, 490 (1996) [Plasma Phys. Rep. **22**, 446 (1996)].
20. H. P. Furth, P. H. Rutherford, and H. Selberg, Phys. Fluids **16**, 1054 (1973).
21. J. A. Wesson, Nucl. Fusion **18**, 87 (1978).
22. B. B. Kadomtsev, Itogi Nauki Tekh., Ser. Fiz. Plazmy **10** (1), 5 (1991).
23. B. N. Kuvshinov and A. B. Mikhaĭlovskiĭ, Fiz. Plazmy **16**, 1102 (1990) [Sov. J. Plasma Phys. **16**, 639 (1990)].
24. J. A. Stratton, *Electromagnetic Theory* (McGraw-Hill, New York, 1941; Gostekhizdat, Moscow, 1948).
25. L. D. Landau and E. M. Lifshitz, *Electrodynamics of Continuous Media* (Nauka, Moscow, 1982; Pergamon, New York, 1984).
26. A. I. Morozov and L. S. Solov'ev, in *Reviews of Plasma Physics*, Ed. by M. A. Leontovich (Gosatomizdat, Moscow, 1963; Consultants Bureau, New York, 1966), Vol. 2.

Translated by G.V. Shepekina

Plasma Physics Reports, Vol. 27, No. 3, 2001, pp. 205–210. Translated from Fizika Plazmy, Vol. 27, No. 3, 2001, pp. 219–224.

TOKAMAKS

Radial Electric Field during Dynamic Processes in a Tokamak and L–H Transitions

V. A. Rozhansky*, S. P. Voskoboĭnikov*, and A. Yu. Popov**

** St. Petersburg State Technical University, Politekhnicheskaya ul. 29, St. Petersburg, 195251 Russia*

***Ioffe Physicotechnical Institute, Russian Academy of Sciences, Politekhnicheskaya ul. 26, St. Petersburg, 194021 Russia*

Received June 29, 2000; in final form, September 7, 2000

Abstract—Expressions for the radial electric field in tokamaks are derived with allowance for an additional contribution of the longitudinal electron viscosity (or the associated Ware drift). It is shown that, in transient processes during which the toroidal electric field at the plasma edge increases, the additional electric field can become rather strong. An increase in the shear of the poloidal plasma rotation can trigger the L–H transition. That the experimentally observed transitions to an improved confinement mode can be ascribed to this effect is illustrated by simulating discharges in the current ramp-up experiments in the Tuman-3M tokamak. © *2001 MAIK "Nauka/Interperiodica"*.

1. INTRODUCTION

Many tokamak experiments have demonstrated that the buildup of transport barriers is associated with the suppression of plasma turbulence by the shear of the poloidal $\mathbf{E}\times\mathbf{B}$ drift [1]. That is why the problem of calculating the radial electric field is very important for understanding the mechanisms for the transition to an improved confinement mode. In the standard neoclassical theory, the radial electric field was calculated in review [2]. In the simplest geometry of the circular magnetic surfaces, the radial electric field has the form

$$E_r^{(\mathrm{STAND})} = \frac{T_i}{e}\left[\frac{d\ln n}{dr} + (1-k)\frac{d\ln T_i}{dr}\right] + B_\theta \bar{u}_\phi, \quad (1)$$

where the numerical coefficient (the collisionality parameter) k depends on the extent to which the plasma is collision-determined (see Appendix), B_θ is the poloidal magnetic field, and $\bar{u}_\phi$ is the mean toroidal velocity. For magnetic surfaces of arbitrary geometry, we have

$$-\varphi'^{(\mathrm{STAND})} = \frac{T_i}{e}[(\ln n)' + (1-k)(\ln T_i)'] + \langle \mathbf{u}_i\mathbf{B}\rangle\frac{\chi'}{2\pi I}, \quad (2)$$

where χ is the poloidal flux, $I = R^2\mathbf{B}\nabla\zeta$, ζ is the toroidal coordinate ($|\zeta| = R^{-1}$), and

$$\mathbf{B} = \frac{\chi'}{2\pi}\nabla\zeta\times\nabla\psi + I\nabla\zeta.$$

This result was obtained from the condition that the magnetic surface–averaged ion viscosity vanishes. The electron viscosity was assumed to be lower than the ion viscosity by a factor of $(m_e/m_i)^{1/2}$ and thus was neglected. However, in the presence of a toroidal electric field, which can increase substantially during the transient processes, the electron viscosity may also become important. In [3, 4], the electron viscosity (or the associated Ware drift) was shown to strongly affect the radial electric field profile in small facilities such as the Tuman-3M tokamak.

Here, we derive a general expression for the radial electric field assuming an arbitrary collisionality parameter and taking into account effects related to the toroidal electric field. To do this, we employ the general approach that was developed by Rozhansky and Tendler [5], in which the anomalous radial transport of the toroidal momentum was taken into account. The same result can also be obtained by using the standard neoclassical approach [2]. Physically, the additional radial electric field that is to be incorporated into Eqs. (1) and (2) stems from an increase in the longitudinal ion viscosity, which, together with the Ware drift, causes the radial plasma flow to become ambipolar. We show that the additional radial electric field can play an important role in both small tokamaks and large present-day facilities.

The additional electric field may become especially strong in unsteady processes (such as plasma current ramp-up and ramp-down, adiabatic compression, and pellet injection) during which the toroidal electric field in tokamaks increases substantially. We describe the results from simulations of the current ramp-up phase of discharges in the Tuman-3M tokamak. We demonstrate that the plasma current ramp-up causes a rapid increase in the radial electric field near the last closed magnetic surface and thus can trigger the L–H transition, in accordance with the experimental observations [6].

1063-780X/01/2703-0205$21.00

2. RADIAL ELECTRIC FIELD

We use the balance equations for the momenta in both the toroidal and longitudinal directions. Averaging the balance equation for the momenta along the magnetic field and taking into account the equality $\langle \mathbf{B}\cdot\nabla p\rangle = 0$, we obtain

$$\langle \mathbf{B}\cdot\nabla\cdot\overleftrightarrow{\pi}\rangle_i + \langle \mathbf{B}\cdot\nabla\cdot\overleftrightarrow{\pi}\rangle_e = \langle \mathbf{F}\cdot\mathbf{B}\rangle, \tag{3}$$

where the external forces and the forces associated with inertia, longitudinal viscosity, and ion–neutral friction are all symbolized by **F**. Presumably, the most important of the internal forces is that related to the radial transport of the toroidal momentum. The projection of Eq. (3) onto the toroidal direction has the form

$$\langle \tilde{j}_r\rangle = \langle j_r|\nabla\psi|\rangle = -\left\langle \frac{\mathbf{F}\cdot\mathbf{B}_\phi}{B_\phi B_\theta}|\nabla\psi|\right\rangle. \tag{4}$$

We can see that the averaged radial current $\tilde{j}_r$ is related to the toroidal force **F**. The contribution of the toroidal viscosity component is zero by virtue of the equality $\left\langle \frac{\nabla\cdot\overleftrightarrow{\pi}\cdot\mathbf{B}_\phi}{\mathbf{B}_\phi\mathbf{B}_\theta}|\nabla\psi|\right\rangle = 0$. Equations (2) and (3) give

$$\langle \tilde{j}_r\rangle = -\frac{\langle \mathbf{B}\cdot\nabla\cdot\overleftrightarrow{\pi}\rangle}{\langle B^2\rangle}\frac{2\pi I}{\chi'} - \left\langle \frac{\mathbf{F}\cdot\mathbf{B}_\phi}{B_\phi B_\theta}|\nabla\psi|\right\rangle + \frac{\langle \mathbf{F}\cdot\mathbf{B}\rangle}{\chi'\langle B^2\rangle}2\pi I; \tag{5}$$

where $\overleftrightarrow{\pi} = \overleftrightarrow{\pi}_e = \overleftrightarrow{\pi}_i$.

In the standard neoclassical theory, the toroidal force **F** is assumed to be zero (in the absence of neutral beam injection), so that, according to Eq. (4), the total radial current through a closed magnetic surface automatically vanishes. In a real situation [5], Eq. (3) with Eq. (4) or (5) determines two quantities, namely, the radial electric field (the poloidal rotation velocity) and the mean velocity of the poloidal rotation. On the other hand, provided that the density and temperature profiles are not too steep, the contribution of the force **F** can be neglected, in which case Eq. (5) implies that the radial current is determined primarily by the longitudinal viscosity. Let us consider the contributions of the ion and electron viscosities separately.

The ion viscosity gives rise to the current $\tilde{j}_r^{(1)}$ such that

$$\langle \tilde{j}_r^{(1)}\rangle = -\frac{\langle \mathbf{B}\cdot\nabla\cdot\overleftrightarrow{\pi}_i\rangle}{\langle B^2\rangle}\frac{2\pi I}{\chi'}. \tag{6}$$

Substituting the longitudinal viscosity (2) into Eq. (6) yields

$$\langle \tilde{j}_r^{(1)}\rangle = \tilde{\sigma}_\perp(\varphi'^{(\mathrm{STAND})} - \varphi'), \tag{7}$$

where $\varphi'^{(\mathrm{STAND})}$ is defined by formula (1). For circular magnetic surfaces, we have

$$\langle j_r^{(1)}\rangle = \sigma_\perp(E_r - E_r^{(\mathrm{STAND})}), \tag{8}$$

where $E_r^{(\mathrm{STAND})}$ is defined by formula (2),

$$\tilde{\sigma}_\perp = \frac{3\left\langle\left(\frac{\mathbf{B}}{B}\cdot\nabla\cdot\mathbf{B}\right)^2\right\rangle}{\langle B^2\rangle^2}\mu_{i1}\left(\frac{2\pi I}{\chi'}\right)^2, \tag{9}$$

and the expression for the viscosity coefficient μ_{i1} is taken from [2] (see also the Appendix). For circular magnetic surfaces, the transverse conductivity in the banana regime has the form

$$\sigma_\perp^b = \frac{3}{2}\frac{\sqrt{\varepsilon}m_i n\nu_i}{B_\theta^2} \tag{10}$$

(where ν_i is the ion–ion collision frequency), and, in the plateau regime, it is equal to

$$\sigma_\perp^p = \frac{3}{\sqrt{2}}\frac{\varepsilon^2 n\sqrt{m_i T_i}}{rBB_\theta}. \tag{11}$$

These expressions coincide with the corresponding expressions presented in [4, 5] correct to a numerical factor because of the different approximate formulas for the longitudinal viscosity.

The electron viscosity is responsible for the current $\tilde{j}_r^{(2)}$, which is proportional to the Ware flux Γ_w and, in the notation of Hirshman and Sigmar [2], has the form

$$\begin{aligned}\langle \tilde{j}_r^{(2)}\rangle &= \langle j_r^{(2)}|\nabla\psi|\rangle = en(\Gamma_w|\nabla\psi|)\\ &= en\frac{(2\mu_{e1}-\mu_{e2}\Lambda_1^e)}{m_e\nu_e}\frac{3\left\langle\frac{\mathbf{B}}{B}\cdot\nabla\cdot\mathbf{B}\right\rangle}{\langle B^2\rangle}\frac{\langle \mathbf{E}\cdot\mathbf{B}\rangle}{\langle B^2\rangle}\frac{2\pi I}{\chi'}.\end{aligned} \tag{12}$$

Here, Λ_1^e is the familiar Spitzer coefficient, which equals 0.55 for a plasma with $Z = 1$, and the viscosity coefficients $\mu_{e1,2}$ are given in the Appendix. For circular magnetic surfaces, the electron viscosity–induced current in the banana regime is equal to

$$\langle j_r^{(2)}\rangle = 2.3en\sqrt{\varepsilon}\frac{E_\phi}{B_\theta}. \tag{13}$$

The radial electric field corresponds to the condition for the total electric current to vanish:

$$\langle \tilde{j}_r^{(1)}\rangle + \langle \tilde{j}_r^{(2)}\rangle = 0. \tag{14}$$

When the forces **F** can be neglected, this equation is completely equivalent to Eq. (3); this corresponds to the standard neoclassical approach. In other words, the

same radial electric field can be obtained from the condition

$$\langle \mathbf{B}\cdot\nabla\cdot\overleftrightarrow{\pi}\rangle_i + \langle \mathbf{B}\cdot\nabla\cdot\overleftrightarrow{\pi}\rangle_e = 0. \quad (15)$$

When the electrons and ions are in the banana regime, Eq. (14) or (15) gives

$$\varphi' = \varphi'^{(\mathrm{STAND})} + \frac{1.53e}{m_i\nu_i}\langle \mathbf{E}\cdot\mathbf{B}\rangle\frac{\chi'}{2\pi I}, \quad (16)$$

so that, for circular magnetic surfaces, we have

$$E_r = E_r^{(\mathrm{STAND})} - \frac{1.53eE_\phi B_\theta}{m_i\nu_i}. \quad (17)$$

For small tokamaks in which the electrons are in the banana regime and the ions are in the plateau regime because the electron temperature is substantially higher than the ion temperature, the more general expression

$$-\varphi' = -\varphi'^{(\mathrm{STAND})} - en\frac{(2\mu_{e1}-\mu_{e2}\Lambda_1^e)}{m_e\nu_e\mu_{i1}}\frac{\left\langle \frac{\mathbf{B}}{B}\cdot\nabla\cdot\mathbf{B}\right\rangle}{\left\langle\left(\frac{\mathbf{B}}{B}\cdot\nabla\cdot\mathbf{B}\right)^2\right\rangle}\frac{\chi'}{2\pi I}\langle \mathbf{E}\cdot\mathbf{B}\rangle \quad (18)$$

is valid and, accordingly, the radial electric field in the case of circular magnetic surfaces is equal to

$$E_r = E_r^{(\mathrm{STAND})} - 1.53\frac{\omega_{ci}R}{\sqrt{2T_i/m_i}\sqrt{\varepsilon}}E_\phi. \quad (19)$$

Finally, the general expression applicable to all collisionality regimes has the form

$$E_r = E_r^{(\mathrm{STAND})} - \frac{2.3en\sqrt{\varepsilon}E_\phi}{(1+\nu_e^*\varepsilon^{3/2})(1+\nu_e^{*1/3}+\nu_e^*)\sigma_\perp^{\mathrm{apprax}}B_\theta}, \quad (20)$$

where

$$\sigma_\perp^{\mathrm{apprax}} = \frac{\sigma_\perp^b}{1+\nu_i^*}, \quad \nu_i^* = \frac{qR\nu_i}{\sqrt{2T_i/m_i}\varepsilon^{3/2}}. \quad (21)$$

3. MODELING OF THE L–H TRANSITION IN THE CURRENT RAMP-UP EXPERIMENTS

We illustrate the role of the additional radial electric field by modeling, as an example, L–H transitions in the Tuman-3M tokamak. The simulations were carried out with the BATRAC code, which is based on the following set of transport equations:

$$\frac{\partial n}{\partial t} - \frac{1}{r}\frac{\partial}{\partial r}r\left[D(\omega_s)\frac{\partial n}{\partial r} - V(\omega_s)n\right] = S,$$

$$\frac{3}{2}n\left(\frac{\partial T_{e,i}}{\partial t} + \frac{\mathbf{\Gamma}}{n}\nabla T_{e,i}\right) + nT_{e,i}\nabla\left(\frac{\mathbf{\Gamma}}{n}\right) - \frac{1}{r}\frac{\partial}{\partial r}r\left[\frac{3}{2}n\chi_{e,i}(\omega_s)\frac{\partial T_{e,i}}{\partial r}\right] = Q_{e,i}, \quad (22)$$

$$\frac{\partial B_\theta}{\partial t} = \frac{\partial}{\partial r}\left[\frac{1}{\mu_0\sigma_\parallel r}\frac{\partial}{\partial r}(rB_\theta)\right].$$

The heat source terms on the right-hand side of the second equation account for the electron–ion heat exchange and the Joule heating of the electrons. (If necessary, the basic set of equations can be supplemented with additional heat sources.) The longitudinal neoclassical conductivity is denoted by $\sigma_\parallel$. The distinctive feature of the BATRAC code is that the transport coefficients (such as diffusivity and thermal diffusivity), as well as the convective velocity, are functions of the shear of the poloidal $\mathbf{E}\times\mathbf{B}$ drift,

$$\omega_s = \frac{RB_\theta}{B}\left|\frac{d(E_r/B_\theta R)}{dr}\right|. \quad (23)$$

In the BATRAC code, the radial electric field is calculated self-consistently from the equations presented in the previous section. The contribution from the toroidal velocity to the neoclassical electric field is neglected because of the intense anomalous radial transport of the toroidal momentum in the Tuman-3M tokamak, which operates in the absence of neutral beam injection. Generally, Eqs. (22) should be supplemented with the transport equation for the toroidal momentum. Note that an analogous set of equations was used by Staebler *et al.* [7, 8] in order to model improved confinement of the DIII-D plasma.

Figure 1 shows a representative dependence of the normalizing diffusion coefficient on the shear of the poloidal $\mathbf{E}\times\mathbf{B}$ drift. The diffusion coefficient has the form $D = D_0 f(r)$ with $f(r) = 1.2 + 3.5(r/a)^2$, and the con-

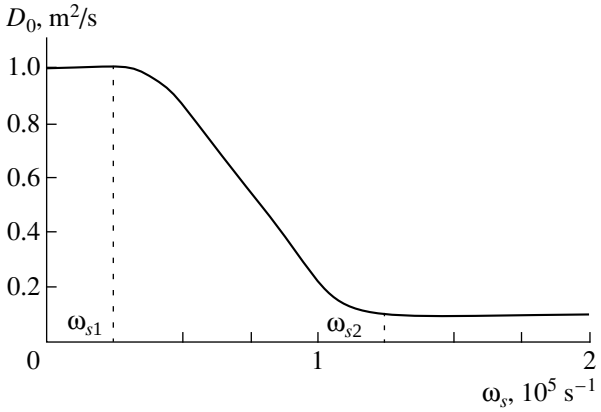

Fig. 1. Normalizing diffusion coefficient vs. the shear of the poloidal drift in crossed fields.

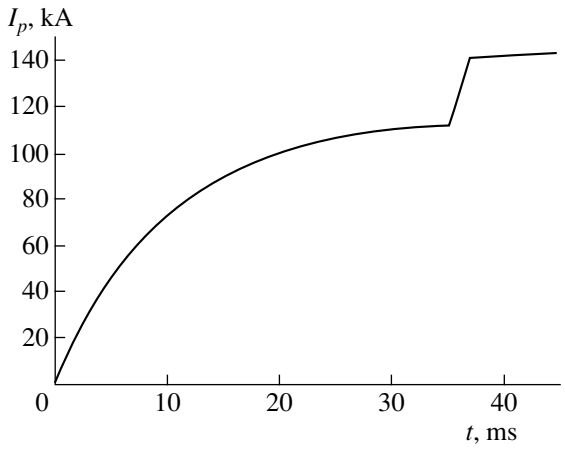

Fig. 2. Total plasma current.

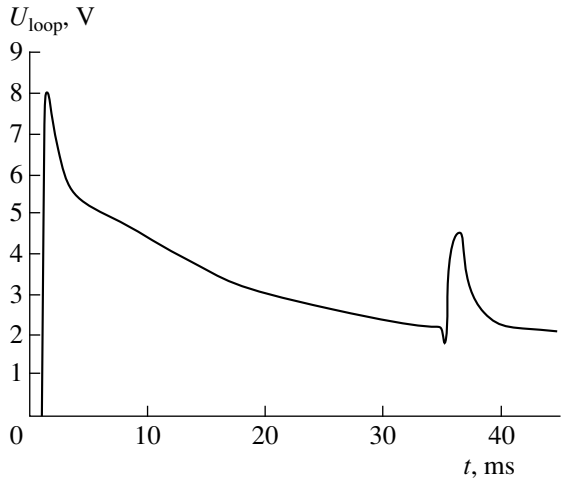

Fig. 3. Loop voltage.

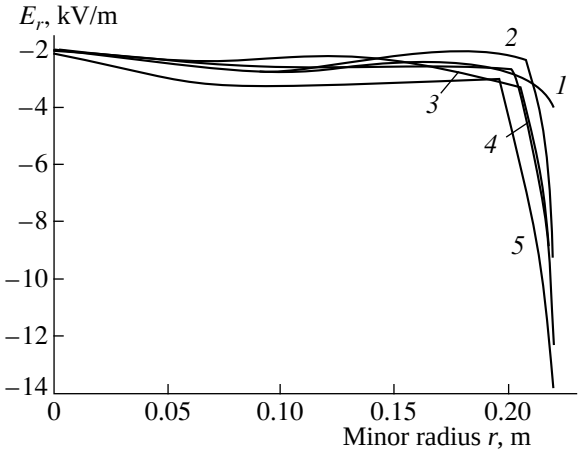

Fig. 4. Profiles of the radial electric field at t = (*1*) 35.0, (*2*) 35.5, (*3*) 37.0, (*4*) 40.0, and (*5*) 45.0 ms.

vective velocity is equal to $V = -(D_0/a)\psi(r)$ with $\psi(r) = (r/a)^2$. The thermal diffusivities were chosen to be $\chi_{e,i} = D$. The radial profiles of the transport coefficients were adjusted to model the density and temperature profiles in the L-mode. In simulations, we used the experimentally measured particle source S.

In our previous studies [3, 4], we modeled a number of L–H transition scenarios. In particular, the density and temperature profiles were chosen to satisfy marginal stability conditions. In other words, the shear ω_s near the last closed magnetic surface was close to ω_1, and the parameter ω_2 was found to play an insignificant role in the transition scenarios. Due to a slight increase in the particle source intensity, the density gradient became larger, the edge shear exceeded the critical value ω_1, and the plasma started to evolve into an improved confinement mode. First, near the last closed magnetic surface, the density and temperature perturbations began to grow, thereby suppressing edge transport processes. Then, the edge transport barrier built up and the density and temperature in the central plasma region increased.

Here, we describe another L–H transition scenario. The time evolutions of the total plasma current and loop voltage are illustrated in Figs. 2 and 3, respectively. The plasma current increases gradually over the first 35 ms; during this time, the discharge plasma remains in the L-mode because the radial electric field (Fig. 4) is insufficiently strong to suppress transport processes. Thereafter, the current starts to increase rapidly, thereby considerably enhancing the toroidal electric field in the edge plasma. According to expression (20), the additional radial electric field, which is proportional to E_ϕ, also increases rapidly and, accordingly, the shear ω_s exceeds the critical value ω_1. The transport processes in the peripheral region are suppressed, and the edge transport barrier builds up. Figures 5 and 6 show representative time evolutions of the diffusion coefficient and plasma density, respectively. In the central region, the plasma density increases primarily due to the inward convection. The thermal-diffusivity and temperature profiles are similar in shape to those shown in Figs. 5 and 6.

After the current ramp-up, the poloidal magnetic field diffuses toward the center of the plasma column and the toroidal electric field at the plasma edge decreases. Inside the transport barrier, the radial electric field remains fairly strong because of the large contribution of the neoclassical electric field, $E_r^{(\mathrm{STAND})}$, which is proportional to the density and temperature gradients. For this reason, the discharge remains in the H-mode.

The computed parameters of the plasma column and the time evolutions of the density and temperature profiles are in satisfactory agreement with the experimental data from Tuman-3M [6].

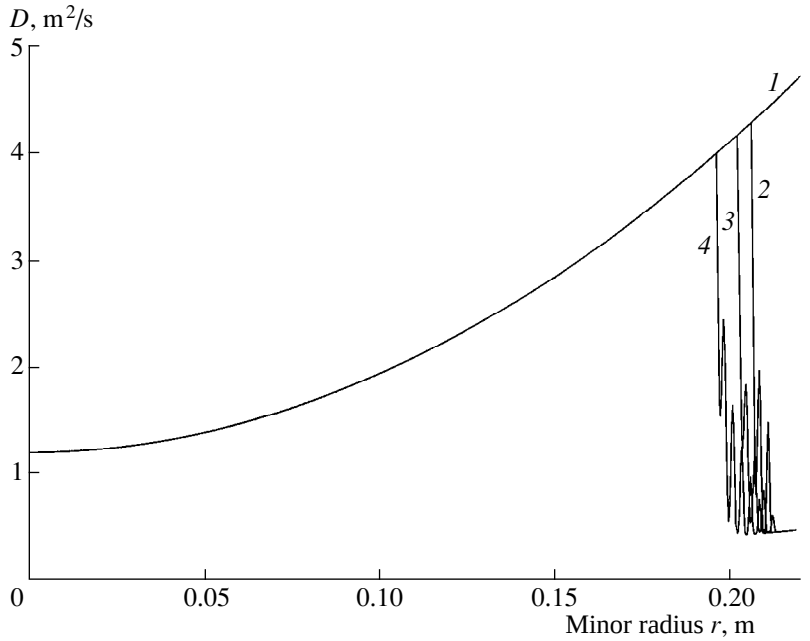

Fig. 5. Radial profiles of the diffusion coefficient at t = (*1*) 35.0, (*2*) 36.0, (*3*) 40.0, and (*4*) 45.0 ms.

4. DISCUSSION

Our simulations show that the additional radial electric field associated with the electron viscosity (or the Ware drift) plays a very important role in transient processes during which the toroidal electric field at the plasma edge increases. An increase in the shear of the poloidal rotation can trigger the L–H transition. Analogous phenomena may also be caused by processes such as plasma heating or cooling, pellet injection, and adiabatic compression, i.e., processes during which the toroidal electric field increases. This effect is important in plasmas with infrequent electron collisions, especially when the electrons are in the banana regime, regardless of the collisionality regime of the ions.

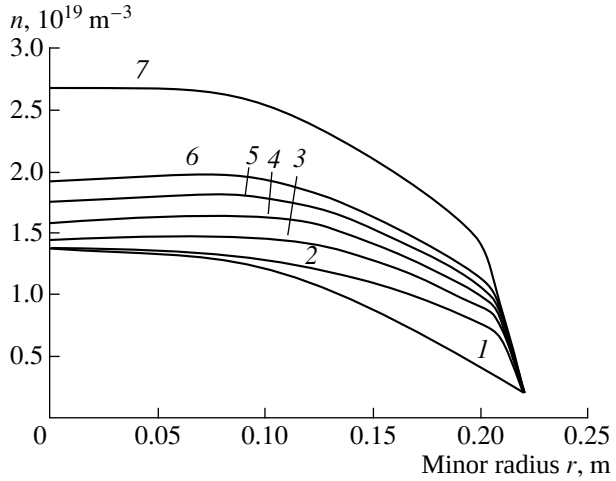

Fig. 6. Radial profiles of the plasma density at t = (*1*) 35.0, (*2*) 36.0, (*3*) 37.0, (*4*) 38.0, (*5*) 39.0, (*6*) 40.0, and (*7*) 45.0 ms.

ACKNOWLEDGMENTS

This work was supported in part by the Russian Foundation for Basic Research (project no. 00-02-16770) and INTAS (grant no. 97-11004).

APPENDIX

At present, there are a number of approximate formulas describing the viscosity coefficients in different collisionality regimes. As an example, we present the expressions that refer to the simple case of a toroidal plasma column consisting of electrons and singly charged ions of one species (see reviews [2, 9]). The electron viscosity coefficients have the form $\mu_{e1} = K_{11}$ and $\mu_{e2} = K_{12} - 5/2K_{11}$; accordingly, the ion viscosity coefficients are $\mu_{ik} = (m_i/m_e)^{1/2}\mu_{ek}$ (k = 1, 2). The coefficients K_{11} and K_{12} are approximated as

$$K_{11} = 1.04qRn_e m_e\sqrt{2T_e/m_e}$$
$$\times\left[\frac{1}{1 + 2.01\sqrt{\nu_e^*} + 1.53\nu_e^*} + \frac{0.51\varepsilon^3\nu_e^*}{1 + 0.89\nu_e^*\varepsilon^{3/2}}\right],$$

$$K_{12} = 1.2qRn_e m_e\sqrt{2T_e/m_e}$$
$$\times\left[\frac{1}{1 + 0.76\sqrt{\nu_e^*} + 0.67\nu_e^*} + \frac{0.46\varepsilon^3\nu_e^*}{1 + 0.56\nu_e^*\varepsilon^{3/2}}\right],$$

where q is the safety factor.

In expressions (1) and (2) for the neoclassical field, the numerical coefficient k is equal to $k = -\frac{\mu_{i2}}{\mu_{i1}}$ and takes on the values –1.69 in the Pfirsch–Schlüter regime, –0.5 in the plateau regime, and +1.17 in the banana regime.

REFERENCES

1. K. H. Burrell, Phys. Plasmas **4**, 1499 (1997).
2. S. P. Hirshman and D. J. Sigmar, Nucl. Fusion **21**, 1079 (1981).
3. V. Rozhansky, A. Popov, and S. Voskoboynikov, in *Proceedings of the International Conference on Plasma Physics and 25th EPS Conference on Controlled Fusion and Plasma Physics, Praha, 1998* [ECA, **22C,** 1876 (1998)].
4. V. Rozhansky, Czech. J. Phys. **48** (3), 72 (1998).
5. V. Rozhansky and M. Tendler, in *Reviews of Plasma Physics*, Ed. by B. B. Kadomtsev (Énergoizdat, Moscow, 1991; Consultants Bureau, New York, 1996), Vol. 19, p. 147.
6. L. Askinasi, M. Andrejko, V. Golant, *et al.*, in *Proceedings of the 26th EPS Conference on Controlled Fusion and Plasma Physics, Budapest, 2000* [ECA, **23C**].
7. G. M. Staebler, F. L. Hinton, J. C. Wiley, *et al.*, Phys. Plasmas **1**, 909 (1994).
8. G. M. Staebler, R. E. Waltz, and J. C. Wiley, Nucl. Fusion **37**, 287 (1997).
9. F. L. Hinton and R. D. Hazeltine, Rev. Mod. Phys. **48** (2), 239 (1976).

Translated by I.A. Kalabalyk

Plasma Physics Reports, Vol. 27, No. 3, 2001, pp. 211–220. Translated from Fizika Plazmy, Vol. 27, No. 3, 2001, pp. 225–234.

PARTICLE ACCELERATION IN PLASMA

Efficiency of Ion Acceleration by a Relativistically Strong Laser Pulse in an Underdense Plasma

A. V. Kuznetsov*, T. Zh. Esirkepov*, F. F. Kamenets*, and S. V. Bulanov**

**Moscow Institute of Physics and Technology, Institutskiĭ per. 9, Dolgoprudnyĭ, Moscow oblast, 141700 Russia*

***Institute of General Physics, Russian Academy of Sciences, ul. Vavilova 38, Moscow, 117942 Russia*

Received July 20, 2000; in final form, September 8, 2000

Abstract—A particle-in-cell simulation is used to investigate ion acceleration by a femtosecond laser pulse propagating in an underdense plasma slab. In plasma slabs with different thicknesses, the ions are found to be accelerated by different mechanisms. It is shown that, for laser pulse intensities in the range $(5–10) \times 10^{19}$ W/cm^2, the ions are accelerated near the plasma–vacuum interface. © *2001 MAIK "Nauka/Interperiodica".*

1. INTRODUCTION

In recent years, much attention has been devoted to the acceleration of high-energy ions during the interaction of high-intensity laser pulses with gaseous and solid targets [1]. Increased interest in this problem stems, first of all, from the creation of high-power lasers capable of generating multiterawatt or even petawatt femtosecond pulses [2]. Experiments on the interaction of such high-intensity laser radiation with plasmas revealed that some of the ions can be accelerated to several tens of megaelectronvolts [1, 3–6]. In experiments with gaseous targets, the gas is rapidly ionized, thereby providing conditions typical of the interaction of laser radiation with an underdense plasma. In most papers, ion acceleration in an underdense plasma is attributed to the so-called "Coulomb explosion," which is associated with a disruption of the plasma quasineutrality inside the self-focusing channel under the action of the ponderomotive force of a laser pulse. The ponderomotive force expels the electrons from the channel, thereby giving rise to the charge-separation electrostatic field, which accelerates the ions in the radial direction. However, recent results from computer simulations [7–10] showed that the plasma becomes especially nonquasineutral in the interaction of a laser pulse with a plasma slab of finite thickness: the ions are most efficiently accelerated at the farther (with respect to the propagation direction of the pulse) plasma–vacuum interface at a time when the laser pulse leaves the plasma slab. The accelerated ions were found to form a dense thin filament, the longitudinal momentum of the ions being much higher than their transverse momentum. This problem requires further investigation because the ion acceleration efficiency depends on many parameters (such as the power, intensity, and energy of the pulse; the plasma density; and the thickness of the plasma slab).

In this paper, we study the efficiency of ion acceleration during the propagation of a femtosecond laser pulse in an underdense plasma slab as a function of the slab thickness. Obviously, in a sufficiently thick plasma slab, a laser pulse can lose its energy completely, so that the ions will be accelerated to moderate energies. On the other hand, in a very thin plasma slab, collective effects are unimportant and ion acceleration by the ponderomotive force of a laser pulse will be governed by the time of laser–plasma interaction, which is too short in this case. Hence, the following questions naturally arise: What is the slab thickness at which the ions can be accelerated most efficiently, and what is the maximum possible kinetic energy of the accelerated ions and their maximum possible density? Below, we will consider only one of these aspects—the maximum achievable kinetic energy of the ions.

The problem was investigated using particle-in-cell (PIC) simulations based on the relativistic electromagnetic code developed by Esirkepov *et al.* [7].

The paper is organized as follows. In Section 2, we formulate the problem and briefly describe the simulation model. In Section 3, we analyze a typical scenario of the propagation of a high-power laser pulse through an underdense plasma slab of finite thickness. In Section 4, we discuss the mechanism for ion acceleration as applied to our problem. In the Conclusion, we summarize the main simulation results.

2. FORMULATION OF THE PROBLEM

We neglect both the ionization-related effects and collisions between particles. This approach is correct when applied to the interaction of a multiterawatt laser pulse with an underdense plasma. The simulations were carried out with a two-dimensional nonparallel version of the 2D3V-PIC electromagnetic relativistic code [7] and with Intel Pentium II personal computers.

The plasma slab thickness was varied from 40 to 300λ, where λ is the laser wavelength. The entire computation region comprised the plasma slab region and a

1063-780X/01/2703-0211$21.00

vacuum region of length 20λ behind the slab. The accelerated ions were observed in the vacuum region.

The incident laser pulse was assumed to originate in the vacuum region to the left of the plasma slab and to propagate from left to right. The calculations were performed for a 40-μm-long 12-μm-wide laser pulse, the laser wavelength and typical intensity being 1.00 μm and $\sim 5 \times 10^{19}$ W/cm^2, respectively. The laser pulse was assumed to interact with a hydrogen plasma of density 10^{21} cm^{-3}. The values of the dimensionless parameters characterizing such laser–plasma interaction were as follows: the amplitude of the electric field in the pulse was $a_e = eE/(m_e\omega c) = 3$–10, the ratio of the pulse length to the laser wavelength was $l_\parallel/\lambda = 40$, the ratio of the pulse width to the laser wavelength was $l_\perp/\lambda = 12$, the ratio of the Langmuir frequency to the laser frequency was $\omega_{pe}/\omega = 0.45$, the plasma density normalized to the critical density was $n/n_{cr} = 0.2025$, and the ion-to-electron mass ratio was $m_i/m_e = 1840$.

In order to save computational time, we simulated ion acceleration during one pass of a laser pulse. After a certain time *t*, all of the information obtained was saved on hard disk. Then, we continued calculations, assuming that the slab thickness corresponds to the distance the pulse had passed over the time *t*. We stopped tracing the motion of the fastest ions after they passed the distance 20λ, which corresponds to the length of the vacuum region, and then analyzed the parameters of the accelerated ions in vacuum. Next, the stored information was again read out from a hard disk and the simulation was continued starting from the same time *t*, but for a thicker plasma slab.

In calculations, the spatial step was 0.125λ. Since the Maxwell equations were solved using an explicit scheme, the time step was chosen to satisfy the Courant–Fredricks–Levi condition. The form factor of quasi-particles was chosen to satisfy the second-order smoothness condition, which substantially reduced the noise level characteristic of the PIC method. The total number of particles was about $\sim 1.5 \times 10^6$.

The results of computer simulations are illustrated in Figs. 1–8. The time is normalized to the period of laser radiation, and the spatial coordinates are expressed in terms of the initial laser wavelength.

3. PROPAGATION OF A HIGH-POWER LASER PULSE IN AN UNDERDENSE PLASMA

Here, we describe the main stages of the evolution of a laser pulse propagating in an underdense plasma. The laser power used in our calculations is above the threshold for relativistic self-focusing. Consequently, at a certain time (approximately equal to $t = 60$) after the pulse enters the plasma, its leading edge experiences a relativistic self-focusing (Fig. 1a), so that the pulse intensity becomes several times higher than the maximum initial pulse intensity.

The onset of an instability caused by stimulated Raman scattering [11] is accompanied by the formation of a sharp front with a width of about 3λ in the pulse envelope. As a result, the pulse with such a sharp front starts to efficiently generate a wake plasma wave [11, 12]. However, under the conditions adopted, the excited wake wave breaks, so that its structure is irregular (this point was discussed in detail in [12]).

After the formation of the first focus, the pulse was defocused. During the defocusing (at a time approximately equal to $t = 100$), the pulse experiences filamentation: five distinct filaments with nearly the same radiation intensities form, two of which subsequently decay in the plasma. The position of filaments at the time $t = 210$ is shown in Fig. 1b. In Fig. 1c, which shows the pulse amplitude as a function of the coordinate along the pulse axis at the time $t = 210$, one can clearly see that the laser pulse has a specific triangular shape with a sharp leading edge (the shock front on the wave-packet envelope [11]). Such a shape is peculiar to the radiation in each of the filaments, which leads to the generation of a wake plasma wave in each of them. This is clearly illustrated by Fig. 2, which shows (a) the distribution of the *x*-component of the electric field in the (*x*, *y*) plane at $t = 170$ (Fig. 2a) and (b) the dependence of the *x*-component of the electric field in the lowermost filament (Fig. 2b). The breaking of a wake plasma wave is responsible for the specific structure of the longitudinal electric field in the leading edge of the pulse (see Fig. 2b). The amplitude of the electromagnetic field in the pulse is large enough for the wake wave to break already during the first half-period of the wake field. For this reason, the longitudinal electric field in the leading edge of the pulse has the form of two oppositely charged layers moving with a velocity equal to the pulse propagation velocity. Such a double layer was studied in [7, 13].

Behind the laser pulse, we can see different coherent structures, in particular, relativistic solitons, which, however, are unlikely to play an important role in ion acceleration. In Fig. 1b, these solitons are seen as relatively small, light and dark regions where the *z*-component of the electric field is, respectively, positive and negative. Solitons are regions in which the plasma density is depressed and the electromagnetic field with a frequency lower than the Langmuir frequency of the surrounding plasma is concentrated [10, 14, 15]. The size of a soliton, which propagates with a nonrelativistic velocity, is on the order of the collisionless skin depth, c/ω_{pe}. The most distinctly seen solitons are those with the oscillating transverse component of the electric field and oscillating azimuthal component of the magnetic field, i.e., *S*-solitons [10, 15]. The solitons form not only inside but also outside the channel, in place of the filaments that have been damped after the passage of the laser pulse. The formation of solitons is attributed to a decrease in the local carrier frequency of the pulse (whose energy is expended on the excitation of wake waves) down to the Langmuir frequency of the

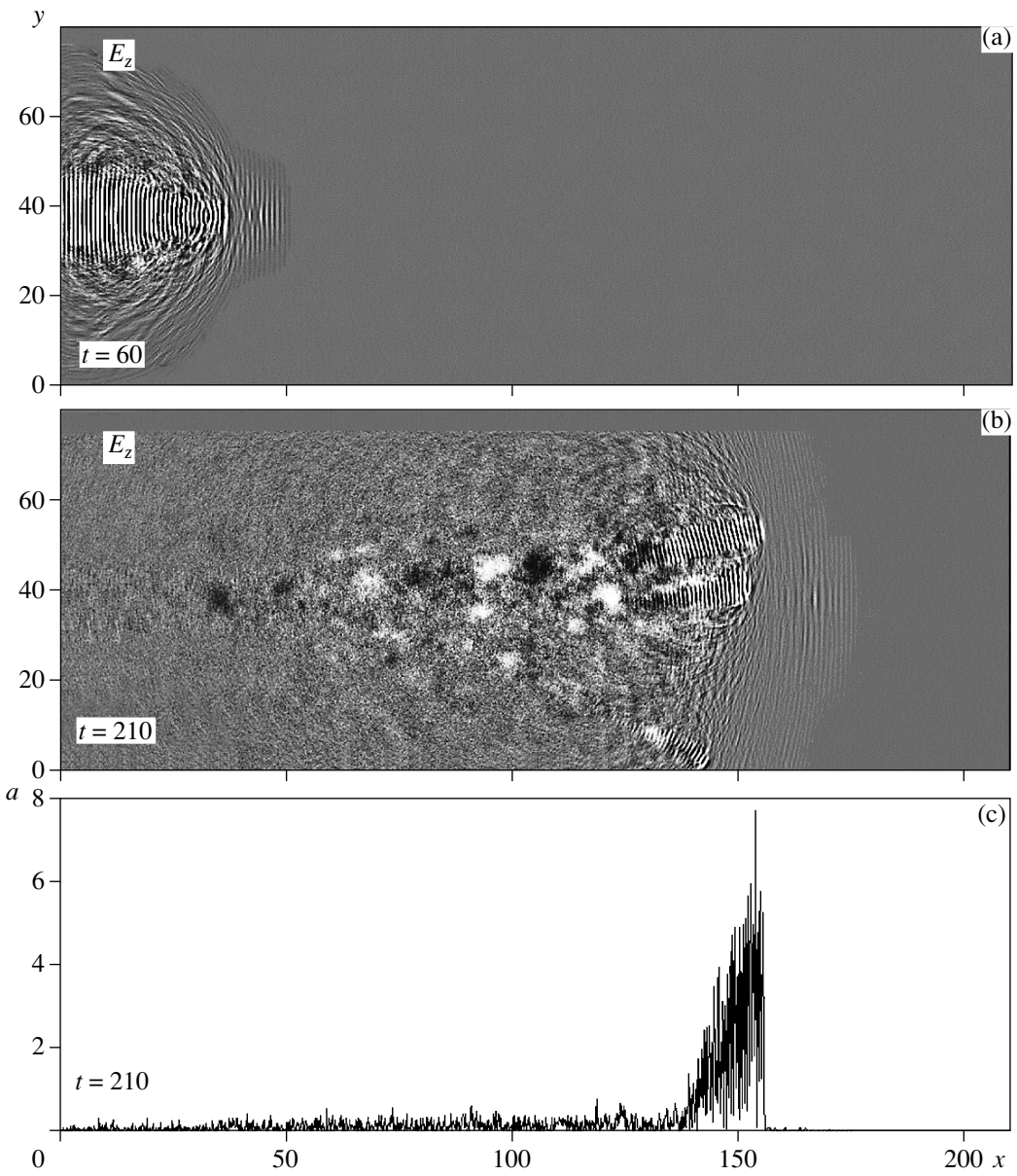

Fig. 1. Evolution of the laser pulse inside the plasma: distribution of the z-component of the electric field in the (x, y) plane at $t =$ (a) 60 and (b) 210 and (c) dependence of the pulse amplitude on the coordinate along the pulse axis at $t = 210$ for $a_e^2 = 50$.

surrounding plasma. The mechanism for the formation of solitons was considered in [10, 15].

Figure 3 shows that the laser radiation produces a channel in which the plasma density is lower than the density of the unperturbed surrounding plasma by a factor of approximately 10. It can be seen that, at the walls of the channel, the plasma is somewhat denser (its density is roughly twice as high as that of the unperturbed plasma). The channel slowly expands.

Behind the pulse, magnetized plasma regions appear that are as long as several collisionless skin depths and are situated along the symmetry axis of the pulse. This axis approximately coincides with the null line of the transverse magnetic field, which is thus positive on one side of the axis and negative on the other side. The direction of the transverse magnetic field and its magnitude correspond to the electric current carried mainly by the plasma electrons. (The role of the ion electric current in the magnetic field generation was analyzed in [9].) This magnetic field is quasistatic and exists over many plasma periods after the passage of the laser pulse. An elementary mechanism for the generation of a quasistatic transverse magnetic field is attributed to the development of an electromagnetic fil-

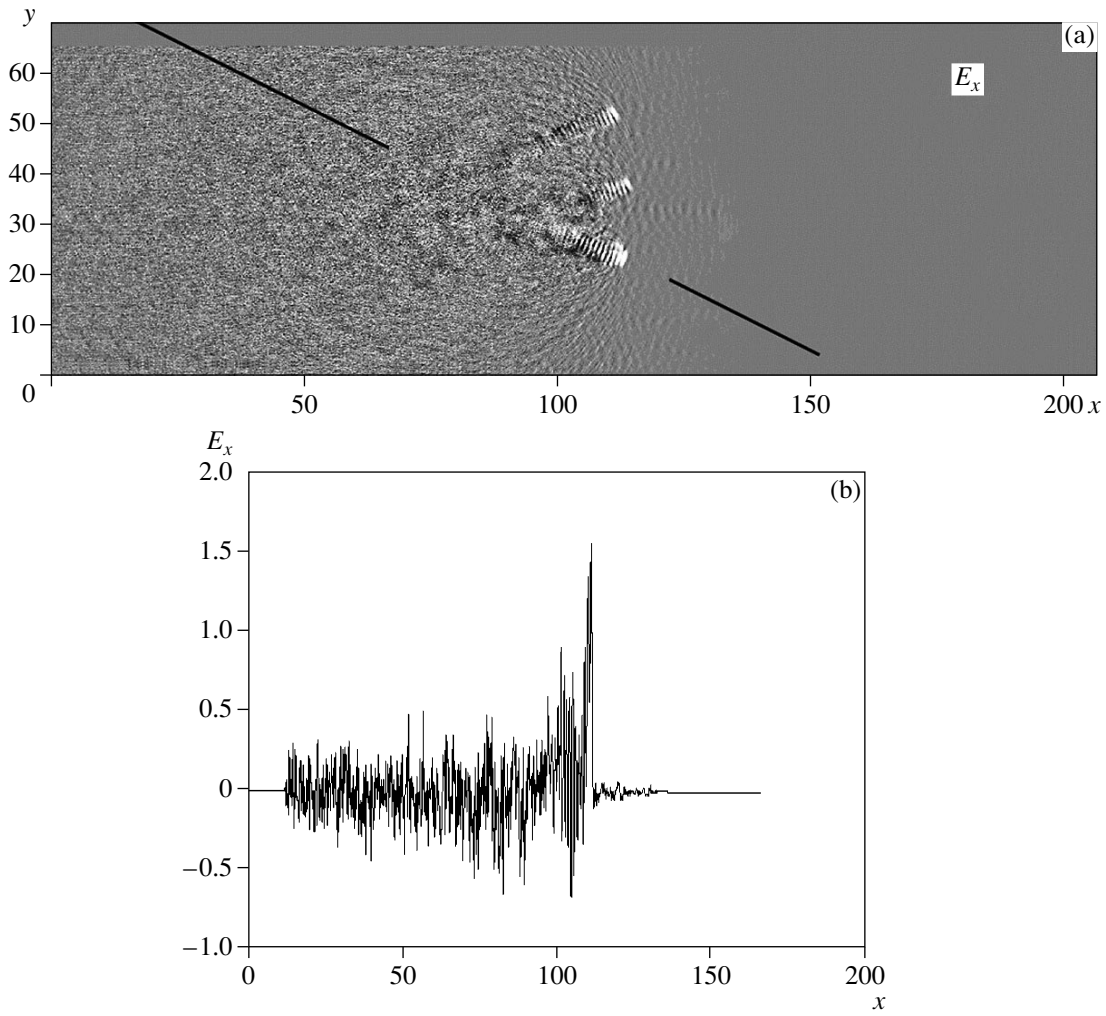

Fig. 2. (a) Distribution of the *x*-component of the electric field in the (*x*, *y*) plane at *t* = 170 and (b) dependence of the *x*-component of the electric field in the lowermost filament for $a_e^2 = 10$.

amentation instability like the Weibel instability, which occurs in a plasma with an anisotropic electron temperature [16–18]. Under the action of a laser pulse, the electrons are accelerated in the longitudinal direction due to the breaking of wake plasma waves. The electric current carried by the fast electrons is neutralized by the return currents carried by slow plasma electrons. This transversely homogeneous configuration is unstable against current filamentation; as a result, a structure arises that is captured well by our simulations and was observed in numerical simulations in [19]. In this structure, the electric current carried by the fast electrons is localized at the channel axis, while the neutralizing (return) current flows at the channel periphery.

Recall that, inside the channels that form in the region where the laser pulse has passed through the plasma and the three filaments are observed, there are regions of elevated plasma density, i.e., the filaments that are stretched along the symmetry axis of the pulse (Fig. 3). The characteristic plasma density in the filaments is on the order of the density of the unperturbed surrounding plasma and is much higher than the plasma density inside the channel. The thickness of the filaments is about several microns. Each filament is, as a whole, electrically neutral. In contrast, the charge of the channel walls is negative. In the initial stage of laser–plasma interaction, the filaments are hardly seen. The most pronounced filaments are those that appear at relatively late stages of the pulse propagation, when the carrier frequency of the laser pulse substantially decreases. According to [11], a decrease in the carrier frequency is attributed to the loss of the laser pulse energy in the adiabatic regime (in which the number of photons in the pulse is conserved).

In the stage during which the decreasing carrier frequency approaches the Langmuir frequency, the pulse–plasma interaction (which is accompanied by the efficient conversion of laser energy into plasma energy and

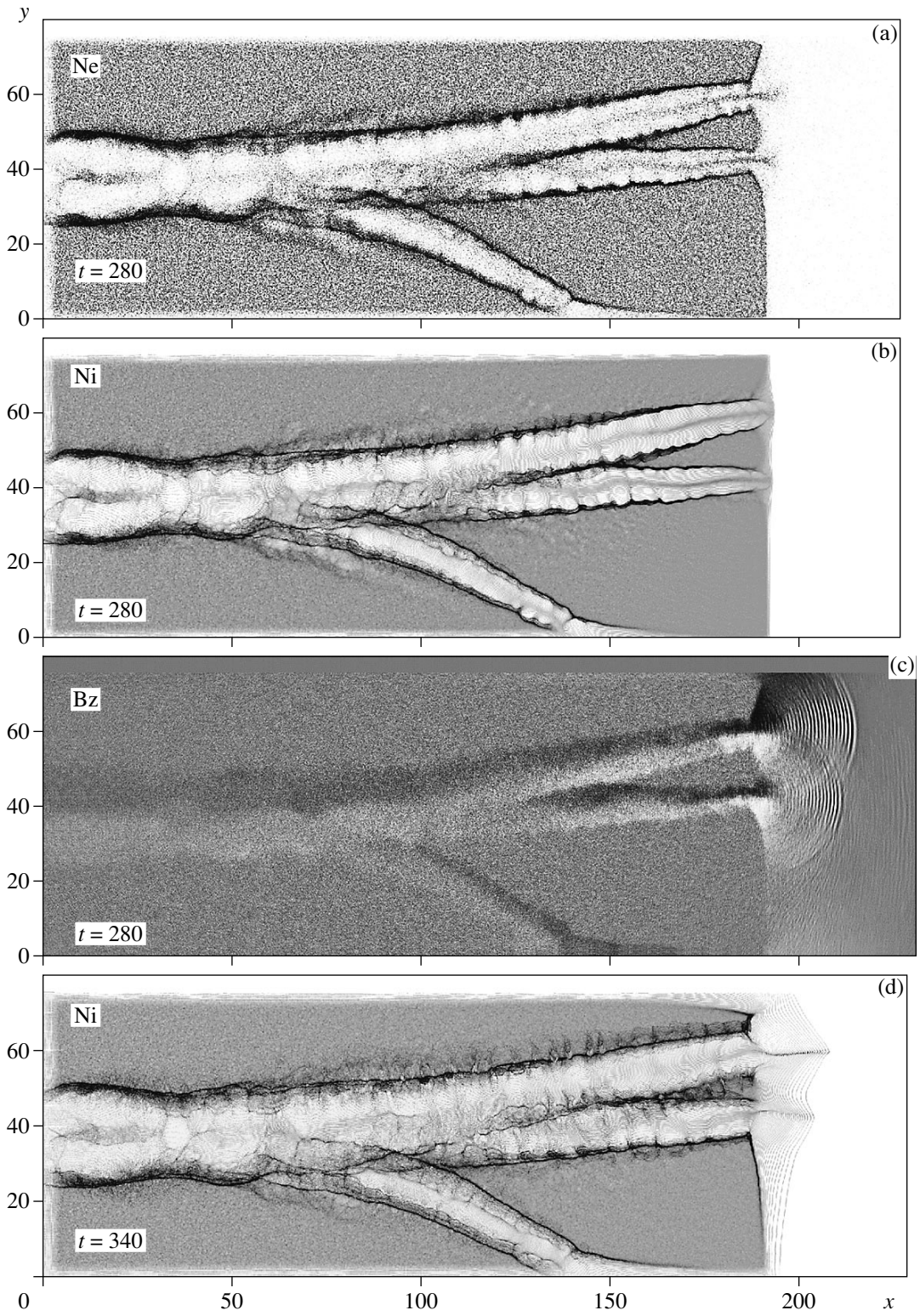

Fig. 3. Channels produced in the plasma under the action of individual filaments of a laser pulse for $a_e^2 = 50$: (a) the electron density distribution in the (x, y) plane at $t = 280$, (b) the channel in the ion component at $t = 280$, (c) the z-component of the magnetic field at $t = 280$, and (d) the ion density distribution at $t = 340$.

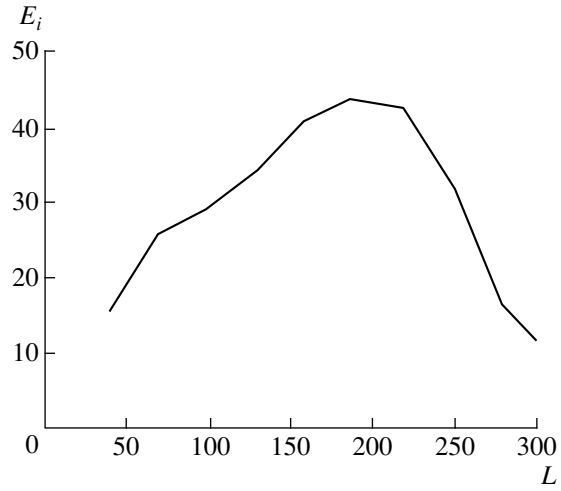

Fig. 4. Dependence of the maximum kinetic energy E_i of the accelerated ions escaping from the plasma on the plasma slab thickness L for $a_e^2 = 50$.

the energy of fast particles) becomes more intense [13]. However, the ion acceleration in a plasma slab of finite thickness is found to be most efficient after the pulse reaches the plasma–vacuum interface [7, 9]. In this stage, the accelerated electrons and ions escape from the plasma just after the pulse. The energy to which the ions can be accelerated depends on the slab thickness, the remaining parameters of the problem being fixed. Figure 4 shows the maximum kinetic energy E_i of the escaping accelerated ions as a function of the slab thickness L. We can see that there exists a range of optimum slab thicknesses for which the ion acceleration is most efficient; in a slab of thickness $L \approx 200\lambda$, the ions can be accelerated to the highest energy $E_i \approx 45$ MeV. In the next section, we will discuss the relevant acceleration mechanism.

Figures 5a, 5c, and 5e present the energy spectrum $n(E_i)$ of the accelerated ions, and Figs. 5b, 5d, and 5f show their distribution over the directions in which they

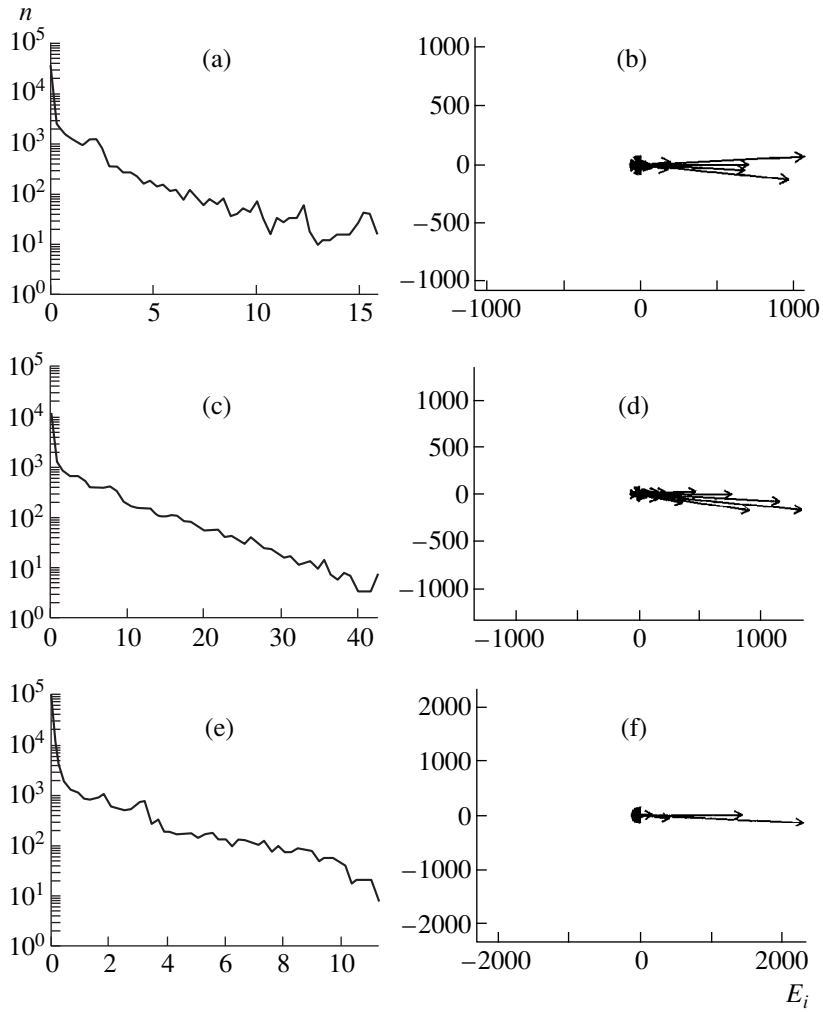

Fig. 5. (a, c, e) Energy spectrum $n(E_i)$ and (b, d, f) distribution of the fast ions over directions into which they are accelerated in plasma slabs with different thicknesses for $a_e^2 = 50$. In Figs. 5b, 5d, and 5f, the length of the arrows is proportional to the number of particles multiplied by their momentum and the direction of the arrows corresponds to direction of the momentum vector. Figures 5a and 5b refer to a slab with the thickness $L = 50\lambda$; Fig. 5c and 5d, to $L = 200\lambda$; and Fig. 5e and 5f, to $L = 300\lambda$.

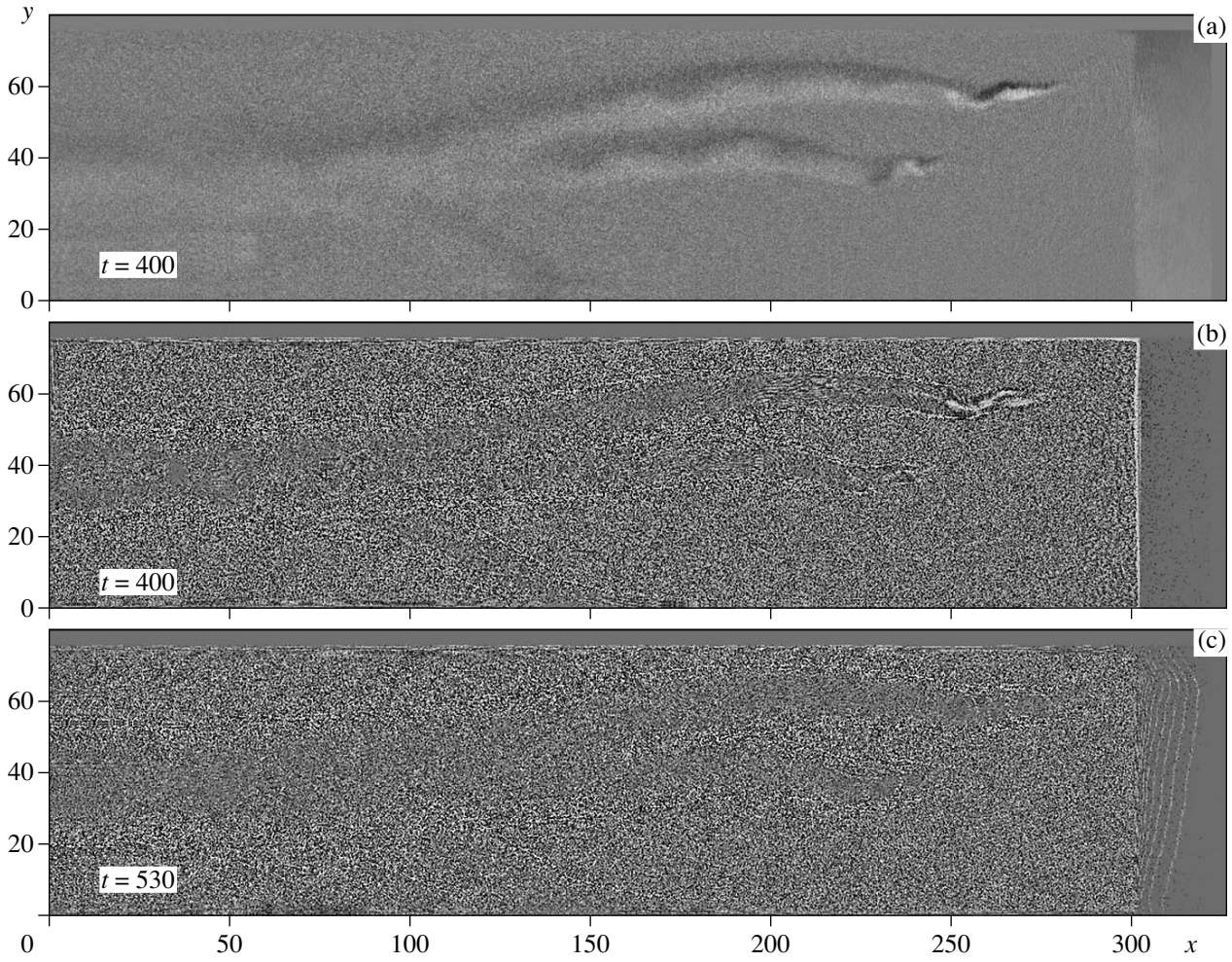

Fig. 6. (a) Distribution of the z-component of the magnetic field at the time $t = 400$ and distributions of the electric charge density at $t =$ (b) 400 and (c) 530 for $L = 300\lambda$ and $a_e^2 = 50$.

are accelerated for different slab thicknesses. In Figs. 5b, 5d, and 5f, the lengths of the arrows are proportional to the number of ions accelerated in the angle $\pi/100$ and the direction of the arrows corresponds to the direction of the ion momentum vector. Figures 6a and 6b refer to a slab with the thickness $L = 50\lambda$; Figs. 6c and 6d, to $L = 200\lambda$; and Figs. 6e and 6f, to $L = 300\lambda$. The energy spectra of the fast ions can be approximated by thermal distributions with the effective temperatures $T_i = 3.7$ MeV (for $L = 50\lambda$), $T_i = 8.7$ MeV (for $L = 200\lambda$), and $T_i = 3.3$ MeV (for $L = 300\lambda$).

Figures 5e and 5f correspond to a slab whose thickness is sufficient for the pulse to lose its energy completely before it reaches the plasma–vacuum interface. Nevertheless, the electrons accelerated inside the slab escape from the plasma, thereby giving rise to the charge separation electric field, which, in turn, accelerates the plasma ions. This regime corresponds to the situation with only one acceleration mechanism; specifically, the fast escaping electrons force the ions to leave the plasma. The damping of the laser pulse is illustrated in Fig. 6. Figure 6a shows the distribution of the z-component of the magnetic field at the time $t = 400$, and Figs. 6b and 6c display the distribution of the electric charge density at the times $t = 400$ and 530, respectively. We can see that the charges are separated in a narrow region near the plasma boundary and that the ions are accelerated over the entire periphery without forming dense filaments. In this case, according to Figs. 4 and 5e, the maximum ion energy is markedly lower than that achieved in a thinner plasma slab.

4. MECHANISM FOR ION ACCELERATION BY A LASER PULSE

Here, we analyze the processes that occur when the laser pulse passes through the plasma–vacuum interface (when the ions are accelerated most efficiently).

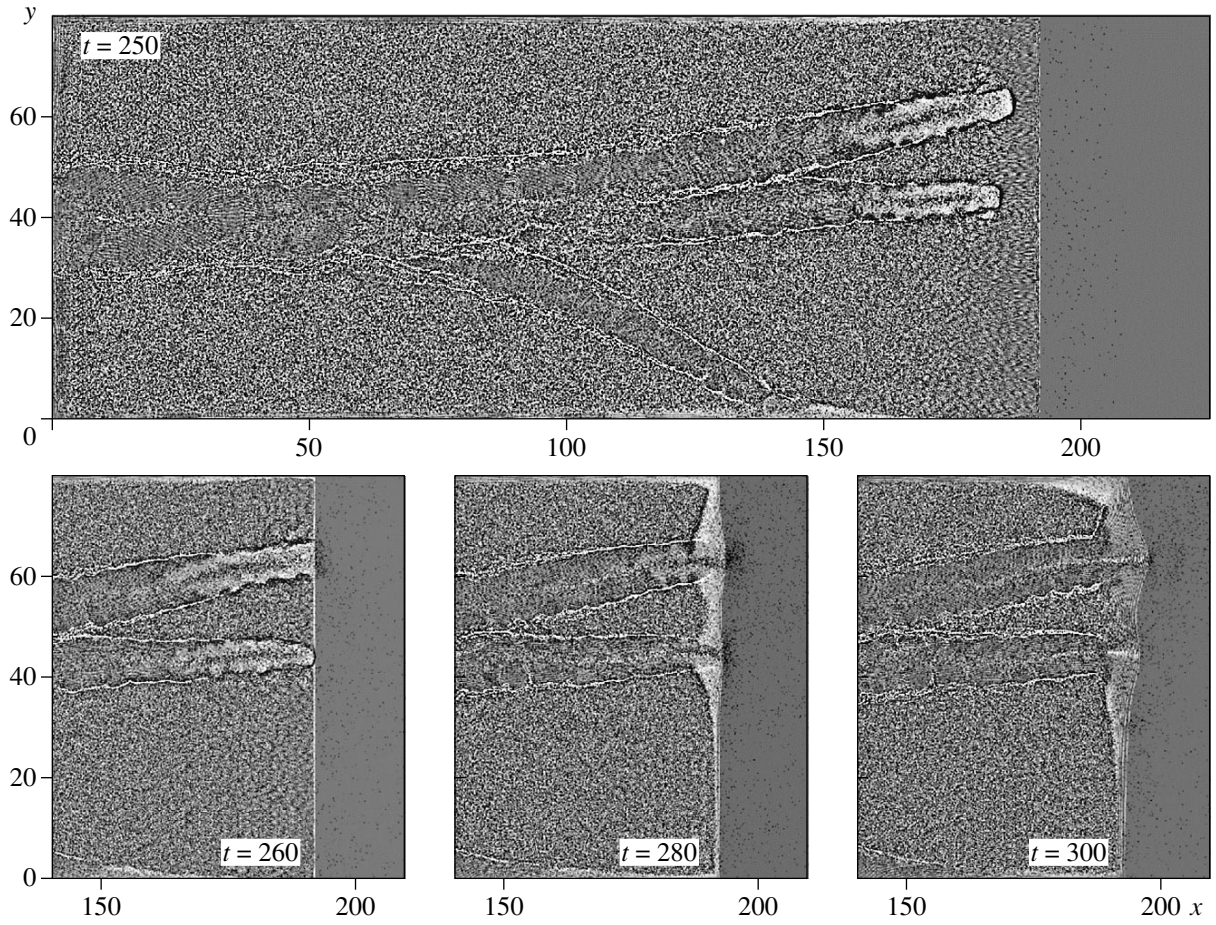

Fig. 7. Distribution of the electric charge density in the (x, y) plane for $a_e^2 = 50$ at the times $t = 250$, 260, 280, and 300. The light and dark regions correspond to the excessive positive and negative electric charges, respectively.

This situation refers to a plasma slab of thickness 200λ (i.e., $90 \times 2\pi c/\omega_{pe}$). First, a cloud of accelerated electrons escapes from the plasma into vacuum. This cloud forms inside the leading part of the pulse and its filaments and rapidly expands. In the vacuum region near the plasma boundary, the escaping electron cloud generates a strong magnetic field, whose polarity coincides with that of the magnetic field inside the channel. The characteristic size of the magnetized regions is about 15λ.

As the electron cloud expands, the magnetic field changes rapidly in time, generating the induction electric field directed toward the vacuum region at the periphery of the channels. In turn, the induction electric field increases the momentum of the plasma electrons in the direction opposite to the propagation direction of the pulse. The plasma ions do not have sufficient time to be displaced substantially. As a result, at the exit of the channel at the plasma boundary, large-scale positively charged plasma regions appear that occupy a symmetric position with respect to the channel axis. Figure 7 shows the distributions of the electric charge density in the (x, y) plane at the times $t = 250$, 260, 280, and 300. The bright and dark regions correspond, respectively, to excessive positive and negative electric charges. The filamentary plasma at the channel axis between these regions is as dense as the unperturbed surrounding plasma and is almost electrically neutral by the time $t = 280$. Then, the electrons leave the axial region, because the magnetized regions that appear at the exit of the channel move along the plasma boundary away from the exit, in which case the induced electric field forces the electrons (and, after a significant delay, the ions) to return back into the plasma. The motion of the magnetized regions can be regarded as the motion of electron-fluid vortices in the direction perpendicular to the electron density gradient. If the plasma slab is limited in each direction, then this process will result in a compression of the slab. In this stage, the ions that form filaments and the ions at the boundaries of the charged plasma regions experience Coulomb repulsive forces. This process results in an anisotropic Coulomb explosion of a filament region approximately $1\lambda \times 10\lambda$ in size. The resulting beam of the accelerated ions is fairly narrow (1λ thick) because of the collimating

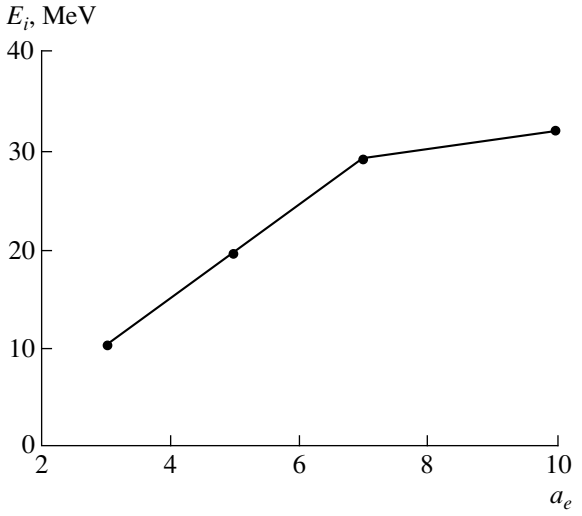

Fig. 8. Dependence of the maximum kinetic energy E_i of the accelerated ions on the amplitude of a laser pulse incident on a plasma slab with the thickness $L = 100\lambda$.

effect of both the charged regions and the magnetic field generated by the electric current carried by the fast ions [9].

Figure 8 shows the maximum kinetic energy of the accelerated ions as a function of the amplitude of a laser pulse incident on a plasma slab of thickness 100λ. We can see that, for pulse amplitudes from 1 to 7, the maximum kinetic energy of the ions escaping from the channel increases linearly. For more intense pulses, the maximum kinetic ion energy increases at a progressively slower rate and saturates, because the magnetic dipole inside the channel near the plasma boundary does not have sufficient time to become intense enough for the above mechanism to result in the required charge separation. Consequently, the ion acceleration efficiency is affected by at least two parameters: the plasma slab thickness and the amplitude of the incident radiation. The acceleration efficiency can be increased by changing both of them. We can expect that, in the plane of these two parameters, an optimum curve (or even an optimum region) should exist over which the maximum kinetic energy of the accelerated ions increases with increasing the amplitude of the incident radiation faster than according to a linear law.

5. CONCLUSION

We have shown that, in the model developed for the interaction of a high-power laser pulse with a plasma slab of finite thickness, the ions are accelerated at the plasma–vacuum interface. The acceleration efficiency is governed by the state of the channel and by the properties of radiation just before it reaches the plasma boundary. The key factors that govern the final kinetic energy of the accelerated ions are as follows.

(i) The density and velocity of the electron cloud at the leading edge of a laser pulse. The higher the density of the beam electrons, the stronger the magnetic fields in the magnetized regions produced by the beam and, accordingly, the stronger the electric field that separates the electron and ion components.

(ii) The density and charge of the ion filament. The higher the ion density and the larger the charge inside the filaments, the more powerful the Coulomb explosion.

The energy spectrum of the fast ions can be described by a thermal distribution with an effective temperature that is a factor of approximately 4 lower than the maximum achievable kinetic ion energy. A beam of accelerated ions is characterized by a small divergence, the longitudinal momentum of the ions being approximately ten times higher than their transverse momentum.

Hence, a fundamentally important point here is that the ions are accelerated most efficiently in the regime in which an ion filament is formed inside the channel and the quasistatic magnetic field is generated at the plasma–vacuum interface. When the ions are accelerated by the only mechanism associated with an expansion of the cloud of fast electrons in the direction perpendicular to the plasma boundary, the efficiency of ion acceleration is much lower.

ACKNOWLEDGMENTS

This work was supported in part by the Ministry of Science of the Russian Federation and the Russian Foundation for Basic Research (project nos. 98-02-16298 and 99-02-16997a).

REFERENCES

1. *Proceedings of the Third International Workshop on Fast Ignition of Fusion Targets, Palaiseau, 2000*, Ed. by P. Mora and J.-C. Gauthier (Ecôle Politechnique, 2000).
2. G. A. Mourou, C. P. J. Barty, and M. D. Perry, Phys. Today **51**, 22 (1998).
3. K. Krushelnik, E. L. Clark, Z. Najmudin, *et al.*, Phys. Rev. Lett. **83**, 737 (1999); K. Krushelnik, E. L. Clark, M. Zepf, *et al.*, Phys. Plasmas **7**, 2055 (2000).
4. G. S. Sarkisov, V. Yu. Bychenkov, V. N. Novikov, *et al.*, Phys. Rev. E **59**, 7042 (1999).
5. S. Hatchett, C. G. Brown, T. E. Cowan, *et al.*, Phys. Plasmas **7**, 2076 (2000).
6. A. Maksimchuk, S. Gu, K. Flippo, *et al.*, Phys. Rev. Lett. **84**, 4108 (2000).
7. T. Zh. Esirkepov, Y. Sentoku, K. Mima, *et al.*, Pis'ma Zh. Éksp. Teor. Fiz. **70**, 80 (1999) [JETP Lett. **70**, 82 (1999)].
8. F. Pegoraro, S. V. Bulanov, F. Califano, *et al.*, IEEE Trans. Plasma Sci. (in press).
9. S. V. Bulanov, T. Zh. Esirkepov, F. Califano, *et al.*, Pis'ma Zh. Éksp. Teor. Fiz. **71**, 593 (2000) [JETP Lett. **71**, 407 (2000)].

10. S. V. Bulanov, F. Califano, G. I. Dudnikova, *et al.*, in *Reviews of Plasma Physics*, Ed. by V. D. Shafranov (Énergoizdat, Moscow, 2000), Vol. 22.
11. S. V. Bulanov, I. N. Inovenkov, V. I. Kirsanov, *et al.*, Phys. Fluids B **4**, 1935 (1992); S. V. Bulanov, I. N. Inovenkov, V. I. Kirsanov, *et al.*, Phys. Scr. **47**, 209 (1993).
12. S. V. Bulanov, T. Zh. Esirkepov, N. M. Naumova, *et al.*, IEEE Trans. Plasma Sci. **24**, 393 (1996).
13. S. V. Bulanov, V. A. Vshivkov, G. I. Dudnikova, *et al.*, Fiz. Plazmy **25**, 764 (1999) [Plasma Phys. Rep. **25**, 701 (1999)].
14. T. Zh. Esirkepov, F. F. Kamenets, S. V. Bulanov, and N. M. Naumova, Pis'ma Zh. Éksp. Teor. Fiz. **68**, 33 (1998) [JETP Lett. **68**, 36 (1998)].
15. S. V. Bulanov, T. Zh. Esirkepov, N. M. Naumova, *et al.*, Phys. Rev. Lett. **82**, 3440 (1999); Y. Sentoku, T. Zh. Esirkepov, K. Mima, *et al.*, Phys. Rev. Lett. **83**, 3434 (1999); S. V. Bulanov, F. Califano, T. Zh. Esirkepov, *et al.*, Physica D (Amsterdam) (in press).
16. E. W. Weibel, Phys. Rev. Lett. **2**, 83 (1959); R. C. Morse and C. W. Neilson, Phys. Fluids **14**, 730 (1971); V. Yu. Bychenkov, V. P. Silin, and V. T. Tikhonchuk, Zh. Éksp. Teor. Fiz. **98**, 1269 (1990) [Sov. Phys. JETP **71**, 709 (1990)].
17. A. B. Mikhaĭlovskiĭ, in *Reviews of Plasma Physics*, Ed. by M. A. Leontovich (Atomizdat, Moscow, 1972; Consultants Bureau, New York, 1975), Vol. 6.
18. F. Pegoraro, S. V. Bulanov, F. Califano, and M. Lontano, Phys. Scr., T **T63**, 262 (1996); F. Califano, F. Pegoraro, S. V. Bulanov, and A. Mangeney, Phys. Rev. E **57**, 7048 (1998); F. Califano, R. Prandi, F. Pegoraro, and S. V. Bulanov, Phys. Rev. E **58**, 7837 (1998); Y. Kazimura, F. Califano, J.-I. Sakai, *et al.*, J. Phys. Soc. Jpn. **67**, 1079 (1998); Y. Kazimura, J.-I. Sakai, T. Neubert, and S. V. Bulanov, Astrophys. J. Lett. **498**, L183 (1998); Y. Sentoku, K. Mima, S.-I. Kojima, and H. Ruhl, Phys. Plasmas **7**, 689 (2000).
19. G. A. Askar'yan, S. V. Bulanov, F. Pegoraro, and A. M. Pukhov, Pis'ma Zh. Éksp. Teor. Fiz. **60**, 240 (1994) [JETP Lett. **60**, 251 (1994)].

Translated by G.V. Shepekina

Plasma Physics Reports, Vol. 27, No. 3, 2001, pp. 221–227. Translated from Fizika Plazmy, Vol. 27, No. 3, 2001, pp. 235–242.

PLASMA DIAGNOSTICS

A Study of Low-Frequency Microturbulence by CO_2-Laser Collective Scattering in the FT-2 Tokamak

V. V. Bulanin*, A. V. Vers*, L. A. Esipov, E. R. Its**, A. V. Petrov*, and V. S. Roĭtershteĭn***

**St. Petersburg State Technical University, Politekhnicheskaya ul. 29, St. Petersburg, 195251 Russia*

***Ioffe Physicotechnical Institute, Russian Academy of Sciences, Politekhnicheskaya ul. 26, St. Petersburg, 194021 Russia*

Received July 27, 2000

Abstract—Results are presented from studies of small-scale plasma density fluctuations in the FT-2 tokamak by the method of far-forward CO_2-laser collective scattering. The frequency and wavenumber spectra of fluctuations are measured using parallel k analysis at various positions of the scattering volume in the plane of the minor cross section of the torus. The data obtained are interpreted using numerical simulations. In phenomenological models, plasma fluctuations are substituted by a superposition of two-dimensional noninteracting cells with Gaussian profiles. A comparison of the calculated and experimental spectra shows that plasma fluctuations should be described based on the concept of strong microturbulence. The poloidal rotation velocity and the characteristic scale length of the scattering fluctuations, as well as the radial position of the region where they are located, are determined. The diffusion coefficient of the cells introduced in the model turns out to be close to the thermal diffusivity determined from the electron energy balance in the ohmic phase of the discharge.

1. INTRODUCTION

According to theoretical predictions [1], anomalous electron and ion energy transport in the confinement region of a tokamak can be related to the development of small-scale drift plasma turbulence. This turbulence was studied in many experiments in tokamaks and stellarators. The data were largely obtained by using nonintrusive diagnostics, such as collective scattering of electromagnetic waves and reflectometry. The main difficulty in determining the contribution of microturbulence to anomalous transport is associated with the fact that these diagnostics allow one to measure only plasma density fluctuations. In addition, the data obtained are difficult to interpret because of the poor spatial resolution of these techniques. For the same reason, the nature of the observed broadening of the frequency spectra of scattered radiation is still unclear. The broadening is attributed either to the turbulent motion of scattering fluctuations [2, 3] or to the Doppler effect due to the nonuniform rotation of fluctuations in the scattering volume (see, e.g., [4]). Furthermore, the assumption that anomalous transport in the confinement region is related to fluctuations has not yet been confirmed quantitatively. Most studies were reduced to the phenomenological comparison of variations in the fluctuation level with variations in the transport coefficients calculated from the charged-particle and energy balance. The only exception is a series of investigations in the Tore Supra tokamak, in which the turbulent diffusion coefficients were deduced directly from the CO_2-laser scattering spectra based on a certain adopted model [3].

In this paper, we present the results from studies of electron density fluctuations in the FT-2 tokamak plasma by the method of far-forward CO_2-laser collective scattering. A specific feature of these experiments is the use of parallel k analysis together with plasma probing along different vertical chords in the minor cross section of the torus. The scattered radiation was collected from the plasma region strongly extended along the probing chord. In this case, the method of modeling scattering fluctuations proved to be fruitful for analyzing the data obtained. Previously, the modeling was used in the scattering experiments in [4] and, to some extent, in [3]. However, the authors of those papers did not consider how the frequency spectra depended on k and on the spatial position of the scattering volume; this introduced uncertainty in the choice of the model for scattering fluctuations. A comparison of the results of numerical simulations performed in this paper with the experimental data indicates that the broadening of the scattering spectra from ohmically heated plasma in the FT-2 tokamak is turbulent in nature. An analysis based on the simulation results made it possible to determine the poloidal rotation velocity and the degree of anisotropy of fluctuations, as well as the radial position of the region where the fluctuations are located. As one of the modeling parameters, we determined the diffusion coefficient of two-dimensional (2D) cells, whose superposition substituted for plasma density fluctuations. This diffusion coefficient was compared with the anomalous thermal diffusivity measured from the electron energy balance.

1063-780X/01/2703-0221$21.00 © 2001 MAIK "Nauka/Interperiodica"

2. METHOD FOR DIAGNOSING FLUCTUATIONS

To study the spectra of electron density fluctuations in the plasma of the FT-2 tokamak (R = 55 cm, a = 8 cm), we used the method of CO_2-laser collective scattering. This diagnostics is described in detail in [5]. We used a CW CO_2 laser at the wavelength λ_i = 10.6 μm. A probing laser beam passed along a vertical chord of the minor cross section of the tokamak. The scattered radiation was observed at a small angle θ with respect to the probing beam; the wave vector $\mathbf{k}_\perp$ of scattering plasma fluctuations was oriented almost perpendicularly to the laser beam. In the experiment, the vector $\mathbf{k}_\perp$ was in the plane of the minor cross section. The value of $k_\perp \approx \vartheta 2\pi/\lambda_i$ could vary within the range of 6.4–40 cm^{-1}, the instrument resolution being $\Delta k_\perp$ = 5 cm^{-1}. A specific feature of the FT-2 diagnostic facility was the use of four detectors, which allowed us to simultaneously measure the scattering from fluctuations with four different scale lengths in the wavenumber range up to 17.5 cm^{-1} during the entire discharge. We used the homodyne technique for receiving the scattered radiation. In this case, the output receiver signal $I(t)$ can be written in the form (see [6])

$$I(t) = C\,\mathrm{Re}\int d^3r[\delta n(\mathbf{r}, t)U_i(\mathbf{r})U_{L0}(\mathbf{r})e^{-i\mathbf{k}_\perp\mathbf{r}}]. \quad (1)$$

Here, $\delta n(\mathbf{r}, t)$ is the electron density fluctuation, C is the dimensional constant, $U_i(\mathbf{r})$ and $U_{L0}(\mathbf{r})$ are the distributions of the electric field amplitude of the incident and reference laser beams in the plasma. The signal $I(t)$ describes the time behavior of the real part of the wavenumber Fourier spectrum determined within a spatial "window" $U_i(\mathbf{r})U_{L0}(\mathbf{r})$, which specifies the resolution of the method. In the FT-2 experiments, the length of the scattering volume, strongly extended along the probing beam, was longer than the minor diameter 2a. Under conditions when there was no spatial resolution along the probing beam, it was important to use the scheme allowing studies of different discharge regions. For this purpose, the laser beam was successively directed along vertical chords displaced from the discharge axis by a distance X in the range from –5 to +6.5 cm, which almost completely covered the minor cross section of the torus. The spatial resolution in the plane perpendicular to the probing direction was determined by the probing beam diameter and was equal to 2 cm. The signals $I(t)$ from four receivers were digitized at a rate of 4 MHz. Further, they were used to obtain the chord-averaged spectral power density $S(F, k_\perp, X)$) as a function of the wavenumber ($k_\perp$) and frequency F for various positions of the scattering volume. Using special calibration methods (see [5]), we could represent these spectra in the same relative units, which allowed us to perform a qualitative comparative analysis of the data obtained.

3. EXPERIMENTAL RESULTS

Using the method of CO_2-laser collective scattering, we studied plasma fluctuations for different discharge scenarios in the FT-2 tokamak. The most complete information on plasma density fluctuations was obtained in the ohmic heating regime for the following experimental parameters: I_p = 27 kA, B_t = 2 T, and $\langle n_e\rangle = 2.4 \times 10^{13}$ cm^{-3}. The measurements were carried out for four positions of the probing chord: X = 0, +3, +5, and +6.5 cm. Figure 1 shows the spectra $S(F, k_\perp, X)$ obtained by averaging over a great number of samples of the photodetector signal during the steady-state phase of several discharges. In discharges with the same signals of monitor diagnostics, statistically consistent estimates of the spectra were obtained. The reproducibility of discharge conditions was monitored by microwave interferograms, soft X-ray detectors, and signals from magnetic probes and loops.

The presented dependences reflect the main features of the spectra, which showed up in different experimental series and were characteristic of the ohmically heated plasma in the FT-2 tokamak. It is seen that all of the frequency spectra are broad and lie in the range up to 500–800 kHz, which corresponds to the range of drift turbulent fluctuations [1]. Such spectra are typical for many tokamak experiments. Figures 2 and 3 show the spectra $S(F, k_\perp, X)$ integrated over the frequency F, $S(k_\perp, X)$. The spectra decrease sharply with increasing $k_\perp$ (Fig. 2). For $k_\perp > 14$ cm^{-1}, they decrease according to the power law $S \sim k^{-5.8}$, which is similar to that observed in the Tore Supra tokamak for the range k = 12–26 cm^{-1} [7]. Similar dependences of the intensity of different components of the $k_\perp$ spectrum on X (Fig. 3) evidence that fluctuations with different scale lengths are located in nearly the same region along the minor radius. Note that the spectra measured at symmetrical positions of the probing chord ($X = \pm 5$ cm) were similar in shape and nearly equal in magnitude. This apparently indicates the absence of a pronounced ballooning effect during the development of the observed fluctuations.

At small scattering angles ($k_\perp$ = 8.5 cm^{-1}), the frequency spectrum demonstrates a pronounced shift, which decreases as the probing chord is displaced toward the periphery (Fig. 1). This shift is easily explained by the Doppler shift $\Delta\omega = \mathbf{k}_\perp \cdot \mathbf{V}_\theta$ due to scattering from perturbations with the poloidal rotation velocity $\mathbf{V}_\theta$. As X increases and, thus, the angle between $\mathbf{k}_\perp$ and $\mathbf{V}_\theta$ increases, the spectral shift should decrease. For probing along the central chord (X = 0), when the wave vector $\mathbf{k}_\perp$ of scattering fluctuations was oriented in the poloidal direction, the frequency shift decreased with increasing the scattering angle (Fig. 1). This kind of behavior of the spectral shift allows us to conclude that the poloidal velocity $\mathbf{V}_\theta$ decreases as the scale length of fluctuations decreases. This dependence of the frequency shift on $k_\perp$ was not observed in other

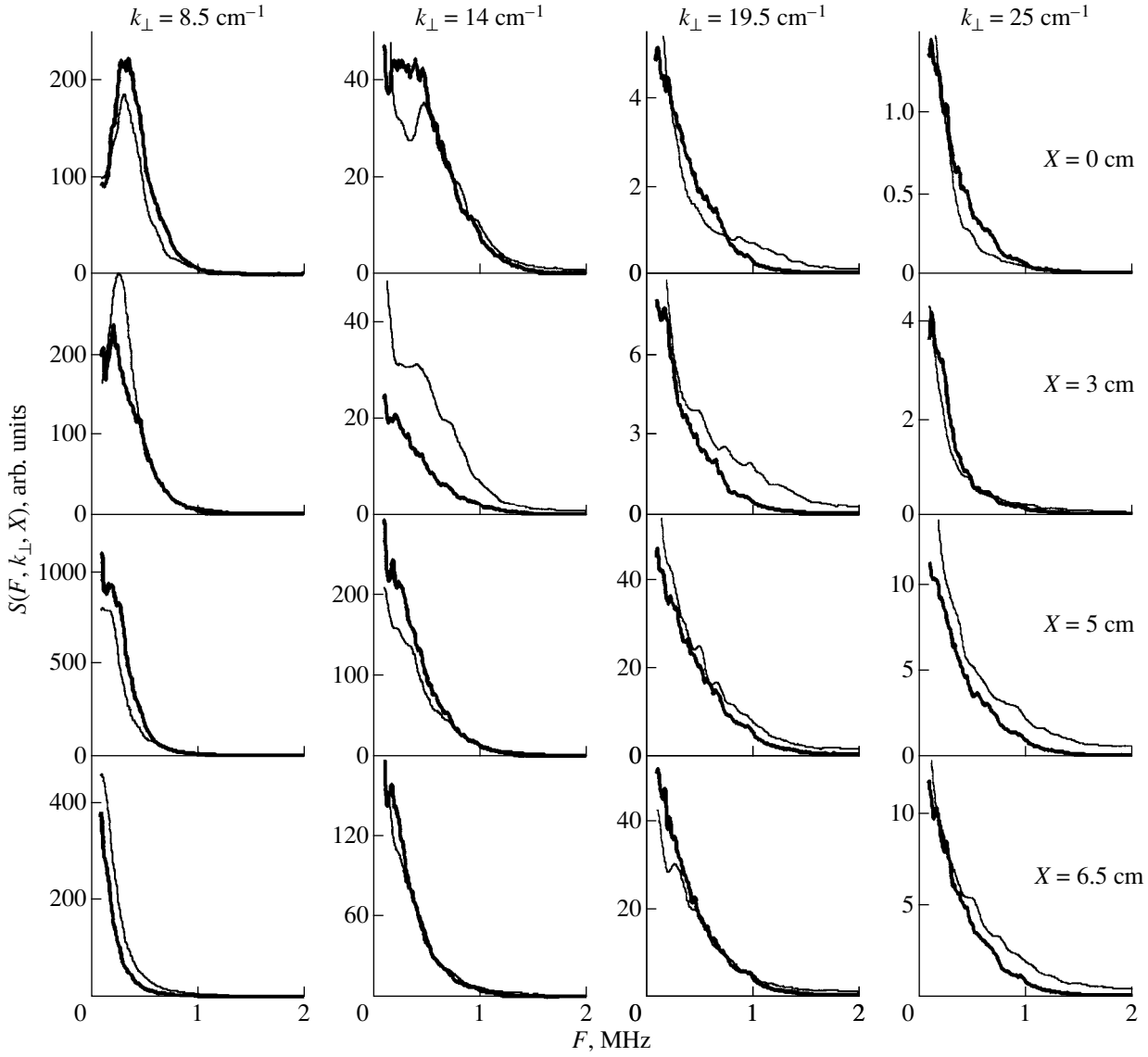

Fig. 1. Measured (heavy lines) and calculated (light lines) wavenumber and frequency spectra of plasma density fluctuations for different probing-chord positions.

tokamak experiments, in which, in contrast, the shift increased with $k_\perp$ (see, e.g., [4, 8]).

The distinguishing feature of the spectra observed in the FT-2 tokamak is the weak dependence of the spectrum width on the wavenumber at high values of $k_\perp$ (Fig. 1). If we assume that fluctuations with different scale lengths move in the same manner, then the spectrum width $\delta\omega$ should increase with $k_\perp$. For the Doppler broadening mechanism, the spectrum width should vary proportionally to $k_\perp$: $\delta\omega \approx \mathbf{k}_\perp \cdot \delta\mathbf{V}$. The spread in the velocities $\delta\mathbf{V}$ may be attributed to the turbulent motion or the velocity shear in the scattering volume. A stronger dependence on $\mathbf{k}_\perp$ is expected when the scale length of the measured fluctuations becomes longer than the correlation length L_V of plasma density perturbations, $L_V k_\perp < 1$ [3]. However, a comparison of the spectra shows that, as $k_\perp$ increases, the spectrum width increases more slowly than by the linear law (on the chords X = +5 and +6.5 cm) and even decreases (on the chords X = 0 and +3 cm for $k_\perp >$ 19.5 cm^{-1}). Such a dependence on $k_\perp$ indicates that the character of motion is different for fluctuations with different scale lengths.

Therefore, the data from spectral measurements show that, in the scattering volume extended along the laser beam, fluctuations with different scale lengths have different poloidal velocities and a different character of motion determining the spectrum broadening.

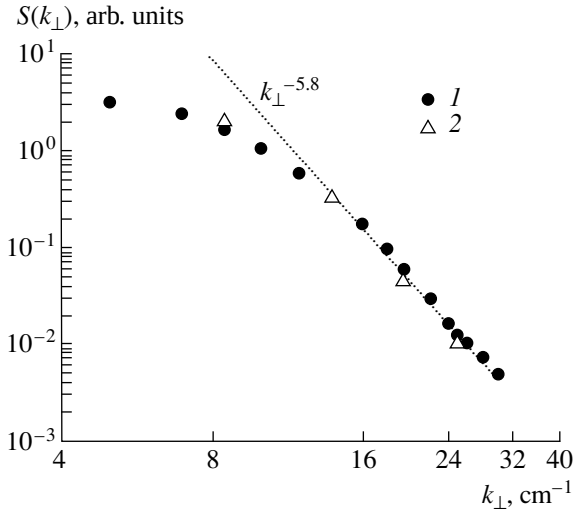

Fig. 2. $k_\perp$ spectra measured along the central probing chord $X = 0$: (*1*) experiment and (*2*) calculation.

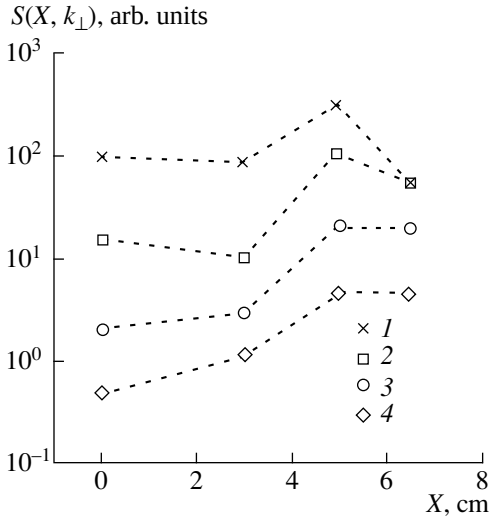

Fig. 3. Intensities of different components of the $k_\perp$ spectrum vs. the probing-chord position: $k_\perp$ = (*1*) 8.5, (*2*) 14, (*3*) 19.5, and (*4*) 25 cm^{-1}.

4. SIMULATION OF PLASMA FLUCTUATIONS

To answer the question of how strongly the turbulent motion and the radial nonuniformity of rotation velocities inside the scattering volume influence the spectrum broadening, a simulation was used to analyze the experimental data. Consistent simulation of the scattered spectra involves the use of a certain model for plasma perturbations $\delta n(\mathbf{r}, t)$ and the computation of the output receiver signals using formula (1). In our phenomenological model, the plasma density fluctuation $\delta n(\mathbf{r}, t)$ was substituted by a superposition of perturbations $\sum \delta n_j(x, y, t)$ in the form of "tubes" (filaments) that were elongated in the toroidal direction and had a Gaussian profile:

$$\delta n_j(x, y, t) = \delta n_j(t) \exp\left[-\frac{(x - r_j(t)\cos(\theta_j(t)))^2}{\delta r_j^2} - \frac{(y - r_j(t)\sin(\theta_j(t)))^2}{\delta r_j^2}\right]. \quad (2)$$

Here, x and y are Cartesian coordinates with the origin in the center of the minor cross section of the torus (the laser beam is directed along the y-axis), δr_j is the tube radius, and $r_j(t)$ and $\theta_j(t)$ are the time-dependent radial and poloidal coordinates of the tube in the plane of the minor cross section of the torus. In the superposition, the cells with negative and positive density perturbations of form (2) were used so that $\langle \delta n(x, y, t) \rangle = 0$. Numerical experiments showed that this superposition can be successfully used to describe a wide class of plasma density perturbations. This class includes axially symmetric harmonic oscillations with different scale lengths in the radial and poloidal directions, as well as completely chaotic fluctuations. The representation of fluctuations by a superposition of cells of form (2) for numerical modeling offers advantages because there is an analytical expression for the homodyne-receiver signal $I_j(t)$ [see (1)] in the case when radiation is scattered by one tube [9]. Therefore, in view of the linearity of expression (1), it is easy to find an analytical expression for the signal from scattering by the superposition of perturbations of form (2): $I(t) = \sum I_j(t)$. The values of the signals $I(t)$ were simultaneously computed for four different values of $k_\perp$ and four probing chord positions. The computed spectra of the signals were compared with the measured spectra.

The first approach to describing fluctuations was a modification of the model proposed in [4]. Unlike in [4], it was assumed that axially symmetric noninteracting poloidal modes are excited on a finite number of rational magnetic surfaces, which agrees with the linear theory of drift instability (see, e.g., [10]). In this model, a wide spectrum width can only be related to the radial nonuniformity of poloidal rotation of these fluctuations in the scattering volume. In this case, the derivation of the model encounters difficulties because, on one hand, perturbations with different scale lengths develop in nearly the same region along the minor radius (Fig. 3), and, on the other hand, these fluctuations should have different mean rotation velocities. This required the presence of the inversion point of the rotation velocity inside the scattering volume, the velocity shear being much higher than the actual shear in the ohmically heated plasma. In addition, numerical experiments revealed an unavoidable discrepancy between the calculated and experimental spectra, which could be understood even without entering into details of the

model. The calculated spectra had spectral peaks that were not observed in the experiments; these peaks were present after multiple averaging even for a short mode lifetime. This was because the model spectrum was formed basically by the modes developing near surfaces with safety factor values $q = 2$, 3, and 4. Moreover, in order to reconstruct the experimentally observed increase in the scattered spectra as the probing chord was displaced toward the periphery of the discharge (Fig. 1), it was necessary to assume that the modes were located in a very narrow radial region $2\delta r$ so that the anisotropy parameter was improbably high: $\lambda_\theta/2\delta r \gg 1$ [here, λ_θ is the poloidal wavelength and δr is the radius of perturbations of form (2), from which the poloidal mode was formed]. Hence, within the model in which the spectral broadening was determined primarily by the nonuniformity of poloidal velocities of modes developing near rational surfaces, even a qualitative agreement was not achieved between the experimental and calculated data.

Another approach to describing plasma density perturbations suggests that the spectral broadening is governed by the turbulent motion of fluctuations. In the model based on the assumption of strong turbulence, plasma density fluctuations were substituted by a great number ($N > 1000$) of noninteracting perturbations of form (2), moving chaotically in the plane of the minor cross section of the torus. The motion of tubes was specified by the spatial displacement $\delta\lambda$ in an arbitrary direction in the plane of the minor cross section of the torus for the time interval Δt. Note that the representation of plasma density fluctuations as a superposition of noninteracting perturbations of form (2) does not imply that the motion of individual cells can be traced in the resultant distribution $\delta n(x, y, t) = \sum \delta n_j(x, y, t)$. This approach only implies that we specify the density fluctuations $\delta n(x, y, t)$ with a short correlation time and short correlation length on the order of the tube size.

The first goal of numerical experiments within the proposed model was to determine the dependences of frequency-integrated spectra on the position of the probing chord. The data of chord measurements (Fig. 3) showed that the scattering fluctuations with different scale lengths were located in nearly the same region along the minor radius, $r = 5$–6 cm. In the model, the distribution of fluctuations in this region was specified phenomenologically by a Gaussian function $B(r)$ with a width $L_r \gg \delta\lambda$ and a maximum at the given radius r_0. As the tube chaotically approached the boundary of the layer, its perturbation amplitude decreased to the value at which the perturbation "died." For the total number of perturbations to be kept constant, a new perturbation was "born" at this moment at the radius r_0. A satisfactory agreement of the dependences was obtained for $r_0 = 6$ cm and $L_r = 2$ cm. In this case, in addition to the choice of the radial region where fluctuations were located, we had to specify a small anisotropy of perturbations, which was characterized

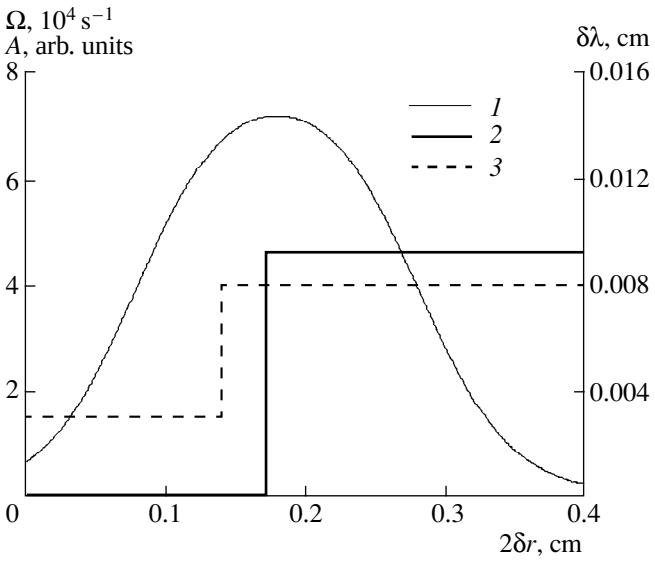

Fig. 4. Functions used in the model of turbulent plasma density fluctuations: (*1*) cell amplitude A, (*2*) angular rotation frequency of perturbations Ω, and (*3*) mean free path $\delta\lambda$ of cells for the time $\Delta t = 6.25 \times 10^{-8}$ s; δr is the tube radius.

by the parameter $\Lambda_\theta/\delta r = 1.3$ (where Λ_θ is the poloidal perturbation length). The perturbations extended in the poloidal direction were modeled by the sum of several nearby cells. For better agreement with the observed k spectra (Fig. 2), it was necessary to introduce different cell sizes. In calculations, we used a statistically uniform distribution of the tubes over sizes (radii) δr; their amplitudes were described by a two-parameter function $A(2\delta r)$ close to Gaussian in shape (Fig. 4). Calculations performed using the free parameters $\delta\lambda$, r_0, and L_r and different functions $A(2\delta r)$ have shown that the model allows us to adequately describe the observed chord dependences and k spectra. It was possible to obtain agreement between the experimental and calculated data within an accuracy no worse than the measurement accuracy (<20%).

When simulating the frequency spectra, two experimental facts should additionally be taken into consideration—the shift of the spectra for small values of $k_\perp$ and the narrowing of spectra with increasing wavenumber $k_\perp$ (Fig. 1). The Doppler shift of the spectra was provided by introducing the angular velocity $\Omega(V_\theta = \Omega r_0 = 2.7 \times 10^5$ cm/s) for large-scale fluctuations with $\delta r \geq 0.2$ cm. In the given model, the narrowing of spectra with increasing $k_\perp$ implied that the step of chaotic motion decreased as the perturbation size decreased. The change in $\delta\lambda$ with increasing δr was described by a step function (Fig. 4). The final refinement of the model, which was introduced to describe the fact that the spectrum intensity decreased as the frequency increased, consisted in that $\delta\lambda$ was defined as a random value with a prescribed distribution.

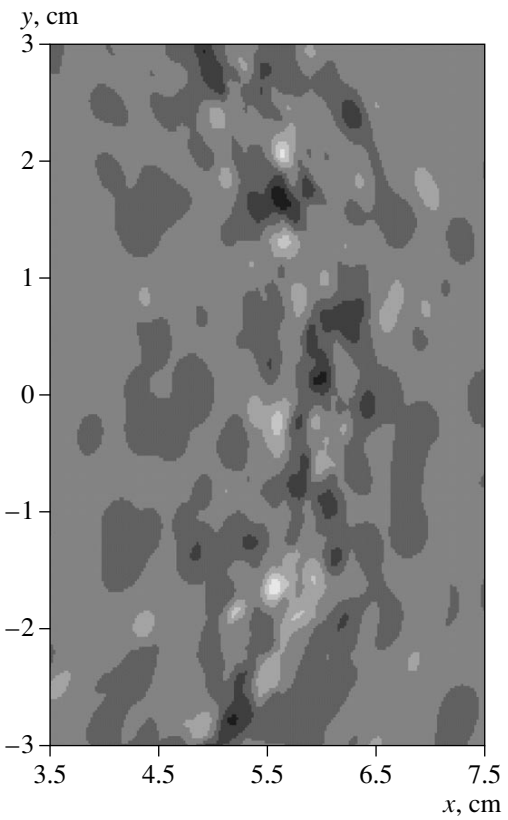

Fig. 5. Fragment of the characteristic relief of the density $\sum \delta n_i(x, y, t)$ calculated for a fixed time. Seven shades of gray (light to dark) correspond to seven equal intervals of the fluctuation amplitude ranging from –15 to 19 arb. units.

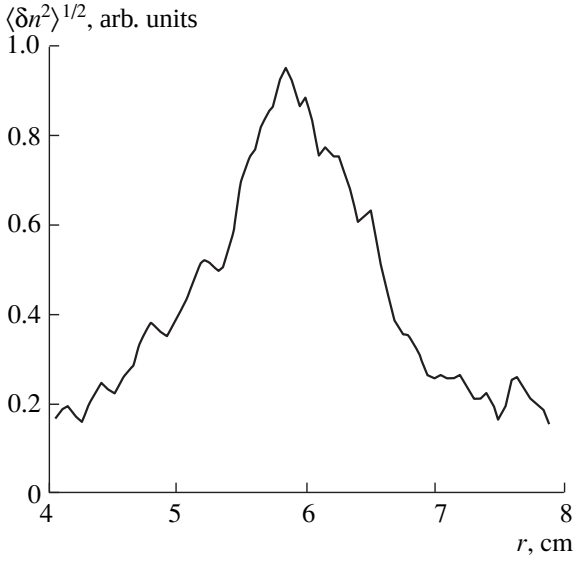

Fig. 6. Calculated radial distribution of density fluctuations averaged over poloidal angles from 0 to 2π.

Figure 1 shows one of the calculated spectra obtained by appropriately choosing the parameters. It is seen that the chosen structure and kinetics of the tube motion, which are characterized by the functions and parameters shown in Fig. 4, correctly describe the variations in the spectral intensity within three orders of magnitude. The calculated dependences of the widths and shifts of the spectra on $k_\perp$ and X are also similar to the experimental dependences. The calculated k spectra for $X = 0$ are compared with the experimental data in Fig. 2. This figure also illustrates the results of calculations for intermediate values of $k_\perp$ at which measurements were not performed. A characteristic pattern of the plasma density fluctuations is demonstrated in Fig. 5, which shows the function $\sum \delta n_j(x, y, t)$ in the given space window of the minor cross section of the torus at a fixed time.

As might be expected for a multiparameter simulation, such an agreement between the experimental and calculated spectra might be obtained with a somewhat different set of parameters. However, an important circumstance is that, with any set of model parameters used, we stably obtained the following mean parameters of turbulent perturbations. Scattering perturbations with a radial-inhomogeneity scale length of $L_r \approx 2$ cm were always located near $r_0 \approx 6$ cm. The characteristic radial perturbation distribution shown in Fig. 6 was similar to that determined previously by the reflectometry technique under similar ohmic discharge conditions [11]. The poloidal rotation velocity of the large-scale fluctuations was always at a level typical of the ohmic phase of the discharge in the FT-2 tokamak [12]. The characteristic cell size $2\delta r \approx 0.2$ cm (Fig. 4), which determined the radial correlation length of the resulting fluctuations, varied only slightly. This size corresponded to the expected scale length of the drift instability $\delta r/\rho_s \approx 4$ (where ρ_s is the Larmor ion radius at the electron temperature) [1]. The diffusion coefficient $D_\perp$ of the tubes, which was defined as the average (over all the cells) ratio of half the square of the cell displacement for a sufficiently long time to this time, also remained unchanged. It is worth noting that this value ($D_\perp \approx 1.6$ m^2/s) was close to the value of thermal diffusivity determined in the FT-2 tokamak from the electron energy balance for the radial region from 5 to 7 cm [13].

5. CONCLUSION

The studies of density fluctuations of the ohmically heated plasma in the FT-2 tokamak by the method of CO_2-laser scattering have provided a great body of information, including the dependences of the scattering spectra on both the wavenumber and the probing-chord position. The measured frequency spectra, even without special treatment, show that scattering fluctuations develop in nearly the same radial region, close to

the periphery of the tokamak. The kinetics of density perturbations is apparently different for different scale lengths. In particular, the mean poloidal rotation velocity of fluctuations is different. The simulation of small-scale plasma density fluctuations, which was performed using the experimental data, made it possible to adequately describe the frequency spectra observed. It was demonstrated that the motion of scattering fluctuations is chaotic and should be described using the model of developed turbulence. Unfortunately, the information obtained on the observed fluctuations (such as the velocity of their propagation in the poloidal direction, the radial position of the region where they are located, the absence of the ballooning effect, the characteristic scale length of fluctuations, and the degree of their anisotropy) does not allow us to unambiguously identify the kind of instability whose strongly nonlinear stage is observed in the experiments. The diffusion coefficient of noninteracting weakly anisotropic cells, which were introduced in the model, turned out to be close to the thermal diffusivity measured in the FT-2 tokamak. This agreement allows us to suggest that the motion of such perturbations corresponds to the motion of test particles. If such an agreement is confirmed by calculating the trajectories of test particles using the known model distribution of fluctuations, then the approach proposed here will deserve consideration as one of the possible ways of estimating the turbulent transport coefficient from the scattering spectra.

ACKNOWLEDGMENTS

We thank A.V. Rozhanskiĭ and D. Gresillon for fruitful discussions. This work was supported in part by the Russian Foundation for Basic Research (project no. 97-02-18119) and the INTAS (grant no. 97-11018).

REFERENCES

1. P. C. Liewer, Nucl. Fusion **25**, 543 (1985).
2. E. Mazzucato, Phys. Rev. Lett. **48**, 1828 (1982).
3. D. Gresillon, B. Cabrit, J. P. Villain, *et al.*, Plasma Phys. Controlled Fusion **34**, 1985 (1992).
4. M. Nagatsu and T. Tsukishima, Nucl. Fusion **27**, 997 (1987).
5. V. V. Bulanin, A. V. Vers, and A. V. Petrov, Fiz. Plazmy **24**, 219 (1998) [Plasma Phys. Rep. **24**, 191 (1998)].
6. E. Holzhauer and J. H. Massing, Plasma Phys. **20**, 867 (1978).
7. C. Honore, R. Sabot, P. Hennequin, *et al.*, in *Proceedings of the 25th EPS Conference on Controlled Fusion and Plasma Physics, Prague, 1998* [ECA, **22C**, 647 (1998)].
8. D. L. Brower, W. A. Peebles, and N. C. Luhmann, Nucl. Fusion **27**, 2055 (1987).
9. D. C. Schram, H. W. H. van Andel, G. le Clair, and P. Brodeur, Plasma Phys. **25**, 1133 (1983).
10. B. A. Carreras, K. Sidikman, P. H. Diamond, *et al.*, Phys. Fluids B **4**, 3115 (1992).
11. V. N. Budnikov, V. V. D'yachenko, L. A. Esipov, *et al.*, Fiz. Plazmy **21**, 865 (1995) [Plasma Phys. Rep. **21**, 817 (1995)].
12. A. Yu. Stepanov, V. N. Budnikov, E. Z. Gusakov, *et al.*, Fusion Eng. Des. **34**, 507 (1997).
13. S. I. Lashkul, V. N. Budnikov, A. A. Borevich, *et al.*, in *Proceedings of the 26th EPS Conference on Controlled Fusion and Plasma Physics, Maastricht, 1999* [ECA, **23J**, 1729 (1999)].

Translated by N.F. Larionova

Plasma Physics Reports, Vol. 27, No. 3, 2001, pp. 228–234. Translated from Fizika Plazmy, Vol. 27, No. 3, 2001, pp. 243–250.

EDGE PLASMA

Real-Time Measurements of Quartz Erosion in Experiments Modeling Heat Loads on Divertor Plates during Disruption in Tokamaks

N. I. Arkhipov, V. P. Bakhtin, S. G. Vasenin, A. M. Zhitlukhin, V. M. Safronov, and D. A. Toporkov

Troitsk Institute for Innovation and Thermonuclear Research, Troitsk, Moscow oblast, 142092 Russia

Received July 20, 2000

Abstract—Time-resolved measurements of quartz erosion are carried out to determine the density of the energy flux incident onto the sample surface. These data are needed to create a reliable code describing the interaction of a thermonuclear plasma with a solid surface. Experiments were performed in the 2MK-200 facility under the program of modeling heat loads on divertor plates during disruptions in tokamaks. A 10-mm-thick plate of fused quartz was exposed to a high-temperature deuterium-plasma stream with the temperature $T_i + T_e \leq$ 1 keV, density $(5–10) \times 10^{15}$ cm^{-3}, $\beta = 0.25$, energy density up to 200 J/cm^2, and power density ~10 MW/cm^2. It is shown that the quartz erosion begins almost immediately after the stream reaches the surface. The eroded material shields the quartz surface from further destruction. Under the given experimental conditions, the integral shielding factor (the ratio of the stream energy to the energy reaching the surface) was rather high (about seventeen). As a result, at a stream energy density of ~150 J/cm^2, the total erosion depth was about 0.75 μm over 35 μs. Based on the measured time dependence of the erosion depth and the reference data on the thermal conductivity of the fused quartz, the power density incident onto the quartz sample was numerically calculated.

1. INTRODUCTION

Since plasma sources capable of producing plasmas with parameters close to those of future tokamak reactors are still lacking, it is impossible to perform an experimental study of the stability of divertor plates against heat loads arising during disruptions. These loads are so high that, in spite of the shielding effect [1], the destruction of the plates can become one of the key factors limiting the reactor lifetime. Consequently, until the first ITER experiments, the extrapolation of results on the erosion of divertor plates to the range of thermonuclear parameters will be based on numerical simulations, which demands a high degree of reliability.

The absence of reliable data on the line emission of multiply charged ions and the constants needed to calculate the populations of the energy levels of these ions, inevitable simplifications adopted when modeling radiative transfer in order to avoid overly laborious computations, an insufficient understanding of the mechanisms governing the destruction of a solid surface at a high-power heat load, etc., lead to a situation in which the results of numerical simulations depend significantly on computer resources and the code used [2–4]. This situation cannot be regarded as being normal; hence, there is a need for reliable experimental data that would be a basis for numerical simulations and would make it possible to create an adequate model of the interaction of a high-temperature plasma with a solid surface. Among these data, the value of the energy that is transferred through the shielding layer and reaches the surface of the material under study and the erosion depth of this material as a function of time are of great importance.

In this paper, we present the results of time-resolved measurements of the erosion of fused quartz in experiments on the modeling of heat loads arising during disruptions. The experiments were carried out in the 2MK-200 facility. The choice of quartz, which is not regarded as a divertor-plate material, is motivated by both the opportunity to employ a very simple measurement scheme and the well-known characteristics of this material. In addition, the very high viscosity of fused quartz, even at the evaporation temperature, prevents the melted quartz from splashing under the action of plasma pressure; hence, common evaporation is a single mechanism for surface destruction. In this case, from the measured erosion depth, taking into account the energy removed from the sample surface due to heat conduction, we can determine the energy incident on the surface as a function of time. Since this quantity is rather difficult to measure directly, the proposed indirect method may provide reliable data that can be used to verify the reliability of a particular numerical code.

1063-780X/01/2703-0228$21.00 © 2001 MAIK "Nauka/Interperiodica"

2. EXPERIMENTAL DEVICE AND MEASUREMENT TECHNIQUE

Real-time measurements of quartz erosion were carried out in the 2MK-200 facility. The design and parameters of this device were described in detail in [5]; for this reason, we present here only the main characteristics needed to understand the conditions of the erosion experiment.

The 2MK-200 facility is a long cusp magnetic confinement system (Fig. 1) consisting of a 1.5-m-long central solenoid with two cusps at its ends (the cusp is a magnetic system consisting of two magnetic mirrors with oppositely directed magnetic fields and two additional coils between them, which create a radially diverging magnetic field with a given radial dependence of the magnetic field strength).

The system is filled with a deuterium plasma produced by two pulsed plasma guns installed at its ends. The plasma streams generated by the guns are injected through the cusps into the central solenoid, collide in the central region, and then thermalize. As a result, the solenoid (the diameter of its vacuum chamber is 14 cm) is filled with a deuterium plasma with the following parameters: $T_e \simeq 300$ eV, $T_i \simeq 700$ eV, and $n_e \simeq (5–10) \times 10^{15}$ cm^{-3}; the total plasma energy attains 50 kJ. The magnetic field is forced out by the plasma toward the metal wall of the vacuum chamber. The characteristic time of plasma confinement in the system (~20 μs) is determined by the radial escape of the plasma through the cusp magnetic slits. The slit width, which depends on the skin depth and, according to [6], is on the order of the ion Larmor radius, determines the thickness of the plasma stream escaping from the confinement system (Fig. 1). The radial magnetic field is maximum (2.5 T) at a radius of 18 cm. In this region, the plasma-stream thickness is minimal and the power density attains 10 MW/cm^2; for this reason, a quartz sample was positioned there. The arrangement of the sample in the cusp is shown in the inset of Fig. 1.

The sample was shaped as a rectangular parallelepiped $45 \times 35 \times 10$ mm in size. The sample was oriented so that its 45×35-mm working surface was perpendicular to the cusp magnetic field and its 35-mm edges were parallel to the system axis. Thus, all measurements were carried out with a plasma stream incident normally onto the sample surface. Due to the interaction of the plasma with the sample, a groove parallel to the long edge of the sample appeared on its surface. The groove depth was measured at the same cross section in the central region of the sample. The orientation of the reference axes is also shown in Fig. 1; the plane $z = 0$ corresponds to the center of the plasma stream.

Metal screens *5* (1-mm-thick copper plates) partially covered the working surface of the sample; the covered regions were not exposed to the plasma. These regions were needed to carry out absolute measurements of the total groove depth with a profilometer. Thus, the exposed area was 45×18 mm^2.

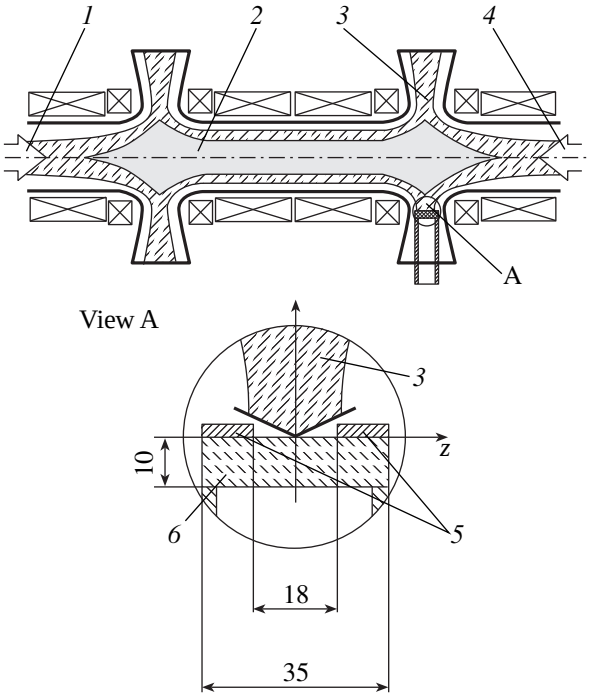

Fig. 1. Schematic of the cusp magnetic confinement system and the arrangement of the sample in the cusp: (*1*, *4*) plasma streams generated by plasma guns, (*2*) plasma confined in the system, (*3*) skin-layer plasma escaping from the system through the magnetic slit of the cusp, (*5*) protecting screens, and (*6*) sample.

The quartz erosion depth was measured using optical interferometry. The erosion depth was determined from the shift of fringes produced by interference of the light reflected from the sample face exposed to the plasma action and that reflected from the opposite (reference) face of the sample. A change in the sample thickness (Δd) and the corresponding fringe shift (ΔN) are related by the well-known relationship $\Delta d = 0.5\Delta N\lambda/\sqrt{n^2 - \sin^2\varphi}$, where λ is the light wavelength, n is the refractive index of the sample material, and φ is the angle of incidence of light on the sample surface. To trace the time history of the erosion process, the interference pattern was recorded with the help of a high-speed streak camera (HSSC).

Figure 2 presents the schematic of the interferometer measurements, which includes a gas laser (*1*), mechanical shutter (*2*), prism (*3*), two diaphragms (*4*, *9*), lenses (*5*, *8*, *10*), sample (*6*), set of filters (*11*), and HSSC (*12*). An LG-106 argon laser operating in continuous mode generated a number of modes with wavelengths from 0.48 to 0.52 μm. The total radiation power was 1 W. The most intensive radiation mode ($\lambda = 0.5145$ μm) was separated out with the help of prism *3* and diaphragm *4* and directed onto sample *6* through cylindrical lens *5*, which slightly broadened the laser beam. The beam cross section at the sample

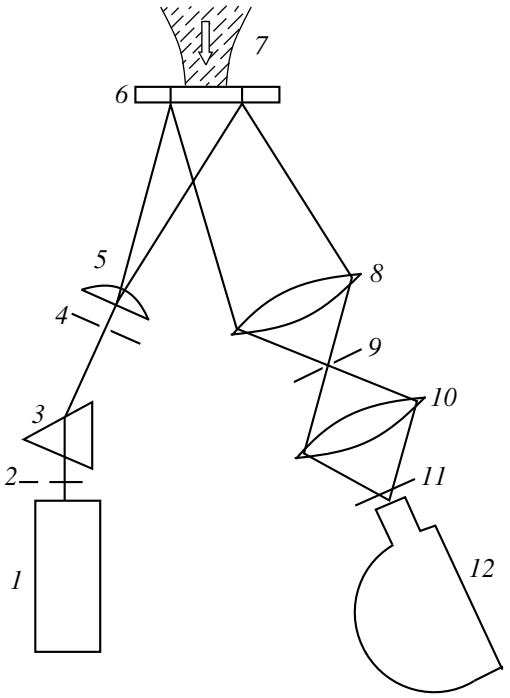

Fig. 2. Experimental layout for time-resolved measurements of quartz erosion: (*1*) gas laser, (*2*) mechanical shutter, (*3*) prism, (*4*, *9*) diaphragms, (*5*) cylindrical lens, (*6*) sample, (*7*) plasma, (*8*, *10*) spherical lenses, (*11*) set of filters, and (*12*) HSSC.

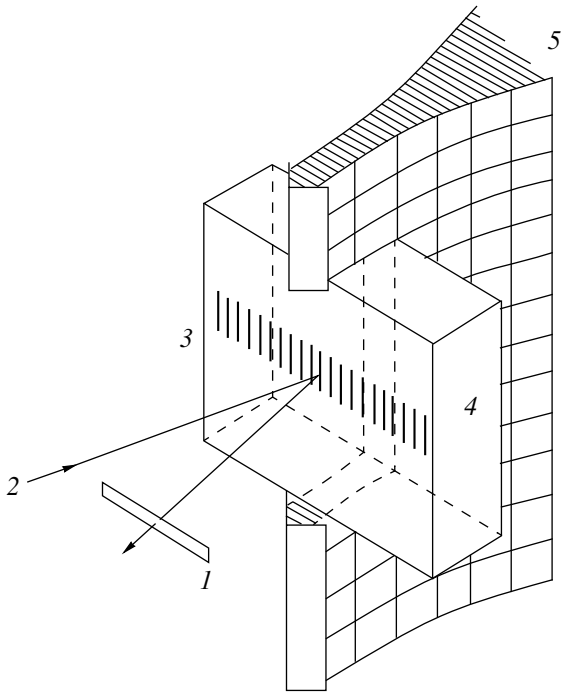

Fig. 3. Orientation of fringes and the HSSC slit: (*1*) entrance slit, (*2*) laser beam, (*3*) fringes, (*4*) sample, and (*5*) plasma.

was approximately rectangular (2×0.5 cm^2) in shape. The angle of incidence of the laser beam onto the quartz sample was about 2°. The interference pattern was produced by interacting light waves reflected from the opposite sample faces.

Spherical lenses *8* and *10* formed an intermediate image of the interference pattern on the HSSC entrance slit, which cut out a narrow streak from the whole interferogram. The orientation of the HSSC slit and fringes is shown in Fig. 3. The fraction of the interference pattern that was cut out by the HSSC slit was a narrow, approximately 1-mm-wide streak on the reference face of the quartz plate.

The HSSC was focused on the sample reference face, which allowed us to minimize the measurement error caused by the bending of the sample under the action of the plasma pressure.

Mechanical shutter *2* used in the scheme was open only for 600 μs, which excluded the possibility of repeated exposures of the film by laser radiation during subsequent revolutions of the HSSC mirror.

The time resolution of the scheme (~0.4 μs) was determined by the width of the slit image on the film and by the speed with which it moved (1.5 km/s) during the rotation of the mirror.

3. RESULTS AND DISCUSSION

The total energy incident onto the sample was measured with the help of a calorimeter (a 75-mm-high and 25-mm-diameter copper cup with a 1-mm-thick wall and a thermocouple attached to it), which was positioned in the same cusp and at the same distance from the system axis as the sample. With the help of this calorimeter, it was found that the average energy density in the plasma stream in the site of the quartz sample was equal to 150 J/cm^2.

Below, it is assumed that the zero time corresponds to the instant when the plasma reaches the sample surface. This instant was determined using a magnetic probe located near the sample. The zero time in the interferogram was determined with the help of a spark discharge, whose light was recorded by the HSSC and made a mark on the film. The corresponding voltage signal was recorded by the same oscillograph as the magnetic probe signal. Taking into account the time resolution of the recording system and the uncertainty in identifying the start of the magnetic probe signal, we estimated the accuracy of determining the zero time in the interferogram to be no worse than ±1 μs.

A typical interferogram of the erosion process for the plasma-stream parameters characteristic of the MK-200 device is shown in Fig. 4. Note that the interference pattern was clearly observed for nearly 50 μs (erosion ended by 35 μs), almost disappeared, and then appeared again after nearly 70 μs with the previous contrast. The reason why the interference pattern disappears is not clear. Nevertheless, after each shot, the

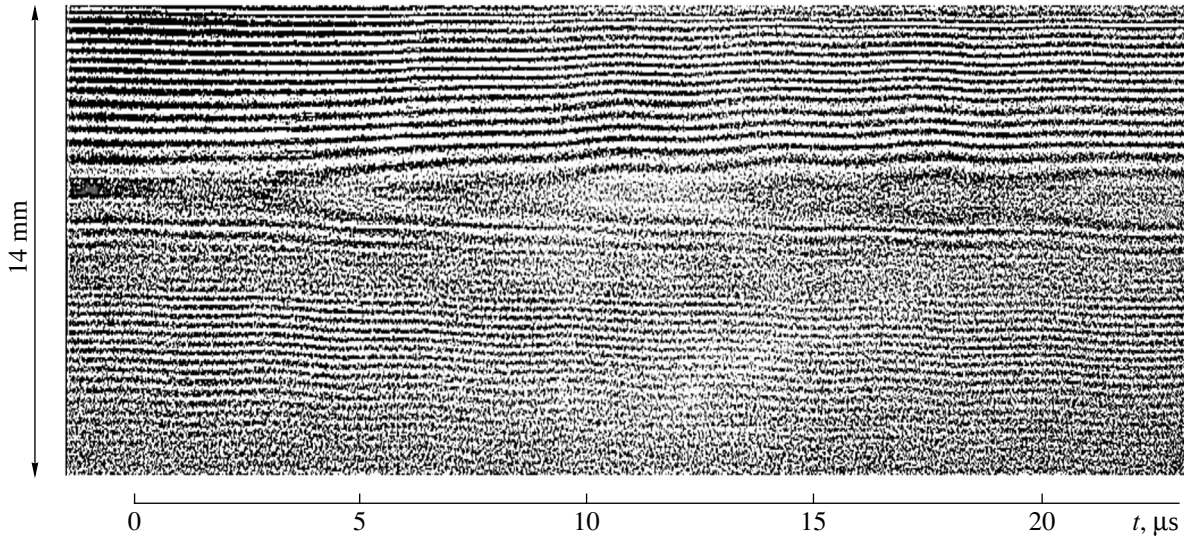

Fig. 4. Typical interferogram of the process of quartz erosion.

interference pattern was restored; this means that the surface facing the plasma does not contain breaks, abrupt changes, or cavities that are typical, e.g., for the surface of a tungsten sample.

The oscillations of fringes, which are seen in the interferogram, are caused by elastic mechanical vibrations of the sample. These vibrations are excited by the plasma pressure. Measurements carried out with piezoelectric pressure gauges showed that, under the standard operating conditions of the MK-200 device, the plasma pressure in the cusp slit at a radius of 18 cm attained 0.6–0.7 MPa for a pulse duration of 15–20 μs; the corresponding oscillogram is shown in Fig. 5. Note that an epoxy-compound layer deposited on the gauge surface facing the plasma in order to shield it from the plasma potential worsened the gauge frequency characteristic. This manifested itself in the broadening of steep leading edges of the pressure pulses of up to 1.5 μs.

Under the action of the plasma pressure, both the thickness of the sample and its refractive index vary, thus producing variations in the optical path of the beam entering the sample through the reference plane and reflected from the working surface, which results in a fringe shift.

This shift is easy to estimate following the results of [7], in which this effect was used to create an optical pressure gauge. It can be shown that the variation in the optical path of the beam passed through the sample and reflected from the working surface is given by the simple relationship $\Delta L \approx 2n_0 d_0(1 - \xi)P/E$, where n_0 is the refractive index for the sample material under normal conditions, d_0 is the initial sample thickness, P is the pressure on the sample surface, E is Young's modulus for the sample material, ξ is a numerical factor ($\xi = (1 - 2\nu)(1 + n_0^2 - 2/n_0^2)/6$), and ν is the Poisson coefficient for the sample material. In deriving this relationship, we took into account that the material refractive index depends on the relative deformation $\left(\frac{\partial u}{\partial x}\right)$ as $n = n_0\left(1 - \xi\frac{\partial u}{\partial x}\right)$ and used Hooke's law $\frac{\partial u}{\partial x} \approx P/E$. Thus, for a 1-cm-thick quartz sample ($n_0 = 1.46$, $E = 73$ GPa, and $\xi = 0.278$) at the pressure $P = 0.6$ MPa, the change in the optical path is equal to $\Delta L \approx 0.2$ μm, which corresponds to a shift of nearly 0.4 fringe for green light ($\lambda = 0.5145$ μm). The time of sound propagation through the sample and back is 3.8 μs; consequently, if a pulsed load is applied to the plate, the oscillations of fringes with a period of ~4 μs and amplitude up to 0.4 fringe should be observed in the interferogram.

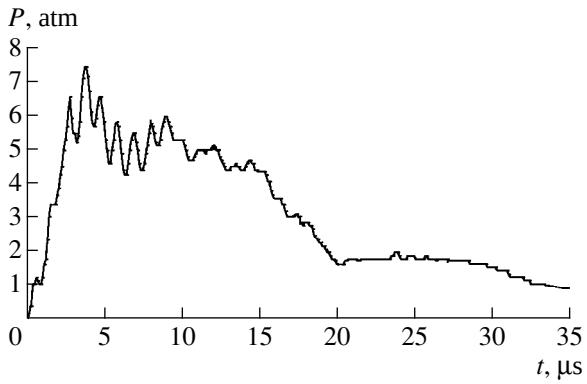

Fig. 5. Typical waveform of the stream plasma pressure at the site of the quartz sample.

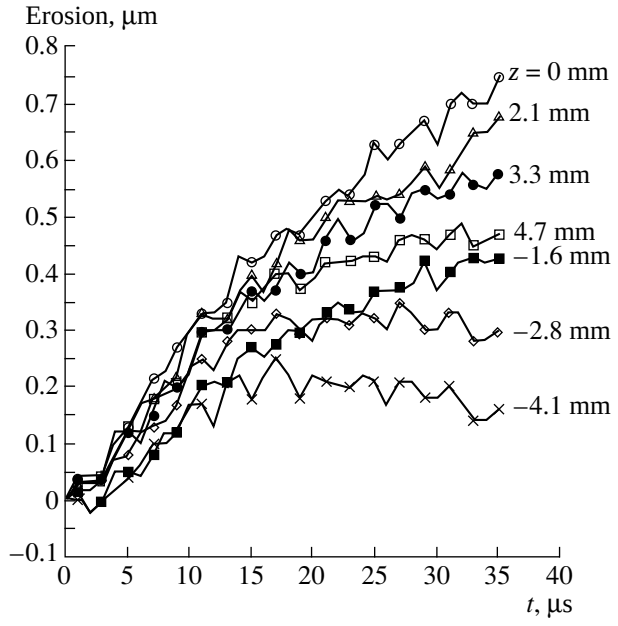

Fig. 6. Time dependence of the erosion depth for several points on the sample surface lying at different distances from the center of the plasma stream ($z = 0$).

Such a fringe shift is easy to detect, and, hence, mechanical vibrations should also appear in the curves illustrating the time behavior of erosion; i.e., these curves should not be smooth. This is clearly seen in Fig. 6, which shows the results of processing one of the interferograms for several points on the sample surface lying at different distances from the center of the plasma stream ($z = 0$). The interferogram was manually processed with a measuring microscope.

It is seen from Fig. 6 that substantial erosion begins nearly 2–3 μs after the plasma reaches the sample surface. For the following 10–15 μs, the erosion rate remains almost constant. The erosion rate is maximum at the center of the stream and decreases at the stream edges. This is natural because the energy density is nonuniform across the plasma stream; it is maximum at the center of the stream and is almost zero at $z = \pm 10$ mm.

By the time $t = 20$ μs, the erosion process on the slope of the groove on the side of the confinement system ($z < 0$) terminates almost completely. This is explained by the fact that, as was mentioned above, the plasma confinement time in the system is equal to ~20 μs. This means that, by this time, the energy flow from the magnetic confinement system almost terminates. At the same time, the plasma continues to flow from the accelerator so that the erosion process becomes asymmetric.

The data obtained are quite sufficient to determine the density of the energy flux incident onto the sample surface (as was mentioned above, this density cannot be measured directly). If we could neglect heat conduction in quartz, the problem would be easy to solve. The usual differentiation of the erosion depth with respect to time and the subsequent multiplication by the quartz mass density and specific sublimation energy could give the power density on the sample surface as a function of time. Unfortunately, although the quartz thermal conductivity is low, neglecting it may introduce large errors. This is illustrated by Fig. 7, which shows the results of one-dimensional numerical calculations.

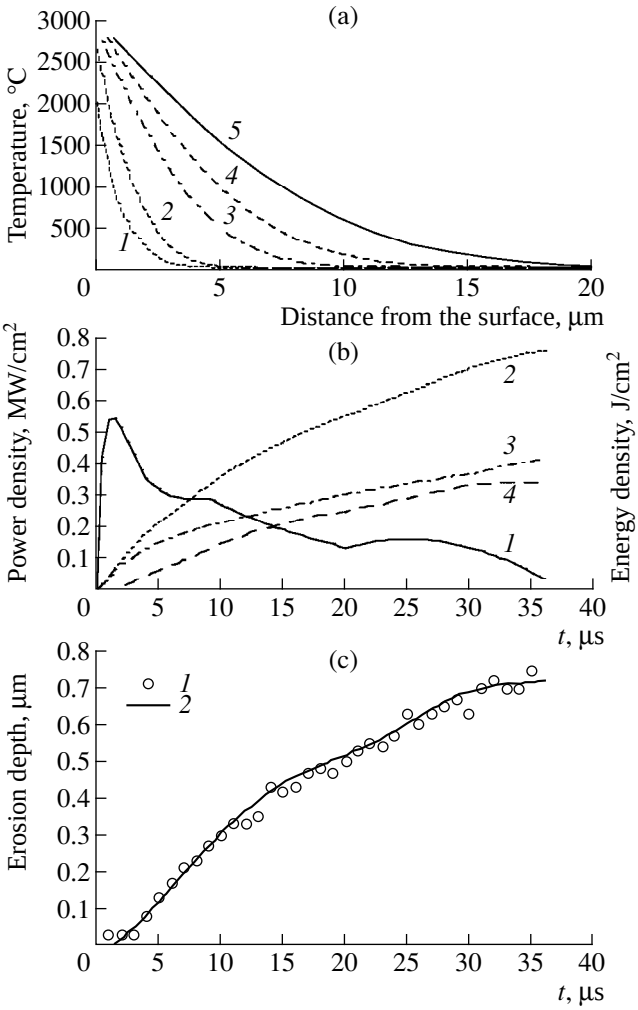

Fig. 7. Results of numerical calculations of the interaction of the plasma stream with the quartz sample. (a) The temperature profile across the sample for five instants: $t =$ (*1*) 1, (*2*) 2, (*3*) 8, (*4*) 16, and (*5*) 35 μs; (b) the time dependence of (*1*) the power and (*2*) the energy density incident on the sample surface, (*3*) the energy expended on heating of the sample by heat conduction, and (*4*) the energy expended on the evaporation of the sample material; and (c) (*1*) the experimental (for $z = 0$) and (*2*) calculated (for the power density described by curve *1* in Fig. 7b) time dependences of the erosion depth.

In calculations, it was assumed that the shielding layer is already formed and the energy incident onto the sample is expended on both evaporation of the surface layers and heating of the sample by heat conduction.

The incident power density was chosen such that the time dependence of the calculated erosion depth coincided with the experimental one. The necessary values of the thermal properties of quartz glass were taken from [8, 9].

Figure 7a shows the temperature profiles across the sample for five instants. As is seen, by $t = 35$ μs, heat has already propagated fairly deep into the sample. This means that a considerable fraction of the energy incident onto the surface is transferred into the internal energy of the surface layers. Note that this ratio is valid only for the specific temperature dependence of the quartz-glass thermal conductivity taken from [10] and extrapolated to high temperatures.

The quantitative energy characteristics of the process are illustrated in Fig. 7b, which shows the time dependences of the power density (*1*) and the energy density (*2*) incident onto the sample surface (the energy density is the time integral of the power density), the energy transferred into the sample by heat conduction (*3*), and the energy expended on the evaporation of the sample material (*4*). For the chosen time dependence of the incident power density, by $t = 35$ μs, when the erosion terminates almost completely, the total energy density incident onto the sample surface is nearly 7.7 J/cm^2. In this case, most of this energy (~4.2 J/cm^2) is expended on heating the sample by heat conduction and only about 3.5 J/cm^2 is expended on erosion.

Note that the time behavior of erosion is sensitive to the time dependence of the power density incident onto the sample surface. A rather good agreement between the calculated and experimental time dependences of the erosion depth (Fig. 7c) is obtained assuming that the incident power density behaves as is shown in Fig. 7b (curve *1*). The shape of this curve resembles the waveform of the stream plasma pressure (Fig. 5) (with regard to the comment concerning the time resolution of the piezoelectric gauge), which is reasonable because the stream power density is proportional to the product of the plasma pressure and stream velocity. It is obvious that the actual time behavior of the power density incident onto the sample surface may be somewhat different from that given in Fig. 7b; however, this difference is related to insignificant details and can hardly change the entire picture of the process.

As was mentioned above, the calculations did not include the energy passing through the sample in the form of radiation (quartz of the KV type is transparent to radiation in the wavelength range 0.2–2.2 μm). To solve the problem more correctly, this energy should be taken into consideration, and, thus, we carried out the relevant measurements. We used a standard IKT solid calorimeter for measurements of the time-integrated energy and a FEU-84 photomultiplier for time-resolved measurements. It was found that about 1.5 J/cm^2 passes through the quartz plate and most of this energy passes at $t > 35$ μs; i.e., the correction to the power density is relatively small. Nevertheless, with all of the components of the energy flux taken into consideration, the energy reaching the surface is about 9 J/cm^2, which comprises only 6% of the total energy of the incident plasma stream (150 J/cm^2). It is unlikely that taking into account the energy of the radiation absorbed in the sample volume will change this value significantly. Hence, the mean value of the power density reaching the solid surface is on the order of 260 kW/cm^2. The same value should be obtained in numerical calculations if the model adequately describes energy transfer across the shielding layer and destruction of the quartz surface.

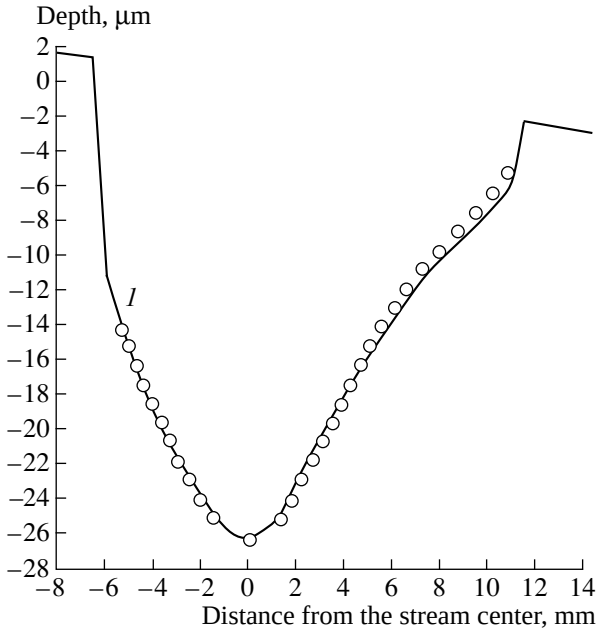

Fig. 8. Profile of the sample surface measured with the profilometer after 35 shots (solid line). Circles show the results of processing the corresponding interferogram.

After 35 shots, the sample was removed from the system. Figure 8 shows the resultant profile of the sample surface measured with a profilometer. The figure also shows the results of processing the interferogram obtained after the 35th shot. In this case, the HSSC was replaced with a Zenit-3M camera. The agreement of the results within the measurement accuracy confirms the reliability of the technique used for real-time erosion measurements.

4. CONCLUSIONS

Based on the results obtained, we can draw the following conclusions:

(i) When a hot-plasma stream acts on a solid surface, only a small fraction of the plasma energy reaches the sample surface. For quartz under our experimental conditions, the total shielding factor (the ratio of the plasma stream energy to the energy reaching the sam-

ple surface) is estimated to be about 16–17. The shielding layer appears as a result of the erosion of the sample material. Significant erosion of quartz begins 2–3 μs after the plasma impacts the surface. It is apparent that, for other materials, this value will be somewhat different at the same power density of the plasma stream. However, this circumstance is of minor importance, because, for time scales characteristic of disruptions in tokamaks (0.1–1 ms), the shielding layer can be regarded as arising instantaneously.

(ii) If the thermal properties of the surface material (the specific heat, the thermal conductivity, the evaporation temperature, and the specific evaporation or sublimation energy) are known, the experimental data on the time dependence of the erosion depth, together with the numerical solution of the heat-conduction problem, make it possible to determine (with a high degree of accuracy) the fraction of energy reaching the sample surface as a function of time.

(iii) For a mean power density reaching the sample surface of 260 kW/cm^2, the erosion rate of the fused quartz is about 0.02 μm/μs.

(iv) Interferometry is a reliable method for measuring the erosion of transparent materials exposed to a hot plasma. The only limitation is that it is impossible to distinguish the fringe shift due to mechanical vibrations of the sample from that caused by erosion. If the shift due to erosion is dominant, the measurements do not encounter serious difficulties.

ACKNOWLEDGMENTS

We thank G. Würz (Karlsruhe Research Center, Germany) for his continued interest in this work and for fruitful discussions. This work was performed under the auspices of the Ministry of Atomic Energy of the Russian Federation (contract no. 1.23.19.19.00.506) and was supported in part by the Russian Foundation for Basic Research (project no. 00-02-18028).

REFERENCES

1. A. Sestero, Nucl. Fusion **17**, 115 (1977).
2. I. Landman and H. Wurz, in *Proceedings of the International Conference on Phenomena in Ionized Gases, Bochum, Germany, 1993*, Vol. 2, p. 201.
3. A. Hassanein and I. K. Konkashbaev, Nucl. Fusion Suppl. **5**, 193 (1994).
4. N. G. Karlykhanov, Yu. V. Martynenko, Yu. I. Matveenko, *et al.*, Fiz. Plazmy **22**, 998 (1996) [Plasma Phys. Rep. **22**, 903 (1996)].
5. N. I. Arkhipov, A. M. Zhitlukhin, V. M. Safronov, and Yu. V. Skvortsov, Fiz. Plazmy **20**, 868 (1994) [Plasma Phys. Rep. **20**, 782 (1994)].
6. I. K. Konkashbaev, I. S. Landman, and F. R. Ulinich, Fiz. Plazmy **8**, 5 (1982) [Sov. J. Plasma Phys. **8**, 1 (1982)].
7. A. A. Bakeev, I. V. Bykov, L. A. Vasil'ev, *et al.*, Prib. Tekh. Éksp., No. 2, 5 (1978).
8. V. K. Leko and O. V. Mazurin, *Properties of Quartz Glass* (Nauka, Leningrad, 1985).
9. *Handbook of Physical Quantities*, Ed. by I. S. Grigor'ev and E. Z. Meĭlikhov (Énergoatomizdat, Moscow, 1991).
10. O. A. Sergeev, A. G. Shashkov, and A. F. Umanskiĭ, Inzh.-Fiz. Zh. **43**, 960 (1982).

Translated by N.F. Larionova

Plasma Physics Reports, Vol. 27, No. 3, 2001, pp. 235–242. Translated from Fizika Plazmy, Vol. 27, No. 3, 2001, pp. 251–259.

NONLINEAR PHENOMENA

Nonquasineutral Model of an Equilibrium Z-Pinch

A. V. Gordeev

Russian Research Centre Kurchatov Institute, pl. Kurchatova 1, Moscow, 123182 Russia

Received April 20, 2000; in final form, September 7, 2000

Abstract—A fundamentally new approach is proposed for describing Z-pinches when the pinch current is governed to a large extent by strong charge separation, which gives rise to a radial electric field in the nonquasineutral core of the pinch. In the central pinch region with a characteristic radius of about $r_0 \sim \sqrt{J_0/en_ec}$, part of the total pinch current $J_0 < J$, is carried by the drifting electrons and the remaining current is carried by ions moving at the velocity $v_{iz} \sim c(2eZJ/m_ic^3)$ in the peripheral region with a radial size of c/ω_{pi}. In the nonquasineutral core of a Z-pinch, the radial ion "temperature" is on the order of ZeJ_0/c. The time during which the nonquasineutral region exists is limited by Coulomb collisions between the ions oscillating in the radial direction and the electrons. Since the magnetic field is not frozen in the ions, no sausage instability can occur in the nonquasineutral core of the Z-pinch. In the equilibrium state under discussion, the ratio of the radial charge-separation electric field E_0 to the atomic field E_a may be as large as $E_0/E_a \sim 137^2(a_0\omega_{pe}/c)\sqrt{J/J_{Ae}}$, where a_0 is the Bohr radius. © *2001 MAIK "Nauka/Interperiodica".*

1. In recent years, ways of optimizing emission from the axial regions of Z-pinches have been studied experimentally in many laboratories around the world [1]. However, a clear theoretical understanding of the structure of Z-pinches [2, 3] has not yet been ascertained and a simple explanation for the onset of quasisteady structures observed in some experiments on Z-pinches is still lacking. Z-pinches are often regarded as unsteady plasma formations in which the magnetic field compresses the plasma until the balance between the compression force and the kinetic plasma pressure is reached. In this case, the problem of the steady equilibrium state of a Z-pinch is analogous to the problem treated by Benford and Book [4] of the current flowing in a plasma. It is well known that a plasma current whose density is independent of the radius is limited because the electrons are captured by their own magnetic field B_θ into Larmor orbits of radius $r_{Le} \sim m_ecv_{ez}/(eB_\theta)$, so that, for $r \sim r_{Le}$, the characteristic limiting current is $J \sim m_ec^2v_{ez}/e$. The existence of a limiting current was predicted as early as 1939 by Alfvén [5]. Further investigations showed that the problems arising from the limiting current can be eliminated by using beams with a special (hollow) structure [6]. However, in the theory developed by Hammer and Rostoker [6] for steady equilibrium states of Z-pinches, an important role is played by the spatial scale c/ω_{pe} (where ω_{pe} is the electron Langmuir frequency), which fails to serve as the characteristic scale of an equilibrium state provided that the magnetic field is sufficiently strong ($B_\theta^2 \gg 4\pi nm_ec^2$). In addition, this theory treats ions merely as an immobile neutralizing background for the resulting hollow structure. For these reasons, it is of interest to seek more realistic equilibrium states of Z-pinch plasmas in which the electrons and ions are both mobile.

Below, we will show that it is possible to construct an equilibrium in which the current J is substantially higher than the Alfvén electron current $J_{Ae} = m_ec^3/e$. With this circumstance in mind, we consider the currents in the range

$$J_{Ae} \ll J \ll J_{Ai}, \tag{1}$$

where $J_{Ai} = m_ic^3/Ze$, m_e and m_i are the masses of an electron and ion, and $-e$ and Ze are their charges. In describing Z-pinches with currents in range (1), the electron inertia can be neglected and the electrons can be treated in the drift approximation, while the ion inertia should necessarily be taken into account.

It should be noted that the electrons can be treated in the drift approximation only at a certain distance from the axis, whereas, near the axis, the electron inertia is important. If the charge separation is strong and the electron drift velocity is on the order of the speed of light, $v_{ez} \sim c$, then, in the axial region of radius $r \sim r_{Le} = m_ec^2/(eB_\theta)$, the current should be on the order of the Alfvén electron current J_{Ae}. Since we are interested in the current range (1), we can exclude from consideration the region of the electron drift motion, where the currents are comparatively low.

An analysis of a large amount of the measured data [1] provides experimental evidence for the presence of a characteristic radial scale on the order of several tens of microns in Z-pinches with currents of about 1 MA and the central plasma density $n_e \sim 10^{20}$ cm^{-3}. Since this radial scale has been observed in Z-pinches under very different experimental conditions, one might expect

that it would be revealed by a simple physical analysis. It is well known that, in the presence of a strong magnetic field, the electron drift motion gives rise to the Hall electric field; as an example, we can mention ion diodes with magnetized electrons [7, 8] and electron vortices that may develop in laser plasmas [9, 10]. In these structures with magnetized electrons, the screening of the electric (and magnetic) field plays an important role. When the electron and ion densities differ appreciably from one another, the Debye screening radius r_D can be estimated from Poisson's equation [see Eq. (9) below]: $r_D^2 \sim \Phi/(4\pi e n_e)$, where Φ is the electrostatic potential. Since, in a strong magnetic field, the electrostatic potential has a Hall nature and is equal to $\Phi \sim B^2/(4\pi e n_e)$, the Debye screening radius is on the order of the magnetic Debye radius r_B: $r_D \sim r_B = B/(4\pi e n_e)$. In the specific case of a Z-pinch with the azimuthal magnetic field $B_\theta = 2J/rc$, the magnetic Debye radius r_B has the form $r_B \sim \sqrt{J/(2\pi e n_e c)}$.

When the charge separation is strong and $E_r \sim B_\theta$, the current in the nonquasineutral plasma region is carried by the electrons drifting with the velocity $v_{ez} \sim c$, in which case the magnetic Debye radius r_B becomes $r_B \sim r_0$, where r_0 is the characteristic electron-current radius. Consequently, in the case at hand, the electron-current radius is on the order of the Debye screening radius, $r_D \sim r_0$. Clearly, this result reflects the fact that the charge-separation electric field is nonzero only in the region where the electron drift current flows. The above expression $r_0 \sim r_B$ with $J_0 \sim 1$ MA and $n_e \sim 10^{20}$ cm^{-3} gives $r_0 \sim 10$ μm. Below, we will see that the current J_0 can be expressed in terms of the total current in a Z-pinch [see formula (29)].

Since the ions moving in the nonquasineutral core of the Z-pinch are unmagnetized, they can be confined in the axial region only by an electric force driven by an excessive negative charge at the axis. In equilibrium, the ions confined in such a manner can be characterized by an oscillatory radial temperature. In the central nonquasineutral region, the current is carried by the drifting electrons. At the pinch periphery, where the electric field is weak, the current can be carried by both electrons (due to Coulomb collisions in a longitudinal electric field) and ions, in which case the longitudinal ion velocity is determined from the conservation law for the generalized momentum,

$$P_z \equiv m_i v_{iz} + \frac{Ze}{c} A_z, \tag{2}$$

where the z-component A_z of the vector potential satisfies the condition $A_z(r = 0) = 0$.

The characteristic radius R of the peripheral region of the Z-pinch is governed by the collisionless ion skin depth: $R \sim c/\omega_{pi} \gg r_0$. Hence, the proposed Z-pinch model involves two spatial scales; the ratio of the scales, $r_0/R \sim \sqrt{J/J_{Ai}} \ll 1$, is determined by the parameter $J/J_{Ai} \ll 1$.

In the nonquasineutral core, the transverse ion energy $\varepsilon_\perp$ is determined by the Hall potential $\Phi \sim B_\theta^2/8\pi e n_e$ and the longitudinal energy $\varepsilon_\parallel$ can be estimated from the conservation law (2). As a result, we obtain $\varepsilon_\perp/\varepsilon_\parallel \sim c^2/(r_0^2\omega_{pi}^2) \gg 1$, which indicates that, in the core of the pinch, the transverse ion energy is high, so that the ions oscillate predominantly in the radial direction. The oscillatory ion energy is determined by the Hall electric field driven by the current J_0 flowing in the region of radius r_0:

$$\varepsilon_0 \sim Ze\Phi \sim ZB_\theta^2/8\pi n_e \sim ZeJ_0/c. \tag{3}$$

For the current $J_0 \sim 1$ MA, the oscillatory ion energy is about several tens of MeV. The energy transfer from oscillating ions to electrons via Coulomb collisions restricts the lifetime of the nonquasineutral core of the Z-pinch; in the energy range under consideration, the ions are decelerated primarily by the electrons. According to [11], for ion energies of about 10 MeV and electron densities of about $n_e \sim 10^{20}$ cm^{-3}, the energy is transferred on a time scale of about 10^{-7} s. This is a time scale on which the nonquasineutral core is completely distorted.

Concluding this section, we emphasize that the proposed approach is aimed at studying the equilibrium states of Z-pinches with currents in range (1). Note that, for protons, $J_{\mathrm{Ai}} \simeq 34$ MA.

2. In this section, we consider the basic idea underlying the proposed Z-pinch model. At first glance, it appears that the dynamics of Z-pinches can be modeled from the very beginning of the electric breakdown in a gas filling the interelectrode gap, but doing so is unrealistic in view of the complexity of the processes involved. That is why the pinch dynamics is usually modeled starting from a certain stage of the electric breakdown. Here, we propose to model the continuous evolution of an electric discharge in the interelectrode gap by distinguishing between two successive evolutionary stages, i.e., to develop a two-stage model of a Z-pinch. The pinch starts to form simultaneously with the beginning of gas ionization and current build-up in the interelectrode gap, in which case the magnetic field generation should be described with allowance for the finite plasma conductivity (or particle inertia) [12]. After this stage has come to an end, the magnetic field continues to increase and becomes strong enough to satisfy inequalities (1), which indicates the full development of the Z-pinch. Below, we will assume that the final equilibrium state of the pinch is independent of the initial longitudinal electric field and is governed exclusively by electron and ion motions in the azimuthal magnetic field, which is generated in the plasma as the

current builds up, and in the radial electric field, which, in turn, is determined by the particle motion.

At this point, it is expedient to draw an analogy between the development of a Z-pinch and ion acceleration in a gas irradiated by a short high-intensity laser pulse [13]. Sarkisov *et al.* [13] showed that, in a plasma produced by the interaction of a laser pulse with a gas, high-energy ion flows are generated as a result of ion acceleration by the ponderomotive force of an electromagnetic wave. However, in [10], a different mechanism for ion acceleration was proposed. As an electromagnetic wave propagates in a plasma, the Weibel instability gives rise to a quasistatic magnetic field [14], which results in the formation of electron vortices [15], so that the ions are accelerated by the Hall electric field of a nonquasineutral vortex. Consequently, the ions not only are accelerated directly by the electromagnetic wave but also acquire energy via a different mechanism associated with the evolution to a new equilibrium state in which the electric and magnetic fields differ radically from the initial fields. The analogy between a Z-pinch and a laser plasma can be extended further: in a laser plasma, the ions can be accelerated to megaelectronvolt energies [16]; the universal nature of the Hall potential in a strong magnetic field makes it inevitable that such ions would also appear in Z-pinches.

In both Z-pinches and vortex structures, the ion motion on spatial scales of about the magnetic Debye radius is unmagnetized. In vortex structures with the magnetic field B_z, which decreases away from the vortex axis, the ions fly apart in the radial direction because $E_r > 0$. In contrast, in Z-pinches with the magnetic field B_θ, vanishing at the pinch axis, the electric force can confine ions in the axial region because $E_r < 0$, which corresponds to an excessive negative charge at the axis.

Hence, we have drawn an analogy between the sequence of processes occurring in a laser-produced plasma and those in the Z-pinch under consideration. The successive processes in a plasma irradiated with a laser pulse are as follows: the ions are accelerated by the ponderomotive force of the pulse, the electron vortices with a quasistatic magnetic field are generated due to the Weibel instability, and the ions in the vortices expand in the radial direction under the action of the Hall electric field. Analogous processes that occur in a Z-pinch after applying the voltage pulse to the electrodes are as follows: the ions are accelerated by the longitudinal electric field, the magnetic field penetrates into the plasma (this processes should be described with allowance for the finite plasma conductivity), and the ions oscillate in the radial direction under the action of the charge-separation electric field.

In both cases, it is the initial electric field that gives rise to a strong quasistatic magnetic field, which, in turn, generates the Hall electric field in another direction. The charge-separation electric field produced during these processes is substantially stronger than the initial inductive electric field.

3. Based on the above analysis, we will systematically describe the proposed model of the evolution of a Z-pinch. In accordance with inequalities (1), we consider the pinch structure assuming that the maximum radius R of the pinch is much larger than the collisionless electron skin depth, $R \gg c/\omega_{pe}$, but is on the order of the collisionless ion skin depth, $R \sim c/\omega_{pi}$, where ω_{pi} is the ion Langmuir frequency. The pinch length L is assumed to be much larger than the characteristic pinch radius, $L \gg R$. Under this assumption, the equilibrium state of the pinch can be treated in the one-dimensional approximation and the dependence on z can be neglected. In other words, we ignore the effect of the electrodes on the pinch equilibrium. This indicates that the onset of the longitudinal electric field E_z can only be described with allowance for unsteady processes.

Since the electron inertia is neglected, the equation of electron motion

$$\frac{d\mathbf{p}_e}{dt} = -e\mathbf{E} - \frac{e}{c}[\mathbf{v}_e \times \mathbf{B}] \tag{4}$$

reduces to the drift equation

$$0 = \mathbf{E} + \frac{1}{c}[\mathbf{v}_e \times \mathbf{B}]. \tag{4'}$$

In this case, the simplest representation of the distribution function of the electrons in a magnetic field B_θ for $|\mathbf{E}| < |\mathbf{B}|$ is

$$f_e = n_{e0} r_0 \delta\left(v_{ez} - c\frac{E_r}{B_\theta}\right)\delta\left(v_{er} + c\frac{E_z}{B_\theta}\right)\delta(r\gamma v_{e\theta}), \tag{5}$$

where the electric field is $\mathbf{E} = -\nabla\Phi$. In the steady state under consideration, we assume that the longitudinal electric field E_z vanishes and consider only the radial electric field E_r. Note that the equation for electron motion along the magnetic field reduces to the conservation law for the azimuthal electron momentum. In writing the electron distribution function in form (5), we neglected the electron pressure in the Z-pinch.

Recall that, in the central nonquasineutral core, the ions oscillate in the radial direction and simultaneously move along the pinch axis. In this case, the ion distribution function can be chosen in the form

$$f_i = F_0 \delta\left(m_i v_{iz} + \frac{Ze}{c}A_z\right)\delta\left(\frac{m_i \mathbf{v}_i^2}{2} + Ze\Phi - \varepsilon_0\right)\delta(r v_{i\theta}), \tag{6}$$
$$F_0 = \text{const},$$

where $\delta(s)$ is the delta function and the distribution function itself depends on the integrals of motion $P_z = m_i v_{iz} + (Ze/c)A_z$, $\varepsilon = m_i \mathbf{v}^2/2 + Ze\Phi$, and $M_\theta = r m_i v_{i\theta}$.

In expression (6), the constant in the delta function for the ion momentum was chosen to satisfy the condition $v_{iz}(0) = 0$, provided that the gauge is $A_z(0) = 0$.

Distribution functions (5) and (6) should be supplemented with the Maxwell equations for the electromagnetic fields

$$\operatorname{curl}\mathbf{B} = \frac{4\pi e}{c}(Zn_i\mathbf{v}_i - n_e\mathbf{v}_e) + \frac{1}{c}\frac{\partial\mathbf{E}}{\partial t}, \quad (7)$$

$$-\frac{1}{c}\frac{\partial\mathbf{B}}{\partial t} = \operatorname{curl}\mathbf{E}. \quad (8)$$

We also use Poisson's equation

$$\operatorname{div}\mathbf{E} = 4\pi e(Zn_i - n_e) \quad (9)$$

because, in our approach, the charge separation plays an important role.

The charges and currents that enter Eqs. (7)–(9) can be determined by integrating distribution functions (5) and (6). The electron density obtained by integrating function (5) is equal to $n_e = n_{e0}r_0/(\gamma r)$. The corresponding expression for the ion density n_i also contains the factor $1/r$ and has a square root singularity at the radius at which the radial ion velocity vanishes [see formula (21) below]. The factor $1/r$ in the expression for the ion density reflects the fact that each oscillating ion with a zero azimuthal momentum passes through the pinch axis.

That the expression for the electron density contains the same factor is more difficult to explain, especially when there is no longitudinal electric field E_z and, accordingly, the electrons in a steady state experience no drift motion in the radial direction. Let us consider in more detail the electron motion along the magnetic field during buildup of the current. In cylindrical geometry, the projection of Eq. (4) onto the magnetic field direction has the form

$$\frac{\partial}{\partial t}(r\gamma v_{e\theta}) + v_{er}\frac{\partial}{\partial r}(r\gamma v_{e\theta}) = 0. \quad (10)$$

In the case at hand, it is convenient to rewrite the induction equation (8) as

$$E_z = -\frac{1}{c}\frac{\partial A_z}{\partial t}, \quad B_\theta = -\frac{\partial A_z}{\partial r}, \quad (11)$$

which enables us to express the radial electron drift velocity $v_r = -c(E_z/B_\theta)$ only in terms of the vector potential A_z. Substituting the drift velocity v_r found in such a way into Eq. (10), we obtain

$$\frac{\partial M}{\partial t}\frac{\partial A_z}{\partial r} - \frac{\partial A_z}{\partial t}\frac{\partial M}{\partial r} = 0, \quad (12)$$

where $M \equiv r\gamma v_{e\theta}$. Consequently, during buildup of the current, the time-dependent azimuthal electron momentum is expressed in terms of a certain function $M(A_z)$ that depends only on the vector potential. If we have $M(A_z) \equiv 0$ at the initial time, then this identity will hold throughout the pinch evolution, in particular, throughout the resulting equilibrium stage. The above analysis explains why formula (5) contains the factor $\delta(r\gamma v_{e\theta})$.

From inequalities (1), we have $v_{iz} \ll c$ and $v_{ez} \sim c$. Applying Eqs. (7) and (9) to an equilibrium Z-pinch, we can obtain the following time-independent ($\partial/\partial t \equiv 0$) equations for the electric (E_r) and magnetic (B_θ) fields such that $\partial/\partial z \equiv 0$:

$$\frac{1}{r}\frac{\partial}{\partial r}(rB_\theta) = -4\pi e n_e\frac{E_r}{B_\theta} - \frac{4\pi Z^2e^2n_i}{m_ic^2}A_z, \quad (13)$$

$$\frac{1}{r}\frac{\partial}{\partial r}(rE_r) = -4\pi e(n_e - Zn_i). \quad (14)$$

Note that below we will consider an equilibrium Z-pinch structure for small values of R, at which the neutron-producing acceleration mechanism comes into play [17].

4. Let us derive an expression for the spatial scale r_0 assuming that, in the nonquasineutral core of the Z-pinch, the electric current is carried by the electrons drifting in crossed electric and magnetic fields. Eliminating E_r in Eqs. (13) and (14) yields

$$\frac{1}{r}\frac{\partial}{\partial r}(rB_\theta) + \frac{4\pi Z^2e^2n_i}{m_ic^2}A_z = \frac{(4\pi e)^2n_e}{rB_\theta}\int_0^r (n_e - Zn_i)rdr. \quad (15)$$

If the characteristic radius r_0 of the nonquasineutral region satisfies the condition $r_0^2\omega_{pi}^2/c^2 \ll 1$, then we can neglect the second term on the left-hand side of Eq. (15) and introduce the current function $J(r) = crB_\theta/2$ to obtain

$$\frac{\partial}{\partial r}\gamma\frac{\partial J^2}{\partial r} = \frac{2}{\gamma}(2\pi e n_{e0}cr_0)^2\left(1 - \frac{Zn_i}{n_e}\right), \quad (16)$$

where Zn_i will be defined below in formula (21). Integrating Eq. (16) twice with respect to r, we find the relationship between the characteristic radius r_0 and the current J_0 flowing in the region of radius r_0:

$$r_0 \sim \sqrt{\frac{J_0}{en_{e0}c}} \ll c/\omega_{pi}, \quad (17)$$

in which case inequalities (1) allow us to neglect the ion current in the pinch core in comparison with the electron current.

We eliminate the electron density in Eqs. (13) and (14) and introduce the potential $\Phi^* \equiv \Phi + ZeA_z^2/(2m_ic^2)$. As a result, we arrive at the following equation, which describes the equilibrium state of the pinch and, in the presence of ions, is analogous to the equilibrium equation for a transmission line [18]:

$$r^2(B_\theta^2 - E_r^2) = 8\pi Ze\int_0^r n_ir^2\frac{\partial\Phi^*}{\partial r}dr. \quad (18)$$

Since $\partial\Phi^*/\partial r > 0$, this equation gives $|B_\theta| > |E_r|$ [see Eq. (5)].

Inserting the Hall estimate for Φ^* into the equilibrium equation (18), we can easily see that the characteristic radius r_0 of the central region coincides with radius (17).

If we multiply the conserved ion energy ε_0 by the ion distribution function f_i and integrate the resulting expression over velocities, we can obtain the following relationship between the temperature $T_i(r) = (1/n_i)\int d^3v f_i m_i v_{ir}^2/2$, associated with the radial ion oscillations, and the potential Φ^*:

$$T_i \equiv \varepsilon_0 - Ze\Phi^*. \tag{19}$$

This indicates that, in the absence of macroscopic ion motion along the radial coordinate r, the force associated with the radial ion pressure gradient is balanced by the electric and magnetic forces.

In this case, according to Eq. (18), the integral Bennett condition at the boundary of the nonquasineutral region in an electrically neutral Z-pinch such that $rE_r|_{r_0} = 0$ contains the ion (rather than electron) pressure (see [19]). Of course, this result stems from the fact that, in the basic equations, the electron inertia is neglected. Below, we will show that this conclusion is valid in view of the moderate values of the relativistic factor, $\gamma < 1.5$.

In order to gain a better insight into the resulting equilibrium state of the Z-pinch, we consider the ion motion in prescribed electromagnetic fields. We start with the equation of ion motion

$$m_i\frac{d\mathbf{v}_i}{dt} = Ze\mathbf{E} + \frac{Ze}{c}[\mathbf{v}_i\times\mathbf{B}]. \tag{20}$$

The ions move in the electric and magnetic fields, which are themselves affected by the charged particles and currents in the pinch. The equilibrium ion density can be obtained by integrating distribution function (6):

$$Zn_i = n_{e0}\frac{r_0}{r}\lambda\sqrt{\frac{\varepsilon_0}{\varepsilon_0 - Ze\Phi^*}}, \tag{21}$$

where λ is determined from the global charge neutrality condition.

For further analysis, it is important that the ion density increases with r; this corresponds to the negatively charged core of the pinch.

A distinguishing feature of the electron and ion distribution functions chosen above is that the electron and ion densities both diverge as $r \longrightarrow 0$. Clearly, the above formulas are valid everywhere except for the immediate vicinity of the pinch axis, $r \sim r_{Le} \ll r_0$. We emphasize that this feature is not a specific feature of the problem under discussion: a nonquasineutral core inevitably appears in Z-pinches with essentially arbitrary electron and ion distributions, in which case the ion energy ε_0 associated with a strong electric field should enter our formulas. The distribution functions were chosen in forms (5) and (6) in order to simplify the equations of particle motion (4) and (20) along the magnetic field and thus to obtain an explicit solution to the resulting general equations for the equilibrium state under study. An important point here is that we are confident of the noncontradictory formulation of the problem, because we removed from consideration the axial region with currents of about $J \sim J_{Ae}$.

In the problem as formulated (i.e., without consideration of the immediate vicinity of the pinch axis), the electric and magnetic fields can no longer vanish as $r \longrightarrow 0$. The relationship $B_\theta = 2J/cr$ implies that the azimuthal magnetic field can be nonzero, $B_\theta \neq 0$ as $J \longrightarrow 0$ and $r \longrightarrow 0$. Analogously, in the immediate vicinity of the pinch axis, the radial electric field can also be nonzero even when the charge Q per unit length is small: $E_r = 2Q/r$ as $Q \longrightarrow 0$ and $r \longrightarrow 0$. Such a situation can be attributed to the existence of an electron beam at the pinch axis. In Section 5, we will show that the magnetic field $2J_0/(cr_0)$ in the nonquasineutral core is on the order of the magnetic field $2J_{Ae}/(cr_{Le})$ on a spatial scale of about the electron Larmor radius. That this is the case can be readily verified by substituting estimate (17) for the characteristic radius r_0 into the expression for the magnetic field in the core. Although the magnetic fields are of the same order of magnitude, the currents on these spatial scales differ markedly ($J_0 \gg J_{Ae}$), because, by virtue of the inequality $B_\theta^2 \gg 4\pi n_e m_e c^2$, the spatial scale $r_{Le} = m_e c^2/(eB_\theta)$ is much shorter than the magnetic Debye radius r_B.

5. In order to convince ourselves that the above assumptions can lead to an exact noncontradictory formulation of the problem, we assume for the moment that the current flows only in the nonquasineutral core of the Z-pinch and that the remaining pinch region is free of currents. In other words, we neglect the current carried by the ions at the pinch periphery. Keeping in mind that, in the central region of radius $r \leq r_0$, the radial ion velocity v_{ir} is substantially higher than the longitudinal ion velocity v_{iz},

$$\frac{v_{ir}}{v_{iz}} \sim \sqrt{\frac{J_{Ai}}{J}} \gg 1, \tag{22}$$

we also assume that the ions in the nonquasineutral core are affected only by the electric force.

In the complete set of equations (13) and (14), we take into account only electron currents and pass over to the dimensionless quantities. As a result, we obtain the following equations describing the nonquasineutral core:

$$\frac{d}{d\rho}\rho\frac{d\varphi}{d\rho} = \frac{1}{\gamma} - \frac{\lambda}{\sqrt{1-\varphi}}, \quad \varphi = \frac{Ze\Phi}{\varepsilon_0}, \tag{23}$$

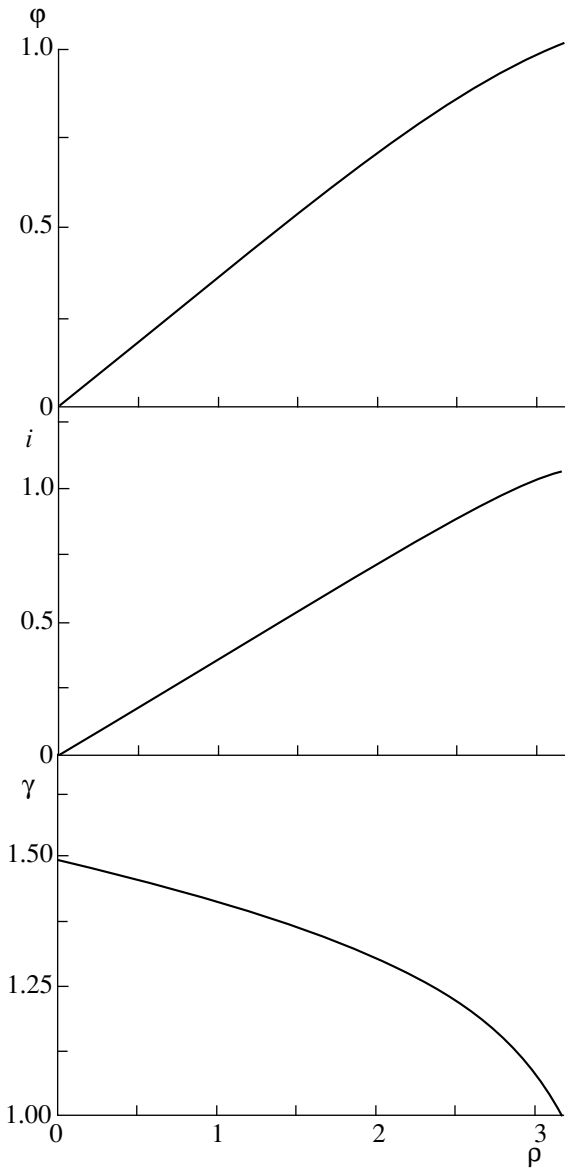

Fig. 1. Radial profiles of the dimensionless potential φ, dimensionless current function *i*, and electron relativistic factor γ in the nonquasineutral core of a Z-pinch.

$$\frac{di^2}{d\rho} = \frac{1}{\gamma}\rho\frac{d\varphi}{d\rho}, \quad i = \frac{\sqrt{2}ZeJ}{c\varepsilon_0}, \tag{24}$$

$$\gamma^2 = \frac{2}{1+\sqrt{1-8(di/d\rho)^2}}, \quad r_0^2 = \frac{\varepsilon_0}{4\pi Ze^2 n_{e0}}, \tag{25}$$
$$r = r_0\rho.$$

Equation (24) implies that, if the current flows along the pinch axis, then the radial electric field E_r and the azimuthal magnetic field B_θ are both nonzero. In the approach based on this set of equations, the boundary conditions for Eq. (23) are as follows:

$$\varphi(0) = 0, \quad \varphi'(0) = \lambda^{1/3} - \lambda, \tag{26}$$
$$\varphi(\rho_0) = 1, \quad \varphi'(\rho_0) = 0.$$

The "extra" boundary conditions make it possible to determine the parameters $\lambda < 1$ and ρ_0. An important point here is that the boundary conditions contain the constant λ, which is the only parameter that accounts for the currents and charges at the pinch axis.

Equations (23)–(25) were derived under the assumption that the radial velocity of the ions vanishes at the boundary of the nonquasineutral region. In other words, in the total potential Φ*, we neglect the magnetic part, which is as small as $J/J_{Ai} \ll 1$. The related numerical results are illustrated in Fig. 1, the parameter values calculated from the extra boundary conditions being $\lambda = 0.3$ and $\rho_0 = 3.179$. Our calculations yield $\gamma < 1.5$, so that we are justified in neglecting electron inertia. From Fig. 1, one can also see that the electric potential is a nearly linear function. This reflects the fact that the electric field is constant in the region between the two "capacitor plates" arising during pinch evolution, at both of which the charge density has singularities (Fig. 2).

The calculated final equilibrium state is sensitive to the shape of the ion distribution function: taking into account ions with different energies can reduce the fraction of the highest energy ions.

With allowance for the ion current, the equilibrium state turns out to be more complicated in structure than expected from Eqs. (23)–(25). The energy of the ions oscillating in the radial direction is conserved:

$$\left(\frac{dr}{dt}\right)^2 = v_{i0}^2 - \frac{2Ze\Phi}{m_i} - \left(\frac{ZeA_z}{m_i c}\right)^2, \tag{27}$$

where v_{i0} is the radial ion velocity at the axis.

If we turn to the condition $J_0 \ll J_{Ai}$ in order to neglect the magnetic force in the central region, then, with allowance for the relationship $r_0^2/t_0^2 = v_{i0}^2 = 2\varepsilon_0/m_i$, we can obtain from Eqs. (25) and (27) the equation for radial ion oscillations on the characteristic time scale $t_0 = 1/(\omega_{pi}\sqrt{2})$, where $\omega_{pi}^2 = 4\pi Ze^2 n_{e0}/m_i$. This oscillatory ion motion is consistent with Eqs. (23)–(25), which result in a singularity in the ion density at the boundary of the nonquasineutral region. However, if we take into account the effect of the magnetic force on the ions, we can see that, as the radial velocity of the ions decreases, they turn backward and their energy decreases from ε_0 at the pinch axis to the value $\varepsilon_0 J_0/J_{Ai} \ll \varepsilon_0$ at the boundary of the nonquasineutral region, outside of which the magnetic field turns the ions backward on a spatial scale of about c/ω_{pi}. In this case, the ion density has a square root singularity at the pinch periphery rather than at the surface with a radius of about $\sim r_0$.

Outside of the nonquasineutral core of the Z-pinch, the radial profile of the current is described by Eq. (13) in which the electron current should be neglected:

$$\frac{1}{r}\frac{\partial}{\partial r}r\frac{\partial A_z}{\partial r} = \frac{4\pi Ze^2 n_{e0}}{m_i c^2}\lambda\frac{r_0}{r}\sqrt{\frac{\varepsilon_0}{\varepsilon_0 - Ze\Phi^*}}A_z. \qquad (28)$$

Note that, in this equation, we can take the total potential Φ^* to be independent of the variations of the electrostatic potential Φ at the pinch periphery.

We integrate Eq. (28) multiplied by $r^2\partial A_z/\partial r$ over r and ignore small terms on the order of $\sim\sqrt{J/J_{Ai}} \ll 1$ to obtain the relationship between the currents J and J_0:

$$J^2 - J_0^2 = 4\pi\lambda\frac{n_{e0}r_0}{Z}c^2\sqrt{\varepsilon_0}\int_{r_1}^{r_2} dr\sqrt{\varepsilon_0 - Ze\Phi^*}. \qquad (29)$$

Here, r_1 is the radius of the surface at which the strong electric field of the nonquasineutral core vanishes and r_2 is the radius of the surface at which the magnetic field of the Z-pinch turns the ions backward.

The radius $r_1 \sim r_0$ is determined by the current J_0, and the radius $r_2 \sim R$ can be found from Eq. (28) only in terms of J_0 and J, because, in the region $r_1 < r < r_2$, the potential is constant. Recall that, in the region $r > r_1$, the expression under the square root on the right-hand side of Eq. (29) contains terms on the order of $(ZeA_z)^2/(m_ic^2) \sim \varepsilon_0 J_0/J_{Ai} \ll \varepsilon_0$, because the potential Φ decelerates the ions in the nonquasineutral core of the Z-pinch. Consequently, using the approximate equality $J_0/J_{Ai} \sim r_0^2/R^2$, we can estimate the right-hand side of Eq. (29) as $4\pi\lambda(n_{e0}/Z)r_0^2c^2\varepsilon_0 \sim J_0^2$. Hence, Eq. (29) relates the current J_0 to the total current J in the Z-pinch; moreover, the estimates yield $J_0 \sim J$.

From the definition of r_0, we can estimate the maximum ion energy at the axis as $\varepsilon_0 \sim ZeJ_0/c$. For the current $J_0 \sim 1$ MA, we obtain an energy of about 30 MeV. In [17], the maximum transverse ion energy measured at a current $J \sim 0.7$ MA was found to be about 7 MeV. A comparison of our result with this experimental finding shows that the current only partially flows in the central nonquasineutral region of the Z-pinch.

Since $J_0 < J$, part of the total current should be carried by the ions and, possibly, electrons (the ohmic current) in the peripheral region of the Z-pinch; moreover, at the periphery, the ion current dominates over the electron current under the condition $4\pi\sigma < \tau\omega_{pi}^2$, where σ is the electric conductivity and τ is the characteristic current rise time. This indicates that, for $n_e \sim 10^{20}$ cm^{-3} and $\tau \sim 10^{-8}$ s, the electron (ohmic) current at the pinch periphery becomes significant only when the electron temperature is about $T_e \sim 10^3$ eV or higher. Physically, the above condition means that, if the electron conductivity is sufficiently high, then the magnetic field of the peripheral current-carrying layer does not penetrate into the plasma from the periphery to the radius about c/ω_{pi} during the characteristic rise time of the pulse ($\tau < \tau_{skin} \equiv 4\pi\sigma/\omega_{pi}^2$), so that the Z-pinch cannot evolve into the equilibrium state described above. Hence, we can conclude that the equilibrium state under discussion can only be achieved when the plasma density in the Z-pinch is sufficiently high.

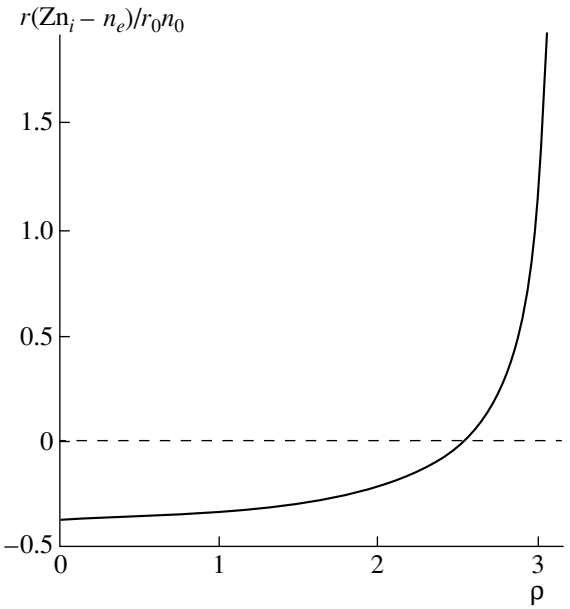

Fig. 2. Normalized electric charge density in the nonquasineutral core of a Z-pinch vs. $\rho = r/r_0$.

6. In this paper, we have analyzed the equilibrium states of Z-pinches with currents in range (1). The distinguishing feature of the overall equilibrium pattern of the pinch currents is that it is characterized by two spatial scales. The internal spatial scale $r_0 \sim \sqrt{J_0/en_ec}$ is governed by the current J_0 of the electrons that drift with a velocity approximately equal to the speed of light. In addition to the current J_0, which is carried by the electrons in the nonquasineutral core, there is the current $J - J_0$, which is carried by the ions moving with the characteristic velocity $v_{iz} \sim c(ZeJ/m_ic^3)$ in the peripheral region with the characteristic radius $R \sim c/\omega_{pi}$. In the nonquasineutral core, the magnetic field is not frozen in the ions. As a result, the core is stable against sausage modes [20]. The ions oscillating in the radial direction (the total oscillatory ion energy being $\varepsilon_0 \sim ZeJ_0/c$) are confined in the Z-pinch precisely by the electric field of the nonquasineutral core. The central region of the Z-pinch acts as a kind of "capacitor" that stores the energy of the ion oscillations and electromagnetic energy. The pinch structure analyzed here has much in common with the vacuum electrodynamic structures discussed in the review by Trubnikov [21].

However, those structures are essentially unsteady, with the electric field directed along the *z*-axis. In contrast to [21], we assume that there are no vacuum regions in the pinch. That is why our results are intermediate between the results described by Trubnikov [21] and those obtained by Vikhrev [22] on the basis of a quasineutral approach.

In conclusion, let us make two remarks. The maximum radius of the equilibrium configuration under discussion is $R \sim c/\omega_{pi}$. According to [23], when $R \ll c/\omega_{pi}$, the instability should be described by a two-fluid approach and the stability criterion may differ significantly from that derived using a one-fluid approach [20], which assumes that $R \gg c/\omega_{pi}$. In the intermediate case $R \sim c/\omega_{pi}$, the question of stability remains open and requires further investigation. However, even if the sausage modes are unstable in the peripheral region, they can never grow in the central region with a radius of about r_0, so that we may speak of the stabilizing role of the nonquasineutral core.

We again wish to stress that Coulomb collisions have a major impact on the evolution of the resulting equilibrium state. For the current $J_0 \sim 1$ MA, the ion energy is $\varepsilon_0 \sim 30$ MeV, in which case the ions should heat the electrons. According to [11], the ion–electron energy transfer time characteristic of Z-pinches with the electron density $n_{e0} \sim 10^{20}$ cm^{-3} is about 10^{-7} s.

Finally, estimates show that the ratio of the charge-separation electric field E_0 to the atomic field is $E_0/E_a \sim 137^2(a_0\omega_{pe}/c)\sqrt{J/J_{Ae}}$, where a_0 is the Bohr radius. It follows from here that, for $J \sim 1$ MA and $n_e \sim 10^{20}$ cm^{-3}, the electric field in the nonquasineutral core of a Z-pinch is comparable in magnitude to the atomic field.

ACKNOWLEDGMENTS

I am grateful to V.D. Korolev and Yu.G. Kalinin for discussing present-day experimental results on Z-pinches, to T.V. Losseva for performing computations, and to V.D. Shafranov for reading the manuscript and making valuable remarks. This study was supported in part by the Russian Foundation for Basic Research (project nos. 97-02-16980 and 00-02-16305) and INTAS (grant no. 97-0021).

REFERENCES

1. *Proceedings of the Fourth International Conference on Dense Z-pinches, Vancouver, 1997*, Ed. by N. R. Pereira, Jack Davis, and P. E. Pulsifer (American Institute of Physics, Woodbury, 1997).
2. V. S. Imshennik and N. A. Bobrova, *Dynamics of Collisional Plasmas* (Énergoatomizdat, Moscow, 1997).
3. V. V. Yan'kov, Fiz. Plazmy **17**, 521 (1991) [Sov. J. Plasma Phys. **17**, 305 (1991)].
4. G. Benford and D. L. Book, *Advances in Plasma Physics*, Ed. by A. Simon and W. Thompson (Wiley, New York, 1969,1971; Mir, Moscow, 1974), Vols. 3, 4.
5. H. Alfvén, Phys. Rev. **45**, 425 (1939).
6. D. Hammer and N. Rostoker, Phys. Fluids **13**, 1831 (1970).
7. A. V. Gordeev and A. V. Grechikha, Pis'ma Zh. Éksp. Teor. Fiz. **61**, 193 (1995) [JETP Lett. **61**, 196 (1995)].
8. A. V. Gordeev and S. V. Levchenko, Fiz. Plazmy **25**, 217 (1999) [Plasma Phys. Rep. **25**, 193 (1999)].
9. A. V. Gordeev and S. V. Levchenko, Pis'ma Zh. Éksp. Teor. Fiz. **67** (7), 461 (1998) [JETP Lett. **67**, 482 (1998)].
10. A. V. Gordeev and T. V. Losseva, Pis'ma Zh. Éksp. Teor. Fiz. **70** (10), 669 (1999) [JETP Lett. **70**, 684 (1999)].
11. B. A. Trubnikov, in *Reviews of Plasma Physics*, Ed. by M. A. Leontovich (Gosatomizdat, Moscow, 1963; Consultants Bureau, New York, 1963), Vol. 1.
12. L. I. Rudakov, M. V. Babykin, A. V. Gordeev, *et al.*, *Generation and Focusing of High-Current Relativist Beams*, Ed. by L. I. Rudakov (Énergoatomizdat, Moscow, 1990).
13. G. S. Sarkisov, V. Yu. Bychenkov, V. T. Tikhonchuk, *et al.*, Pis'ma Zh. Éksp. Teor. Fiz. **66**, 787 (1997) [JETP Lett. **66**, 828 (1997)].
14. E. S. Weibel, Phys. Rev. Lett. **2**, 83 (1959).
15. G. A. Askar'yan, S. V. Bulanov, F. Pegoraro, and A. M. Pukhov, Pis'ma Zh. Éksp. Teor. Fiz. **60**, 240 (1994) [JETP Lett. **60**, 251 (1994)].
16. K. Krushelnick, E. L. Clarck, Z. Najmudin, *et al.*, Phys. Rev. Lett. **83**, 737 (1999).
17. F. C. Young, S. J. Stephanakis, and D. Mosher, J. Appl. Phys. **48**, 3642 (1977).
18. A. V. Gordeev, Preprint No. 3076 (Kurchatov Institute of Atomic Energy, Moscow, 1978) [Preprint No. PIIR-12-79 (Phys. Int. Comp., San Leandro, CA, 1979)].
19. Yu. L. Bakshaev, V. V. Vikhrev, E. M. Gordeev, *et al.*, in *Proceedings of the XXVI Zvenigorod Conference on Plasma Physics and Controlled Nuclear Fusion, Zvenigorod, 1999*, p. 163.
20. B. A. Trubnikov, in *Plasma Physics and Problems of Controlled Nuclear Fusion*, Ed. by M. A. Leontovich (Akad. Nauk SSSR, Moscow, 1958), Vol. 1, p. 289.
21. B. A. Trubnikov, Fiz. Plazmy **12**, 468 (1986) [Sov. J. Plasma Phys. **12**, 271 (1986)].
22. V. V. Vikhrev, Fiz. Plazmy **12**, 454 (1986) [Sov. J. Plasma Phys. **12**, 262 (1986)].
23. A. V. Gordeev, A. S. Kingsep, and L. I. Rudakov, Phys. Rep. **243**, 215 (1994).

Translated by O.E. Khadin

Plasma Physics Reports, Vol. 27, No. 3, 2001, pp. 243–250. Translated from Fizika Plazmy, Vol. 27, No. 3, 2001, pp. 260–267.

PLASMA OSCILLATIONS AND WAVES

Effect of the Radial Plasma Profile on the Surface Wave Structure in a Plasma Waveguide

M. V. Kuzelev, R. V. Romanov, and A. A. Rukhadze

Institute of General Physics, Russian Academy of Sciences, ul. Vavilova 38, Moscow, 117942 Russia

Received April 20, 2000

Abstract—A study is made of the effect of the radial plasma profile on the spectra and fields of the surface waves in a plasma waveguide. It is shown that the surface wave is localized in the region where the plasma permittivity vanishes. In waveguides with smoother radial plasma profiles, the region where the surface wave can exist is narrower and may even disappear. © *2001 MAIK "Nauka/Interperiodica".*

Waves that are localized near the boundary of a medium and whose field decreases abruptly (exponentially) at least in one direction away from the boundary are usually called surface waves. There are many types of surface waves in a plasma. The simplest surface waves are excited in a homogeneous unmagnetized plasma cylinder with a sharp boundary $r = r_p < R$, where r_p is the radius of the plasma cylinder and R is the radius of the metal wall (the waveguide radius), which may in principle be infinite; for $r < r_p$, the Langmuir frequency ω_p is assumed to be constant. The main properties of surface waves in such a system are as follows [1, 2].

(i) As the longitudinal (along the plasma cylinder) wavenumber k_z increases from zero to infinity, the wave frequency ω increases monotonically from zero to $\omega_p/\sqrt{2}$.

(ii) At the sharp boundary of the plasma cylinder, the wave electric field E_z is maximum and has a discontinuous radial derivative; on both sides of the plasma surface r_p, the wave electric field decreases abruptly.

It is of interest to investigate the properties of a surface wave in a plasma cylinder with a smeared-out boundary and, in general, the effect of the radial plasma profile on the wave structure. This problem takes on special importance because surface waves are being actively studied experimentally in real devices operating with plasmas with smeared-out boundaries.[1] In our investigations, we consider as an example an unmagnetized plasma column in a metal waveguide.

In the absence of an external magnetic field, the plasma is isotropic, so that the waveguide eigenmode splits into an E-wave (a wave with $B_z = 0$) and a B-wave (a wave with $E_z = 0$). Here, we are interested only in E-waves and, for simplicity, restrict ourselves to considering axisymmetric waveguides. The field components of the E-waves satisfy the Maxwell equations

$$k_z B_\varphi = \frac{\omega}{c}\varepsilon E_r, \quad ik_z E_r - \frac{dE_z}{dr} = i\frac{\omega}{c}B_\varphi, \qquad \frac{1}{r}\frac{d}{dr}(rB_\varphi) = -i\frac{\omega}{c}\varepsilon E_z. \tag{1}$$

Here, (r, φ, z) are cylindrical coordinates; E_z, E_r, and B_φ are the only nonzero components of the electromagnetic field; and

$$\varepsilon = 1 - \frac{\omega_p^2(r)}{\omega^2} \tag{2}$$

is the plasma permittivity. Since the Langmuir frequency ω_p depends generally on the radius, the plasma permittivity is also a function of the radial coordinate, $\omega_p = \omega_p(r)$, $\varepsilon = \varepsilon(r)$.

For a homogeneous plasma cylinder with a sharp boundary, we have ω_p = const in the plasma region ($r < r_p$) and $\omega_p = 0$ in the vacuum region ($r_p < r < R$). In this case, Eqs. (1) are solved separately for $r < r_p$ and $r_p < r < R$ and the solutions are matched at the plasma boundary $r = r_p$ with allowance for the continuity of the tangential field components E_z and B_φ. Taking into account the fact that the component E_z vanishes at $r = R$ and all of the field components are finite at $r = 0$, we arrive at a dispersion relation that accounts for the above properties of the simplest surface waves. However, this approach is inapplicable for describing an inhomogeneous plasma cylinder.

We eliminate the components E_r and B_φ in Eqs. (1) to obtain one equation for E_z:

$$\frac{d^2E_z}{dr^2} + \left(\frac{\kappa^2}{\varepsilon}\frac{d(\varepsilon/\kappa^2)}{dr} + \frac{1}{r}\right)\frac{dE_z}{dr} - \kappa^2 E_z = 0, \tag{3}$$

where $\kappa^2 = k_z^2 - \varepsilon\omega^2/c^2$ and ε is a function of r. Equation (3), which is valid over the entire plasma region

[1] Applications of surface waves in plasma microwave electronics are described, e.g., in [3].

1063-780X/01/2703-0243$21.00 © 2001 MAIK "Nauka/Interperiodica"

$0 < r < R$, is supplemented with the boundary conditions

$$\frac{dE_z}{dr}(r = 0) = 0, \quad E_z(r = R) = 0, \tag{4}$$

the first of which is equivalent to the condition for the component B_φ to vanish at the waveguide axis.

Since, for arbitrary ω and k_z, the solution to Eq. (3) cannot simultaneously satisfy both of the boundary conditions (4), we propose the following method for solving the eigenvalue problem described by Eq. (3) with boundary conditions (4). First, we fix a certain value of k_z. Then, for $r > 0$, we solve the Cauchy problem for Eq. (3) supplemented with the boundary conditions

$$\frac{dE_z}{dr}(r = 0) = 0, \quad E_z(r = 0) = \text{const}. \tag{5}$$

Since Eq. (3) is a linear homogeneous equation and the boundary conditions (4) are uniform, the value of the constant in conditions (5) is unimportant. When solving the Cauchy problem, the frequency ω is adjusted to satisfy the second boundary condition in (4). The frequency adjusted in such a manner is the desired eigenfrequency $\omega(k_z)$, and the corresponding solution to Eq. (3) is the desired eigenfunction.

Note that Eq. (3) has a singularity at a surface of radius r at which $\omega = \omega_p(r)$. The existence of surface waves stems precisely from this singularity: in the case at hand, the surface wave manifests itself as oscillations of resonant electrons in a plasma layer around the surface of radius r. We emphasize that this is not the resonance of an individual electron with the wave (or wave–particle resonance). In fact, the wave–particle resonance is described by the poles of the plasma permittivity. However, the plasma permittivity (2) contains no poles except for the trivial one at $\omega = 0$. Consequently, we will not speak of wave damping by resonant electrons. The relationship $\omega = \omega_p(r)$ refers to the collective resonance described by the zero of the plasma permittivity (2). At the surface of radius r at which the collective resonance condition is satisfied, the component E_z is continuous but has a discontinuous radial derivative, the component B_φ is continuous and has a continuous radial derivative, and the component E_r is discontinuous.

In the vicinity of the surface of radius r at which the plasma permittivity (2) vanishes, the qualitative behavior of the field components is fairly easy to investigate. Near this surface (which, however, should not coincide with the waveguide axis), we can retain only the leading-order terms in Eq. (3):

$$\frac{1}{U}\frac{dU}{dr} = -\frac{1}{\varepsilon}\frac{d\varepsilon}{dr}, \quad U = \frac{dE_z}{dr}, \tag{6}$$

Integrating this equation yields

$$\frac{dE_z}{dr} = \frac{C}{\varepsilon(r)} \approx C\frac{\omega_p(r)}{[\omega - \omega_p(r)]},$$

$$E_r = -i\frac{k_z}{\kappa^2}\frac{dE_z}{dr} \approx -iC\frac{k_z^{-1}\omega_p(r)}{[\omega - \omega_p(r)]}, \tag{7}$$

$$B_\varphi = -i\varepsilon\frac{\omega}{c\kappa^2}\frac{dE_z}{dr} \approx -iC\frac{k_z^{-1}\omega_p(r)}{k_z c},$$

where C is an arbitrary constant. The last two relationships in (7) were derived using Eqs. (1). Note that Eqs. (7) do not apply to a plasma with a sharp boundary and with discontinuities in $\omega_p(r)$.

Let r^* be the radius of the surface at which the collective resonance condition $\omega = \omega_p(r)$ holds. Then, near the resonance surface of radius r^* (which is, of course, frequency-dependent), the first equation in (7) gives

$$E_z(r \approx r^*) \approx -C\frac{\omega_p^2(r^*)}{\omega_p'(r^*)}\ln|r - r^*| + N, \tag{8}$$

where N is a constant, which cannot be found exclusively from Eqs. (7). We can see that, near the resonance surface, the component E_z, although continuous, diverges logarithmically. However, this divergence can be avoided by introducing dissipation (the finite collision frequency or finite temperature), in which case the components E_r and B_φ, as well as the field energy, also become finite. Solving the exact equation (3) numerically yields a nondivergent component E_z, which, however, increases substantially when approaching the resonance surface r^*.

Now, we consider the results of numerically solving Eq. (3) with boundary conditions (4). In this series of simulations, we fixed the waveguide radius, $R = 2$ cm, and varied the plasma profile. The results illustrated in Fig. 1 refer to the well-known case of an almost homogeneous plasma cylinder with a sharp boundary and are presented merely for completeness. Figure 1a shows the radial profile of the Langmuir frequency $\omega_p(r)$. The sharp plasma boundary is at $r = r_p = 1$ cm. Inside the plasma ($r < r_p$), the Langmuir frequency is constant and is equal to $\omega_{p\max} = 5 \times 10^{10}$ rad/s. The region $r > r_p$ is free of plasma.[2] Figure 1b displays the dispersion curves $\omega(k_z)$ calculated by solving Eq. (3) with boundary conditions (4) for the profiles $\omega_p(r)$ in Fig. 1a. For completeness, we also plotted the dispersion curves of high-frequency spatial electromagnetic waves, which lie above the solid line $\omega = k_z c$. The dispersion curve of the low-frequency surface wave, in which we are interested here, is below the line $\omega = k_z c$. This dispersion

[2] In fact, our calculations were performed for a plasma cylinder whose boundary was smeared over a narrow (0.1-cm-thick) radial interval.

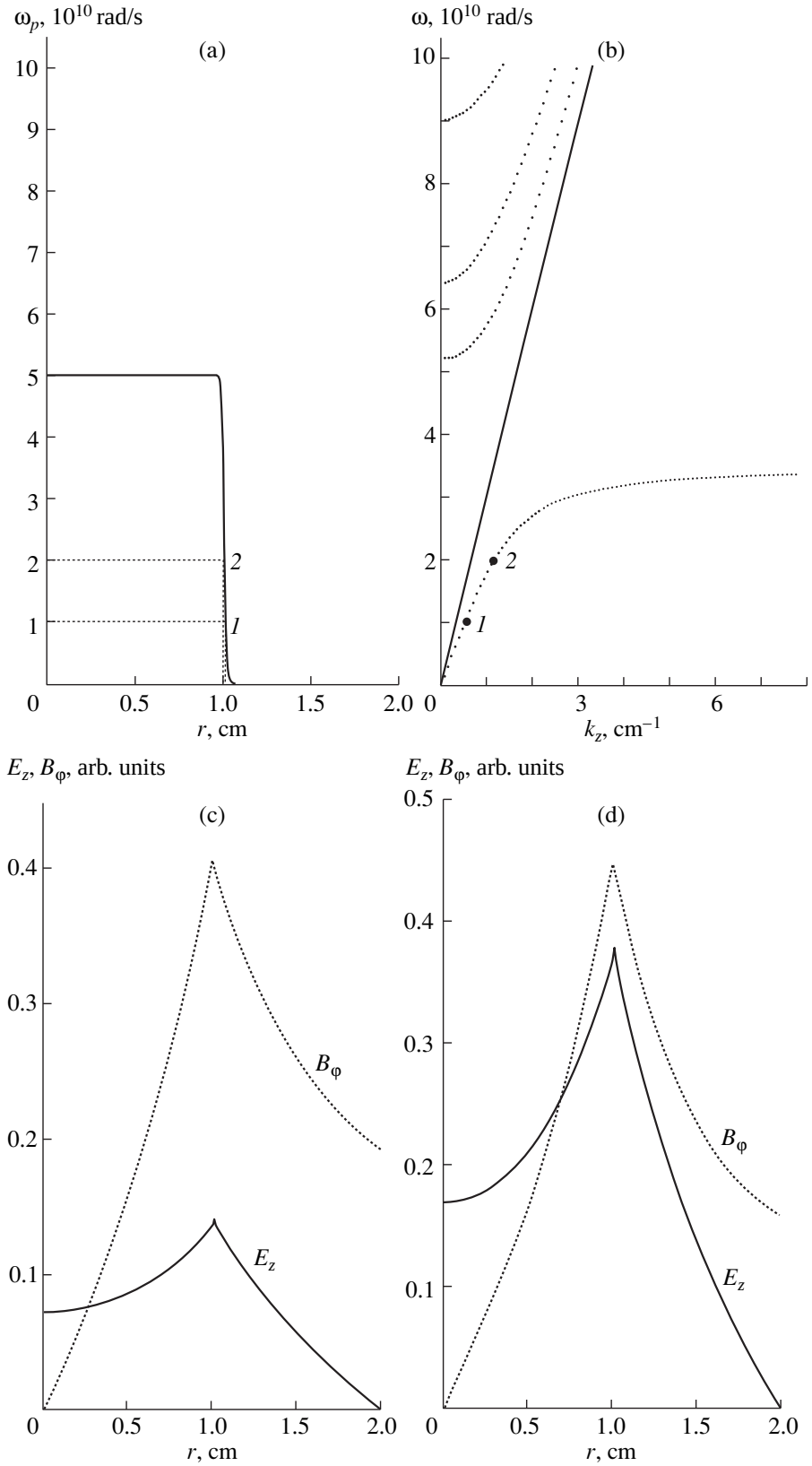

Fig. 1. Plasma with a sharp boundary: (a) radial profile of the Langmuir frequency; (b) dispersion curves; and (c, d) field structures of the surface wave calculated, respectively, for points *1* and *2* on the dispersion curve in plot (b).

curve, which originates at the point ($k_z = 0$, $\omega = 0$) and approaches the level $\omega = \omega_{p\max}/\sqrt{2} = 3.46 \times 10^{10}$ rad/s as $k_z \longrightarrow \infty$, can, of course, be obtained not only by solving Eq. (3) with boundary conditions (4) but also by applying the traditional method used with dispersion relations, i.e., by matching the solutions to the field equation at $r = r_p$ [1, 2]. Note that, according to the corresponding dispersion relation, the phase velocity of the surface wave is maximum in the long-wavelength range ($k_z \longrightarrow 0$), the maximum being equal to

$$\left.\frac{\omega}{k_z}\right|_{\max} = c\sqrt{\frac{\theta}{1+\theta}}, \quad \theta = \lambda \ln\frac{R}{r_p}\frac{I_1(\lambda)}{I_0(\lambda)}, \tag{9}$$

where $I_{0,1}$ are the modified Bessel functions and $\lambda = \omega_{p\max} r_p/c$ is the ratio of the radius of the plasma cylinder to the penetration depth of the electromagnetic field into the plasma.

Figures 1c and 1d illustrate the field structures of the surface wave (the radial profiles of the components $E_z(r)$ and $B_\varphi(r)$ in arbitrary units) that were calculated, respectively, for points *1* ($\omega = 10^{10}$ rad/s) and *2* ($\omega = 2 \times 10^{10}$ rad/s) on the low-frequency dispersion curve in Fig. 1b. The structures are seen to be typical of surface waves. At the sharp boundary $r = r_p$ of the plasma cylinder, the radial derivative of the component E_z is discontinuous and the component B_φ is maximum, so that the surface wave may be said to be localized near the plasma boundary. Note that the higher the frequency ω (and, accordingly, the larger the wavenumber k_z), the narrower the localization region of the surface wave near the boundary $r = r_p$. In the range of large wavenumbers k_z, the field decreases away from the sharp boundary according to the law

$$E_z \approx \exp(-k_z|r - r_p|). \tag{10}$$

Let us refine the notion of the localization region or localization boundary of the surface wave. We define the localization boundary as the surface $r^* = r^*(\omega)$ at which the plasma permittivity (2) vanishes. In Fig. 1a, points *1* and *2* mark the localization regions of the surface waves corresponding to points *1* and *2* on the dispersion curve in Fig. 1b. Since, for a plasma with a sharp boundary, the radius r^* is frequency-independent, the localization region seems to be defined somewhat incorrectly. However, below we will show that, for a plasma with a smeared boundary, this definition is physically meaningful. On the other hand, the situation with a plasma with a sharp boundary is not so simple as it appears at first glance. Thus, not all of the points on the profile $\omega_p(r)$ correspond to the surface at which the surface wave can be localized, although, for any frequency ω from zero to $\omega_{p\max}$, there exists a surface of radius r at which the plasma permittivity (2) vanishes. In fact, in the frequency range $\omega_{p\max}/\sqrt{2} < \omega < \omega_{p\max}$, surface waves never exist, although the resonance condition $\varepsilon = 0$ can definitely hold in this range.

Now, we consider a plasma column with a smeared boundary. The related results are illustrated in Fig. 2. Figure 2a shows the radial profile of the Langmuir frequency $\omega_p(r)$, which is maximum at the waveguide axis, the maximum again being equal to $\omega_{p\max} = 5 \times 10^{10}$ rad/s. Figure 2b presents the dispersion curves obtained for this Langmuir frequency profile by numerically solving Eq. (3) with boundary conditions (4).We can see that the dispersion curve for the surface wave is qualitatively the same but the maximum (at $k_z \longrightarrow 0$) phase velocity is almost one order of magnitude lower than that for a plasma column with a sharp boundary [see formulas (9) and Fig. 1b]. The limiting (at $k_z \longrightarrow 0$) frequency is also almost one order of magnitude lower than $\omega_{p\max}/\sqrt{2}$.

Figures 2c and 2d illustrate the field structures of the surface wave that were calculated, respectively, for points *1* ($\omega = 10^{10}$ rad/s) and *2* ($\omega = 2 \times 10^{10}$ rad/s) on the dispersion curve in Fig. 2b. The radial profile of the component E_z is seen to coincide qualitatively with that in the case of a plasma column with a sharp boundary (see Figs. 1c, 1d), while the component B_φ is a considerably smoother function of the radius.

In the case of a plasma column with a smeared boundary, the notion of the localization region of the surface wave acquires a physical meaning. From Figs. 2a and 2d, we can see that the component E_z is maximum and its radial derivative is discontinuous at the surface of radius r at which $\omega = \omega_p(r)$ holds. In Fig. 2a, the corresponding localization boundary of the surface wave is marked by point *2*. Point *1* in Fig. 2a corresponds to an analogous localization boundary. Hence, the localization boundary of the surface wave is the resonance surface $r = r^*$ at which the plasma permittivity (2) vanishes. In our problem, the eigenfrequency $\omega(k_z)$ is a monotonically increasing function. Therefore, as the wavenumber k_z increases from zero to infinity, the localization boundary of the surface wave is displaced from its initial position very near the waveguide wall toward the surface corresponding to point *3* in Fig. 2a.

Figure 3 refers to a situation that differs qualitatively from what we have analyzed above. Figure 3a shows the radial profile of the function $\omega_p(r)$ that is nonzero at $r = R$, which indicates that the plasma is in contact with the waveguide wall. Let $\omega_{p\min} = \omega_p(R) < 0.1\omega_p(0)$ be the minimum Langmuir frequency of the plasma in the waveguide. In the frequency range $\omega < \omega_{p\min}$, no surface waves can exist because the resonance condition $\varepsilon = 0$ always fails to hold. Figure 3b displays the dispersion curves corresponding to the profile of ω_p in Fig. 3a. We can see that the dispersion curve of the surface wave no longer extends into the region of small k_z and ω values but goes over to a new branch of the

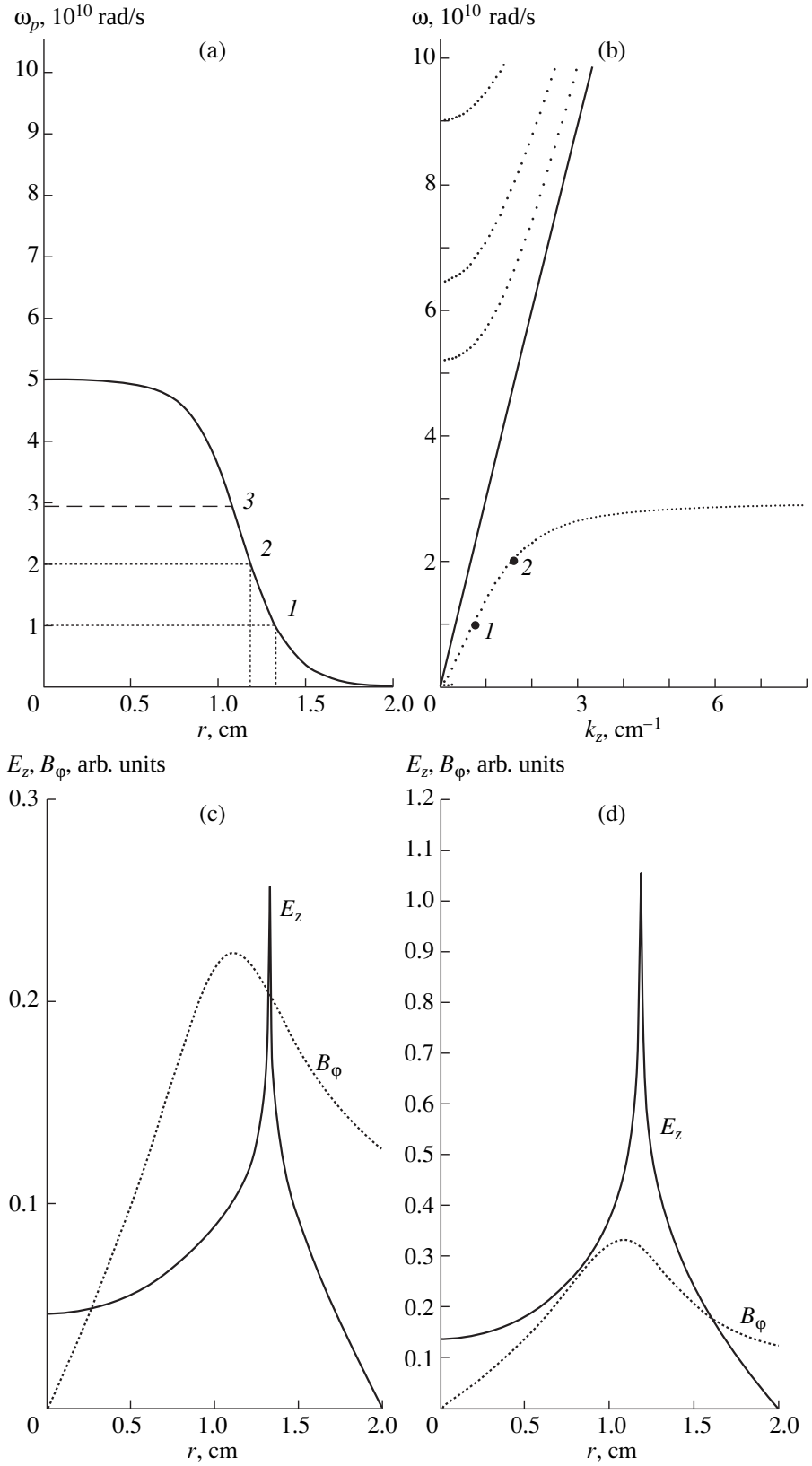

Fig. 2. Plasma with a smeared boundary in the case when the Langmuir frequency ω_p vanishes at the waveguide wall, $\omega_p(R) = 0$: (a) radial profile of the Langmuir frequency; (b) dispersion curves; and (c, d) field structures of the surface wave calculated, respectively, for points *1* and *2* on the dispersion curve in plot (b).

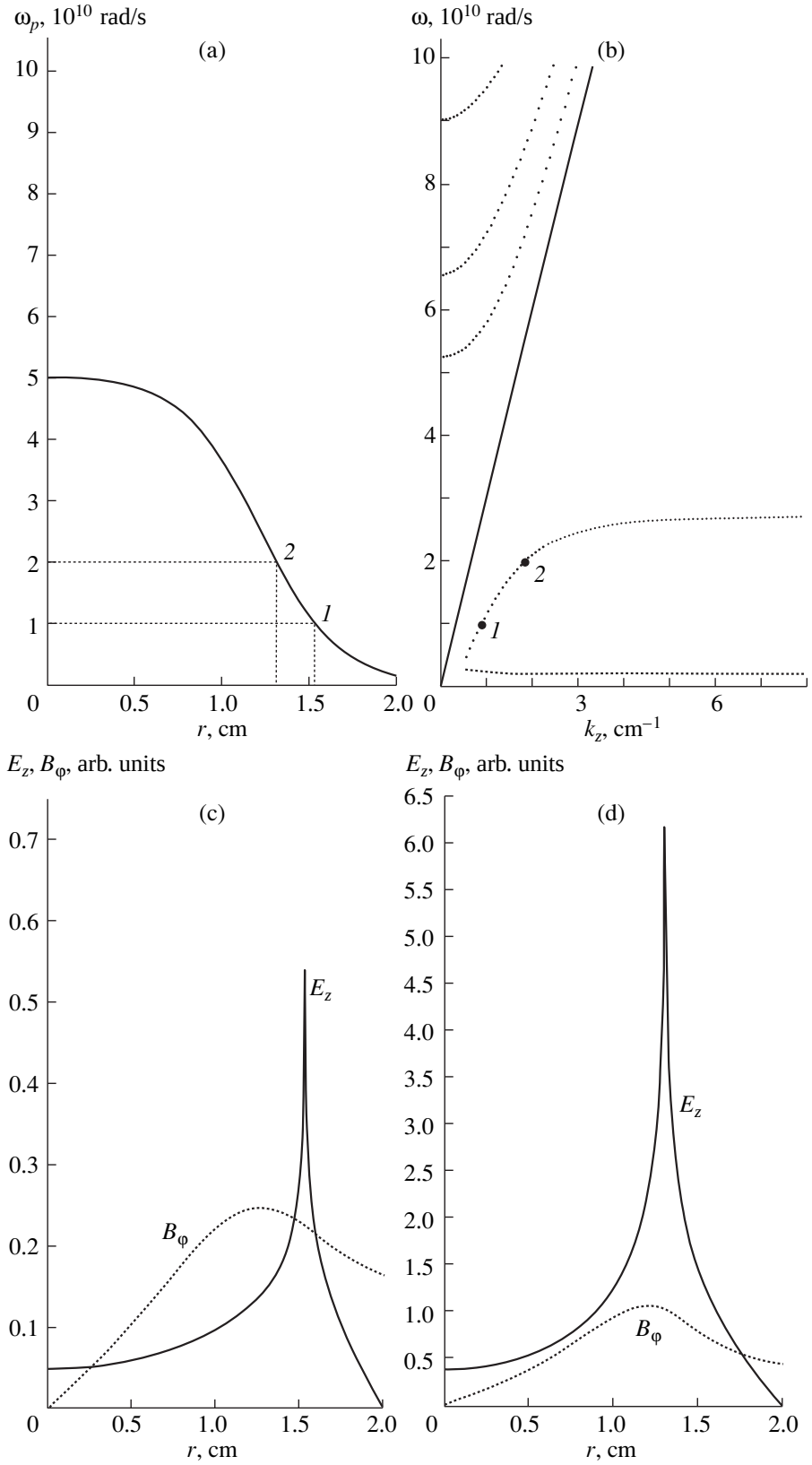

Fig. 3. Plasma in contact with the waveguide wall, $\omega_p(R) < 0.1\omega_{p\,\max}$: (a) radial profile of the Langmuir frequency; (b) dispersion curves; and (c, d) field structures of the surface wave calculated, respectively, for points *1* and *2* on the dispersion curve in plot (b).

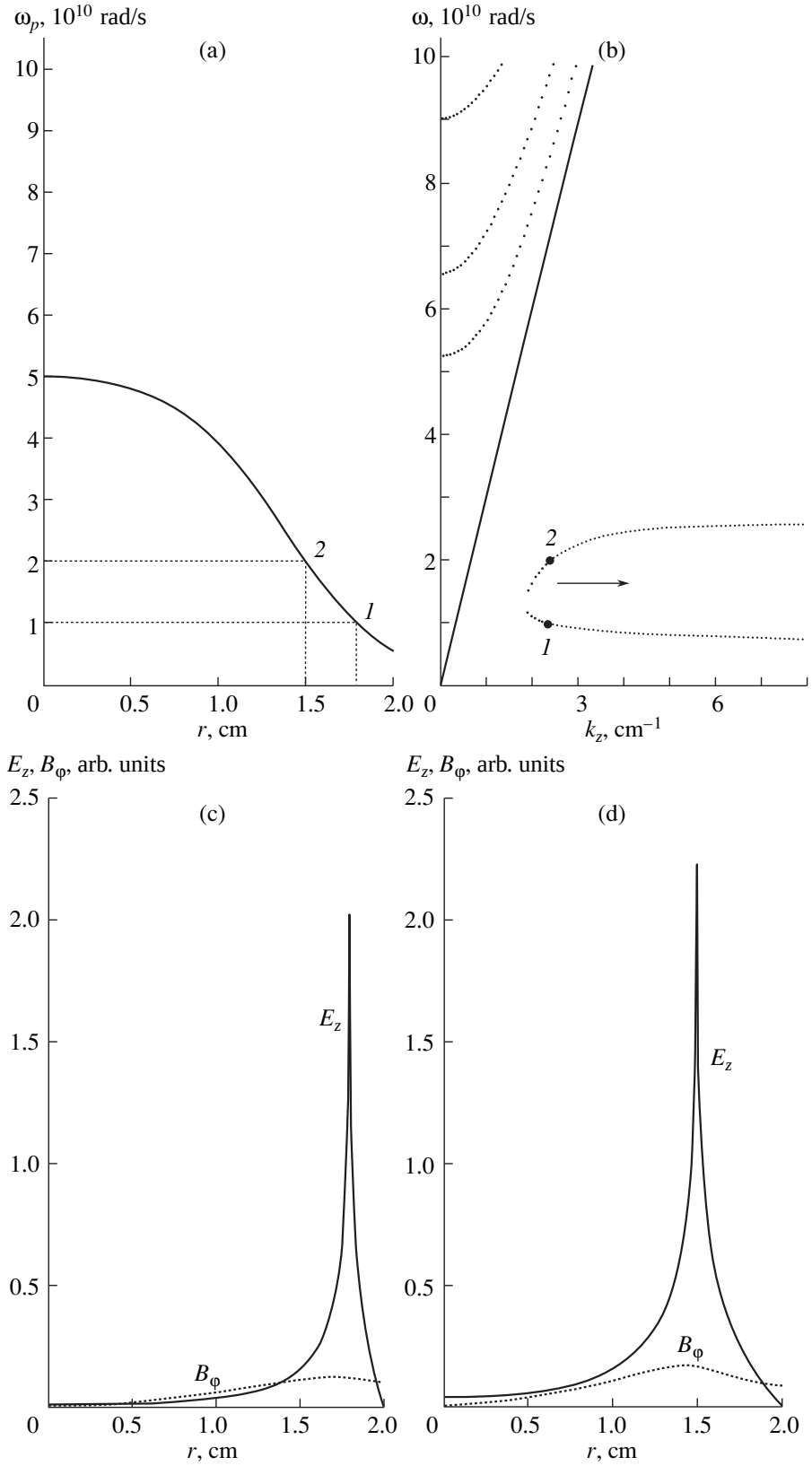

Fig. 4. Plasma in contact with the waveguide wall, $\omega_p(R) > 0.1\omega_{p\,\max}$: (a) radial profile of the Langmuir frequency; (b) dispersion curves; and (c, d) field structures of the surface wave calculated, respectively, for points *1* and *2* on the dispersion curve in plot (b).

low-frequency surface wave. Hence, in this situation, the surface wave cannot exist in the long-wavelength range and splits into two modes described by two branches, specifically, the high-frequency branch, which corresponds to the dispersion curve analyzed above, and a new, low-frequency branch. By analogy with the above figures, Figs. 3c and 3d illustrate the field structures of the high-frequency surface wave that were calculated, respectively, for points *1* and *2* on the dispersion curve in Fig. 3b; the corresponding localization boundaries are marked by points *1* and *2* on the Langmuir frequency profile in Fig. 3a. At large wavenumbers k_z, the low-frequency branch approaches the level $\omega = \omega_{p\min}$, so that the corresponding surface mode is localized very near the waveguide wall. In order to investigate this surface wave, it is more convenient to turn to the case illustrated in Fig. 4.

Figure 4a shows the radial profile of the Langmuir frequency $\omega_p(r)$; at the wall of the waveguide, its minimum value $\omega_{p\min}$ is far larger than in the previous case, $\omega_{p\min} = \omega_p(R) > 0.1\omega_{p\max}$. Accordingly, in the (k_z, ω) plane, the region where the surface waves cannot exist is larger. The upper (high-frequency) branch is seen to lie below that in Fig. 3b, and the lower (low-frequency) branch is markedly displaced upward. The wavenumber k_z at which the upper branch goes over to the lower branch is larger than that in Fig. 3b. As $k_z \longrightarrow \infty$, the upper branch approaches a limiting frequency that is lower than $\omega_{p\max}/\sqrt{2}$. The higher the minimum Langmuir frequency $\omega_{p\min}$, the lower the limiting frequency. In the same limit ($k_z \longrightarrow \infty$), the lower branch approaches the level $\omega_{p\min}$. As $\omega_{p\min}$ increases, the upper and lower branches come together and the point at which the upper branch goes over to the lower branch is displaced rightward, as is indicated by the arrow in Fig. 4b. When $\omega_{p\min}$ becomes equal to $\omega_{p\max}$, no surface waves can be excited, as is the case with a waveguide filled entirely with a homogeneous plasma.

Figures 4c and 4d illustrate the field structures of the surface wave under consideration that are calculated, respectively, for points *1* ($\omega = 10^{10}$ rad/s) and *2* ($\omega = 2 \times 10^{10}$ rad/s) on the dispersion curve in Fig. 4b. Figures 4c and 4d refer to the lower and upper branches of the surface wave. We can see that the radial profiles of the components E_z and B_φ do not change qualitatively in comparison with those analyzed above. As before, the surface modes are localized at the resonance surfaces $r = r^*$. The low-frequency surface mode is localized closer to the waveguide wall, and the localization boundary of the high-frequency surface mode is closer to the waveguide axis. As $k_z \longrightarrow \infty$, we have $r^* \longrightarrow R$, whereas, for the high-frequency surface mode, the radius r^* decreases to a certain minimum radius $r^*_{\min}$; moreover, the higher the frequency $r^*_{\min}$, the larger the radius $\omega_{p\min}$. As the wavenumber k_z decreases, the difference between the frequencies of the surface modes decreases and their localization regions come together and merge into one region at a certain minimum k_z. In a waveguide with the second (inner) boundary of the plasma column or in the presence of an external magnetic field, the structure of surface waves is far more complicated. This issue will be addressed in a separate paper.

ACKNOWLEDGMENTS

This study was supported by the Ministry of Science and Technology of the Russian Federation (under the grants “Russian Universities” and “Physics of Microwaves”).

REFERENCES

1. A. F. Aleksandrov and A. A. Rukhadze, *Course on Electrodynamics of Plasmalike Media* (Mosk. Gos. Univ., Moscow, 1999).
2. N. A. Krall and A. W. Trivelpiece, *Principles of Plasma Physics* (Academic Press, New York, 1973; Mir, Moscow, 1975).
3. M. V. Kuzelev and A. A. Rukhadze, Usp. Fiz. Nauk **167**, 1026 (1997) [Phys. Usp. **40**, 975 (1997)].

Translated by I.A. Kalabalyk

Plasma Physics Reports, Vol. 27, No. 3, 2001, pp. 251–258. Translated from Fizika Plazmy, Vol. 27, No. 3, 2001, pp. 268–275.

PLASMA OSCILLATIONS AND WAVES

Effect of Plasma Nonlinearity on the Beam–Plasma Interaction in a Hybrid Plasma Waveguide

A. N. Antonov, Yu. P. Bliokh, O. F. Kovpik, E. A. Kornilov, M. G. Lyubarskiĭ, K. V. Matyash, V. O. Podobinskiĭ, V. G. Svichenskiĭ, and Ya. B. Faĭnberg

Kharkov Institute for Physics and Technology, National Science Center, Akademicheskaya ul. 1, Kharkov, 61108 Ukraine

Received June 26, 2000; in final form, August 14, 2000

Abstract—A study is made of the characteristic features of the effect of plasma nonlinearity in a slow-wave structure on microwave generation by an electron beam and on electron beam energy losses. Theoretical results on the plasma density variation, the amplitude of the excited microwaves, and the velocity distribution function of the beam electrons are compared with the experimental data. It is shown that the self-consistency between the decreasing plasma density gradient and the spatial variation of the amplitude of an amplified wave in a slow-wave structure leads to a significant (severalfold) increase in the efficiency with which the electron beam energy is converted into microwave energy in short pulses. The predictions of the theoretical model developed to describe the non-steady-state beam–plasma interaction agree well with the experimental data. © *2001 MAIK "Nauka/Interperiodica".*

1. INTRODUCTION

In [1–4], it was shown that oscillators and amplifiers with plasma-filled slow-wave (hybrid) structures based on the Cherenkov mechanism for microwave generation have certain advantages over similar vacuum devices. The presence of plasma in the transport channel increases the coupling between an electron beam and a synchronous wave, thereby raising the efficiency with which microwaves are generated (or amplified) [5–12]. More recent investigations [13–15] have shown that filling the transport channel with a plasma has other important consequences. As the power of the excited microwave increases, the nonlinear properties of the plasma come into play and may significantly influence the parameters of the beam–plasma instability. According to [13–15], the plasma nonlinearity manifests itself, first of all, in the dependence of the plasma density on the wave amplitude and, accordingly, in the nonlinear dispersion of the excited microwave. Since the beam–plasma instability, being resonant in nature, is very sensitive to variations of the phase velocity of the excited wave, the plasma-related nonlinear dispersion of the wave may strongly affect the development of the beam–plasma instability. In particular, the efficiency with which the beam energy is converted into the energy of the beam-driven microwave depends strongly on the shape of the density profile of the plasma in which the wave propagates.

This paper, which is a continuation of papers [2, 13–15], presents the results of our experimental and theoretical investigations of the characteristic features of electron beam energy losses caused by the plasma nonlinearity in a slow-wave structure. We show that a self-consistent variation of the plasma density leads to a prolonged synchronization between the beam and the beam-driven wave, thereby increasing the efficiency with which the beam electron energy is converted into microwave energy to an anomalously high level. This important theoretical conclusion is confirmed experimentally.

2. EXPERIMENTAL DEVICE AND DIAGNOSTIC TECHNIQUES

In order to measure the energy spectra of an electron beam after its interaction with the eigenmodes of a hybrid waveguide and to determine the energy expended on producing plasma in the transport channel, we modified the device used in our previous experiments [5, 14] so as to ensure both electric and thermal insulation of the slow-wave structure, solenoid, and current collector. A schematic of the experimental device is given in Fig. 1.

An electron gun (*1*) with a cathode made of lanthanum hexaboride produces 5- to 10-mm-diameter electron beams with an energy of up to 35 keV and a current of 1–10 A. After passing through the entrance and exit chambers (*3*), the slow-wave structure (*5*) (a sequence of inductively coupled resonators), and solenoidal coils (*4*), the beam reaches the current collector (*6*). A collimator, which extracts a fraction of the beam electrons in order to determine the energy distribution function by means of an electrostatic energy analyzer (*7*), is placed at the end of the current collector. The fraction of the electron current that is to be analyzed is amplified by a vacuum photomultiplier.

The plasma in the transport channel of the slow-wave structure was produced via ionization of a gas by the beam electrons and the excited microwave oscilla-

1063-780X/01/2703-0251$21.00

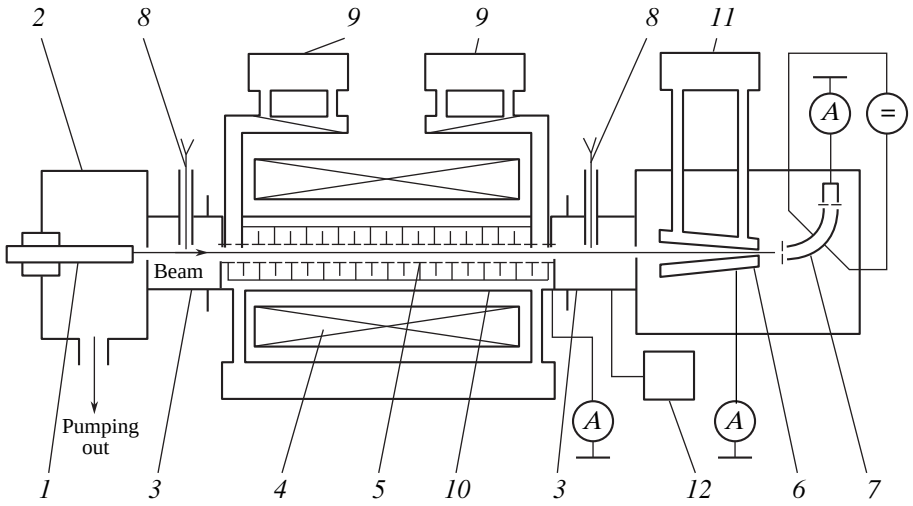

Fig. 1. Schematic of the experimental device: (*1*) electron gun, (*2*) electron-gun chamber, (*3*) entrance and exit chambers, (*4*) solenoid, (*5*) slow-wave structure, (*6*) current collector, (*7*) electrostatic energy analyzer, (*8*) movable Langmuir probes, (*9–11*) calorimeters, and (*12*) gas-puffing unit.

tions. In experiments, the plasma density varied from 10^9 to 10^{12} cm^{-3}. The plasma density and beam velocity were chosen so as to excite microwaves with a normal dispersion. The gas pressure in the transport channel of the slow-wave structure was varied from 5×10^{-4} to 10^{-5} torr. The magnetic field was 1.8 kG.

Low-frequency plasma density waves were detected by single and double electrostatic probes (*8*) placed in chambers (*3*) near the entrance and exit ends of the slow-wave structure. Measurements at different depths in the plasma were provided by moving the probes in the radial direction. Oscillations recorded by the probes were amplified by broadband amplifiers with a low input resistance.

High-frequency oscillations from the entrance and exit ends of the waveguide were recorded with the help of a high-speed oscillograph, calibrated detectors, and spectrum analyzers. Calorimeters (*9*) for measuring the microwave power were linked to all of the waveguide sections of the slow-wave structures.

The energy fluxes to the slow-wave structure of the waveguide and to the current collector were measured by calorimeters (*10*) and (*11*). The released heat was measured to within an error of 2%. All of the signals were converted to digital form by an analog-to-digital converter and then were stored in a computer memory for further processing.

3. ENERGY DISTRIBUTION FUNCTION OF AN ELECTRON BEAM

The coupling between the amplitude of the wave propagating in a plasma and the plasma density stems from such factors as the microwave ponderomotive force, which expels the plasma from the region where the wave field is strong, and a microwave discharge, which additionally increases the plasma density. The experimental data presented below indicate that, in the hybrid, plasma-filled slow-wave structure under investigation, the nonlinear nature of the plasma is primarily governed by the action of the microwave ponderomotive force. Therefore, we will restrict ourselves to the plasma nonlinearity stemming just from this factor and analyze qualitatively how it affects the dynamics of the beam–plasma instability. A detailed theoretical analysis is presented in [13].

Since the wave amplitude increases toward the exit end of the slow-wave structure, the plasma is pushed toward its entrance end. The phase velocity of the amplified microwave in the slow-wave structure decreases as the plasma density decreases. The microwave ponderomotive force acts to form a decreasing gradient in the plasma density, thereby maintaining a prolonged synchronization between the electron beam and the beam-driven microwave, because, as the beam loses its energy, the phase velocity of the excited microwave decreases with the beam velocity. Prolonged synchronization makes it possible to generate more intense microwaves [14–16]. Calculations show that, in this case, the microwave amplitude may be larger than that in a slow-wave structure filled with a homogeneous plasma by a factor of 2 or 2.5.

The important conclusion of the theory [13] is that the beam–plasma instability may evolve into a self-modulation regime, because the microwave ponderomotive force gives rise to ion acoustic waves that propagate in the direction opposite to the propagation direction of the beam, thereby ensuring low-frequency distributed feedback. As a result, the system under consideration starts to function as a generator of low-

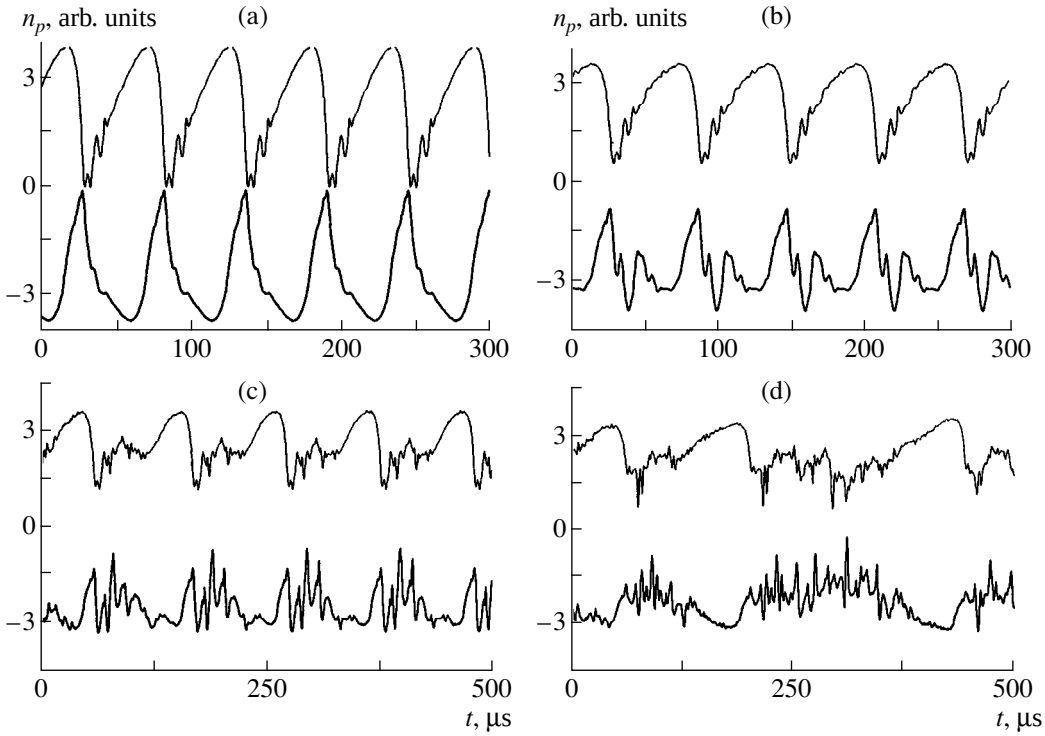

Fig. 2. Deviation of the plasma density n_p from its initial value, calculated as a function of time t at the entrance (upper curve) and exit (lower curve) ends of a hybrid structure for different values of the reflection coefficient for an ion acoustic wave: q = (a) 0.0, (b) 0.2, (c) 0.4, and (d) 0.6.

frequency plasma waves, which, in turn, change the phase velocity of the amplified wave and thus influence the dynamics of the beam–plasma instability. This effect manifests itself, in particular, in the modulation of the output signal.

The self-consistent model developed in [13] in order to describe the beam–plasma instability with allowance for plasma density variations in the excited microwave fields makes it possible to follow the time evolutions of the output signal amplitude and plasma density. Clearly, both the plasma density variations and microwave field strength depend strongly on the reflection coefficient q of the ends of the plasma column for ion acoustic waves. Figure 2 shows waveforms of the plasma density calculated at the entrance and exit ends of the slow-wave structure for different values of the reflection coefficient.

Figure 3 shows the related waveforms, which were obtained experimentally. A good correlation between the theoretical and experimental waveforms (Figs. 2b, 3a) allows us to conclude that the excitation of ion acoustic waves by the microwave ponderomotive force governs the dynamics of the plasma density variations in a slow-wave structure.

Although the plasma in a slow-wave structure is produced by a beam–plasma discharge (this is evidenced by a high plasma density, on the order of $\sim 10^{11}$ cm^{-3}), the key factor governing the plasma inhomogeneity is the microwave ponderomotive force. This conclusion is supported by the fact that, in a slow-wave structure, the plasma evolves into a state with a decreasing density gradient. In the case of excitation of high-power microwaves, the degree of gas ionization is low (less than 10%), so that the resulting plasma contains a large number of neutral molecules and atoms. The frequency of the excited microwave oscillations (2.4–4.0 GHz) is lower than the electron cyclotron frequency. We can expect that, under these conditions, the plasma density either will be constant along a hybrid waveguide or will increase toward the exit end of the waveguide, as does the microwave field amplitude. However, our experiments showed that the situation is the opposite: the plasma density decreases in the region where the microwave field is the strongest. This indicates that, when the amplitude of the forward microwave becomes maximum, the additional gas ionization does not play a governing role. If the plasma inhomogeneity were caused by additional ionization in a microwave field, the plasma density would be expected to increase in the propagation direction of the beam, because the generated microwave is the most intense at the exit end of the structure.

That the theoretical model is quite realistic is also confirmed by the good agreement between the calculated and measured cross-correlation functions of the signals from the Langmuir probes that are located on both sides of the slow-wave structure (see Fig. 4).

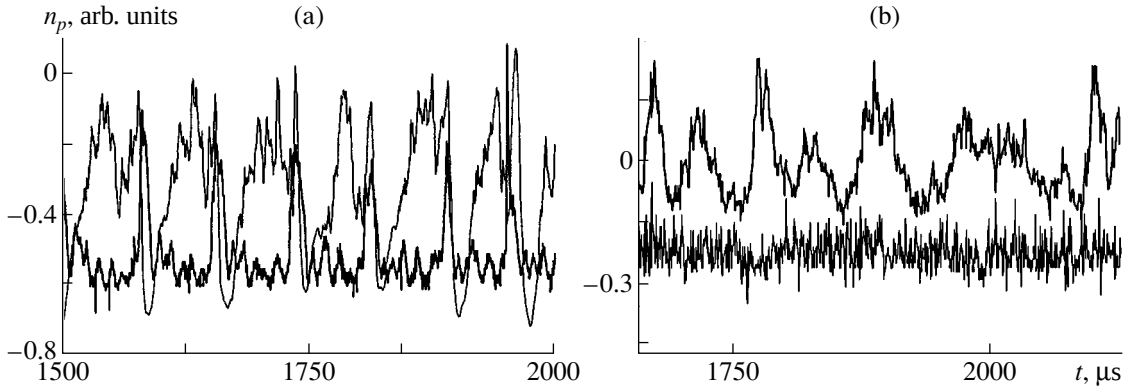

Fig. 3. Measured deviation of the plasma density n_p from its initial value at the entrance (upper curve) and exit (lower curve) ends of a hybrid structure in (a) the low-frequency self-modulation regime and (b) during the onset of spike-mode generation.

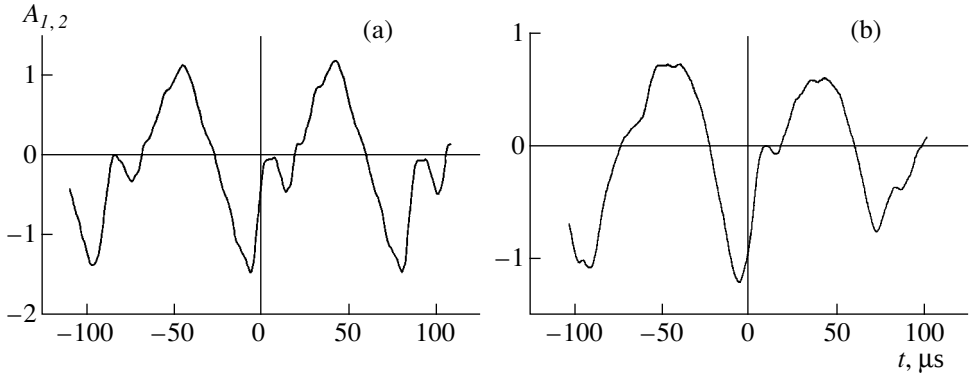

Fig. 4. Cross-correlation functions $A_{1,2}$ of signals from Langmuir probes obtained (a) from numerical calculations and (b) by processing the experimental data.

Because of the self-consistent plasma-density variation, the properties of the energy distribution function of the beam electrons differ from those characteristic of a beam instability in a homogeneous plasma. Self-synchronization between the beam velocity and the phase velocity of the excited microwave gives rise to a dense electron bunch in the region of the decelerating phase of the microwave field, in which case the energy lost by the bunch electrons is anomalously high. On the outside of the region of the decelerating phase, the energy of the beam electrons remains essentially unchanged, because they are not trapped by the slowed wave and do not exchange energy with the microwave field. Figure 5 shows the velocity distribution functions of the beam electrons calculated numerically at different times. In this and other figures, the dimensionless velocity v, which is defined as the relative deviation of the electron beam velocity from its value at the entrance to the slow-wave structure, is normalized to the dimensionless growth rate of the beam–plasma instability.

The experimental and theoretical energy distribution functions of the beam electrons, averaged over low-frequency oscillations, are shown in Figs. 6a and 6b, respectively.

Experimental profiles *1–4* in Fig. 6a illustrate how the distribution function of the beam electrons changes as the working gas pressure (or, equivalently, the plasma density) in a slow-wave structure increases. Profile *2* corresponds to a regime with a quasi-periodic low-frequency (on a time scale of about tens of μs) self-modulation of both the plasma density (see Fig. 3a) and the amplitude of the output microwave signal. The occurrence of a broad and relatively low peak (instead of a large narrow peak) in the averaged distribution function of the decelerated beam electrons is explained by the fact that, as time elapses, this peak gets displaced along the energy axis, which leads to the smearing of the decelerated electrons over a broad energy interval.

It is interesting to note that the autophasing of the excited wave results in the formation of two bunches in the phase plane of the beam electrons. The beam's phase planes at the time of the most intense microwave generation in a plasma with a constant density and in a plasma with a self-consistent density variation are

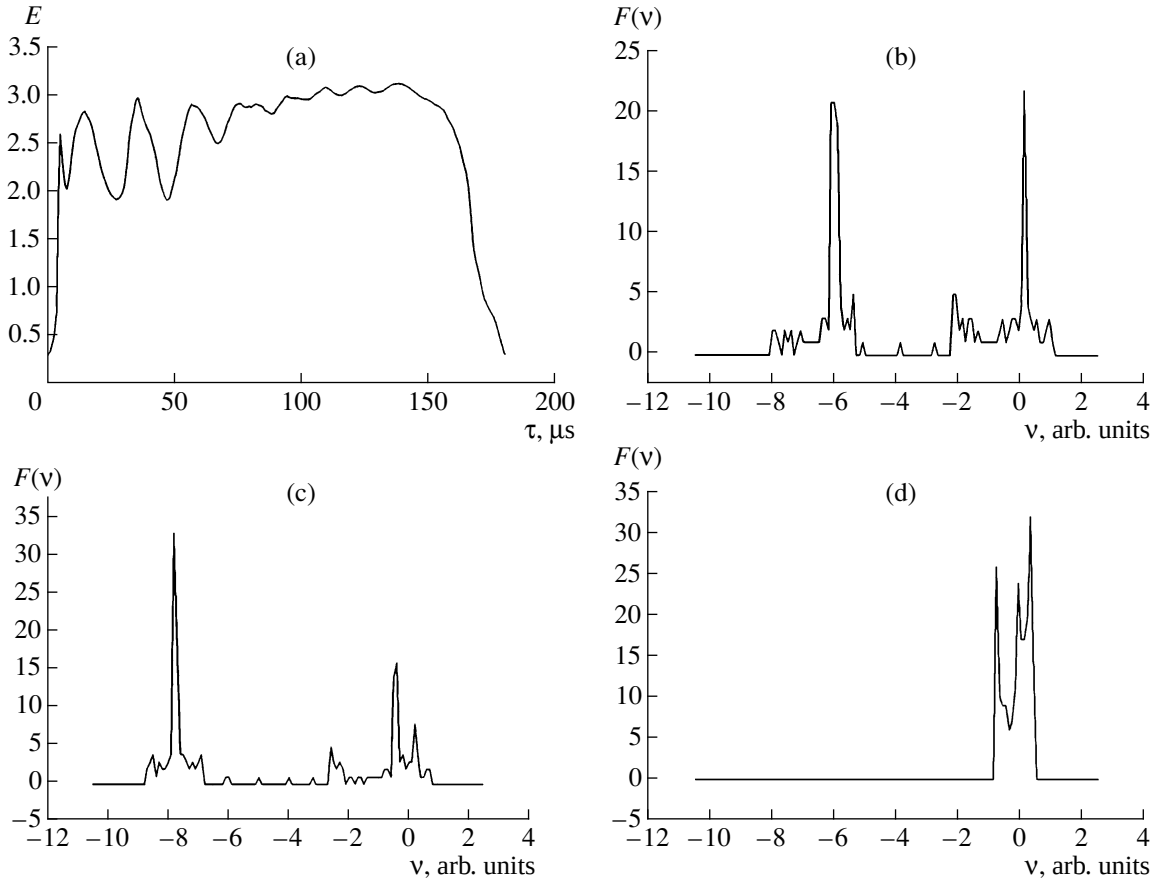

Fig. 5. (a) Calculated waveform of the microwave field amplitude at the exit end of the structure over the low-frequency self-modulation period and the profiles of the velocity distribution function of the beam electrons, obtained from numerical simulations at the times t = (b) 70, (c) 140, and (d) 175 μs.

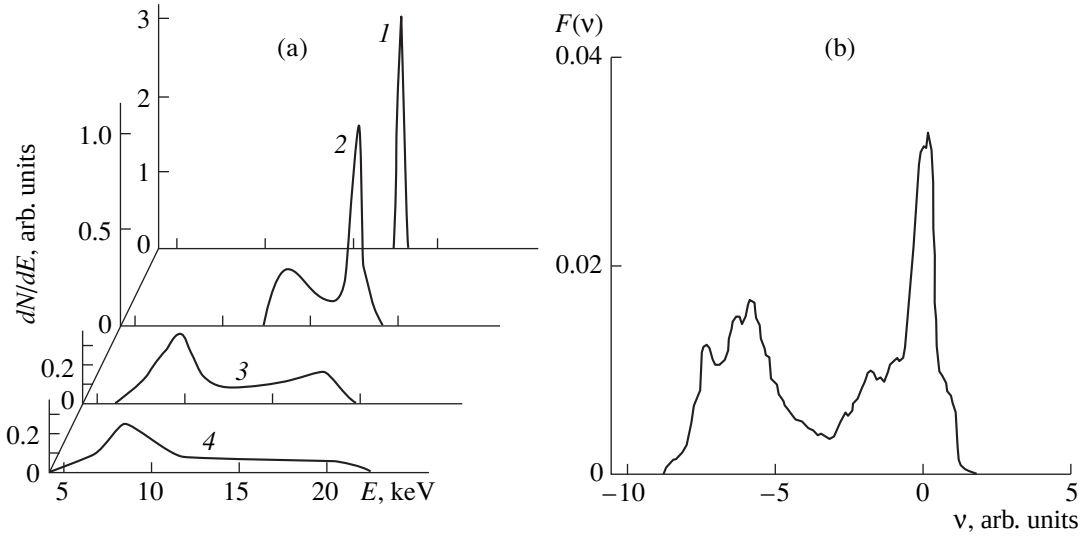

Fig. 6. Instantaneous profiles of the energy distribution function of the beam electrons, (a) obtained experimentally for a 3-A beam current at different pressures p = (*1*) 10^{-5}, (*2*) 2×10^{-5}, (*3*) 4×10^{-5}, and (*4*) 6×10^{-5} torr and (b) calculated numerically.

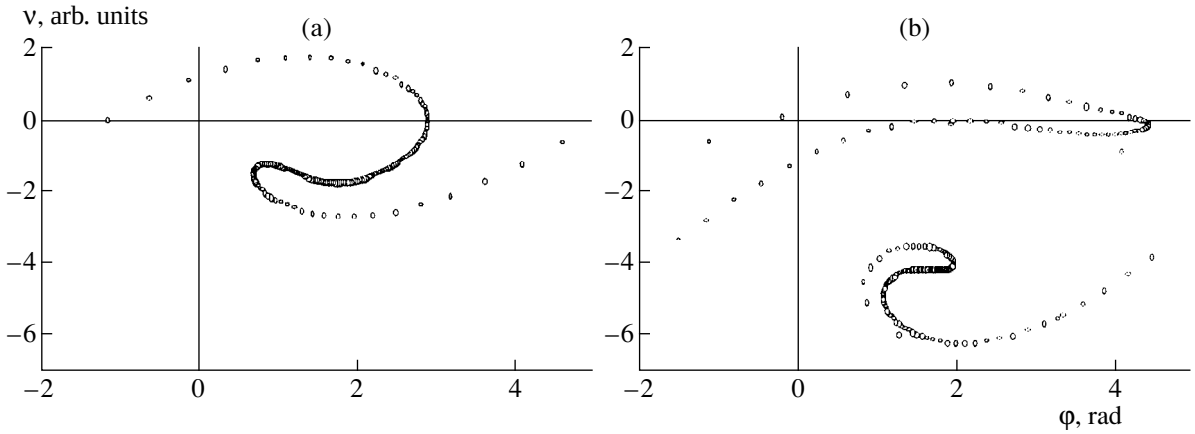

Fig. 7. Distribution of the beam electrons over velocities and over the phase of the excited microwave in the cases of (a) a beam instability in a homogeneous plasma and (b) a self-consistent variation of the plasma density (the zero on the velocity axis corresponds to the initial beam velocity).

shown in Figs. 7a and 7b, respectively. We can see that, in a plasma with a self-consistent density variation, the beam electrons lose a much greater amount of energy. We can also see the formation of a second bunch with a small energy spread, the bunch energy being nearly equal to the initial beam energy (see the right narrow peak in the instantaneous profiles of the distribution functions in Fig. 7a). That the position and width of the second bunch change only slightly explains the appearance of a large peak in the experimentally obtained and theoretically calculated averaged distribution functions in a narrow interval around the initial beam energy.

As the plasma density increases further, it becomes strongly modulated (the relative modulation depth can amount to 100%); this process is accompanied by the modulation of the amplitude of the microwave signal on a time scale of about 1 μs and shorter. The characteristic time scale of the low-frequency self-modulation is determined by the time required for an ion acoustic wave to propagate along the slow-wave structure and, in experiments, was observed to be about 20 μs. Figure 3b shows the typical signals from Langmuir probes during the onset of spike-mode microwave generation. The distribution functions in the initial stage of spike-mode generation are illustrated by instantaneous profiles *3* and *4* in Fig. 6a. Without going into mathematical detail, note that, according to a more thorough analysis of the theoretical model of the excitation of ion acoustic waves, the time scale on which the plasma density and microwave signal amplitude become self-modulated decreases with increasing plasma density, but it still remains substantially longer than the time scale characteristic of spike-mode microwave generation.

Hence, the excitation of ion acoustic waves by the microwave ponderomotive force can serve as the main mechanism for the observed plasma nonlinearity only when the plasma density (and/or the beam current) is not too high. Presumably, the spike-mode microwave generation stems from other nonlinear effects, whose nature is still unclear.

An important consequence of the self-consistent variation of both the plasma density and the amplitude of the beam-driven microwave field is that, under conditions of a prolonged synchronization between the beam and the beam-driven wave, the electron beam energy losses are anomalously large. This conclusion is confirmed by Fig. 5, which shows instantaneous profiles of the velocity distribution function of the beam electrons. The dimensionless electron velocity is expressed in units of $v = (\delta v/v_0)/(\delta k/k_0)$, where δv is the deviation of the velocity of the beam electrons from their initial velocity v_0, δk is the growth rate of the beam–plasma instability, and k_0 is the wavenumber of the excited microwave. In a homogeneous plasma, the beam electrons are decelerated to velocities that are lower than the initial beam velocity by at most a factor of 1.5 to 2 (Fig. 7a). Under conditions of prolonged synchronization between the decelerated beam electrons and the beam-driven wave in an inhomogeneous plasma with a self-consistent density variation caused by the microwave ponderomotive force, the beam electrons are decelerated to markedly lower velocities (lower than the initial beam velocity by a factor of 3 to 4, see Fig. 7b), in which case the conditions for the onset of the beam–plasma instability are far more favorable.

4. BALANCE BETWEEN THE CHANNELS OF ELECTRON BEAM ENERGY LOSSES

Electric and thermal insulation of the elements of our experimental device made it possible to determine the channels of electron beam energy losses. Under the conditions of steady-state microwave generation (i.e., before a transition to the low-frequency self-modula-

tion regime), essentially all of the energy lost by the beam electrons is expended on the excitation of microwaves and only a small fraction (about several percent) of the beam energy is spent on producing the plasma. After the microwave ponderomotive force–induced transition to the low-frequency self-modulation regime, the balance between these channels of electron beam energy losses remains the same.

In the initial stage of spike-mode generation, the balance between the channels of electron beam energy losses changes drastically because of the generation of the plasma current to the wall of the slow-wave structure and an increase in the heat released in it. Since the measured ion and electron temperatures amount to 10–20 eV and 100 eV, respectively, and the guiding magnetic field is fairly strong (1.8 kG), we can conclude that the plasma current to the wall of the structure is generated by the high-energy beam electrons scattered in the transverse direction. This conclusion is confirmed by the fact that the total current to the wall of the structure and to the collector is equal to the current of the beam produced by an electron gun.

Knowing the magnitude of the current to the wall of the structure and the energy released in it, we were able to determine the mean energy of the particles that reach the wall. Under different experimental conditions, this energy amounted from 50 to 70% of the initial electron beam energy.

In our experiments, the microwave radiation power corresponding to the onset of both the spike-mode generation and the plasma current to the wall of the slow-wave structure depended on the beam diameter. When the diameters of the beam and transport channel were close to one another (10 and 12 mm, respectively), the spike-mode generation was observed to occur at a microwave power of 20 kW and the plasma current to the wall of the structure was 30% of the initial beam current. When the beam diameter was half as much, the beam current being the same, the microwave power scattered in the slow-wave structure was much lower: for the same power of the generated microwaves, it was comparable in magnitude to the energy lost in the skin layers of the resonators. The microwave power level at which the electrons started to be ejected onto the wall of the slow-wave structure and the amplitude of a microwave signal became strongly modulated was higher than 40 kW.

5. DISCUSSION OF THE RESULTS

The assumptions that underlie our theoretical model and concern such effects as the excitation of ion acoustic waves by the ponderomotive force of a microwave amplified by a beam and the inverse action of plasma density perturbations propagating in the system on the development of the beam–plasma instability have been mostly confirmed by the experimental observations. As the microwave power increases, the nonlinear nature of the plasma in a hybrid slow-wave structure manifests itself precisely in these effects.

Under conditions of self-consistency between the decreasing plasma density gradient and the spatial variation of the amplitude of an amplified wave in a slow-wave structure, the efficiency with which the electron beam energy is converted into microwave energy is significantly (several times) higher. This effect arises in a plasma with a sufficiently high density and becomes more pronounced as the plasma density (and/or the beam current) increases. As the beam–plasma interaction efficiency increases, the steady-state microwave generation becomes unstable, giving rise to a strong low-frequency self-modulation of the output signal amplitude. With increasing plasma density and/or beam current, the peak microwave power continues to grow, but the mean microwave power either increases at a much slower rate or even starts to decrease. Our theoretical model predicts a strong coupling between the unsteady nature of the beam–plasma interaction and the anomalously high interaction efficiency. If the steady-state plasma density (and/or the beam current) is above a certain critical level, the plasma density gradient caused by the microwave ponderomotive force becomes too large, thereby restricting the efficiency with which the microwaves are generated by the beam. In the non-steady-state regime, the density perturbations repeatedly escape from the interaction region, so that conditions favorable for maintaining synchronism between the wave and the beam along the entire slow-wave structure are restored periodically. When this happens, the efficiency with which the microwaves are generated becomes anomalously high, such that it is never observed in systems with a longitudinally homogeneous plasma. Since the properties of the slow-wave structure are restored every time the density perturbations escape from the interaction region, the low-frequency variations in the interaction efficiency may be regarded as a relaxation process.

The results of our experimental and theoretical investigations allow us to conclude that, although, at first glance, the idea of increasing the mean microwave power by suppressing the low-frequency instability seems to be attractive, doing so may lead to the opposite result—the power of the generated microwaves may become lower.

A further increase in the beam current (and/or the neutral gas pressure) gives rise to other processes, for which an unambiguous explanation is still lacking. By this, we mean the processes that occur on much shorter time scales and result in a transition to the spike-mode regime of the interaction between an electron beam and a plasma-filled waveguide structure, in which case the output signal is observed as an irregular sequence of short (about 1 μs or shorter) microwave pulses. During spike-mode generation, some of the electrons are ejected onto the wall of the slow-wave structure. This effect indicates that the transverse motion of the beam

electrons may play an important role in the onset of spike-mode generation. However, it still remains unclear whether the transverse motion of the beam particles is a cause or a consequence of the onset of spike-mode generation. A detailed investigation of the mechanism for spike-mode microwave generation, which is also observed in other plasma-filled waveguide systems (e.g., in magnetized plasma waveguides), is the subject of our further study.

ACKNOWLEDGMENTS

This study was supported by the Center for Science and Technology of Ukraine, project no. 256.

REFERENCES

1. Ya. B. Faĭnberg, Yu. P. Bliokh, E. A. Kornilov, *et al.*, Dokl. Akad. Nauk Ukr. SSR, Ser. A: Fiz.-Mat. Tekh. Nauki, No. 11, 55 (1990).
2. Ya. B. Faĭnberg, Y. P. Bliokh, M. G. Lyubarskiĭ, *et al.*, Fiz. Plazmy **20**, 757 (1994) [Plasma Phys. Rep. **20**, 681 (1994)].
3. W. R. Lou, Y. Carmel, T. M. Antonsen, *et al.*, Phys. Rev. Lett. **67**, 2481 (1991).
4. Yu. P. Bliokh, E. A. Kornilov, L. A. Mitin, and Ya. B. Faĭnberg, Fiz. Plazmy **20**, 767 (1994) [Plasma Phys. Rep. **20**, 690 (1994)].
5. A. N. Antonov, Yu. P. Bliokh, Yu. A. Degtyar', *et al.*, Fiz. Plazmy **20**, 777 (1994) [Plasma Phys. Rep. **20**, 699 (1994)].
6. M. A. Zavjalov, L. A. Mitin, V. I. Perevodchikov, *et al.*, IEEE Trans. Plasma Sci. **22**, 600 (1994).
7. Y. Carmel, K. Minami, R. A. Kehs, *et al.*, Phys. Rev. Lett. **62**, 2389 (1989).
8. Y. Carmel, W. R. Lou, J. M. Antonsen, *et al.*, Phys. Fluids B **4**, 2286 (1992).
9. A. G. Shkvarunets, A. A. Rukhadze, and P. S. Strelkov, Fiz. Plazmy **20**, 682 (1994) [Plasma Phys. Rep. **20**, 613 (1994)].
10. G. S. Nusinovich, Y. Carmel, T. M. Antonsen, *et al.*, IEEE Trans. Plasma Sci. **26**, 628 (1998).
11. A. G. Shkvarunets, S. Kovayashi, Y. Carmel, *et al.*, IEEE Trans. Plasma Sci. **26**, 648 (1998).
12. G. S. Nusinivich, L. A. Mitin, and A. N. Vlasov, Phys. Plasmas **4**, 4394 (1997).
13. Y. P. Bliokh, Y. B. Fainberg, M. G. Lyubarsky, and V. O. Podobinsky, Proc. SPIE **3158**, 182 (1997).
14. A. N. Antonov, V. A. Balakirev, Y. P. Bliokh, *et al.*, in *Proceedings 12th International Conference on High-Pover Particle Beams (BEAMS'98), Haifa, Israel, 1998*, p. 286.
15. A. N. Antonov, Yu. P. Bliokh, E. A. Kornilov, *et al.*, Fiz. Plazmy **26**, 1097 (2000) [Plasma Phys. Rep. **26**, 1027 (2000)].
16. V. B. Krasovitskiĭ and L. A. Mitin, Fiz. Plazmy **23**, 230 (1997) [Plasma Phys. Rep. **23**, 209 (1997)].

Translated by G.V. Shepekina

Plasma Physics Reports, Vol. 27, No. 3, 2001, pp. 259–264. Translated from Fizika Plazmy, Vol. 27, No. 3, 2001, pp. 276–281.

PLASMA KINETICS

Exact Solution of the Boltzmann Kinetic Equation for a Lorentzian Gas

M. N. Gritsyn

Moscow State University, Vorob'evy gory, Moscow, 119899 Russia

Received April 11, 2000; in final form, August 22, 2000

Abstract—The classical methods of mathematical physics are applied to construct an integral solution to the Chapman–Cowling–Davydov equation, which is derived from the kinetic Boltzmann equation with a collision term in the Lorentzian-gas approximation. For a particular initial distribution, the solution is obtained in an explicit form in terms of a Whittaker function. It is shown that, on long (macroscopic) time scales, the evolving distribution function with an arbitrary initial shape approaches a Maxwellian distribution. This result agrees with the accepted views regarding the overall temporal evolution of an arbitrary unsteady isolated system. *© 2001 MAIK "Nauka/Interperiodica".*

1. INTRODUCTION

Since the formulation of the Boltzmann equation (see [1]), the problem of solving it has been the subject of significant research efforts and continues to be one of the fundamental issues in molecular kinetic theory [2]. Exact analytic solutions to the Boltzmann equation have been obtained only for specific forms of the collision integral, which is very involved in the general case.

The first attempts to solve the Boltzmann equation exactly and to apply the solutions obtained to analyze particular physical systems were made in [3–5]. The next class of exact solutions was constructed for a Maxwellian gas, which consists of monatomic particles such that the attractive forces between them are described by the short-range pair potential function $U(r) = \alpha/r^4$. In this particular case, it is somewhat easier to perform calculations involving the collision integral, because the scattering cross section is inversely proportional to the absolute value of the relative molecular velocities.

In 1975, Bobylev [6, 7] and, independently, Krook and Wu [8] constructed an exact self-similar solution to the nonlinear Boltzmann equation for a Maxwellian gas. An explicit solution was obtained for a spatially homogeneous gas by using the integral Fourier transformation with respect to velocities and then by applying the method of separation of variables. This approach has come to be widely used and has stimulated further investigations for exact solutions to kinetic equations. Significant results in this area were obtained by Ernst [9]; in particular, he published a review paper on exact solutions to the Boltzmann equation [10].

The Bobylev–Krook–Wu method serves as the basis for solving numerous generalized problems (see, e.g., [6, 11–17]). At the same time, more specific approaches to solving various particular problems are presently being developed [18–20].

In this paper, we develop an approach based on the simplest kinetic theory of collisional interactions in a Lorentzian gas or in a system of particles stochastically scattered like billiard balls, assuming that the effective cross section of the potential elastic scattering is independent of energy.

2. FORMULATION OF THE MODEL PROBLEM

It seems expedient to study various kinetic phenomena using simple theoretical models that can be generalized to more complicated systems in which the particle dynamics should be described in terms of the theory of stochastic processes. The model of a Lorentzian gas with scattering point particles of infinite mass incorporates only pair interactions between structureless microparticles under the condition that, in each collision event, the particle velocity changes only slightly. This model applies to a weakly ionized, isotropic low-density plasma in which the collisions between particles are infrequent and the particle energy is low in comparison with the electromagnetic field energy. Analogous models can also be used to describe other kinetic phenomena, e.g., particle scattering in a mixture of two gases that differ greatly in both density and molecular mass, as well as some kinetic processes in reacting gases and dilute solutions.

The most general way to describe the time evolution of the distribution function is to turn to the nonlinear kinetic Boltzmann equation (see [21], p. 25)

$$\frac{\partial f}{\partial t} + \mathbf{v}\frac{\partial f}{\partial \mathbf{r}} + \mathbf{F}\frac{\partial f}{\partial \mathbf{p}} = \sum_b \int d\mathbf{p}\, v_{ab} d\sigma_{ab} \{ f'_a f'_b - f_a f_b \}, \quad (1)$$

1063-780X/01/2703-0259$21.00 © 2001 MAIK "Nauka/Interperiodica"

where the subscripts a and b refer to the quantities characterizing colliding particles of the same or different species.

Let us make a number of simplifying assumptions.

If there are no external forces ($\mathbf{F} = 0$) or external fields ($\mathbf{E} = 0$, $\mathbf{B} = 0$) and if the spatial distribution of the particles in an unbounded plasma is uniform, then the time-dependent distribution function is described by the following Boltzmann equation with a collision term:

$$\frac{\partial f}{\partial t} = \sum_b \int d\mathbf{p}\, v_{ab} d\sigma_{ab} \{ f'_a f'_b - f_a f_b \}. \qquad (2)$$

In any realistic model, Eqs. (1) and (2) are extremely difficult to integrate exactly. For this reason, the problems of kinetic theory are most often treated with a perturbation technique, based on the linearization of the initial equation by seeking the desired solution in the form of a power series in a characteristic small parameter (small correction). The correctness of the final solution is directly related to the assumptions regarding the range of applicability of quasilinear theory to a description of unsteady processes.

In studying conduction electrons in metals, Hendrik Antoon Lorentz [22] applied the method of expanding the distribution function in a series in spherical harmonics. This classical approach implies that the distribution function satisfying Eq. (2) is expanded in a series in Legendre polynomials (see, e.g., [23], p. 61):

$$f(v, \chi, \varepsilon) = f_0(v) + f_1(v)\cos\chi + f_2(v)\sin\chi\cos\varepsilon + \ldots . \qquad (3)$$

Here, f_0 is the symmetric (isotropic) part of the distribution function and its asymmetric part is described by the expansion coefficients f_1 and f_2 (such that $f_1/f_0 \ll 1$) of the higher harmonics of the angular variables—the polar (χ) and azimuthal (ε) angles in spherical coordinates. Centrosymmetric quasi-equilibrium media, which have no preferential directions, can be described by scalar solutions. Morse *et al.* [24] were the first to apply this approach to an electron gas in a plasma.

More recently, Chapman and Cowling (see [25], p. 418) and, independently, Davydov [26] applied the method of substituting expansion (3) into Eq. (2) and derived (in two different ways) the following parabolic differential equation for the symmetric part f_0 of the electron distribution function:

$$\frac{\partial f_0}{\partial t} = \frac{1}{v^2}\frac{\partial}{\partial v}\left(\frac{kTv^3}{Ml}\frac{\partial f_0}{\partial v} + \frac{mv^4}{Ml} f_0\right), \qquad (4)$$

where m and M (such that $m \ll M$) are the masses of the colliding particles and l is the mean free path. The approach to deriving Eq. (4) is, to a large extent, analogous to that used in the theory of diffusion and Brownian motion in order to derive the Fokker–Planck equation from the integral Smoluchowski–Chapman–Kolmogorov equation.

Using the assumption that the electron–atom collision frequency is independent of the electron velocity, Sever'yanov [27] constructed an electron velocity distribution function satisfying Eq. (4). The distribution function that will be constructed below in solving the same equation differs greatly from the solution obtained by Sever'yanov. Note that my interest in the problem under consideration was stimulated, in particular, by Sever'yanov's doctoral dissertation [27] and that the mathematical approach to constructing the desired solution is similar to that used in [27].

3. SOLUTION OF THE KINETIC EQUATION

Let us assume that the distribution function of an ensemble of particles evolves according to a law that makes it possible to predict its future history from the state at an arbitrary instant of time. We also assume that the law of evolution is determined by the initial state of the ensemble and not by its history.

We start by rescaling the original variables (v, t). To do this, we define the energy space of the solutions by passing over to the dimensionless time

$$\tau = 2\frac{mv}{Ml}t, \quad t \in \mathbb{R}_+ \qquad (5)$$

and to the normalized energy

$$\xi = \frac{mv^2}{2kT}, \quad \xi \in \mathbb{R}\backslash 0, \quad \pm\infty, \qquad (6)$$

such that the spectrum of the velocities of the thermal particle motion corresponds to the finite energies.

Then, the basic kinetic equation (4) for the symmetric part of the distribution function can be rewritten in dimensionless form:

$$\frac{\partial f_0}{\partial \tau} = \frac{1}{\xi}\frac{\partial}{\partial \xi}\left(\xi^2\frac{\partial f_0}{\partial \xi} + \xi^2 f_0\right). \qquad (7)$$

The above change of variables can be regarded as a nonlinear transformation or as the introduction of a homogeneous coordinate system.

Since we can choose an arbitrary initial time $\tau = \tau_0$, we will seek the solution to Eq. (7) in the class of functions that have the form

$$f_0(\xi, \tau) = \exp(-\xi)u(\xi, \tau), \qquad (8)$$

and satisfy the normalization condition

$$\int_{-\infty}^{\infty} f_0(\xi, \tau)d\xi = 1. \quad (9a)$$

Because of the causal dependence between $f_0(\xi_1, \tau_1)$ and $f_0(\xi_2, \tau_2)$, the distribution function is continuous and differentiable and can be parameterized by time. In particular, in class (8), Eq. (7) admits a solution that satisfies the limiting condition

$$\lim_{|\xi| \to \infty} f_0(\xi, \tau) = 0. \quad (9b)$$

Equations (7)–(9) constitute an internally closed set of equations that can be used in principle to describe the kinetics of the distribution function with a prescribed initial shape.

Substituting function (8) into Eq. (7) yields

$$\frac{\partial u}{\partial \tau} = \xi\frac{\partial^2 u}{\partial \xi^2} + (2 - \xi)\frac{\partial u}{\partial \xi}. \quad (10)$$

Then, the exact solution of Eq. (10) can be reduced to the solution of an eigenvalue problem using the method of expansion in a Fourier series. The solution is sought in the factored form

$$u(\xi, \tau) = \Phi(\xi)\varphi(\tau). \quad (11)$$

As a result of this factorization (the separation of time and space variables), Eq. (10) splits into the following two ordinary homogeneous differential equations for the functions φ and Φ:

$$\frac{d\varphi}{d\tau} + \nu\varphi = 0, \quad (12)$$

$$\xi\Phi'' + (2 - \xi)\Phi' + \nu\Phi = 0. \quad (13)$$

Here and below, the prime denotes the operator of differentiation with respect to ξ.

To within a constant, Eq. (12) immediately yields a trivial result:

$$\varphi = \exp(-\nu\tau), \quad (14)$$

where ν is an independent real parameter such that $\nu \geq 0$.

Equation (13) has an infinite number of discrete eigenvalues ν. Equation (13) with integer values of ν is well known (see [28]); its analytic particular solutions are generalized Laguerre polynomials:

$$\Phi_\nu(\xi) = L_\nu^\alpha(\xi) = \exp(\xi)\frac{\xi^{-\alpha}}{\nu!}\frac{d^\nu}{d\xi^\nu}(\exp(-\xi)\xi^{\nu+\alpha}). \quad (15)$$

In the specific case at hand, we have $\alpha = 1$.

We represent an arbitrary function that is defined on the interval $(0, \infty)$ and satisfies certain conditions (see [28]) as a converging series of Laguerre polynomials and seek the desired solution (the symmetric part of the time-dependent distribution function) on an infinite time interval in the form of a Fourier series

$$f_0(\xi, \tau) = \sum_{\nu=0}^{\infty} C_\nu \exp(-\xi - \nu\tau)L_\nu^1(\xi). \quad (16)$$

We express the Fourier coefficients C_ν through the symmetric part of the distribution function,

$$f_0(\xi, 0) = \sum_{\nu=0}^{\infty} C_\nu \exp(-\xi)L_\nu^1(\xi) = f(\xi), \quad (17)$$

which is assumed to be specified at the initial time $\tau = 0$. From the orthogonality relations for the Laguerre polynomials with different ν, weighted by $\exp(-\xi)\xi^\alpha$, on the interval $(0, +\infty)$ (see [28]), we obtain

$$\int_0^\infty f(\eta)\eta L_\nu^1(\eta)d\eta = C_\nu\int_0^\infty \exp(-\eta)\eta[L_\nu^1(\eta)]^2 d\eta. \quad (18)$$

Taking into account the relationship

$$\int_0^\infty \exp(-\eta)\eta^\alpha[L_\nu^\alpha(\eta)]^2 d\eta = \frac{\Gamma(\nu + \alpha + 1)}{\nu!}, \quad (19)$$

where Γ is the gamma function, we find the coefficient of the νth term in the expansion of the symmetric part of the disturbing function:

$$C_\nu = \frac{1}{\nu + 1}\int_0^\infty f(\eta)\eta L_\nu^1(\eta)d\eta. \quad (20)$$

For a continuous function, we can change the order of summation and integration, in which case expression (20) permits us to rewrite the assumed solution (16) as

$$f_0(\xi, \tau) = \int_0^\infty \exp(-\xi) f(\eta)\eta d\eta \times \sum_{\nu=0}^{\infty} (\nu + 1)^{-1}\exp(-\nu\tau)L_\nu^1(\eta)L_\nu^1(\xi). \quad (21)$$

In expression (21), the infinite sum of the weighted products of Laguerre polynomials with different ν can be taken with the help of the integral representation of Laguerre polynomials [28]:

$$L_\nu^\alpha(\xi) = \frac{1}{\nu!}\exp(\xi)\xi^{-\alpha/2} \times \int_0^\infty t^{\nu+\alpha/2}J_\alpha(2\sqrt{\xi t})\exp(-t)dt, \quad (22)$$

where $J_\alpha(z)$ is an αth-order Bessel function. Expression (21) with representation (22) can be reduced to

$$\exp(\xi+\eta)(\xi\eta)^{-1/2}(2/\gamma)\sum_{\nu=0}^{\infty}\frac{((\gamma/2)\sqrt{uv})^{2\nu+1}}{\Gamma(\nu+1)\Gamma(\nu+2)} \times\int_0^\infty\int_0^\infty \exp(-u-v)J_1(2\sqrt{\xi u})J_1(2\sqrt{\eta u})\,du\,dv, \tag{23}$$

where we have used the notation

$$\gamma/2 = \exp(-\tau/2).$$

The series in formula (23) is a representation of the Bessel function $I_1(\gamma\sqrt{uv})$ of the imaginary argument [28].

The double integral in formula (23) can be taken with the help of the representation [28]

$$I_\nu(z) = \exp(i\pi\nu/2)J_\nu[z\exp(-i\pi/2)] \tag{24}$$

and the standard integral (see formula (6.615) in [29])

$$\int_0^\infty \exp(-\alpha\kappa)J_\nu(2\beta\sqrt{\kappa})J_\nu(2\gamma\sqrt{\kappa})\alpha^\kappa = (1/\alpha)I_\nu(2\beta\gamma/\alpha)\exp\left(-\frac{\beta^2+\gamma^2}{\alpha}\right), \tag{25}$$

where $\mathrm{Re}\,\nu > -1$. As a result, we arrive at the following integral form of the general solution to the time-dependent Boltzmann equation for the symmetric part of the distribution function:

$$f_0(\xi,\gamma) = 8\exp\left(-\frac{4\xi}{4-\gamma^2}\right)/\gamma\sqrt{\xi}(4-\gamma^2) \times\int_0^\infty f(\eta)\sqrt{\eta}\,d\eta\exp\left(-\frac{\eta\gamma^2}{4-\gamma^2}\right)I_1\left(\frac{4\gamma\sqrt{\xi\eta}}{4-\gamma^2}\right). \tag{26}$$

Solution (26) can be rewritten in a form similar to that frequently used in papers dealing with steady solutions:

$$f_0(v,\tau) = \left(\frac{mv^2}{2kT}\right)^{-1/2}\frac{1}{e^{-\tau/2}(1-e^{-\tau})} \times\exp\left[-\frac{mv^2}{2kT}(1-e^{-\tau})^{-1}\right]\int_0^\infty f(\eta)\sqrt{\eta}\,d\eta \times\exp\left(-\eta\frac{e^{-\tau}}{1-e^{-\tau}}\right)I_1\left[2\sqrt{\eta}\left(\frac{mv^2}{2kT}\right)^{1/2}\frac{e^{-\tau/2}}{1-e^{-\tau}}\right]. \tag{27}$$

In the particular case of an initial symmetric Maxwellian distribution function $f(\eta)$, expression (26) gives an exact solution to the Boltzmann kinetic equation:

$$f_0(\xi,\gamma) = \frac{4-\gamma^2}{\xi\gamma^2}\exp\left[-\xi\frac{8-\gamma^2}{2(4-\gamma^2)}\right]M_{-1,\frac{1}{2}}\left(\xi\frac{\gamma^2}{4-\gamma^2}\right), \tag{28}$$

where $M_{\lambda,\mu}(z)$ is a Whittaker function. Solution (28) was derived in the usual way with the help of a standard integral (see formula (6.643.2) in [29]).

A distinctive feature of our approach to transforming the basic kinetic equation (4) is that it was nondimensionalized by introducing variables (5) and (6). A similar approach was used, e.g., by Sever'yanov [27], who introduced dimensionless time (5), and by Stiller (see [30], p. 96), who introduced dimensionless energy (6).

4. OVERALL EVOLUTION OF AN ARBITRARY INITIAL DISTRIBUTION FUNCTION AND ASYMPTOTIC INVARIANCE PRINCIPLE FOLLOWING FROM THE BEHAVIOR OF THE SOLUTION AT INFINITY

It is well known that the Boltzmann equation is an averaged equation describing the deterministic evolution of a one-particle distribution function [31].

We assume that the energy transfer processes can perturb the distribution function and that an ensemble of dynamically interacting particles can relax to an equilibrium (most probable) state on arbitrarily long time scales. The relaxation of a particle ensemble to a steady state as a consequence of the law of large numbers was analyzed by Stankevich (see [1], p. 117). In order to examine the relaxation process in more detail, we determine the established equilibrium solution of the parameterized equation (26). To do this, we calculate the exact upper limit on solution (26) at $t \longrightarrow \infty$. Resolving the indeterminateness and using the representation of the Bessel function of the imaginary argument by a series (see [28]), we obtain the following explicit expression for the steady-state distribution function:

$$\lim_{\gamma\to 0} f_0(\xi,\gamma) = \exp(-\xi)\int_0^\infty f(\eta)\eta\,d\eta.$$

We can see that, on the time interval $(0, +\infty)$, an unsteady isotropic particle velocity distribution relaxes to a final (at $t \longrightarrow \infty$ or, equivalently, $\gamma \longrightarrow 0$) equilibrium Maxwellian distribution; moreover, the asymptotic solution (the established distribution function) is independent of the shape of the initial distribution function $f(\eta)$.

On the whole, the local properties of a Lorentzian gas and analogous particle systems remain unchanged, and a particle ensemble whose evolution is described

by a kinetic model that admits an exact solution relaxes to an asymptotically stable state of external equilibrium and remains in this state for an arbitrary long time. The uniqueness of the scenario of the natural evolution of a physical system consisting of a statistically large number of particles is in agreement with the principles of thermodynamics, which imply that any closed (isolated) system relaxes spontaneously to a stable steady state, which is not spontaneously disordered and is regarded as being equilibrium.

This result is not an obvious consequence of the choice of the model of a physical system. Thus, for a mixture of two gases, one of which is a Lorentzian gas, an equilibrium solution that is independent of the spatial coordinates and time is an arbitrary isotropic distribution function (see [21], p. 324).

5. CONCLUSION

In conclusion, let us make two remarks about the justification and application of the distribution function that we obtained in solving the kinetic equation.

(i) The exact limits of applicability of unsteady solutions describing the local equilibrium kinetics of particles in weakly nonequilibrium (i.e., slightly non-Maxwellian) systems can be established using a rigorous nonequilibrium kinetic theory that is based on the investigation of kinetic equations describing the time evolution of the distribution functions.

(ii) In order for the unsteady processes occurring on time scales shorter than the time of relaxation to an equilibrium Maxwellian distribution to be adequately described using, e.g., the energy balance equation and the real values of transport coefficients, it is necessary to take into account the unsteady character of the particle distribution function.

ACKNOWLEDGMENTS

I am grateful to the referee for amending the manuscript.

REFERENCES

1. B. V. Stankevich, Uch. Zap. Imp. Mosk. Univ., Otd. Fiz.-Mat. **6**, 77 (1885).
2. G. E. Uhlenbeek, in *Proceedings of the International Symposium "100 Years Boltzmann Equation," 1972*, Ed. by E. G. Cohen and W. Thirring (Springer-Verlag, New York, 1973), p. 107; *Proceedings of the International Congress on Mathematics, 1958*, Ed. by J. A. Todd (Cambridge Univ. Press, Cambridge, 1960), p. 256.
3. H. Grad, Commun. Pure Appl. Math. **2**, 331 (1949).
4. M. Kac, in *Proceedings of the Third Berkeley Symposium on Mathematical Statistics and Probability* (California Univ. Press, California, 1956), Vol. 3, p. 171.
5. N. B. Maslova, Vest. Leningr. Univ., Ser. 1, No. 13, 88 (1968).
6. A. V. Bobylev, Dokl. Akad. Nauk SSSR **225**, 535 (1975) [Sov. Phys. Dokl. **20**, 740 (1975)]; Dokl. Akad. Nauk SSSR **225**, 1041 (1975) [Sov. Phys. Dokl. **20**, 820 (1975)]; Dokl. Akad. Nauk SSSR **225**, 1296 (1975) [Sov. Phys. Dokl. **20**, 822 (1975)]; Dokl. Akad. Nauk SSSR **231**, 571 (1976) [Sov. Phys. Dokl. **21**, 632 (1976)]; Dokl. Akad. Nauk SSSR **251**, 1361 (1980) [Sov. Phys. Dokl. **25**, 257 (1980)]; Teor. Mat. Fiz. **60**, 280 (1984); A. V. Bobylev, E. Gabetta, and Z. Pareschi, Math. Methods Appl. Sci. **5**, 253 (1995); A. V. Bobylev, Math. Methods Appl. Sci. **19**, 825 (1996); A. V. Bobylev and G. Spiga, SIAM J. Appl. Math. **58**, 1128 (1998).
7. A. V. Bobylev, *Exact and Approximate Solution Methods in Theory of Nonlinear Kinetic Boltzmann and Landau Equations* (Inst. Prikl. Mat., Moscow, 1987).
8. M. Krook and T. T. Wu, Phys. Rev. Lett. **36**, 1107 (1976); **38**, 991 (1977); Phys. Fluids **20**, 1589 (1977).
9. M. H. Ernst, Phys. Lett. A **69A**, 390 (1979); J. Stat. Phys. **34**, 1001 (1984); M. H. Ernst and E. M. Hendriks, Phys. Lett. A **70A**, 183 (1979); **81A**, 315 (1981); **81A**, 371 (1981); M. H. Ernst, in *Nonequilibrium Phenomena: I. The Boltzmann Equation*, Ed. by J. Lebowitz and E. W. Montroll (North-Holland, Amsterdam, 1983; Mir, Moscow, 1986), p. 51.
10. M. H. Ernst, Phys. Rep. **78** (1), 1 (1981).
11. D. Ya. Petrina and A. V. Mishchenko, Dokl. Akad. Nauk SSSR **298**, 338 (1988) [Sov. Phys. Dokl. **33**, 32 (1988)]; A. V. Mishchenko and D. Ya. Petrina, Teor. Mat. Fiz. **77**, 135 (1988).
12. C. Cercignani, in *Modern Group Analysis: Advances in Analytic and Computing Methods in Mathematical Physics* (Kluwer, Dordrecht, 1993), p. 125.
13. O. P. Bhutani, M. H. Moussa, and K. Vijaykumar, Int. J. Eng. Sci. **33**, 331 (1995).
14. H. Cabannes, in *Comp. Fluid Dynamics* (Springer-Verlag, Berlin, 1995), p. 103; Eur. J. Mech. B: Fluids **16**, 1 (1997).
15. H. Cornille, J. Math. Phys. **32**, 3439 (1991); in *Nonlinear Hyperbolic Problems: Theoretical, Applied and Computational Aspects* (Vieweg, Braunschweig, 1993), p. 150; J. Math. Phys. **39**, 2004 (1998); J. Phys. A **31**, 671 (1998).
16. C. R. Garibotti and G. Spiga, J. Phys. A **27**, 2709 (1994).
17. T. Platkowski, Arch. Mech. **43** (1), 115 (1991); T. Platkowski and G. Spiga, Eur. J. Mech. B: Fluids **11**, 349 (1992).
18. F. Shurrer, J. Stat. Phys. **65**, 1045 (1992).
19. G. Spiga, Transp. Theory Stat. Phys. **25**, 699 (1996); **26**, 243 (1997).
20. Tiem Dang Hong, Math. Methods Appl. Sci. **3**, 655 (1993).
21. V. P. Silin, *Introduction to the Kinetic Theory of Gases* (Fiz. Inst. Ross. Akad. Nauk, Moscow, 1998).
22. H. A. Lorentz, *The Theory of Electrons and Its Applications to the Phenomena of Light and Radiant Heat* (Dover, New York, 1952; Gostekhizdat, Moscow, 1953).
23. L. P. Shkarofsky, T. W. Johnston, and M. P. Bachynski, *The Particle Kinetics of Plasmas* (Addison-Wesley, Reading, 1966; Atomizdat, Moscow, 1969).
24. P. M. Morse, W. P. Allis, and E. S. Lamer, Phys. Rev. **48**, 412 (1935).

25. S. Chapman and T. G. Cowling, *The Mathematical Theory of Nonuniform Gases* (Cambridge Univ. Press, Cambridge, 1970; Mir, Moscow, 1960).
26. B. I. Davydov, Zh. Éksp. Teor. Fiz. **6**, 463 (1936).
27. V. V. Sever'yanov, Doctoral Dissertation in Mathematical Physics (Inst. Obshch. Fiz. Ross. Akad. Nauk, Moscow, 1993).
28. N. N. Lebedev, *Special Functions and Their Applications* (Fizmatgiz, Moscow, 1963; Prentice-Hall, Englewood Cliffs, 1965).
29. I. S. Gradshteyn and I. M. Ryzhik, *Tables of Integrals, Series, and Products* (Nauka, Moscow, 1971; Academic, New York, 1980).
30. W. Stiller, *Arrhenius Equation and Non-Equilibrium Kinetics* (BSB B. G. Teubner Verlagsgesellschaft, Leipzig, 1989; Mir, Moscow, 2000).
31. O. E. Lanford, III, Lect. Notes Phys., No. 38, 1 (1975).

Translated by I.A. Kalabalyk

Plasma Physics Reports, Vol. 27, No. 3, 2001, pp. 265–269. Translated from Fizika Plazmy, Vol. 27, No. 3, 2001, pp. 282–286.

BRIEF COMMUNICATIONS

Electromagnetic Oscillations near the Critical Surface in a Magnetized Plasma

A. V. Timofeev

Russian Research Centre Kurchatov Institute, pl. Kurchatova 1, Moscow, 123182 Russia

Received July 19, 2000

Abstract—It is shown that, in a plasma whose density varies across the magnetic field lines, electromagnetic oscillations that are localized near the critical surface can exist. Such oscillations can be excited spontaneously in a nonequilibrium plasma of closed magnetic confinement systems. © *2001 MAIK "Nauka/Interperiodica".*

1. We consider electromagnetic oscillations in a plane slab of a cold magnetized plasma, assuming that the magnetic field is uniform and the plasma density varies across the magnetic fields lines. The well-known dispersion relation characterizing oscillations in a cold plasma can be represented as

$$D = N_\perp^4\varepsilon_\perp + N_\perp^2(N_\parallel^2(\varepsilon_\perp + \varepsilon_\parallel) - 2\varepsilon_\perp\varepsilon_\parallel - \varepsilon_\perp + \varepsilon_\parallel) + \varepsilon_\parallel(N_\parallel^2 - \varepsilon_+)(N_\parallel^2 - \varepsilon_-) = 0, \quad (1)$$

where $\varepsilon_\pm = 1 - \dfrac{\omega_{pe}^2}{\omega(\omega - \omega_e)}$, $\varepsilon_\perp = (\varepsilon_+ + \varepsilon_-)/2$, $\varepsilon_\parallel = 1 - \dfrac{\omega_{pe}^2}{\omega^2}$, ω_{pe} is the electron plasma frequency, and ω_e is the electron cyclotron frequency. The oscillation frequency ω is assumed to be high enough to neglect the ion contribution to the plasma permittivity.

In order to qualitatively understand the behavior of the profile $N_\perp^2$, i.e., the dependence of $N_\perp^2$ on the plasma density $q = \omega_{pe}^2/\omega^2$, it is sufficient to note that the quantity $N_\perp^2(q)$ vanishes at $q_\pm = (1 - N_\parallel^2)(1 \pm \Omega_e)$ and $q_0 = 1$ and tends to infinity at $q_s = 1 - \Omega_e^2$ (where $\Omega_e = \omega_e/\omega$) and that two roots of biquadratic equation (1) coincide at $q_v = 1 + \Omega_e^2\left(\dfrac{N_\parallel^2 - 1}{2N_\parallel}\right)^2$.

We will be interested in oscillations with $\omega < \omega_e$ ($\Omega_e > 1$), in which case we have $N_\parallel > 1$. Inside the plasma slab, there is a transparency region ($N_\perp^2 > 0$) between the critical density surface $q = q_0$ and the surface at which the condition $q = q_-$ holds. For $N_\parallel < N_{\parallel c} = \dfrac{\Omega_e}{\Omega_e - 1}$, the latter surface lies ahead of the critical surface ($q < 1$), and, for $N_\parallel > N_{\parallel c}$, it lies behind the critical surface. The electromagnetic oscillations may become locked in the transparency region.

Under the conditions $\omega = \omega_{pe}$ and $N_\parallel^2 = \varepsilon_-$, the transparency region contracts into the surface at which we have

$$\omega_{pe} = \omega_{pec} = \frac{(k_\parallel c)^2}{2\omega_e}\left(\sqrt{\left(\frac{2\omega_e}{k_\parallel c}\right)^2 + 1} - 1\right). \quad (2)$$

For oscillations whose frequency differs from $\omega_c = \omega_{pec}$, the transparency region has a finite thickness, which can be found from the expression for the transverse refractive index. For $\delta\omega \ll \omega_c$, we have

$$N_\perp^2 \approx -\varepsilon_\parallel(N_\parallel^2 - \varepsilon_-)A,$$

where $A = \dfrac{N_\parallel^2 - \varepsilon_+}{\varepsilon_\perp(N_\parallel^2 - 1)} \approx 2\dfrac{\omega_e - \omega_c}{\omega_e}$.

We approximate the dependence $q(x)$ by the linear function $dq/dx = 1/L$ to obtain

$$N_x^2 \approx -N_y^2 + \frac{2}{L^2}\frac{\omega_c}{\omega_e}\left(\left(\frac{\Delta x}{2}\right)^2 - x^2\right),$$

where $\Delta x = L\dfrac{|\delta\omega|}{\omega_c}\dfrac{\omega_e(2\omega_e - \omega_c)}{\omega_c(\omega_e - \omega_c)}$ is the thickness of the transparency region for oscillations with $N_y = 0$. (We work in a Cartesian coordinate system with the x- and z-axes directed along the density gradient and magnetic field, respectively, the coordinates being nondimensionalized by multiplying by the factor ω_c/c.)

The frequency spectrum of the natural oscillations is determined in a standard way from the "quantization" condition

$$\oint N_x dx = 2(n + 1/2)\pi.$$

1063-780X/01/2703-0265$21.00

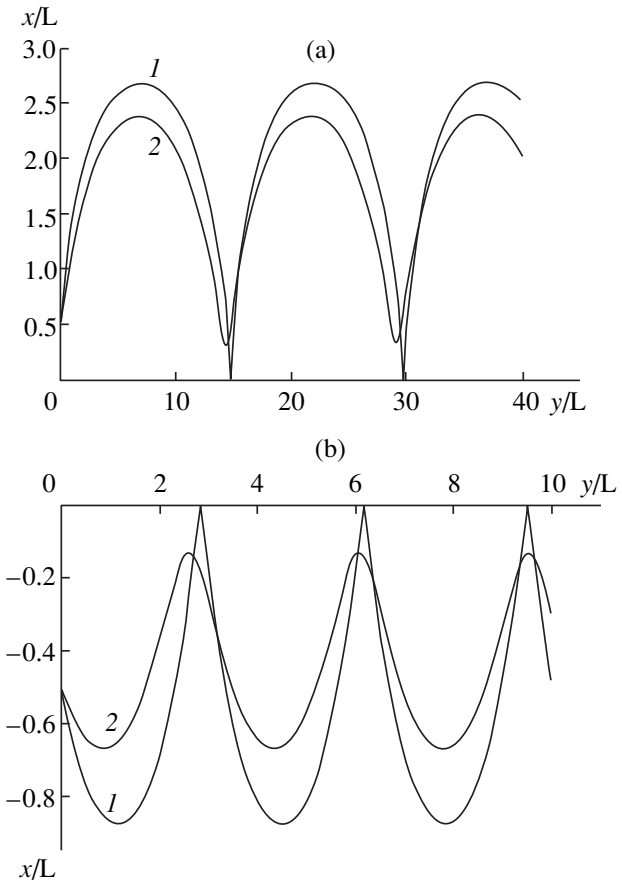

Fig. 1. Ray trajectories in a plane plasma slab: (a) $N_\parallel$ = 2.1614 and N_y = (*1*) 0 and (*2*) –0.769; (b) $N_\parallel$ = 1.0596 and N_y = (*1*) 0 and (*2*) –0.377.

As a result, we obtain

$$\omega \approx \omega_c \pm \sqrt{\frac{2\omega_c}{\omega_e}}\frac{\omega_e - \omega_c}{2\omega_e - \omega_c}\left(N_y^2 + \sqrt{\frac{2\omega_c}{\omega_e}}\frac{2n+1}{L}\right)^{1/2}. \quad (3)$$

One boundary surface of the transparency region is the critical surface, and the other boundary surface lies either in the higher density plasma region [for oscillations with $\omega < \omega_c$, which correspond to the upper sign in formula (3)] or in the lower density plasma region [for oscillations with $\omega > \omega_c$, which correspond to the lower sign in formula (3)].

The polarization of the oscillations under discussion is rather peculiar and is conveniently characterized by the longitudinal component $E_\parallel$ of the electric field and its circular components $E_\pm = (E_x \pm iE_y)/\sqrt{2}$, one of which rotates in the same direction as the electrons and the other, in the same direction as the ions. These electric-field components satisfy the relationships $E_\pm = E_0\dfrac{N_\pm}{\varepsilon_\pm - N^2}$ and $E_\parallel = E_0\dfrac{N_\parallel}{\varepsilon_\parallel - N^2}$, where $N_\pm = (N_x \pm iN_y)/\sqrt{2}$.

Assume that $N_y = 0$. At the quasiclassical turning points, the *x*-component of the refractive index vanishes; this indicates that the oscillations propagate along the magnetic field lines. One of the turning points is a critical point at which the condition $\omega_{pe} = \omega$ ($\varepsilon_\parallel = 0$) holds and the oscillations transform into electron Langmuir waves with longitudinal polarization. At the other turning point, the condition $\varepsilon_- = N_\parallel^2$ is satisfied and the oscillations are circularly polarized, with the electric vector rotating in the same direction as the electrons. For $N_y \neq 0$, the electric-field components $E_\pm$ and $E_\parallel$ are nonzero in the region between the turning points as well as in the entire transparency region.

2. The conclusion that the oscillations can be localized near the critical surface is confirmed by numerical calculations of the ray trajectories.

The ray trajectories satisfy the following standard equations of the geometrical-optics (GO) approximation:

$$\frac{d\mathbf{r}}{dt} = -\frac{\partial D/\partial \mathbf{N}}{\partial D/\partial \omega},$$
$$\frac{d\mathbf{N}}{dt} = \frac{\partial D/\partial \mathbf{r}}{\partial D/\partial \omega}.$$

In the steady-state case (when we are interested only in the shape of the ray trajectories), it is convenient to parameterize the ray trajectories in terms of the time variable τ related to the time t by $d\tau/dt = (\partial D(\mathbf{r}(t), \mathbf{N}(t))/\partial\omega)^{-1}$, in which case the equations of the GO approximation become

$$\frac{d\mathbf{r}}{d\tau} = -\frac{\partial D}{\partial \mathbf{N}},$$
$$\frac{d\mathbf{N}}{d\tau} = \frac{\partial D}{\partial \mathbf{r}}.$$

Figure 1 shows representative ray trajectories of oscillations with $\omega = \omega_e/2$ in a plane plasma slab ($dq/dx = 1$). In accordance with the above analysis, the transparency region is seen to lie ahead of the critical surface if $N_\parallel < N_{\parallel c}$ and behind the critical surface if $N_\parallel > N_{\parallel c}$.

Note that, at the critical surface, the ray trajectories are cusp-shaped. The other boundary of the transparency region is a conventional caustic surface. These characteristic features of the ray trajectories can be readily explained as follows.

We represent the dependence $N_x(x, N_\parallel)$ in the form

$$N_x \approx \left[\frac{2\omega_e}{\omega}\frac{x}{L}\left(\left(\frac{N_\parallel}{N_{\parallel c}}\right)^2 - 1 - \frac{\omega}{\omega_e}\frac{x}{L}\right)\right]^{1/2}. \quad (4)$$

In the xz plane, the ray trajectories are described by the equation

$$\frac{dx}{dz} = \frac{\partial\omega/\partial N_x}{\partial\omega/\partial N_z} = \frac{\partial D/\partial N_x}{\partial D/\partial N_z} = -\left(\frac{\partial N_x}{\partial N_z}\right)^{-1}. \quad (5)$$

Formulas (4) and (5) yield the following equation for ray trajectories in the vicinity of the critical surface:

$$\frac{dx}{dz} \approx \frac{a_1}{x^{1/2}}, \quad (6)$$

where $a_1 = \left(\frac{\Delta x}{2}\right)^{1/2}\frac{1}{N_{\parallel c}}\frac{\omega}{\omega_e - \omega}$. The solution to this equation is a semicubical parabola:

$$\pm x^{3/2} = \frac{3}{2}a_1(z - z_0). \quad (7)$$

Equation (6) and solution (7) imply that, near the critical surface, the ray trajectories are parallel to the density gradient ∇n_0 and, therefore, are perpendicular to the magnetic field lines. This feature is attributed to the potential nature of oscillations at the critical surface. In fact, it is well known that the group velocity of potential oscillations is perpendicular to their wave vector, which is parallel to the magnetic field near the critical surface (see, e.g., [1]).

Ray trajectories with cusps at the critical surface were also obtained in [2] when studying a plasma in which the density gradient makes a small angle with the magnetic field. The cusp shape is also peculiar to both the ray trajectories of potential oscillations near the plasma resonance surface [1] and the ray trajectories of the perturbations of an inhomogeneous gas flow near the boundary between the regions of supersonic and subsonic flow velocities [3]. (In the latter case, the cusps occur on the so-called hodograph plane.)

Near the other boundary surface of the transparency region ($x \approx \Delta x$), we have

$$\frac{dx}{dz} = a_2(\Delta x - x)^{1/2}, \quad (8)$$

where $a_2 = \frac{1}{N_{\parallel c}(2\Delta x)^{1/2}}\frac{\omega}{\omega_e - \omega}$. From Eq. (8), we obtain

$$\pm(\Delta x - x)^{1/2} = \frac{a_2}{2}(z - z_0). \quad (9)$$

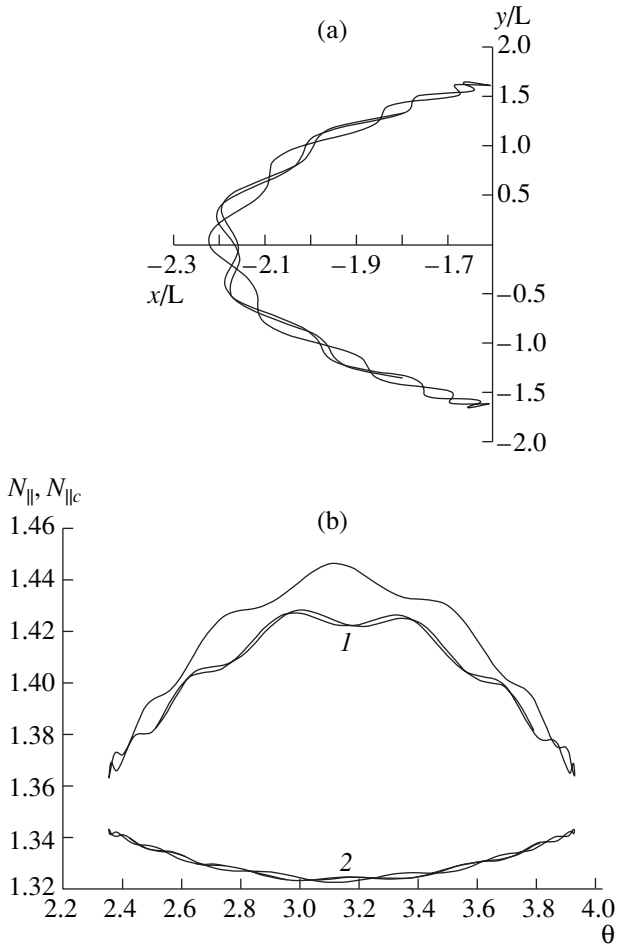

Fig. 2. Propagation of oscillations behind the critical surface ($q > 1$) in a tokamak plasma: (a) the projection of a ray trajectory onto the vertical cross section of the torus (the magnetic axis intersects the plane of the figure at the origin of the coordinate system) and (b) the quantities $N_\parallel$ (curve *1*) and $N_{\parallel c}$ (curve *2*) as functions of the poloidal angle along the trajectory.

The parabolic dependence $x(z)$ corresponds to a conventional caustic surface.

Formulas (6)–(9) refer to the case $N_\parallel > N_{\parallel c}$, in which $\Delta x > 0$, so that $x > 0$ inside the transparency region. For $N_\parallel < N_{\parallel c}$, the pattern of ray trajectories can be obtained by means of a mirror image reflection about the critical surface.

3. The idealized model of a plane plasma slab in a uniform magnetic field described above roughly reflects a characteristic feature of plasmas in magnetic confinement systems, namely, the constancy of the plasma density at the magnetic surfaces. For this reason, it is natural to expect that, being appropriately modified, the results of our analysis will be valid for electromagnetic oscillations in such plasmas. In particular, the frequency spectrum of the natural oscillations

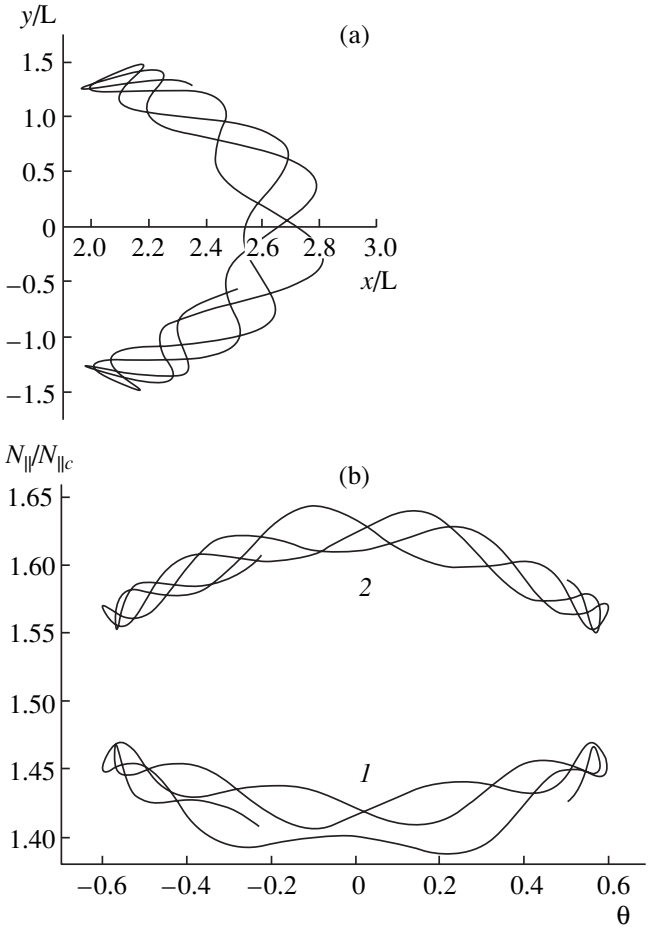

Fig. 3. The same as in Fig. 2, but for oscillations propagating ahead of the critical surface ($q < 1$).

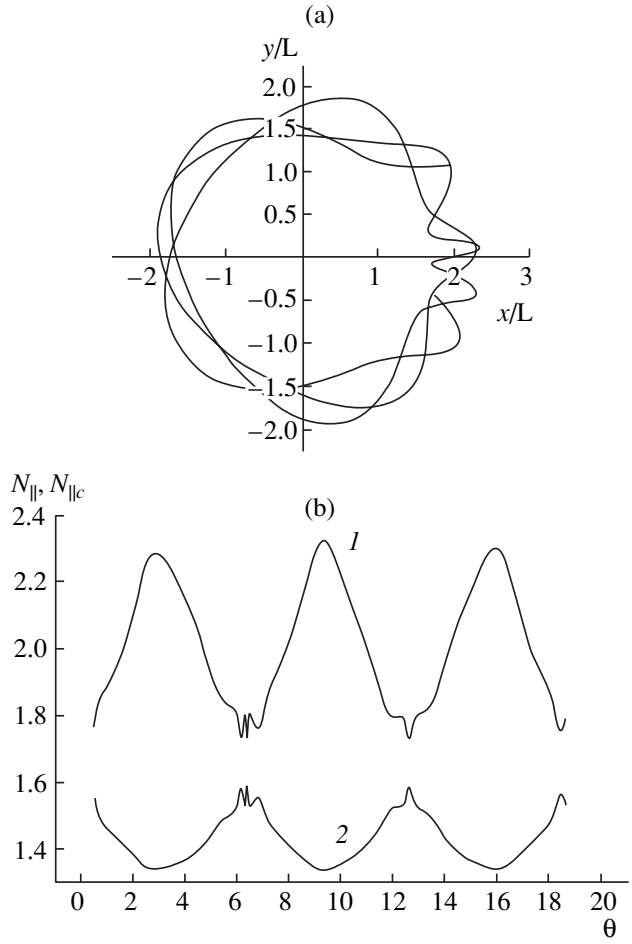

Fig. 4. The same as in Figs. 2 and 3, but for oscillations propagating behind the critical surface ($q > 1$) and for $N_{\|}$ much larger than $N_{\|c}$.

with $N_{\|} \approx N_{\|c}$ should be approximately described by formula (3).

The existence of the transparency region near the critical surface in closed magnetic confinement systems is demonstrated by the calculations of ray trajectories in a tokamak plasma. Let us consider a confinement system that is symmetric in the toroidal angle φ and assume that the cross sections of the magnetic surfaces are concentric circles. Calculations were carried out for the following characteristic parameter values: $\omega = \omega_e/2$, $q(r) = 3\exp(-(r/L)^2)$, and $R_0/L = 6\sqrt{5}$, the safety factor being $rB_\varphi/R_0B_\theta = 3$.

In toroidal systems, the magnetic field is non-one-dimensional, $\mathbf{B} = (0, B_\theta, B_\varphi)$, and its strength depends on the poloidal angle, $B \approx B_\varphi \approx B_0(1 - r/R_0\cos\theta)$. For this reason, the quantities $N_{\|}$ and $N_{\|c}$ also depend on the poloidal angle θ; moreover, the first quantity $N_{\|} \approx N_\varphi(1 - r/R_0\cos\theta)/R_0$ is maximum at the inner circumference of the torus, while the second quantity $N_{\|c} \approx (\omega_e/(\omega_e - \omega))^{1/2}$ is maximum at the outer circumference. Consequently, if $N_{\|}$ and $N_{\|c}$ differ only slightly, then the oscillations with $N_{\|} < N_{\|c}$ should propagate ahead of the critical surface ($\omega_{pe} < \omega$) and, accordingly, can be localized on the outer side of the torus, while the oscillations with $N_{\|} > N_{\|c}$ should propagate behind the critical surface ($\omega_{pe} > \omega$) and, accordingly, can be localized on the inner side of the torus (Figs. 2, 3). On the other hand, if $N_{\|}$ and $N_{\|c}$ differ markedly from one another, then the oscillations propagate over the full length of the torus along the toroidal axis (Fig. 4).

In magnetic confinement systems, the plasma is often nonequilibrium. Tokamak plasmas may contain beams of runaway electrons, which may even acquire relativistic energy. The anisotropy of the electron velocity distribution function in a confined plasma is associated with ECR heating.

A characteristic feature of plasmas with charged-particle beams is the excitation of potential oscillations propagating parallel to the beam. Near the critical sur-

face, the oscillations under study are also potential. Note that such oscillations can grow via the Cherenkov mechanism because their longitudinal refractive index is larger than unity. In a plasma with an anisotropic distribution function, oscillations propagating obliquely to the magnetic field, as well as circularly polarized oscillations propagating along the magnetic field, are unstable. Our analysis shows that these properties are peculiar to oscillations propagating in regions far from the critical surface. Hence, we can expect the oscillations under discussion to be excited spontaneously in toroidal confinement systems.

REFERENCES

1. A. D. Piliya and V. I. Fedorov, in *High-Frequency Plasma Heating*, Ed. by A. G. Litvak (Inst. Prikl. Fiz., Gorki, 1983), p. 281.
2. A. V. Timofeev, Fiz. Plazmy **26**, 874 (2000) [Plasma Phys. Rep. **26**, 820 (2000)].
3. L. D. Landau and E. M. Lifshitz, *Fluid Mechanics* (Nauka, Moscow, 1986; Pergamon, New York, 1987).

Translated by O.E. Khadin

Plasma Physics Reports, Vol. 27, No. 3, 2001, pp. 270–271. Translated from Fizika Plazmy, Vol. 27, No. 3, 2001, pp. 287–288.

Al'bert Abubakirovich Galeev (In Honor of His 60th Birthday)

On October 19, 2000, we celebrated the 60th birthday of Academician Al'bert Abubakirovich Galeev, a member of our Editorial Board, an eminent theoretical physicist, and Director of the Institute for Space Research of the Russian Academy of Sciences.

A.A. Galeev was born in the city of Ufa in 1940. After completing school with a gold medal, he entered the Moscow Power Engineering Institute, from which he transferred to the Physics Department at Novosibirsk State University on the initiative of R.Z. Sagdeev. After graduating in 1963, he worked at the Institute of Nuclear Physics, which was founded by G.I. Budker. By 1964, he had already defended his candidate's dissertation and, in less than four years, he defended his doctoral dissertation. In 1970, he moved to Moscow, where he worked first at the Institute of High Temperatures of the Academy of Sciences of the USSR and, since 1973, at the Institute for Space Research, where he was head of the Department of Solar–Terrestrial Physics. In 1988, he was elected director of the Institute by his colleagues. In 1992, A.A. Galeev was elected a member of the Russian Academy of Sciences.

The development of A.A. Galeev as a scientist proceeded under the guidance of academicians G.I. Budker and R.Z. Sagdeev. His first paper, which was written together with V.N. Oraevskiĭ, was published in 1962 while he was a student of Novosibirsk State University. During his work at the Institute of Nuclear Physics, A.A. Galeev together with V.I. Karpman developed a theory of the weak interaction of plasma waves, which became one of the building blocks of the theory of weak plasma turbulence. This important contribution to scientific research was highly evaluated. In 1967, A.A. Galeev, being a young scientist, was awarded the Lenin Komsomol Prize for a series of papers on plasma turbulence. Together with R.Z. Sagdeev, he developed the neoclassical theory of transport processes in tokamaks. For this work, which today has become classic, he and several other scientists were awarded the 1984 Lenin Prize in science and engineering. Together with V.N. Oraevskiĭ and R.Z. Sagdeev, he contributed greatly to the solution of the problem of the universal instability of a nonuniform plasma and, together with S.S. Moiseev and R.Z. Sagdeev, to the solution of the problem of anomalous plasma diffusion.

A large number of investigations on space plasma physics were carried out by A.A. Galeev at the Institute for Space Research. Together with his students and colleagues, he developed a model of the interaction of solar wind with comets; in particular, a hybrid model of solar wind loading by comet ions revealed the important role of charge exchange processes in the comet coma. They developed a consistent theory of the ionization of a rarefied gas by a magnetized plasma flowing with a velocity exceeding the critical value (Alfvén phenomenon) and studied the dynamics of magnetic reconnection in planetary magnetospheres. Galeev's research on the tearing instability, carried out in collaboration with L.M. Zelenyĭ, led to the discovery of explosive reconnection (magnetic burst), accompanied by the generation of fast ions with energies of up to several MeV. This theoretical prediction was then verified by processing the data from numerous space experiments and has been of fundamental importance in the planning of the Interball space project. The acceleration of the fast solar wind from coronal holes by Alfvén waves was also investigated. Together with R.Z. Sagdeev, V.D. Shapiro, and V.I. Shevchenko, he developed the theory of strong Langmuir turbulence and electromagnetic wave generation during the relaxation of charged-particle beams in a plasma. He also studied the dynamics of beam–plasma discharge during the injection of electron beams from space vehicles into the ionosphere.

A.A. Galeev made an important contribution to plasma astrophysics. Lynden-Bell (1969) and Galeev

1063-780X/01/2703-0270$21.00 © 2001 MAIK "Nauka/Interperiodica"

(1979) were the first to understand that magnetic bursts may occur in accretion disks. Later, Galeev, Rosner, and Vaiana showed that the coronas of the accretion disks of black holes contain magnetoplasma loops, which are heated to high temperatures due to magnetic reconnection, as is the case in solar coronal loops. In particular, magnetoplasma loops formed in high-luminosity accretion disks experience Compton cooling, whereas Compton scattering of soft X radiation from the accretion disk results in bursts of hard X radiation observed in experiments. In order to interpret the observed generation of ultrarelativistic electrons, an ion–electron mechanism for charged-particle acceleration was proposed. It was shown that the ions reflected from the front of a collisionless shock wave can excite lower hybrid waves, which, in turn, can accelerate suprathermal electrons along the magnetic field lines up to ultrahigh energies.

It is worth noting that the theoretical investigations by A.A. Galeev are closely related to space experiments. He took part in a series of international space projects. In particular, he was the deputy research manager of the Vega project; the research manager of the Prognoz-8, Intershock, Interball, and Mars-96 projects; and a participant in the Phobos project. The theoretical investigations by A.A. Galeev laid the basis for two international projects performed onboard the Prognoz-8 and Prognoz-10–Intershock spacecrafts, which were specially designed to study shock waves receding from the Earth. The results of these experiments yielded new insights into the physical processes occurring in shock fronts at high Mach numbers and the mechanisms for charged-particle acceleration.

The great contributions of Academician A.A. Galeev to scientific research have been widely recognized: he is a member of the Max Planck Society, European Academy of Sciences, International Academy of Astronautics, and Tsiolkovsky Academy of Cosmonautics. In 1993, he was awarded a doctor *honoris causa* of the University of Paris. In 1996, he won the von Karman Prize of the International Academy of Astronautics, and, in 1997, he received the Alexander von Humboldt Prize. For his participation in the Venus–Halley's comet project, he was awarded the Order of the Red Banner of Labor. A.A. Galeev is a member of the Bureau of the Department of General Physics and Astronomy of the Russian Academy of Sciences, a member of the Expert Committee of the Max Planck Institute for Extraterrestrial Physics, and a member of the Editorial Board of *Space Science Review.* He is also the chairman of the section "The Solar System's Planets and Small Bodies" of the Space Committee of the Russian Academy of Sciences.

Since 1964, A.A. Galeev has been teaching continuously, first, at Novosibirsk State University and, then, at the Moscow Institute for Physics and Technology. He has formed his own school in space plasma physics, and among his students are doctors and candidates of science. Being a member of the Editorial Board of *Plasma Physics Reports*, he has helped greatly to enhance the prestige of the journal.

As a head of the Institute for Space Research, A.A. Galeev is currently working on new projects, in particular, the Phobos–Grunt, Interball-3, Resonance, and Roy projects.

The colleagues and friends of Al'bert Abubakirovich heartily congratulate him on his birthday and wish him robust health, many happy days, and further success in scientific, pedagogical, and administrative activities.

V.M. Balebanov, A.A. Boyarchuk, N.S. Erokhin, V.E. Zakharov, L.M. Zelenyĭ, V.I. Karas', B.Coppi, É.P. Kruglyakov, R.A.Kovrazhkin, E.A. Kuznetsov, A.G. Litvak, J.G. Lominadze, G.A. Mesyats, A.B. Mikhaĭlovskiĭ, E.V. Mishin, S.S. Moiseev, V.N. Oraevskiĭ, O.A. Pokhotelov, R.Z. Sagdeev, K.N. Stepanov, R.A. Syunyaev, Ya.B. Faĭnberg, and A.M. Fridman